Manufacturing of Pyrochlore ($A_2B_2O_7$) Nanoparticles using Sol Gel Method

by

Suneela Sardar

Submitted in accordance with the requirements for the degree of

Doctor of Philosophy

School of Chemical and Process Engineering

The University of Leeds

August, 2020

Publications

1. **Suneela Sardar,** Girish Kale, Mojtaba Ghadiri 'Microstructure and impedance spectroscopy of high density holmium hafnate ($Ho_2Hf_2O_7$) from nanoparticulate compacts' *Materials Science and Engineering B, Volume 265, March 2021, 114989.*

2. **Suneela Sardar,** Girish Kale, Mojtaba Ghadiri, 'Influence of processing conditions on the ionic conductivity of holmium zirconate ($Ho_2Zr_2O_7$)' *Ceramics International, 46:8 (2020), pp. 11508-11514.*

3. **Suneela Sardar,** Girish Kale, Oscar Cespedes, Mojtaba Ghadiri, **'**Environmentally sustainable facile synthesis of nanocrystalline holmium hafnate ($Ho_2Hf_2O_7$): Promising new oxide ion conducting solid electrolyte' *SN Applied Sciences, 2:541 (2020).*

4. **Suneela Sardar**, Girish Kale, Mojtaba Ghadiri, Oscar Cespedes, 'Structural study of holmium zirconate nanoparticles obtained through carbon neutral sol gel method' *Thermochimica Acta, 676 (2019), pp. 120-12.*

Acknowledgement

First of all I thank Allah (SWT) for all the blessings and enabling me to reach this stage. I want to thank my worthy supervisors Dr Girish Kale and Professor Mojtaba Ghadiri for their guidance, support and encouragement. Special thanks to them for the hard work they put in mentoring me.

I would like to thank all the staff, group members and friends for their help in carrying out different activities. I like to acknowledge Dr Oscar Cespedes from School of Physics and Astronomy for his support in Raman analysis.

Financial support from Commonwealth Scholarship Commission is greatly appreciated and I would like to take this opportunity to thank Professor Mojtaba Ghadiri for all the financial and moral support.

I am really fortunate to have an amazing husband and cannot thank enough for his absolute love and cooperation in making things happen.

In the end, I love to thank my devoted and ever praying mother, lovely kids, cool brother and other family members for their love and support.

Abstract

Pyrochlores have been considered as an important class of electrolyte materials for solid oxide fuel cell (SOFC), gas sensors and oxygen separation membranes. In this research, ionic conductivities of $A_2B_2O_7$ type materials have been investigated to check their suitability as an electrolyte materials of SOFC. Nanopowders of four different pyrochlore materials have been synthesised using sodium alginate mediated sol-gel process, and their properties have been evaluated for use in the intermediate-temperature Solid Oxide Fuel Cell (IT-SOFC) applications. Sodium alginate based ion exchange process was used to synthesise high purity nanopowders of holmium hafnate ($Ho_2Hf_2O_7$), holmium zirconate ($Ho_2Zr_2O_7$), lanthanum hafnate ($La_2Hf_2O_7$) and lanthanum zirconate ($La_2Zr_2O_7$) after calcining the dried gel. Dried gel was analysed using simultaneous thermogravimetric analysis and differential thermal scanning calorimetry (TGA/DSC) and high temperature X-ray diffraction (HT-XRD) to determine the evolution of crystallite structure as a function of calcination temperature. Nano-crystalline powders of high purity, single phase holmium hafnate and holmium zirconate were obtained by calcining the dried gel at 700°C and lanthanum hafnate and lanthanum zirconate at 900°C. Rietveld refinement of X-ray diffraction (XRD) data confirmed the formation of single phase defect fluorite structure of $Ho_2Hf_2O_7$ and $Ho_2Zr_2O_7$ and evidence of presence of oxygen ion vacancy was supported by Raman spectroscopy. $La_2Hf_2O_7$ and $La_2Zr_2O_7$ has the cubic pyrochlore structure as confirmed by XRD and transmission electron microscopy (TEM).

Microstructural and ac-impedance analyses of sintered pellets were carried out to confirm their suitability for fuel cell applications. Holmium based materials can be considered as a promising new oxide ion conducting solid electrolyte for IT-SOFC. Lanthanum based materials showed lower ionic conductivities than holmium based materials.

Process description of the sol gel method along with theoretical detail on kinetic study of diffusion have also been provided. Evolved gas analysis (EGA) from TGA were also carried

out for holmium hafnate to estimate from the gaseous emission for mass and energy balance of the process.

Sodium alginate based sol-gel method, also named as Leeds alginate Process (LAP), has the capability of consistently yielding the single phase nanoparticles of electrolyte materials for SOFC in environmentally sustainable, cost effective and energy efficiently manner.

Table of Contents

List of Tables

List of Figures

Nomenclature

Na-ALG	Sodium Alginate
SOFCs	Solid Oxide Fuel Cells
DSC	Differential Scanning Calorimetry
GOF	Goodness of Fit
LAP	Leeds Alginate Process
SAED	Selected Area Electron Diffraction
SEM	Scanning Electron Microscopy
TEM	Transmission Electron Microscopy
GMS	Gatan Microscopy Suite
TGA	Thermogravimetric Analysis
HT-XRD	High Temperature X-ray Diffraction
XRD	X-ray Diffraction
d(hkl)	Interplanar spacing (nm) of the plane (hkl)
Rexp	Expected residual factor (%)
Rwp	Weight residual (%)
λ	Wavelength (nm)
SSS	Single Step Sintering
TSS	Two Step Sintering

Chapter 1

Introduction

The Solid Oxide Fuel Cell (SOFC) produces electricity efficiently through direct conversion of chemical energy with low level of pollutant emission. As compared to other types of fuel cells such as proton exchange membrane fuel cell (PEMFC), alkaline fuel cell (AFC) and phosphoric acid fuel cell (PAFC), a SOFC is based on solid oxide electrolyte and is a solid state fuel cell [1]. SOFC is capable of direct utilization of large variety of fuels from hydrogen, natural gas, coal gas, reformed gasoline and diesel and, gasified carbonaceous solids (biomass and municipal solid waste) [2-3]. SOFCs are simple, reliable, environmental safe and efficient; exhibit up to 85% efficiency in combination with gas turbines as compared to engines and modern thermal power plants (30%) [4]. However, high temperature operation in SOFC may cause problem of accelerating corrosion and fracturing of components as tough and chemically unreactive materials are required for high temperature operation. To overcome this issue specialized materials for different parts of cell are required [5]. SOFC overpotentials are strongly affected by structural parameters, such as the thickness and porosity of the electrode, and by operating parameters, such as pressure and temperature. Electrolyte having high ionic conductivity with transport number of ions close to unity and a transport number of electrons close to zero is significant in lowering the operating temperature and maintaining high conversion efficiency of SOFC [6].

Lanthanide based pyrochlores are emerging as an important class of solid oxide material with potential applications as solid electrolytes. Oxide pyrochlores found their applications as antireflective/protective coatings and refractory matrices for optical devices, dielectric ceramics for microwave wireless communication devices, nuclear waste-storage materials, catalysts and oxygen conductors in fuel cells [7]. Ternary oxides having general formula of

$A_2B_2O_7$ depict crystal structure of pyrochlore type. Larger and trivalent rare earth elements with 8-coordinated cations occupy A-site. Smaller and tetravalent transition metals with 6-coordinated cations like Zr, Ti and Hf occupy site-B [8]. Pyrochlore stability can be predicted by tolerance factor which is cations ionic radius ratio (r_A/r_B). For lanthanide pyrochlores the disordered phase forms at equilibrium when $r_A/r_B < 1.46$ [9]. Pyrochlore structured compositions have a large range of technically important properties, such as high ionic conductivity, superconductivity, luminescence and ferromagnetism [10]. These applications are due to the flexibility of pyrochlore structure and specifically mobility of anions [7].

Synthesis of Zirconates and Hafnates of Holmium (Ho) and Lanthanum (La) through the sol-gel method [11-13] and studying the oxygen vacancy of pyrochlore in defect fluorite structure help to enhance the ionic conductivity of the material and reducing the temperature for nanoparticles synthesis. Synthesising the materials with sol-gel and solution methods enhance the understanding and significance of sol gel technique. Solution method involves the heating of aqueous solutions of metals salts on hot plate to remove the water followed by calcination process to obtain the powders of the materials. Studying the effect of different parameters help to change the properties of final product for more efficient applications.

1.1. Description of Research:

The overall aim of this research programme is preparation and characterisation of hafnates and zirconates of holmium and lanthanum. The composite materials such as holmium hafnate and holmium zirconate, prepared through a novel synthesis technique based on the sol-gel method, [11-13] act as electrolyte materials of SOFC and leads to lowering the operating temperature and good electrochemical behaviour with improved ionic conductivity.

In this research work nanopowders of pyrochlore based materials like holmium hafnate ($Ho_2Hf_2O_7$), holmium zirconate ($Ho_2Zr_2O_7$), lanthanum hafnate ($La_2Hf_2O_7$) and lanthanum

zirconate ($La_2Zr_2O_7$) have been prepared using the sodium alginate based synthesis method which is also called Leeds Alginate Process (LAP). This method has been developed and extensively researched by Kale and co-workers [11-13]. Metal nitrate salts solution is prepared as sodium alginate is soluble in water to the extent of 3 to 10 wt. % depending upon the molecular weight forming a viscous colloidal solution [14]. Drops of sodium alginate solution are introduced in the metal nitrate salts solution. Ion-exchange process takes place and sodium ion in the sodium alginate bead is replaced by metal ions from the solution. After this ion-exchange process metal ion beads are collected, washed with distilled water and dried in the oven. Metal ions become immobile. After that beads are calcined at specific temperature for certain time to obtain the metal oxide nanopowders. The collapse of gel structure results in small nanoparticles at comparatively low temperature. The energy required to heat the dried beads for calcination can be obtained from the specific heat emitted during the oxidation of alginate.

Studying the thermal response of materials with rise in temperature is also part of this research work which helps to understand the structural transformation of materials.

Grain growth and densification affected the microstructural properties of the materials which ultimately affected the electrical properties. So to understand them, single step and two step sintering techniques have been used. These helped to find out the optimum sintering temperature and time for the materials to obtain the best microstructure for electrical properties.

This research work has compared the findings of holmium hafnate and lanthanum hafnate prepared from solution method and LAP.

The findings have proved that LAP is simple, efficient, environment friendly and cost effective technique to synthesise ternary pyrochlore based complex metal oxides ($Ho_2Hf_2O_7$, $Ho_2Zr_2O_7$,

3

$La_2Hf_2O_7$ and $La_2Zr_2O_7$) as well as simple metal oxides like Ho_2O_3, HfO_2, La_2O_3 and ZrO_2 which is also part of this thesis.

1.2. Structure of Thesis:

This thesis report consists of seven chapters including Introduction, Literature Review, Experimental Detail, Results and Discussions, Comparison, Process Detail and Conclusions & Future work.

Chapter 1 covers a brief introduction of the topic along with description of research work carried out and structure of thesis. Chapter 2 focuses on literature search regarding SOFC, its components and different electrolyte materials for SOFC. It also includes some literature on sol-gel method and other methods. Significance of sol-gel method with its advantages and disadvantages is also included. Literature related to ion-exchange kinetics and effect of temperature on the structure and densification of materials is also part of this chapter.

Chapter 3 gives the detailed description of methodology and different characterization techniques used in this study. Detail on both synthesis methods such as sodium alginate mediated Leeds Alginate Process (LAP) and solution method described here. It also includes the synthesis of granules and material synthesis from granules. Working principle and theories of different analytical techniques like simultaneous TGA/DSC, HT-XRD, powder XRD along with Rietveld size/strain structural refinement, Raman spectroscopy and Transmission Electron Microscopy (TEM) are also part of this chapter. Details on the techniques to study microstructural and electrical properties such as sintering, density measurement, Scanning Electron Microscopy (SEM) and Impedance Spectroscopy (IS) are also part of this chapter.

Chapter 4 provides results and discussions on the findings of various pyrochlore nanoparticles synthesized from the called Leeds Alginate Process (LAP). It includes the details on characterization, microstructural properties and electrical properties of holmium hafnate

($Ho_2Hf_2O_7$), holmium zirconate ($Ho_2Zr_2O_7$), lanthanum hafnate ($La_2Hf_2O_7$) and lanthanum zirconate ($La_2Zr_2O_7$). This chapter also includes the synthesis and characterization of metal oxides of holmium oxide (Ho_2O_3), hafnium oxide (HfO_2), lanthanum oxide (La_2O_3) and zirconium oxides (ZrO_2). These are also called the parent oxides of the materials chosen for research.

Chapter 5 compares both synthesis methods; i.e. the LAP and solution method. This chapter compares the findings of holmium hafnate and lanthanum hafnate nanoparticles obtained from both methods. Process details of LAP is mentioned in Chapter 6 along with evolved gas analysis (EGA) and process block diagram.

In Chapter 7 the conclusions of this research work are described, also including the suggestions on the future research directions. Reference list is given at the end of the thesis.

Chapter 2

Literature Review

The development in Solid Oxide Fuel Cell (SOFC) is a remarkable area for research. This research area involves the concepts and knowledge from different fields like chemical engineering, materials science and electrochemistry. Finding the high performance and efficient materials for SOFC development is a key area of research now a days. Nanoparticles are considered attractive materials for SOFC components because of their properties to sinter at low temperature, larger surface area and high mechanical strength. This chapter contains the detailed literature review on SOFC, its working principle, materials for components and preparation methods with detail on sol-gel technique.

2.1. Solid Oxide Fuel Cell (SOFC)

Fuel cell is an electrochemical device which directly converts the chemical energy of fuel to electricity. A solid oxide fuel cell (SOFC) is based on a solid oxide electrolyte hence an all solid state fuel cell compared to other types of fuel cells. SOFCs are an efficient producer of electrical energy with least impact on environment. As the emissions are minimum so considered environmentally safe.

Many types of fuel cells have been studied throughout the years. Components of a single cell are two electrodes; cathode and anode separated by a solid oxide electrolyte (an ionic conductor). Electrodes are porous and at SOFC operating temperature they exhibit electronic conductivity and ionic conductivity as well. Electrolyte layer conducts ions and charged atoms from one side to other [15].

Different fuel cells are identified on the basis of their electrode and electrolyte materials. Comparison of different fuel cells is made in Table 2.1.

Table 2.1: Comparison of different fuel cells [16] [17] [18]

Type of Fuel Cell	Operating Temp. °C	Electrolyte	Fuels/ Anode Gas	Oxidant/ Cathode Gas	Refor-ming	Electric Effici-ency %	Power kW	Features/ Applications
PEMFC (Proton Exchange Membrane) Fuel Cell	60-110 Upto 200	Polymer-water based Acid based	H_2	O_2/ Atmospheric O_2	External	50-70	0.01-250	Portable, Mobile, Low Power Generation
AFC (Alkaline Fuel Cell)	50-250	Potassium Hydroxide	H_2	O_2	External	35-70	0.1-50	Mobile, Military, Space Vehicles
PAFC (Phosphoric Acid Fuel Cell)	175-210	Phosphoric Acid	H_2	Atmospheric O_2	External	35-50	50-1000	Medium to Large Scale Power generation and CHP(Combined Heat and Power)
MCFC (Molten Carbonate Fuel Cell)	550-650	Molten Alkali Carbonates	H_2	Atmospheric O_2	External / Internal	50-60	200-100,000	Large Scale Power generation and CHP

Type of Fuel Cell	Operating Temp. °C	Electrolyte	Fuels/ Anode Gas	Oxidant/ Cathode Gas	Refor-ming	Electric Effici-ency %	Power kW	Features/ Applications
SOFC (Solid Oxide Fuel Cell).	500-1000	Ceramic Oxide	H_2, CH_4	Atmospheric O_2	External / Internal	40-72	0.5-2000	Vehicle Auxiliary Power units, Medium to Large scale Power generation and CHP, Off-grid power and micro CHP
DMFC(Direct Methanol Fuel Cell)	70-130	Solid Polymer	CH_3OH in H_2O	Atmospheric O_2	External /Internal	35-40	0.001-100	Mobile, Portable, Small CHP

Schematic of solid oxide fuel cell (SOFC) is shown in Fig. 2.1.
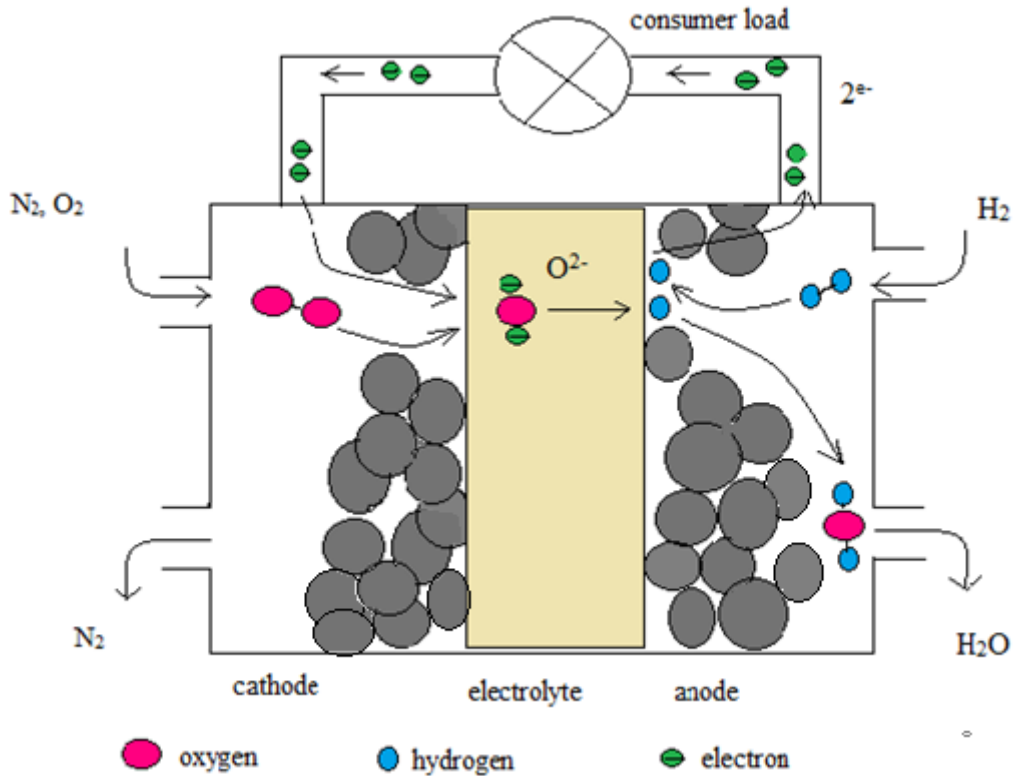
Fig. 2.1: Schematic of a solid oxide fuel cell (SOFC) [19]

Three-phase boundary (TPB) is a site where the actual electrochemical reaction takes place as electronic, ionic conductors and gas phases are in contact with each other. Features of TPB strongly influence the electrochemical performance of cell.

Single cell under open circuit conditions with air at cathode and pure hydrogen at anode has the ideal voltage of 1.01 V at 800 °C calculated using Nernst equation [20]. Equation 2.1 shows the useful voltage output (V) under operation

$$V = E° - IR - \eta_c - \eta_a \tag{2.1}$$

where $E°$ is the ideal voltage, I is the current passing through the cell, R cell resistance, η_c and η_a are cathode and anode polarization losses respectively shown in Fig. 2.2 [21]
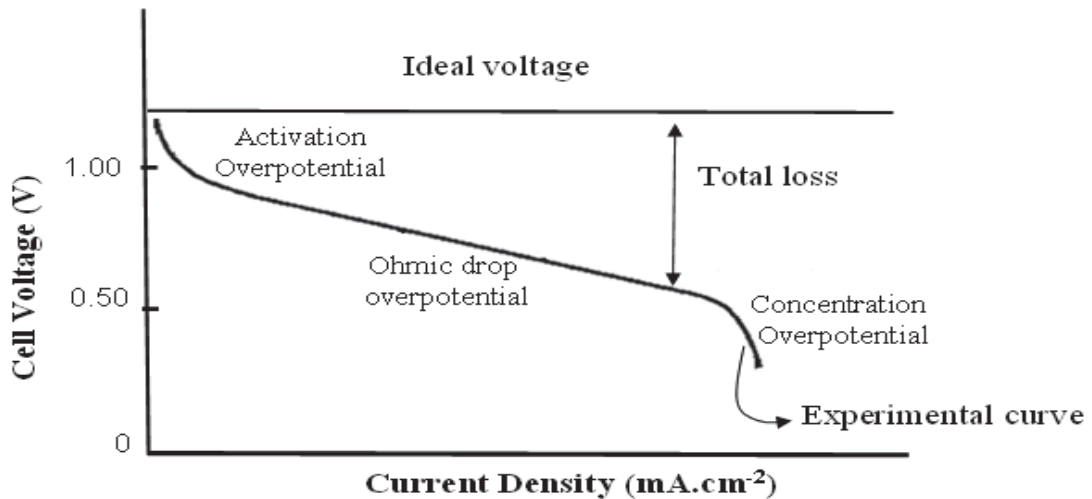
Fig. 2.2: Fuel cell voltage-current characteristic at 800ºC using pure hydrogen as fuel

[21]

2.2. SOFC Components

2.2.1. Cathode

One of the SOFC electrode is cathode and electrochemical reduction of oxygen occurs here.

Following working specifications cathode must have: [22-26]

1. Well matched thermal expansion coefficient (TEC) with other components

2. Under operating conditions should be chemically compatible with other contacting components

3. Large three-phase boundaries

4. For oxygen reduction reaction high catalytic activity

5. Under oxidizing atmosphere chemical and microstructure stability required throughout the operation and fabrication

6. Binding/adhesion to electrolyte surface

7. Good conductor of ions and electrons

8. Sufficient porosity for oxygen diffusion about 30-40%

9. Simple and economical fabrication process

10. Non-volatile

10

In IT-SOFC (Intermediate Temperature SOFC) the low operating temperature reduces oxidative degradation and makes it possible to use metallic interconnects. In contrast the slower electrode kinetics results in large interfacial polarization resistance particularly at cathode. With suitable selection of cathode material and optimization of interface microstructure, cathode polarization losses can be minimized. Due to cathode polarization maximum cell efficiency cannot be achieved. Selection of cathode material is mostly electrolyte dependent. So it is necessary to match the TECs to avoid undesirable chemical reactions at interface. Equation 2.2 shows the reaction at cathode:

$$\frac{1}{2} O_2 \text{ (g)} + 2e^- \text{ (cathode)} \quad \rightarrow \quad O^{2-} \text{ (electrolyte)} \qquad (2.2)$$
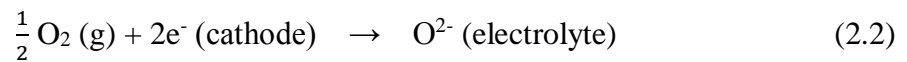
TPB is the site where most of the electrochemical reactions occur. Fig. 2.3 below represented the TPB:
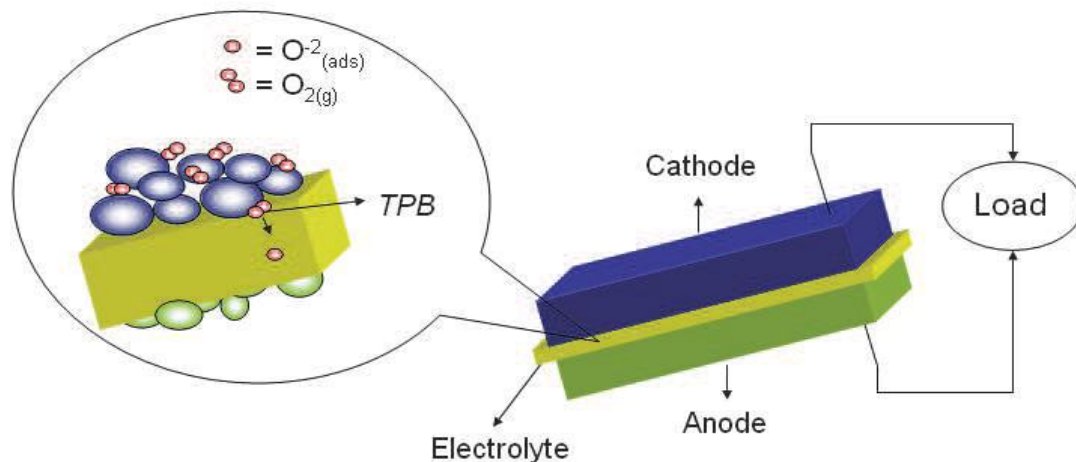
Fig. 2.3: Triple-Phase Boundaries (TPB) [27]

Lanthanum Manganite ($LaMnO_3$) doped appropriately with alkaline earth elements is used to meet the requirements of cathode material [28]. Defect chemistry, behaviour of cathodic polarization and electrical conductivity are characteristics of alkaline earth element doped lanthanum manganite which meets the requirements of an effective air electrode. Skipping of an electron hole between +3 and +4 valence states of Manganese (Mn) is the main reason of

electronic conductivity of LaMnO$_3$. Doping of a divalent ion like calcium or strontium enhances this conductivity [29].

Most commonly used cathode materials are Lanthanum Strontium Manganite (LSM) and Lanthanum Calcium Manganite (LCM) with perovskite structure. These materials have remarkable thermal expansion that matches well with zirconia electrolytes and at operating temperature of above 800 ˚C give adequate performance [30]. Electrodes should be mixed conductor (both ionic and electronic) to lower down the interfacial polarization in case of LSGM electrolyte and LSM (LaSrMnO$_3$) cathode. Oxygen ion conductivity can be enhanced by mixing LSGM with LSM, which is a p-type semiconductor [31].

Miniaturised solid oxide fuel cell (micro-SOFC) are designed using thin film techniques can attain high specific energy and energy density using nanoporous metal electrodes. In micro-SOFC (m-SOFC) strontium doped lanthanum cobalt iron oxide (LSCF) along with LSGM electrolyte has also been used [32]. Mixing LSCF with LSGM would not lower the interfacial polarization significantly as LSCF is a mixed conductor already. There is mismatch of upto 50 % in thermal expansion coefficient of LSGM electrolyte material and LSCF electrode material. In order to lower the interfacial thermal stresses it is necessary that cathode should be a LSCF-LSGM composite electrode. LSCF-LSGM composite cathode yields maximum power density of 5700 W/m^2 at 650 ˚C with thin LSGM electrolyte For possible applications in IT-SOFC numerous cathode materials LSM-LSCF, LSM-LSGM and LSCF-LSGM composite electrodes along with LSGM electrolyte are being used. Using YSZ electrolytes LSCF and LSM cathodes are also used for SOFC [33].

2.2.2. Anode

Electrochemical oxidation of fuel gas takes place at anode in solid oxide fuel cell. A satisfactory anode must have: [34, 27]

1. High electrical conductivity

2. Particle size of anode material should be fine which results in high specific surface area and enhanced reaction at electrode-electrolyte interface

3. Well matched TEC with connecting components

4. Capacity to avoid deposition of coke and sulphur poisoning

5. At operating temperature in reducing atmosphere chemical compatibility with other cell components such as interconnector and electrolyte.

6. Large TPB

7. To oxidise the selected fuel gas, catalytic or electrochemical activity should be high

8. Sufficient high porosity about 20-40% for reaction product removal and fuel supply

9. Good ionic and electronic conductors

10. Low cost and easy fabrication

Reaction at anode is shown in Equations 2.3 & 2.4:

$$H_2 \text{ (g)} \rightarrow 2H^+ + 2e^- \qquad (2.3)$$

$$2H^+ + O^{2-} \rightarrow H_2O \text{ (g)} + 2e^- \qquad (2.4)$$
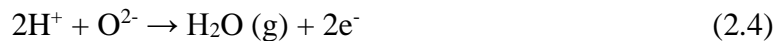
In SOFC, Ni/YSZ cermet is widely used anode material and apply hydrogen as fuel. Reason of this selection is chemical stability, low cost and well matched TEC with YSZ electrolyte. Use of Ni is justified by its relatively low cost and high catalytic activity of H-H bond breaking. Cu, Co and phosphorous composites are also studied as catalytic components but for their effective utilization need to be improved further [34, 35, 21].

Conductivity of cermet takes place under two phases: through YSZ phase (ionic) and through metallic Ni phase (electronic). Conductivity is mainly ionic if Ni concentration is less than 30% in volume and for greater than 30% it is electronic as characterised for metals. Ni/YSZ cermet with a porosity of above 30 % achieves its maximum electrical conductivity [15, 34].

Area Specific Resistance (ASR) of anode is strongly influenced by activation polarization resistance (related to the process of charge transfer), concentration polarization resistance (associated with transportation of gaseous species through electrodes), internal resistance (relevant to transportation of electrons within anode) and contact resistance (due to poor adherence between electrolyte and anode). Performance of anode is mainly dependent on its thickness, number of TPBs and its microstructure (grain morphology, distribution of grain size, porosity, Ni particles connectivity) [29].

Keeping in mind the cell design porous anode layers are used for cell support with different thicknesses, range from 1-3 mm in planar designs.

Ni/YSZ cermet is least tolerant of sulfur and carbon deposition so in SOFC using natural gas, gasoline, methanol and ethanol as fuels is not a good choice. Development of alternate anode materials and reduced operating temperature prevent this problem. Cu anodes based on Cu/Ni alloy are also used but Ni is a better electrocatalyst than Cu and power density of Cu anodes is lower than that with Ni anodes in case of YSZ electrolyte [36]. Activity and stability of Cu based anodes can be enhanced by alloying Cu with second metal and Ni is a good option for this purpose. For direct oxidation of methane (CH_4) many metallic alloys such as (Cu, Co, Fe) and Ni–YSZ, (Ni,Co)–YSZ, (Ni,Fe)–YSZ, (Ni,Cu)–YSZ and (Cu,Co)-YSZ are used as components of cermet [36,37].

Alternate materials with mixed electronic and ionic conductivity are studied as prospective SOFC anodes having ability to reform hydrocarbons. Under reducing atmosphere ceramic based CeO_2 behaves as good mixed conduction material and the reason is reduction of Ce^{+4} to Ce^{+3}. These ceramics are resistant to carbon deposition and have remarkable catalytic activity to reform hydrocarbons. Due to this direct supply of dry hydrocarbons to anode is possible [29].

It is found that CeO_2 based materials have efficient catalytic activity [29] and C-H bonds in hydrocarbons can be easily broken with the addition of Ni, Co or Pt, Rh, Ru, Pd noble metals [29, 25]. With many hydrocarbons Ru-Ni-GDC anodes showed good results when used in ceria based SOFC [38].

SOFC with anode material of Ni-YSZ cermet are more prone to sulfur poisoning at 1000˚C even with H_2S contents as low as 2ppm [39]. It is also reported that 2–15 ppm H_2S impurity deteriorates the electrode at 1000˚C but this poisoning effect is reversible if the H_2S-free fuel is supplied again.

2.2.3. Electrolyte

Electrolyte is an important component of cell which is responsible to conduct predominantly ions between two electrodes, forcing the electron to flow through external circuit to separate reacting gases and for the blockage of internal electronic conduction [26]. Without significant ion conduction, current would pass through the cell and only a lower potential difference would be registered by the cell. On the basis of ion transport mechanism, three types of electrolytes are: protonic, anionic and mixed ionic. Conduction of oxygen ion (O^{2-}) from air to fuel electrode is the basis of operation in many high temperature fuel cells. This conduction takes place due to the oxygen ion vacancy so there must be unoccupied anionic site in the crystallites forming electrolyte. Energy requirement must be small for the oxide ion to migrate from one site to neighbouring unoccupied equivalent site [40].

For adequate performance electrolyte must have following working specification to limit selection of material: [22, 23, 41]

1. At operating temperature, conductivity of oxide ion should be greater than 1 $S.m^{-1}$

2. High density for gas impermeability

3. Compatibility of thermal expansion coefficient (TEC) with electrodes and other components of cell from ambient to operating temperature of cell

4. Electronic conduction should be negligible, thus electronic transport number near to zero

5. Thermodynamically stable over varied temperature and oxygen partial pressure range

6. Reasonable mechanical properties and at room temperature resistance to fracture should be greater than 400 MPa

7. To prevent establishing phases for interface blocking, under operating and fabrication conditions chemical interaction must be least with electrode materials

8. Ability to be expanded as thin layer

9. Economical starting material and process of fabrication

10. High strength and durability

Reactions with electrolyte:

Equations 2.5 to 2.7 are for oxide ion generating reaction:

$$1/2\ O_2\ (g) + 2e^- \quad \rightarrow \quad O^{2-}\ (electrolyte) \qquad (2.5)$$

$$H_2\ (g) + O^{2-} \quad \rightarrow \quad H_2O\ (g) + 2e^- \qquad (2.6)$$

$$2H_2 + O_2 \quad \rightarrow \quad 2H_2O \qquad (2.7)$$

Reaction (2.7) is exothermic in nature and emits 57 kcal per mole of reactant.

For proton generating reactions are shown from Equations 2.8 to 2.10:

$$H_2\ (g) \quad \rightarrow \quad 2H^+ + 2e^- \qquad (2.8)$$

$$1/2\ O_2\ (g) + 2e^- \quad \rightarrow \quad O^{2-} \qquad (2.9)$$

$$2H^+ + O^{2-} \quad \rightarrow \quad H_2O\ (g) \qquad (2.10)$$
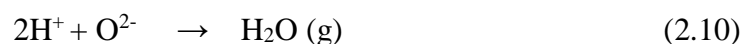
Electrons produce from above reactions flow through external circuit for providing electricity [42].

At high temperatures, most studied and developed electrolytes are ceramic materials of zirconia. Pure zirconia has monoclinic structure at room temperature. Large volume change (3-

5%) (contraction on heating and expansion on cooling, a rare exception to the normal trend) happens and it experiences phase transition to tetragonal structure at 1170 ˚C. It converts to cubic fluorite structure above 2370 ˚C. And it remains cubic till melting point at 2680 ˚C as shown in Equation 2.11. [25, 40]

$$\text{Monoclinic} \quad \xrightarrow{1170˚C} \quad \text{Tetragonal} \quad \xrightarrow{2370˚C} \quad \text{Cubic} \quad \xrightarrow{2680˚C} \quad \text{Molten Phase} \quad (2.11)$$
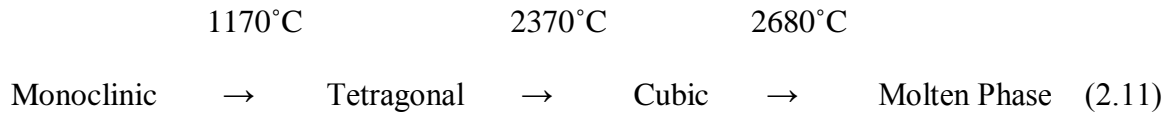
The fluorite lattice is an interpretation of cubic oxygen lattice in the middle of face centred cubic zirconium lattice as shown in Fig. 2.4.
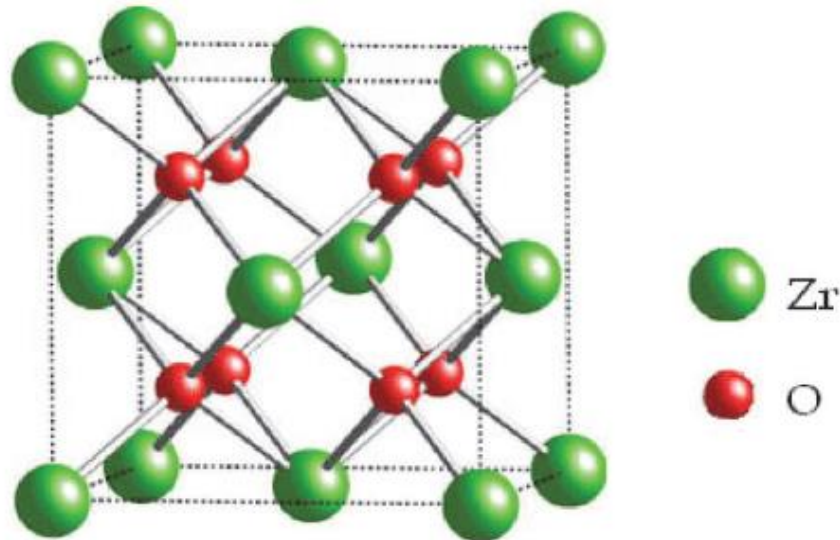
Fig. 2.4: Unit cell of zirconia fluorite (Adapted from Crystal Maker ® Demonstration version)

2.2.3.1. Oxide ion conducting electrolytes

Extensive range of materials come under this category of electrolytes mainly include; fluorite, perovskite and brownmillerite structured materials.

2.2.3.2. Fluorite structured electrolytes

Ceria and zirconia related materials are widely studied for SOFC electrolytes as ceria adopts the fluorite structure at room temperature and zirconia at high temperature [43]. By adding

divalent and trivalent cations cubic structure of zirconia is stabilized at room temperature [44, 45]. At room temperature ceria forms solid solutions of fluorite structure with divalent and trivalent cations to enhance the ionic conduction [46]. YSZ is not the best ionic conductor [47]. Oxide materials based on bismuth, ceria and strontium doped lanthanum show better conductivity than shown by zirconia based materials [48]. Amongst these δ-Bi_2O_3 materials have structure of oxygen deficient fluorite and $1/4^{th}$ of normal anion sites are vacant. Very high conductivity is due to this vacancy. Chemical instability is its drawback. Its structure is cubic at high temperature and monoclinic at room temperature. At low oxygen partial pressure it reduces easily and if oxygen partial pressure ranges less than 10^{-8} Pa it decomposes to bismuth metal [49, 50]. Using bismuth oxides as SOFC electrolyte is not very practical due to the volatility of bismuth oxide at high temperature. Sintering of bismuth oxide materials is a problem too as the toxic nature of vapours further add to the difficulty. Materials based on ceria and zirconia are considered better for SOFC electrolyte application.

2.2.3.3. Zirconia based oxide ion conductors

Characteristics of solid electrolytes for high temperature fuel cell must be good oxide ion conductivity and no conduction of electrons, non-porous, high mechanical strength, phase stability, resistant to thermal shock, chemically inert towards reactive gas, well matched TEC with electrodes and chemically inert towards electrodes. Doped zirconia appropriately meets these characteristics. At room temperature monoclinic zirconia is stabilized to cubic fluorite phase with the addition of lanthanide and alkaline earth oxides. This also enhances conduction of ions for SOFC operation over an extended range of oxygen partial pressure.

For high temperature operation any SOFC electrolyte has to face high pressure at anode side. Because of its poor mechanical strength and conduction of electrons doped ceria is not successful in this situation. Yttria (Y_2O_3), scandia (Sc_2O_3), magnesia (MgO) and calcia (CaO) are mostly used dopants for zirconia. Over a wide temperature range stabilized zirconia remains

stable and ionic conductivity does not depend on oxygen partial pressure for several order of magnitude [51, 52].

2.2.3.4. Ceria-based oxide ion conductors

For IT-SOFC 500-750˚C electrolytes based on ceria materials have potential application because of their higher ionic conductivity [53]. As compared to high temperature SOFC, IT-SOFC is favourable. With reduced temperature additional benefits are achieved: less tendency for mechanical and thermal stresses, shortened start-up time, maintained easily, good range of selecting materials, economical, thermal management is better and impact of thermally activated process is least [54]. Problems associated with ceria based materials are that they tend to reduce at low oxygen partial pressure, which is prevalent on the anode side of SOFC, that leads to electronic conductivity [55] and possible high mechanical disintegration under large oxygen chemical potential gradients typical of SOFC operation [56,57]. This problem can be solved by decreasing operating temperature to below 650° to 700°C.

2.2.3.5. Perovskite-structured oxide ion conductors

For SOFC doped perovskite materials (ABO_3) are used as solid electrolyte materials. Highest oxide ion conductivity is demonstrated by calcium titanate ($CaTiO_3$) when doped with Mg or Al [58]. Lanthanum strontium gallium magnesium oxides ($La_{0.9}Sr_{0.1}Ga_{0.8}Mg_{0.2}O_3$) exhibit lower oxide ion conductivity than the ion conductors based on Bi_2O_3 [59, 60]. This material shows limited conduction of oxide ion and conduction of electrons up to oxygen partial pressure of 10^{-18} Pa[61], but it possess poor mechanical strength [62, 63]. YSZ electrolyte based sensors does not show much difference in the sensitivity from that of the ScSZ-electrolyte ones. However, the sensor utilizing the perovskite-type oxygen ion conductor (LSGM) $La_{0.85}Sr_{0.15}Ga_{0.8}Mg_{0.2}O_{(3-0.35/2)}$ displays much lower sensitivity and much slower response to the test gas than those based on stabilized zirconia [64].

2.2.3.6. Brownmillerite-structured oxide ion conductors

General formula of this material is $A_2B_2O_5$ or $A_2B'B''O_5$. It has vacancy at $1/6^{th}$ oxygen site with perovskite structure. In this group $Ba_2Ln_2O_5$ is significant for SOFC applications. These materials are more conductive than oxides with fluorite structure [65]. Hole is major carrier of electrical conductivity beyond oxygen partial pressure of 101.3 Pa. Conductivity in this material is highly increased at 900°C. This can be related to convention from ordered brownmillerite with oxygen vacancy to oxygen disordered pseudo-perovskite structure. Proton conduction is also shown by this material below 400°C. Proton conduction is due to $Ba_2Ln_2O_5.H_2O$ [66, 67]. Thermodynamic properties of cuprous and cupric yttrates ($CuYO_2$ and $Cu_2Y_2O_5$) and oxygen potentials corresponding to three phase field in the Cu-Y-O system using the solid state galvanic cell in the presence of YSZ solid electrolyte over the temperature range of 873 – 1323 K have studied. The oxygen potentials corresponding to the coexistence of phases are found to be the same over the measurement temperature range thus indicating the negligible solid solubility of Y_2O_3 in $CuYO_2$ and $Cu_2Y_2O_5$ [68].

2.2.3.7. Pyrochlore structured oxide ion conductors

Pyrochlore materials are used as oxygen electrodes and solid electrolytes in fuel cells [69]. Fundamentally, pyrochlore compounds are characteristic ionic conductors and their properties can be changed by varying the processing conditions and with the doping of different elements on various sites. Altered materials can also be used in SOFC as solid electrolytes [70].

Binary oxides having general formula $A_2B_2O_7$ exhibit crystal structure of pyrochlore type. Pyrochlore structure results after removing oxygen anion at 8a site from fluorite and ordering in cation sub lattice. As a result ordered pyrochlore structure (space group Fd3m) can be separated from fluorite with space group Fm3m by the super lattice coming from ordering both ionic and cationic arrays. Larger, trivalent and 8-coordinated cations occupy site-A, mostly rare earth elements. Cations at site-B are smaller, tetravalent and 6-coordinated; transition metals [71]. For a pyrochlore type oxides many combinations of chemical compositions are possible.

When the ratio of ionic radii $r = r_A/r_B$ is ranging between 1.46 and 1.78, ordered structure occurs. From La to Gd pyrochlore structure is stable in zirconates. Superlattice does not occur in smaller lanthanides but stoichiometry is same due to lack of 1/8 oxygen ions in relation to MO_2 fluorite. Usually these compounds are stated as defected fluorite or disordered pyrochlores [72]. Fig. 2.5 below represents this.
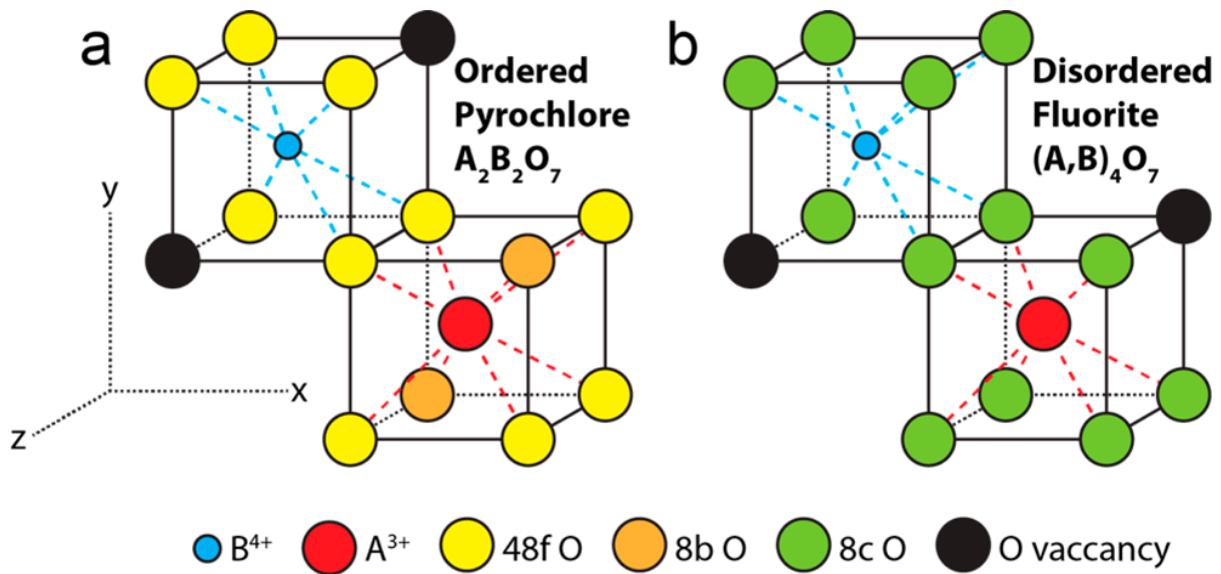
Fig. 2.5: Crystal structure of (a) Ordered Pyrochlore, in which all of the A^{3+} ions occupy at the A-site with 8-Fold Coordination with oxygen and the smaller B^{4+} cations occupy at the B-Site and have 6-Fold Coordination with oxygen, and (b) Disordered Fluorite, in which all of the A^{3+} and B^{4+} cations occupy the same cation site with 7-Fold Coordination [73]

Table 2.2 below shows the anion to cation ratio for different structures and 'M' represent any metal.

Table 2.2: Anion to Cation ratios for different structures

Compound	Stoichiometry	Anion-Cation ratio
Fluorite	MO_2	2.000

Pyrochlore	M_4O_7	1.750
δ –phase	M_7O_{12}	1.714

Defect pyrochlores exhibit wide range of physical and chemical properties as structure allows substitution at A, B or O sites resulting in large number of compositions. These materials are widely used in photocatalytic reactions. From literature following deductions are made: [74]

- Defect pyrochlores are efficient catalysts to degrade organic compounds and dyes for the decomposition of water.

- Operational parameters like porosity, particle size, crystallinity, morphology, crystal structure, surface area, reaction type and time, charge separation and concentration of substrates strongly influence the rate of photoactivity.

- Photocatalytic efficiency is enhanced by filling the materials with metal ions

Lanthanide Hafnates $Ln_2Hf_2O_7$ (Ln= La, Pr, Nd, Sm-Tm) were investigated with a combination of neutron powder diffraction and synchrotron XRD along with X-ray absorption and Raman spectroscopy [75]. Fitted patterns of synchrotron spectroscopy and neutron diffraction for $La_2Hf_2O_7$ and $Er_2Hf_2O_7$ are shown in Fig. 2.6.
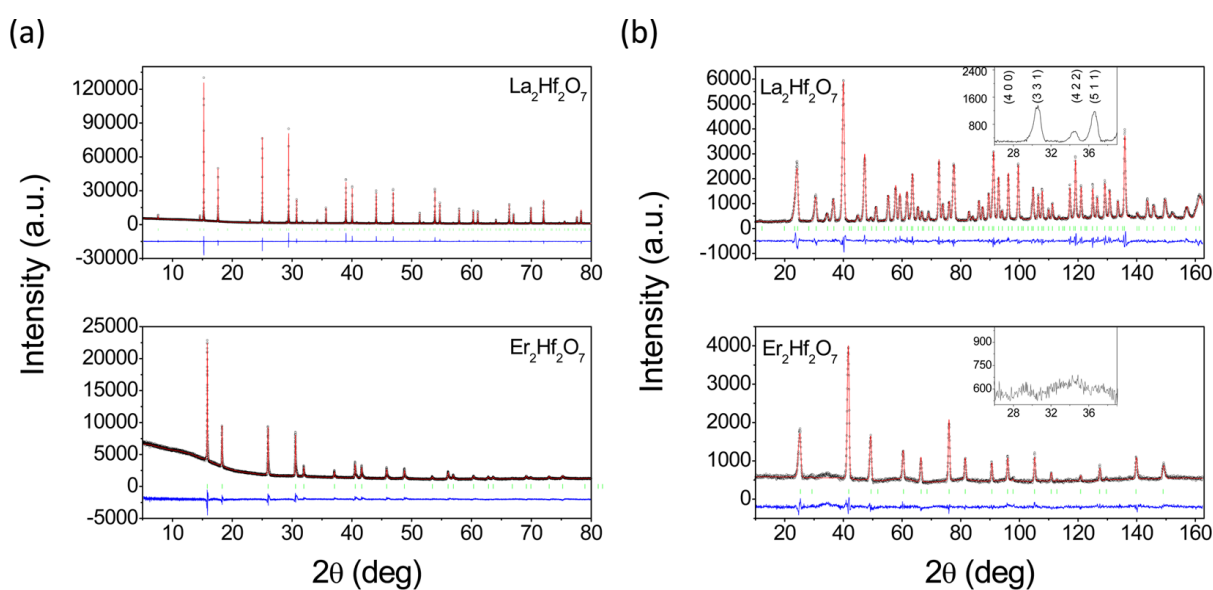
Fig. 2.6: Fitted (a) synchrotron X-ray and (b) neutron diffraction patterns for La₂Hf₂O₇ (top) and Er₂Hf₂O₇ (bottom). The insets in (b) highlight selected superlattice reflections, indexed to the pyrochlore structure, of La₂Hf₂O₇ and the diffuse background of Er₂Hf₂O₇. [75]

Patterns related to oxides with Ln = La, Pr, Nd, Sm-Tb were distinguished as pyrochlore structure and pattern of oxides with Ln = Dy-Tm are refined as fluorite structure. For Ln = Sm, Eu and Gd neutrons diffraction patterns cannot be collected due to their high neutron absorption coefficient but synchrotron XRD patterns are used to obtain their structural information [75].

2.2.3.8. LAMOX Family

LAMOX (La₂Mo₂O₉) are good conductors of oxygen ions as compared to YSZ materials. Around 580˚C LAMOX experiences reverse phase transition from nonconductive monoclinic (α) to highly conductive cubic (β) form. Repetition of phase transition cycle causes mechanical failure in this material [76].The main problem with LAMOX is its reactivity toward electrode materials [77].
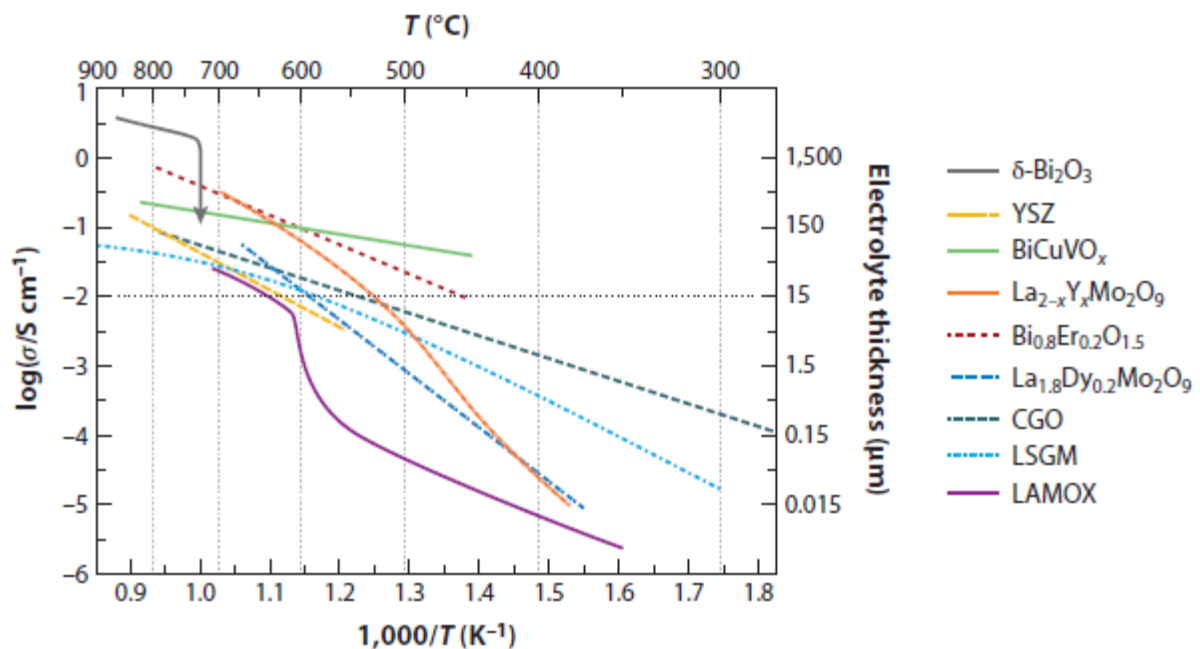
Fig. 2.7: Oxygen ion conductivity of important electrolyte materials for SOFC.

Horizontal dotted line shows the limit of conductivity necessary to construct devices

with an electrolyte thickness of 15 μm or less. Abbreviations: CGO, $Ce_{1-x}Gd_xO_{2-x/2}$;

LAMOX, $La_2Mo_2O_9$; LSGM, $La_{0.8}Sr_{0.2}Ga_{0.8}Mg_{0.2}O_{2.8}$; YSZ, yttria stabilized zirconia

[78]

Fig. 2.7 shows the ionic conductivity data of important electrolyte materials for SOFC.

2.2.4. Interconnect

Ceramic cells with cathode, electrolyte and anode are stacked up with interconnecting metal plates. The interconnect shows adequate electronic conductivity in both air and fuel. Air electrode is protected by interconnection from reducing environment due to fuel on fuel electrode side. Interconnection must have following requirements:

1. Electronic conductivity almost 100%

2. As interconnect is exposed to fuel on one side and air on other, so it should be stable in reducing and oxidizing atmosphere

3. During cell operation to avoid direct combination of fuel and oxidant oxygen and hydrogen permeability should be low

4. Well matched thermal expansion with electrolyte and air electrode

5. Inertness towards electrical contact potential and air electrode

Interconnects are made with less expensive stainless steel for stacks of low temperature operation. Ferritic stainless steel is also used for interconnects [79]. For IT-SOFC metallic bipolar plates are being used [80]. Stainless steel bipolar plates is an economically viable option. Frequently, 316 stainless steel alloy is of choice for metallic bipolar plates [81]. Use of stainless steel is only possible with protective coatings due to the formation of an oxide layer with high resistivity and corrosive products poison the membrane electrode assembly (MEA) [82].

Fig. 2.8 below shows materials for different components of SOFC and issues related to them.
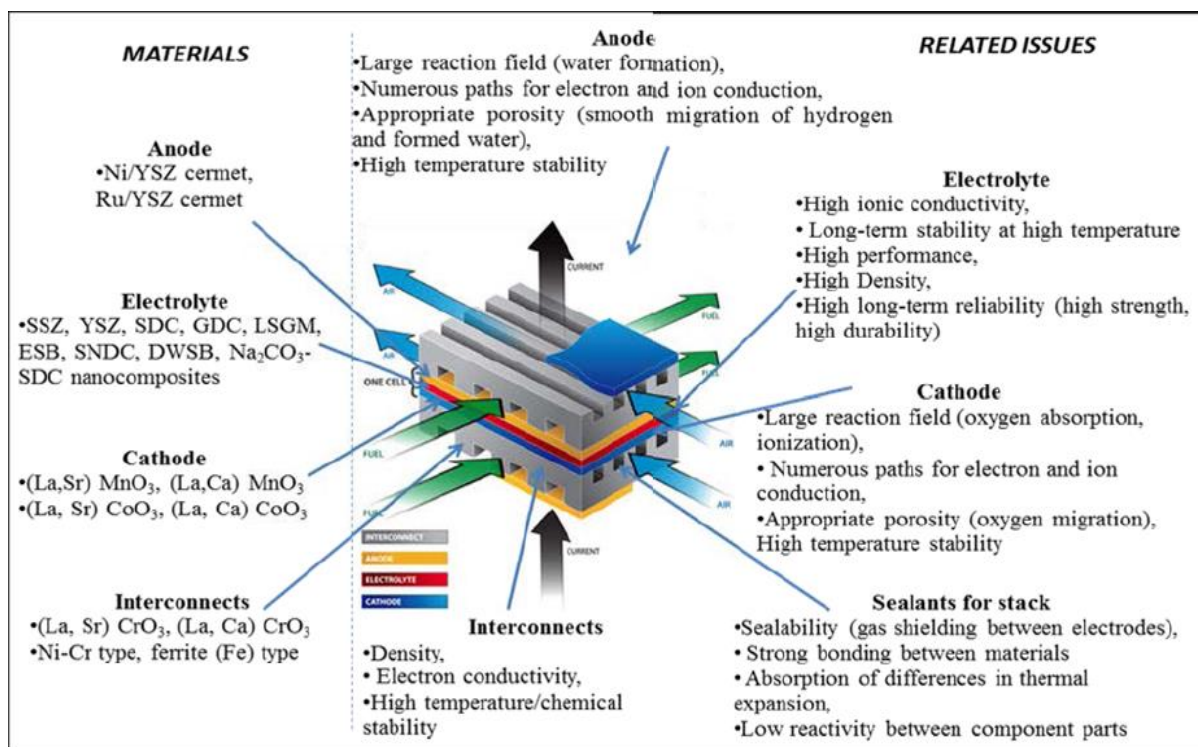
Fig. 2.8: Materials and related issues for SOFC [83]

2.3. Sol Gel Method

In a sol-gel process, molecular precursor forms oxide network in a liquid through polycondensation reactions. Liquid phase enclosed in three dimensional continuous organic network is a gel. Mostly gel systems are used to synthesize materials and due to covalent nature of interactions, process of gel formation is irreversible. Sol gel synthesis involves dissolution of compound in liquid.

Sols of different compounds are mixed to form multi-component compounds with measured stoichiometry. Sol gel process also overcomes the problems with co-precipitation such as inhomogeneity. In sol gel process ion exchange took place at atomic scale forms small and easily sinterable particles.

Sol gel method was established in 1960s as a new synthesis technique required for nuclear industry. The new technique must have lower sintering temperature and reduced dust as compared to ceramic method. And it should be possible to control this technique remotely.

Quick clay is well-known example of sol gel system. Appropriate washing of clay converts it into quick clay (sol) by removing counter ions. Quick clay can convert to gel by adding sufficient counter ions for colloidal particles aggregation.

Sol processing forms materials with different shapes like dense powders, porous structure, thin fibres and films. Xerogel formed by drying gel through evaporation which results in capillary forces shrinkage and collapsing of gel network. If drying is carried out under supercritical conditions, network structure is maintained and gel with large pores formed. Its density is very low (<0.005 g/cm3) and called aerogel.

Fig. 2.9 below shows different options of sol-gel process.
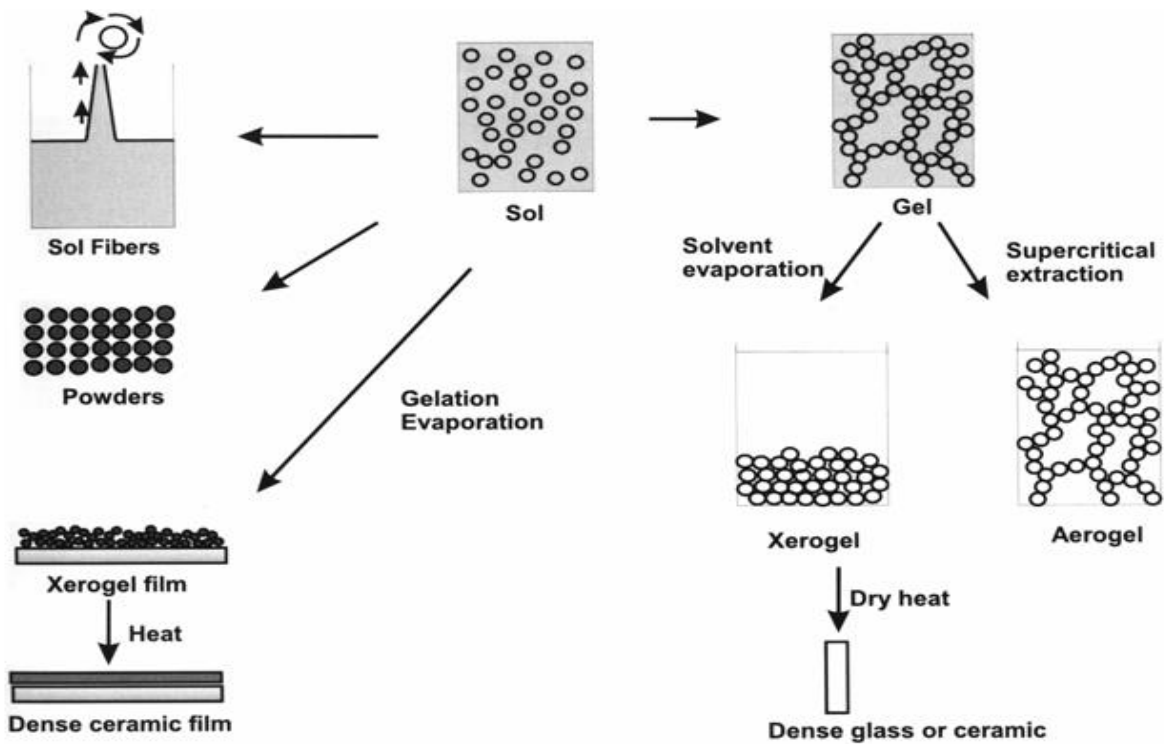
Fig. 2.9: Sol-gel processing options [84]

Sol-gel process is viable for the production of ceramic materials at low temperature. Several advantages of sol-gel process in materials synthesis are: [85] [86]

1. Low cost approach to prepare novel structured materials

2. Solution routes at room temperature

3. Enable synthesis of materials with desired hardness

4. Synthesize chemically durable materials

5. Prepare materials with tailored porosity and thermal resistance

6. Excellent compositional control of final material

7. Homogeneity at molecular level

8. Least emission of pollution depends on precursor used

Some of the drawbacks of sol-gel process are:

1. Limited large scale production as starting materials are expensive

2. Lengthy drying process

Sol-gel process is mainly categorized in two routes; polymeric gel and particulate gel. Fig.2.10 below shows the flow chart of sol-gel routes.
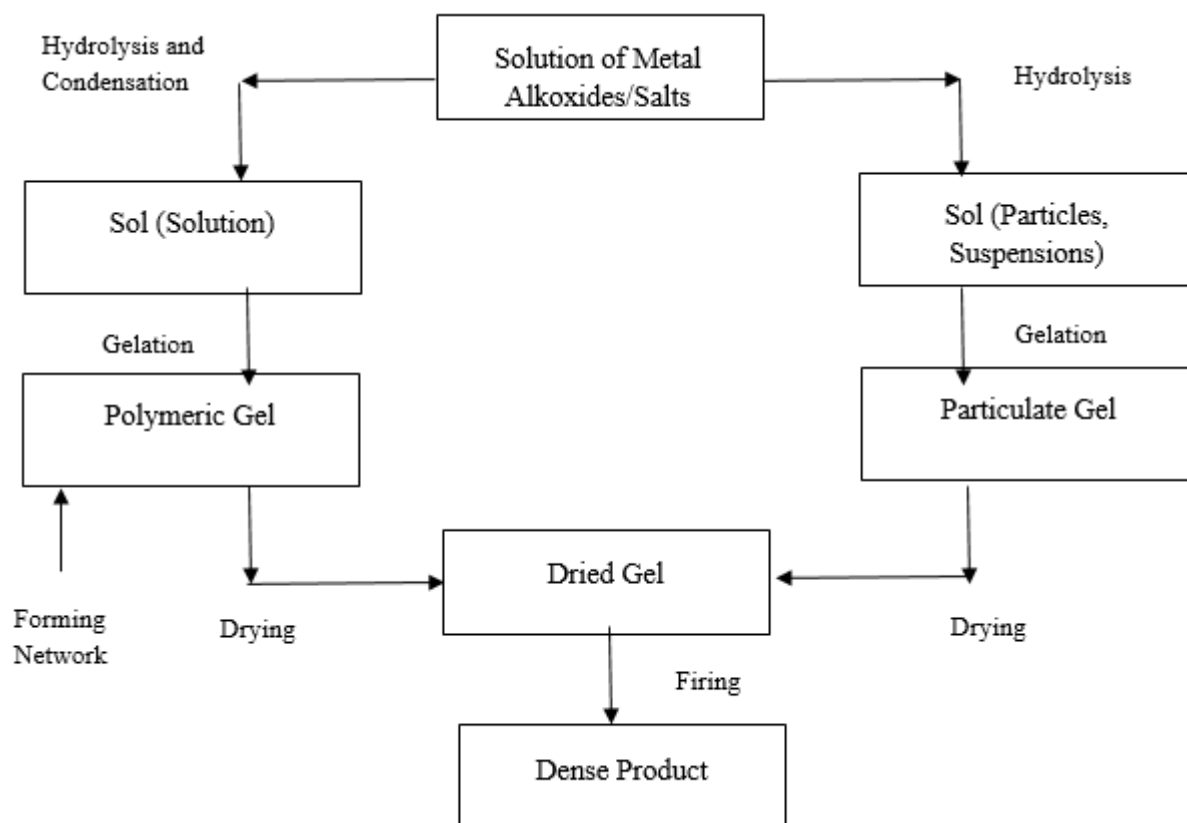
Fig. 2.10: Sol-gel flow chart [87]

Sol is formed after many hydrolysis and polymerization reactions in particulate gel route. Solid particles with diameter of few hundred nanometres are suspended in sol due to Brownian motion. Preparation of sol particle depends on size, pH and temperature of solution.

In polymeric gel route, salts or metal alkoxides lead to branching and crosslinking after partial hydrolysis. This polymerization reaction avoids any segregation process and forms three dimensional structures. Rigid and coherent gel is then dried and heated at temperatures significantly lower than other techniques [87].

This heating serves many purposes; removes solvent, decomposes anions like carbonates, hydroxides or alkoxides to form oxides, permits rearrangements of solid structure and occurring of crystallization. In favourable cases, both time and temperature required in sol-gel processes can

be reduced than that in direct ceramic method, time from days to hours and temperature by several

hundred degrees [88].

 Different synthesis methods are used for the preparation of nanopowders. Table 2.3 compares the

different synthesis route for oxide powder synthesis.

Table 2.3: Comparison of oxide powder synthesis route [89]

Synthesis method	Solid-state Reaction	Coprecipita-tion	Sol-gel	Spray/Freeze Drying	Spray Pyrolysis	Emulsion Synthesis	Hydrothermal Synthesis
state of development	commercial	commercial	R&D	demonstration	R&D	demonstration	demonstration
compositional control	poor	good	excellent	excellent	excellent	excellent	excellent
morphology control	poor	moderate	moderate	moderate	excellent	excellent	good
powder reactivity	poor	good	good	good	good	good	good
particle size (nm)	>1000	>10	>10	>10	>10	>100	>100
purity (%)	<99.5	>99.5	>99.9	>99.9	>99.9	>99.9	>99.5
agglomeration	moderate	high	moderate	low	low	low	low
calcination step	yes	yes	yes	yes	no	yes	no
milling step	yes	yes	yes	yes	no	yes	no
costs	low-moderate	moderate	moderate-high	moderate-high	high	moderate	moderate

2.3.1. Sodium Alginate

Sodium alginate is a polymer with general formula $(C_6H_7NaO_6)n$ and extracted from brown

seaweeds. It has varying amounts of α-L-guluronic acid (G) and 1, 4 linked β-D-mannuronic acid

(M) residues linked together covalently in different sequence like -MM- or -GG- structures or -

GM- block copolymers. In aqueous solution metal ions interact with alginate, gelation of alginate

takes place [90]. Structure of alginate is shown below in Fig. 2.11:
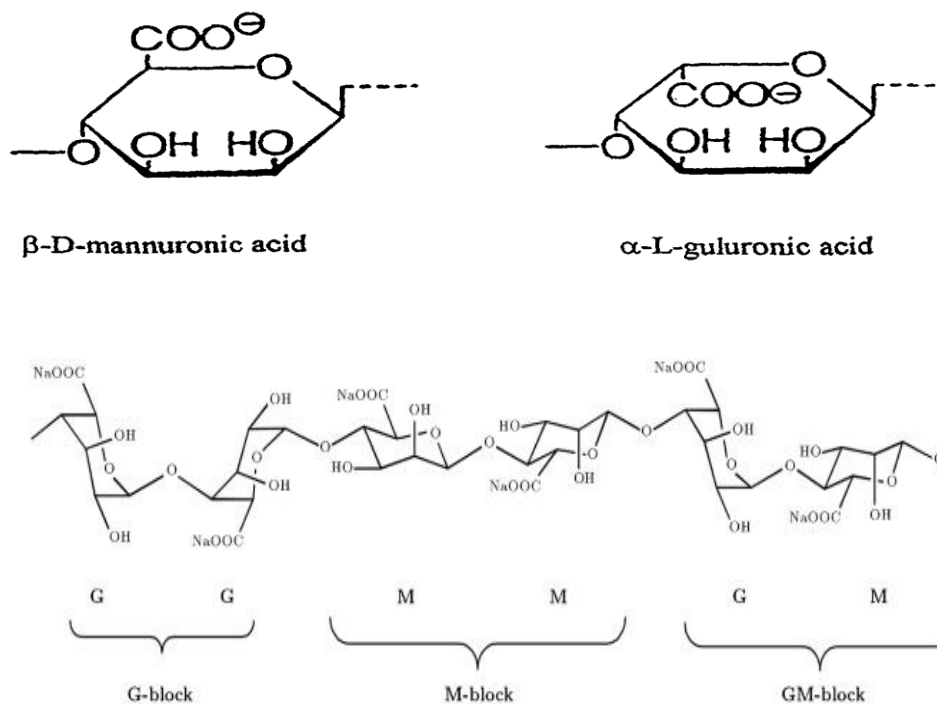
Fig. 2.11: Structure of Alginate; monomers and chain conformation [90]

Metal ions prefer to bind on electronegative G blocks during gelation of metal ions and alginate. Metal ions get immobile in the gelled structure and cannot come close to each other, this leads to the production of small nanoparticles of metal oxides [90].

The ''zig-zag'' structure of poly-G explains the higher specificity for metal ions as it can accommodate the metals ion more easily. Mechanical properties of alginate gels typically are enhanced by increasing the length of G-block and molecular weight. Through dimerization of poly-G sequences in the presence of divalent cations of similar size, alginates adopt an ordered solution conformation. It is the rigid and buckled shape of the poly-G sections which results in an alignment of two chain sections yielding an array of coordination sites with cavities favourable to divalent cations because they are lined with carboxylate and other electronegative oxygen atoms. This description is known as the "egg-box" model [90].

Nanoparticles of Zinc Oxide (ZnO) were prepared through ionic gelation between zinc solution and sodium alginate [91]. By dissolving the suitable quantity of zinc nitrate in ultrapure water,

zinc solution is formed. Under magnetic stirring suitable quantity of sodium alginate is dissolved in ultrapure water to form alginate solution with concentration of 1% w/w. Zinc alginate beads were formed by dropping the sodium alginate solution in zinc solution in ratio of 1:2 using stainless steel needle under continuous stirring. Gentle stirring was carried out for 30 mins after the formation of gel beads. After separating the beads calcination is carried out at 450 and 800°C for 24 hrs with heating rate of 10°C/min. Product is then characterized using X-Ray Diffraction (XRD). Fig. 2.12 below shows the detail of XRD patterns of ZnO nanoparticles.
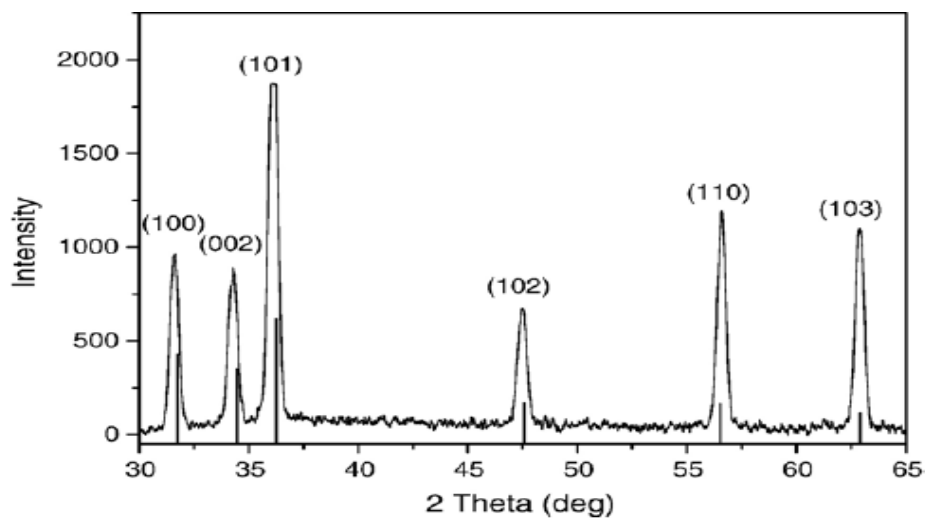
Fig. 2.12: XRD patterns of ZnO prepared through thermal decomposition of zinc alginate at 800°C [91]
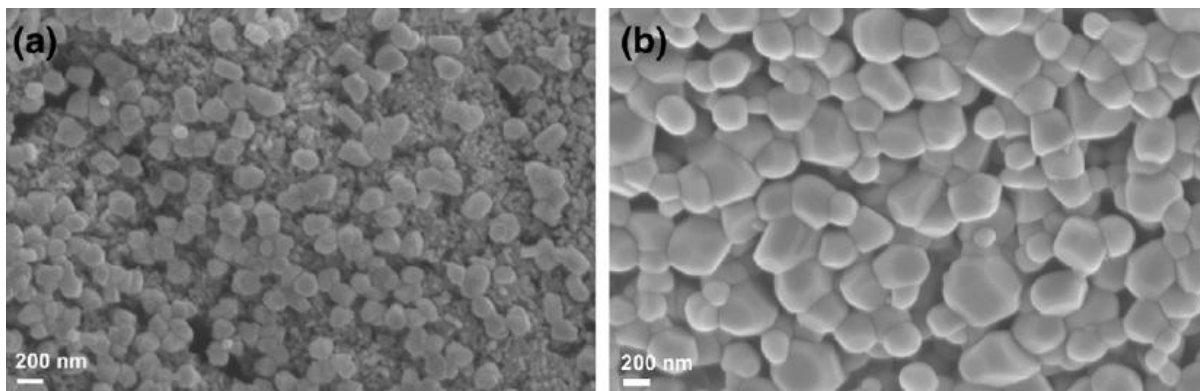
Fig. 2.13: SEM micrographs of ZnO crystals at a) 450°C and b) 800°C [91]

Morphological characterization of product was performed using Scanning Electron Microscope (SEM) as shown in Fig. 2.13.

It was concluded by the author that ZnO nanoparticles can be produced through sol gel method using sodium alginate. The size of these nanoparticles depends on calcination temperature and zinc crosslinking agent. Alginate has the ability to bind metals which is important to produce technologically important oxides [91].

2.3.2. Ion-Exchange Kinetics

Gelation kinetics of alginate gel beads was determined by measuring the time-based evolution of Ca^{2+} and Na^+ concentrations after immersing in $CaCl_2$ solution. Calcium absorption and sodium release of beads were examined by diffusion theory regarding concentration gradient of Ca^{2+} and Na^+ between alginate beads and $CaCl_2$ solution. Considering a unidirectional diffusion in a sphere with constant dimensions, constant diffusivity and homogeneous structure. Equation 2.12 is the solution yielded by Fick's second law of unsteady state diffusion with the assumptions of symmetry of concentration, uniform initial concentration and equilibrium concentration equal to surface cation concentration:

$$(C_A - C_A^{eq})/(C_A^o - C_A^{eq}) = \frac{6}{\pi^2} \sum_{n=1}^{\infty} (\frac{1}{n})^2 \, exp(-(\frac{n\pi}{R})^2 D_{ef} \, t) \tag{2.12}$$

where C_A is the concentration of Ca^{2+} and Na^+ ions in 'mol.dm^{-3}' at time t in 'sec', C_A^{eq} is concentration of ions at equilibrium and C_A^o is initial concentration, average radius of sphere is R in 'mm' and D_{ef} is effective diffusivity of ions in 'm^2/s'. For long diffusion time Equations 2.13 and 2.14 yield the general solution for Ca^{+2} and Na^+ ions.

$$C_{Ca} = C_{Ca}^{eq} - C_{Ca}^{eq} \exp(-\frac{\pi^2}{R^2} D_{ef} t) \tag{2.13}$$

$$C_{Na} = C_{Na}^{eq} + C_{Na}^{eq} \exp(-\frac{\pi^2}{R^2} D_{ef} t) \tag{2.14}$$

Ca^{2+} and Na^+ concentration measured in the alginate beads after immersion in the $CaCl_2$ solution for different time intervals have fitted by nonlinear curve fitting. [90]

Alginic acid based sol gel method was used in investigating the kinetics of ion exchange process in metal ion rich solutions where initial concentration of Fe^{2+} was higher than that of H^+ [92]. Residual value of Fe^{2+} ion concentration was measured until it achieves steady state condition of ion exchange reaction using ICP-AES. Fig. 2.14 shows the experimental data of the variation of Fe^{2+} concentration in alginate beads with time. The initial rate of ion exchange is significantly rapid which reaches to an equilibrium at 10 min. A rapid ion exchange take place between H^+ and Fe^{2+} cations when Fe^{2+} ions come in contact with alginic acid beads. From the core of alginic acid beads H^+ ions were started diffusing outward into the Fe^{2+} electrolyte solution through converted shell layer and to maintain charge neutrality Fe^{2+} ions diffuse inward simultaneously. This counter current transfer of ions leads to a growth of converted shell. Based on initial rate of uptake of Fe^{2+}, the kinetic of ion exchange is in fact very fast and ion diffusion through converted layer controls the mass transfer. Simple kinetic model was used to analyse the chronographic data obtained and to fit the data 1st order and 2nd order model was used. Equations 2.15 & 2.16 are expressions of first order kinetic model

$$\frac{d_{qt}}{dt} = k_1(q_e - q_t) \qquad (2.15)$$

$$q_t = q_e[1 - \exp(-k_1 t)] \qquad (2.16)$$

where q_t is concentration of ion in solution at 't', q_e is equilibrium value, k_1 is first order rate constant and t is reaction time in seconds.

Equations 2.17, 2.18 & 2.19 represent the 2nd order kinetic model.

$$\frac{1}{(q_e - q_t)} = \frac{1}{q_e} + k_2 t \qquad (2.17)$$

$$\frac{t}{q_t} = \frac{1}{k_2 q_e^2} + \frac{t}{q_e} \qquad (2.18)$$

$$\frac{t}{q_t} = \frac{1}{h} + \frac{t}{q_e} \tag{2.19}$$

Where h is $\frac{1}{k_2 q_e^2}$ and k_2 is second order rate constant. From Fig. 2.16 it is visible that data fits better with second order model than with first order model. 1st order model fits the data well with initial fast ion exchange stage with reaction time less than 2min but 2nd order fits the entire experimental data considerably better. Hence the 2nd order model can be better applied to this ion exchange process. [92]
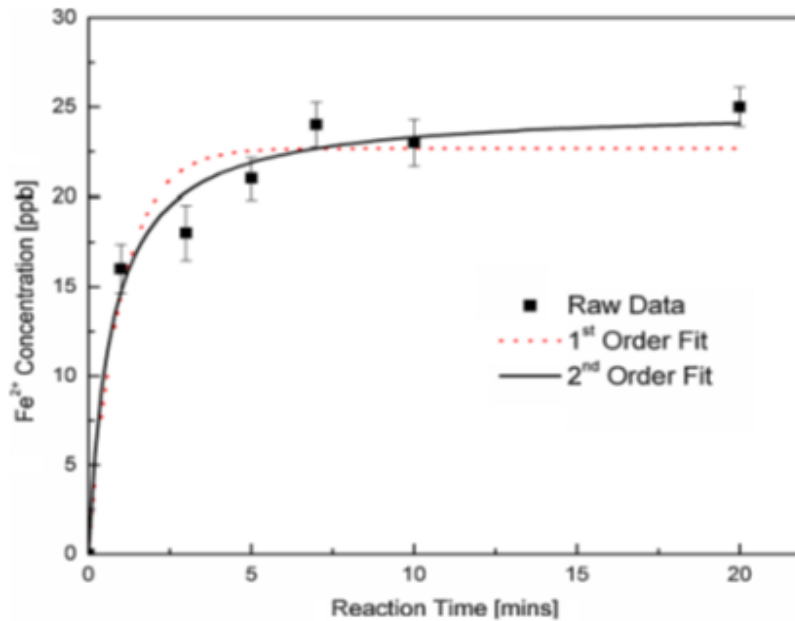
Fig. 2.14: 1st and 2nd order fit for the Fe^{+2} ion exchange reaction between aqueous phase and alginate gel beads as function of contact time. Dotted line for the 1st order and solid line for the 2nd order fit of the data [92]

2.4. Parametric Study

2.4.1. Transformation from ordered pyrochlore structure to disordered (fluorite) with temperature

In $A_2B_2O_7$ oxides order-disorder transition is realized by different factors such as radiation exposure, treatment by high temperature and chemical doping [93].

Powdered $Gd_2Zr_2O_7$ was prepared with suitable rare earth nitrate and aqueous mixture of zirconyl chloride solution using sol-gel method followed by treatment at high temperature.

Amorphous precursor of $Gd_2Zr_2O_7$ started crystallizing at temperature above 700 ˚C. Cation and anion sublattices form ordered pyrochlore structure at higher temperature. Powder samples were heat treated in air from 1100 to 1550 ˚C for 24 h each to obtain pyrochlore structures with different degrees of cation order. Limited cation order in pyrochlore structure is achieved below 1200 ˚C. Degree of cation disorder increases with an increase in annealing temperature. But perfectly ordered pyrochlore structure of $Gd_2Zr_2O_7$ has not achieved even with longer heating time. Heating above 1550 ˚C has not resulted in pyrochlore structure as Gd^{3+} and Zr^{4+} cations were disordered because thermal energy overcame the cation defect formation energy [94]. Fig. 2.15 below shows the experimental and predicted values of transition temperatures from pyrochlores to defect fluorite for zironates and hafnates pyrochlores.
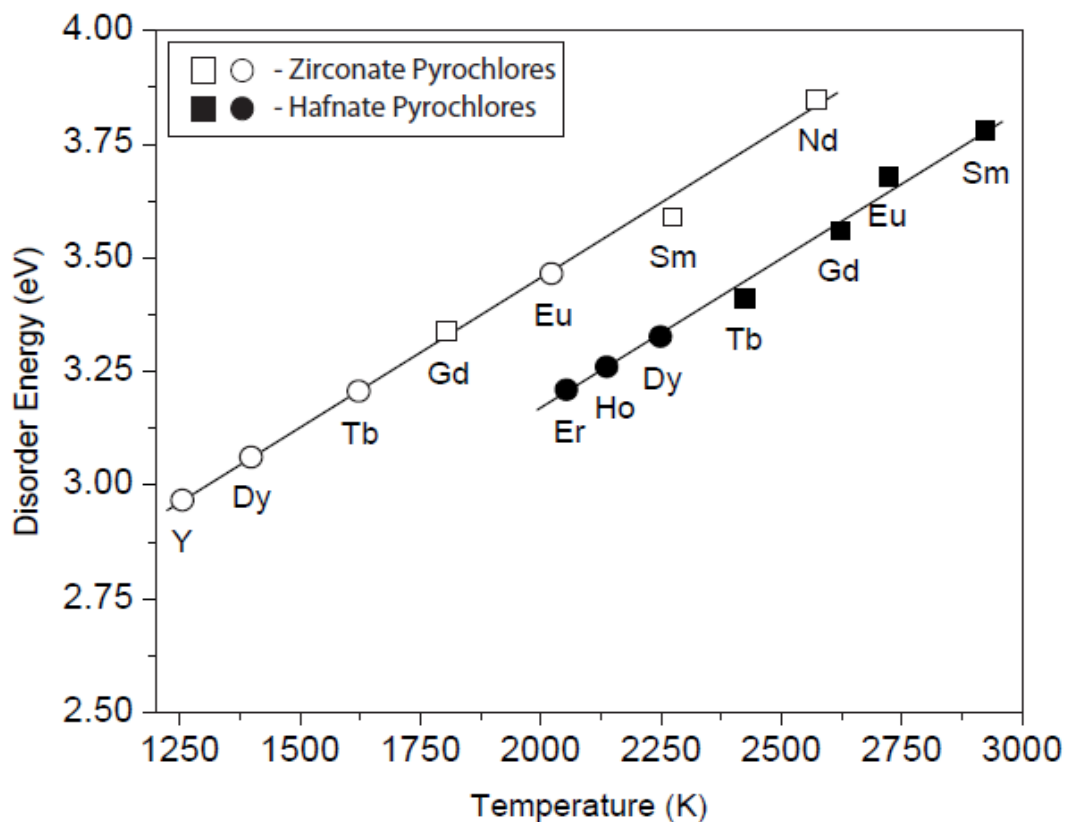
Fig. 2.15: Pyrochlore to defect fluorite transition temperatures for zirconate and hafnate pyrochlores; Squares: experimental disorder temperatures, Circles: predicted values [95]

Fig. 2.16 shows the phase map of stability of cubic, non-cubic and disordered fluorite at low temperatures.
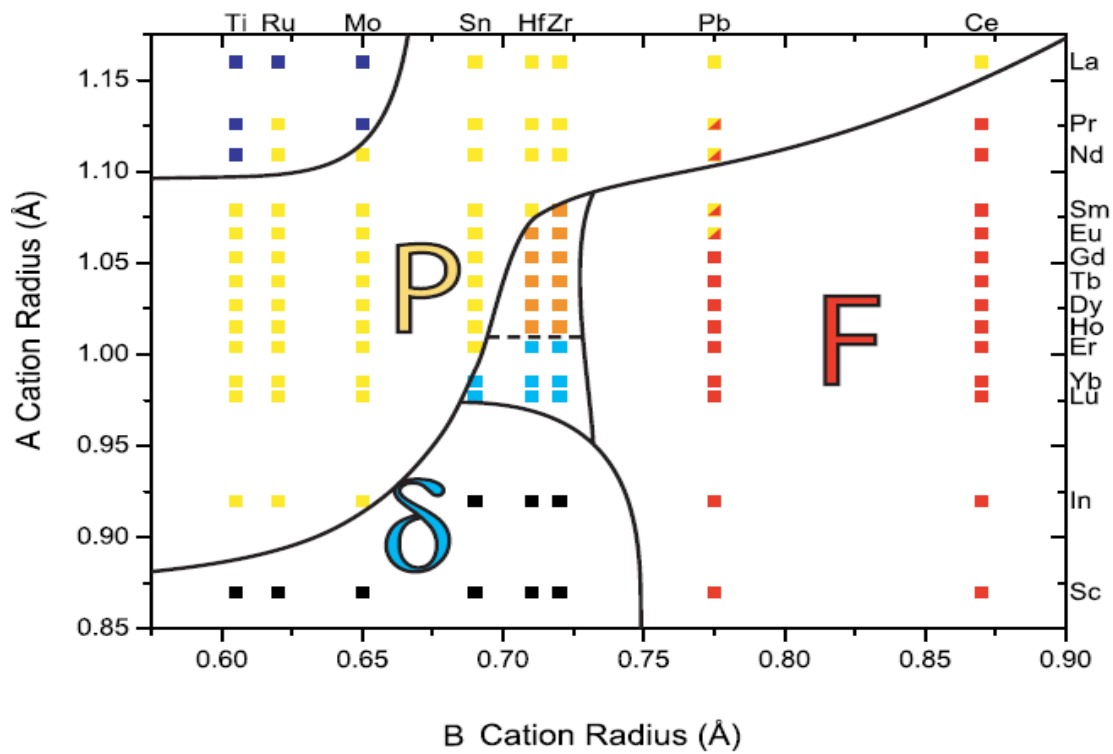
Fig. 2.16: Phase map presenting the stability of cubic $A_2B_2O_7$, non-cubic $A_2B_2O_7$, disordered fluorite and $A_4B_3O_{12}$ phases at low temperatures. Key: Blue: Non cubic (possibly monoclinic pyrochlore), Yellow: Cubic Pyrochlore forming from the melt, Orange: Cubic pyrochlore formed by order-disorder transformation, Black: δ -phase postulated to form from the melt, Light Blue = δ -phase formed by an order-disorder transformation, Red: Disordered fluorite, Yellow/Red: Cubic pyrochlores formed under high pressure [96].

Fig. 2.17 below shows the stability of different structures at high temperatures.
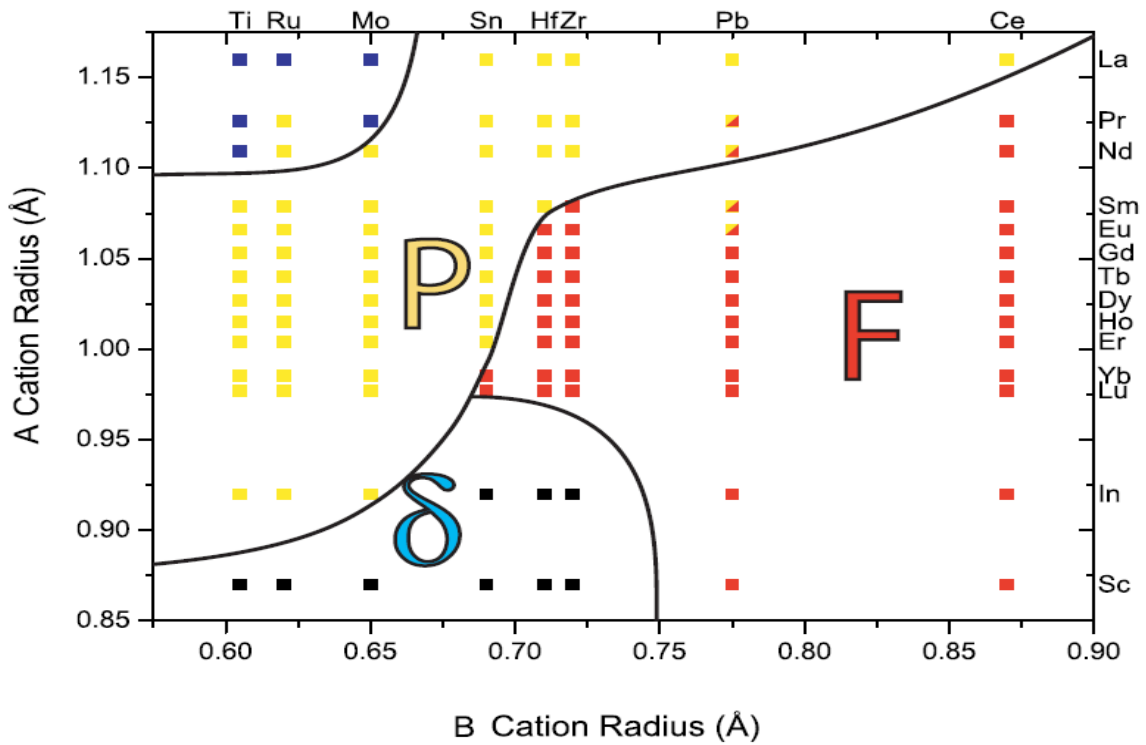
Fig. 2.17: Phase map with stability of different structures at high temperatures. Key: Blue: Non cubic (possibly monoclinic pyrochlore), Yellow: Cubic Pyrochlore, Black: δ - phase, Red: Disordered fluorite, Yellow/Red: Cubic pyrochlores formed at 300 Kbar [96].

Pyrochlores with heavy A-site cations like Ho suggest the unique opportunity to study order/disorder transformation as cation substitution on the B-site induced the disorder. To characterize the average structure, neutron diffraction is ideal as it is sensitive to oxygen sublattice whereas pair distribution function (PDF) from neutron total scattering probes the local structure. Structural refinement of fully ordered $Ho_2Ti_2O_7$ shows that the local structure assessed through PDF (Fig. 2.18, a) is in excellent agreement with the isometric pyrochlore structure, Fd3m (Fig. 2.18, b).

$Ho_2Ti_2O_7$ can be intrinsically disordered to the fluorite type average structure by substituting large Zr atom to the site-B and form $Ho_2Zr_2O_7$, which has a value of r_A/r_B below the stability field of pyrochlore structure. Disordered fluorite data fit well to the diffraction data of

Ho$_2$Zr$_2$O$_7$ as shown in Fig. 2.19 (a&b). Hence, PDF analysis is necessary to study the local crystal structure. [97]
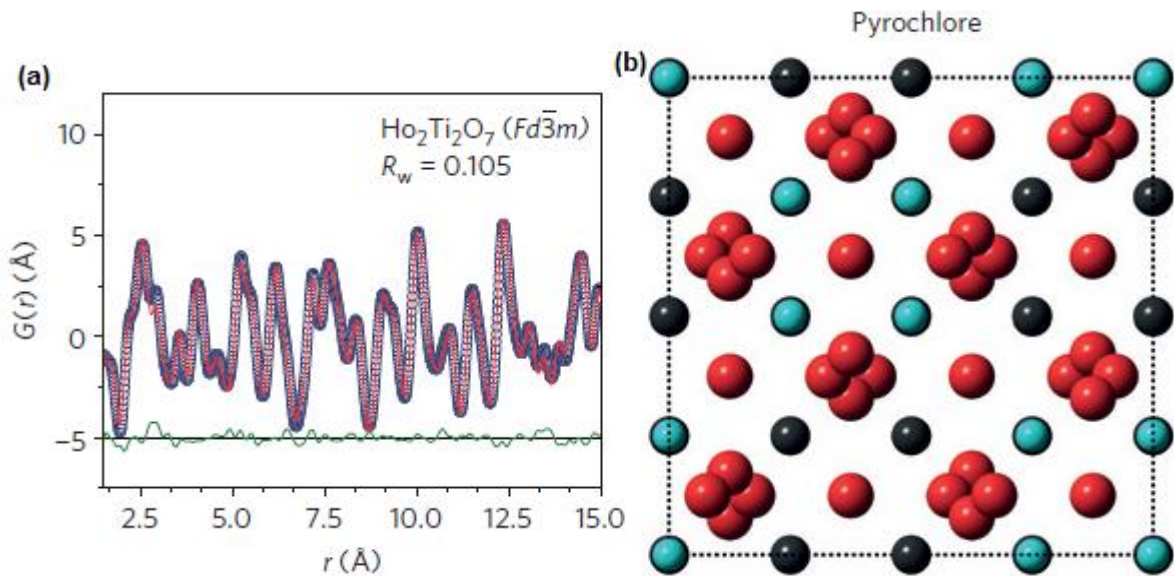
Fig.2.18: (a) Small-box refinement of the neutron PDF, *G(r)*, as a function of distance, *r*, using the ordered Ho$_2$Ti$_2$O$_7$ pyrochlore structure shown in (b). [97]
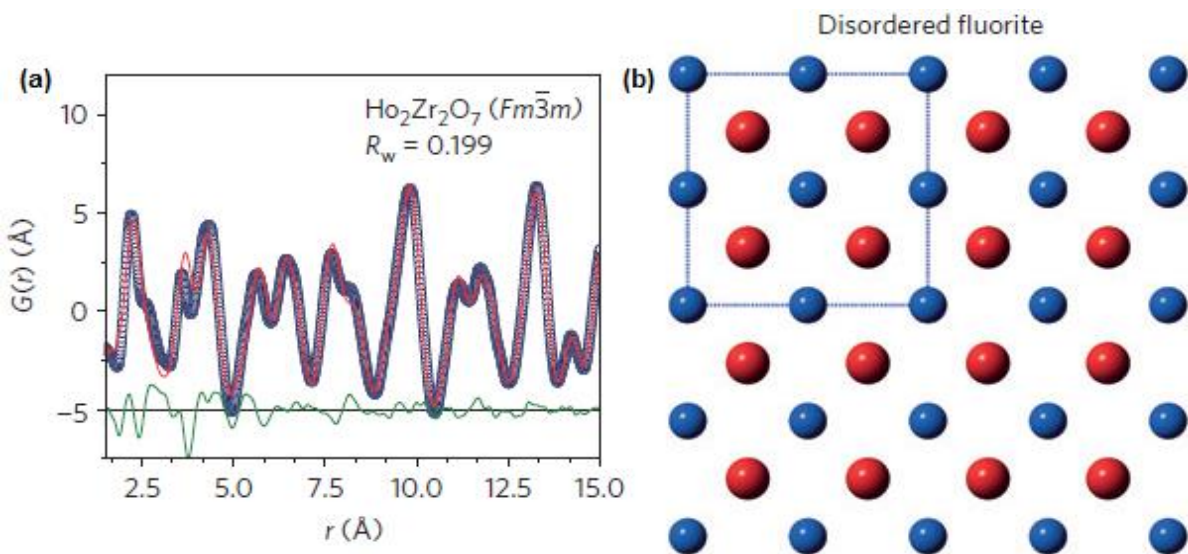
Fig. 2.19: (a) Small-box refinement of the neutron PDF for Ho$_2$Zr$_2$O$_7$ with the disordered fluorite structure shown in (b) [97]

2.4.2. Effect of precursor concentration on properties and quality of final product

Ni/CGO as anode film were deposited on YSZ electrolyte and using ultrasonic spray pyrolysis technique [98]. Precursor solutions were prepared so that total concentration of metal ions can

range between 0.025 mol l^{-1} and 0.4 mol l^{-1}. Processing variables like deposition temperature, precursor solution concentration and feed rate were studied. Samples were annealed for 2 h at 800 ˚C to endorse crystallization of deposited films. Composition and morphology of deposited Ni/CGO film were inspected by SEM and XRD. SEM images were further analysed by ImageJ to calculate porosity values [98].

Fig. 2.20 shows that larger particles deposit result from high precursor solution concentration. With the increase in precursor solution concentration from 0.025 moll^{-1} and 0.4 moll^{-1} particle size also increase from 2 μm to 20 μm [98].
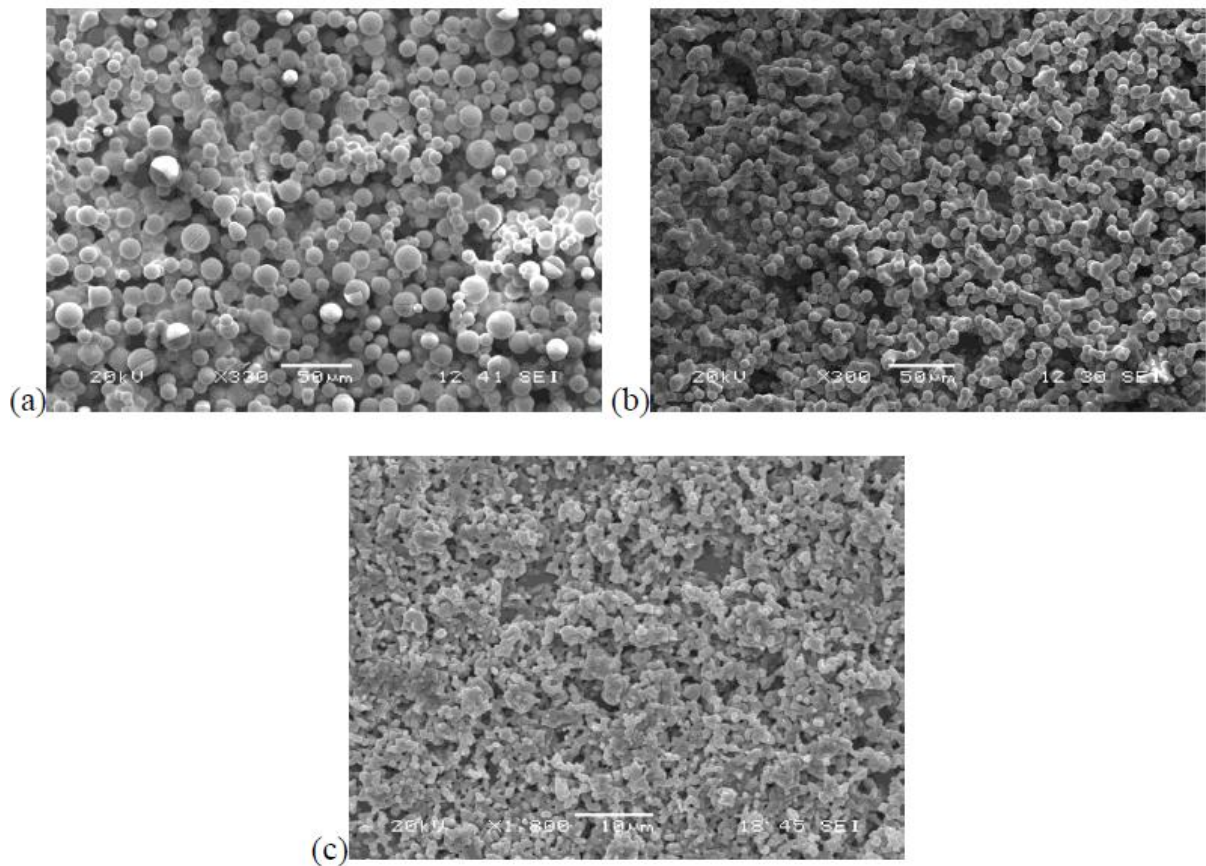
Fig. 2.20: Images of deposited Ni/CGO film at different concentration of precursor solution, T= 300˚C; (a) C = 0.4 mol l^{-1} (b) C = 0.1 mol l^{-1} (c) C = 0.025 mol l^{-1} [98]

Higher porosity was achieved with the increase in solution concentration due to the development of large particles with high degree of agglomeration as shown in Fig. 2.21 below.
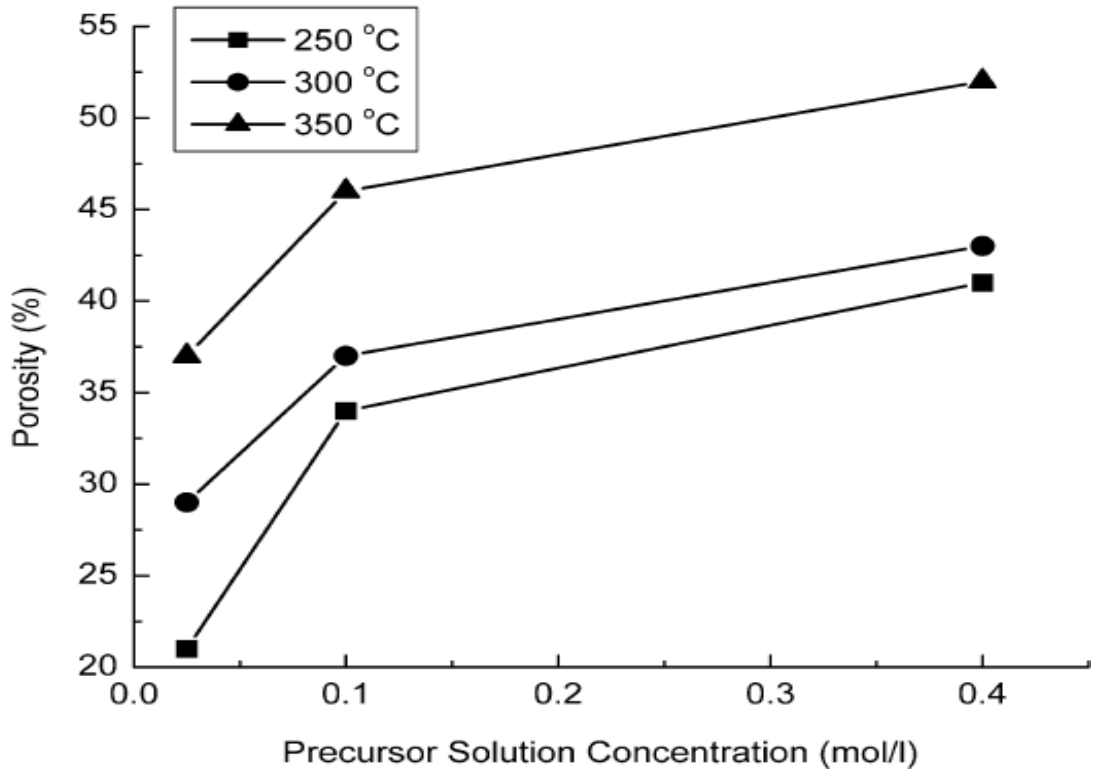
Fig. 2.21: Effect of precursor solution concentration and temperature on the porosity of Ni/CGO film [98]

With the change in precursor solution concentration from 0.025moll^{-1} to 0.4moll^{-1} porosity changed from 21 to 38% at deposition temperature of 250˚C. Precursor concentration should not exceed the solubility limit of the chemical compounds and should not be too low to achieve a suitable deposition rate [98].

2.4.3. Effect of alginate concentration on ion exchange kinetics

Effect of sodium alginate concentration on ion exchange kinetics of calcium alginate ferrogel beads was studied through external gelation [90]. To achieve the effective diffusion coefficients of Ca^{+2} and Na$^+$ calcium absorption and sodium release of beads were fitted to Fick's second law for unsteady state diffusion. TGA and SEM were used to characterize and study the morphology of calcium alginate beads. White coloured calcium alginate beads were spherical with diameter range of 4-5 mm as shown in Fig. 2.22.

Fig. 2.22: Calcium alginate beads produced by dripping method; pure alginate in gel state [90]

Ionic concentrations of beads formed with 1%, 2% and 3% alginate solution were studied during different immersion times in $CaCl_2$ solution. Kinetics of Ca^{+2} absorbance and Na^+ release from alginate matrices is shown in Fig. 2.23 below.
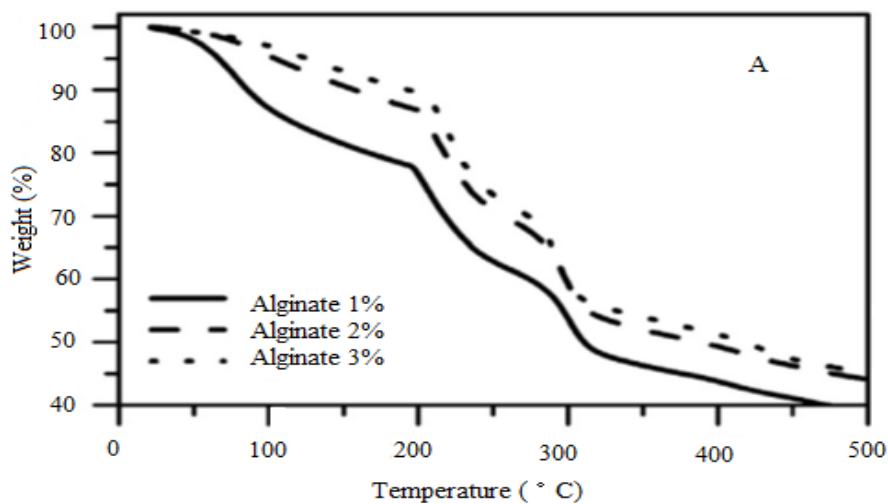
Fig. 2.23: TGA curves obtained for calcium alginate beads formed with 1%, 2% and 3% sodium alginate solutions [90]

During the first 30 min of processing Ca^{2+} concentration started increasing and after that there is decrease in cation migration Ca^{2+} concentration tends to equilibrium. The higher the alginate concentration the faster the equilibrium condition is reached. Effective Ca^{2+} diffusion coefficient was not much effected with the increase in alginate solution concentration from 1 to 3 wt.%. Alternatively 1 to 2 wt.% increase in the alginate concentration boosted the Ca^{2+} equilibrium concentration but this was not the case with 2 to 3 wt.% increase in alginate

concentration. Electronegative cavities of G-block are promoted with the increase of alginate concentration from 1-2 %, which enhances the cross linking of Ca^{2+} ions and results in increased Ca^{2+} concentrations in beads. Concentration of alginate higher than 2 % promoted saturation of binding sites at beads surface. During the first 60 min of process main diffusion of ions (Ca^{2+} in and Na^+ out) from bead took place and about 85-90 % of Ca^{2+} equilibrium concentration was attained which shows that this duration is adequate for the formation of calcium alginate beads with greater crosslinking of polymer network [90].

2.4.4. Effect of sintering temperature and time on grain growth and surface area

Finely dispersed powder of zirconates and hafnates of lanthanum and gadolinium were formed from inorganic salts of respective metal oxides through Pechini method [99]. For zirconate and hafnate of gadolinium the mean crystallite size calculates using Scherrer formula was 5 nm. BET method was used to determine specific surface area of powders ranging from 20-21 m^2 g^- ^{1} for $La_2Zr_2O_7$ and $La_2Hf_2O_7$ to 30–37 m^2 g^{-1} for $Gd_2Hf_2O_7$ and $Gd_2Zr_2O_7$. Sintering of pellets from powders was studied at 800, 900 and 1000°C in air for 1, 2 and 4 h. IR spectroscopic data was used to observe the formation of cubic phase with pyrochlore structure even at minimum temperature and time in all samples. Fig. 2.24 below shows that when pellets are sintered at 1000 °C the structure is more ordered.
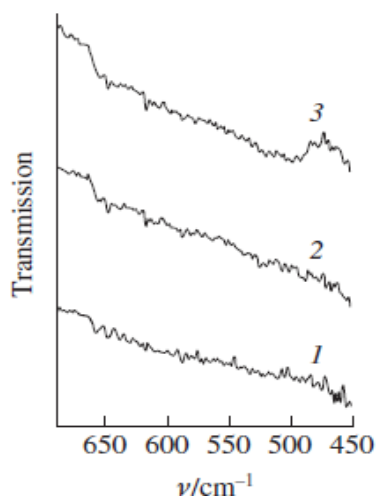
Fig. 2.24: IR spectra of La₂Zr₂O₇ pellets sintered for 1h at (1) 800 °C (2) 900 °C and (3) 1000 °C. [99]

Through XRD analysis of $Gd_2Hf_2O_7$ it is noticed that during sintering mean crystallite size changes from 5 nm (800 ˚C, 1 h) to 19 nm (1000 ˚C, 4 h) [99]. Mean crystallite size of $Gd_2Zr_2O_7$ increases from 7 to 103 nm during similar thermal treatment conditions. Similarly for hafnate and zirconte of lanthanum crystallite size changes from 38-53 nm and 17-38 nm, respectively. It is noticed that increase in temperature affects crystallite growth more than exposure time. Specific surface area also changes along with grain growth during sintering of metal oxide pellets. After 1 h sintering specific surface area of $Gd_2Hf_2O_7$ decreased from 19 (800 ˚C) to 9 m^2g^{-1} (1000 ˚C). Specific surface area of $La_2Hf_2O_7$ first increased from 6 (800 ˚C) to 13 m^2g^{-1} (900 ˚C) and then decrease to 12 m^2g^{-1} (1000 ˚C). Increase in surface area is due to opening of pores when heated to 900 ˚C. After sintering at 1000 ˚C for 4 h scanning electron microscopy reveals that oxide particles grow significantly on thermal treatment. Mean particle size of $(La/Gd)_2Hf_2O_7$ and $La_2Zr_2O_7$ was 45-55 nm. Mean particle size of $Gd_2Zr_2O_7$ was 130 nm. At even higher temperatures growth of powder particles was studied in case of zirconates only. During thermal analysis powders were heated to 1200 ˚C twice. On sintering oxide films developed network morphology revealed by SEM morphology study as shown in Fig. 2.25 below. Mean particle size was 30 and 40 nm for $Gd_2Zr_2O_7$ and $La_2Zr_2O_7$, respectively [99].
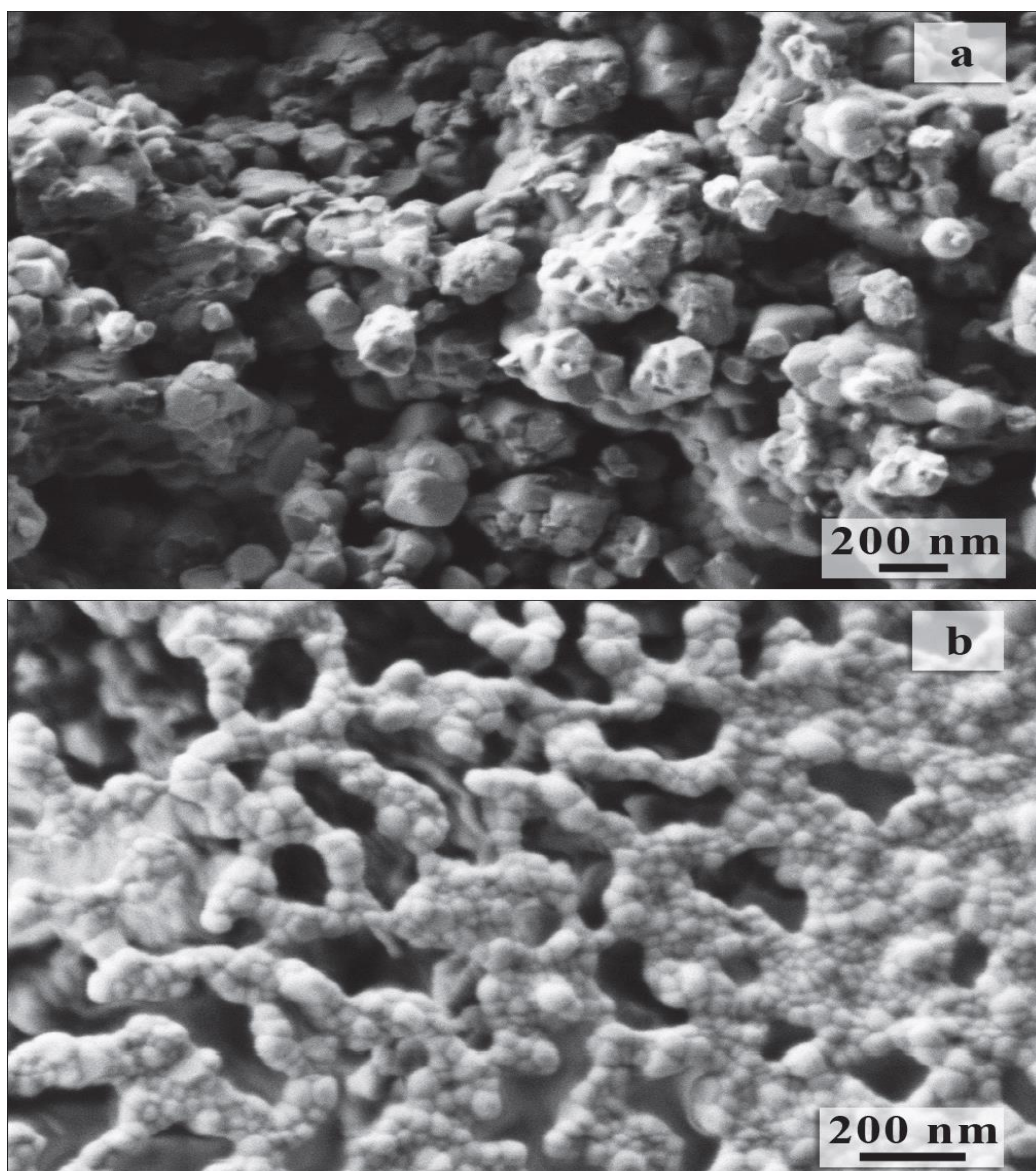
Fig. 2.25: (a) Microstructure of a Gd$_2$Zr$_2$O$_7$ sample after sintering pellet at 1000 °C for 4 h and (b) powder after twice repeated heating to 1200 °C in air [99]

2.4.5. Applications of nanoparticles with change in size range

Inorganic nanoparticles of simple and complex nature possess unique physical and chemical properties which make them excellent materials for the development of nanodevices for physical, biological, biomedical and pharmaceutical applications [100-102]. Nanoparticles having properties of narrow size distribution, high magnetization value and a size less than 100 nm are required for biomedical applications [103].

Nanoparticles with size less than 10 nm possess high surface area which make them efficient materials to facilitate the photodegradation reaction for environmental applications [104].

Applications of metal oxide nanoparticles are mainly categorized as: materials with high surface area and materials benefiting the size-dependence of physical properties. Materials with large surface area per weight are used in supercapacitors. This thought is geometrical mostly and not relevant to size dependant physical properties [105].

$A_2B_2O_7$ type metal oxide nanoparticles with high mechanical strength and good ionic conductivity were used in the fuel cell applications. Fluorite structured $A_2B_2O_7$ type materials like holmium hafnate was used in semiconductors and solid oxide fuel cells as electrolyte materials due to their high ionic conductivity [106]. Pyrochlore structured lanthanum based metal oxide nanoparticles were used as thermal barrier coating for thermal applications [107].

2.5. Scope

According to literature search solid oxide fuel cell produces electricity efficiently through direct conversion process with low level of pollutant emission. Main challenges in wide commercialization of this technology are high operating temperature, lengthy start up and shut down times, expensive starting materials, higher running cost and thermal stresses.

This project mainly focused to develop novel sol-gel manufacturing of pyrochlore based nanoparticles and evaluate their ionic conductivities as electrolyte materials for SOFC. Fuel cells are generally characterised with their electrolyte material, SOFC has oxide ion conducting ceramic electrolyte. Lanthanide based pyrochlore are emerging as an important class of solid oxide materials with potential applications. A lot of these applications are due to flexibility of pyrochlore structure and specifically mobility of anions.

In this research zirconates and hafnates of Holmium (Ho) and Lanthanum (La) were synthesised first time through sol-gel method. The selection of these metals (La and Ho) were based on the fact that the compounds formed with lanthanum exhibit pyrochlore and with that

of holmium exhibit defect-fluorite structures. It is intended to synthesise these metals based materials with more oxygen ion vacancy at low temperature using LAP. Sodium alginate solution was used for ion-exchange with metal salt solutions to form gels. Formed gels were calcined into nanopowders after performing TGA/DSC analysis and sintered at different temperature to study rate of crystal growth. Transmission Electron Microscope (TEM) and XRD Rietveld refinement used to measure crystallite size. Literature [92] shows that solution of sodium alginate forms gel in the presence of multivalent ions and promotes chemical gelation. Beads and granules of sodium alginate are used for ion exchange. Sample preparation time is reduced with the preparation of granules using a commercial pan granulator. Beads are prepared either using syringe or by adjusting the flow rate of sodium alginate solution using burette. The detail on process is available in chapter 3.

Studying the structural properties of pyrochlores ($A_2B_2O_7$) presence of oxygen vacancy in defect fluorite structure helped to enhance the ionic conductivity of materials. XRD, TEM and SEM used to analyse crystallite size, morphology and microstructure. Raman spectroscopy used to study the fluorescence and spectroscopic properties of the synthesised nanopowders.

Effect of different parameters like sintering temperature and time also studied because it helped to change the densification and mechanical properties of final product for more solid oxide fuel cell applications. Sintering temperature affects particle size and in some cases transform materials from ordered pyrochlore to disordered fluorite structure. Results in literature show that with the increase in sintering temperature, mean crystallite size and cation disorder increase for zirconates and hafnates of La and Ho. SEM used to analyse grain size and microstructure of pellets after single step and two step sintering.

Effect of sintering temperature and time on densification and grain growth of particles studied using SEM. Temperature dependence of AC-impedance analysis carried out to study the ionic conductivity of pellets prepared from nanoparticles, to make them eligible as SOFC electrolyte.

Thermal, structural, morphological and spectroscopic properties of metal oxide nanopowders formed from sol gel method are very important to study as they decided the applications of these materials for SOFC electrolyte. The detail on characterisation, microstructural and electrical properties is available in chapter 4.

Materials synthesis using granules and investigation of synthesis through the metals salts solution followed by calcination for pyrochlore is available in chapter 5.

Ion exchange kinetics of meal alginate beads using UV-vis spectroscopy for the nanoparticles synthesis and values of diffusion coefficients studied. Evolved gas analysis (EGA) of components released during the calcination stage and their quantification are available in chapter 6. Proposed reaction scheme and overall mass and energy balance of Leeds Alginate Process (LAP) also provided in chapter 6.

Chapter 7 of the thesis comprises of conclusions and possible future work in this regard.

Chapter 3

Experimental Detail

3.1. Materials

Materials used for the synthesis are commercially available holmium (III) nitrate pentahydrate, $Ho(NO_3)_3 \cdot 5H_2O$ (purity 99.9%) and hafnium (IV) tetrachloride, $HfCl_4$ (purity 99.9%) purchased from Alfa Aesar (Heysham, UK). Lanthanum (III) nitrate hexahydrate, $La(NO_3)_3 \cdot 6H_2O$ (purity 99.9%) and zirconium (IV) oxychloride octahydrate, $ZrOCl_2*8H_2O$ (purity 99.5%) were purchased from Sigma Aldrich Ltd (Gillingham, UK). Sodium alginate (Na-ALG) was purchased from Sigma Aldrich Company Ltd. (Birmingham, UK)

3.2. Production of Metal Complex Nanoparticles

3.2.1. Sodium Alginate Beads (Leeds Alginate Process-LAP)

In this study nanoparticles of hafnate and zirconate of holmium and lanthanum are prepared using Sodium Alginate (Na-ALG) method. The whole process is described in Fig. 3.1.

Metal alginate beads are prepared using this method. Sodium alginate solution (4%) is prepared by dissolving calculated amount of Na-ALG powder in distilled water under magnetic stirring. Metal complex solution is prepared by dissolving appropriate amount of metal nitrates and chlorides in 100 ml of distilled water along with magnetic stirring. Na-ALG solution is dripped in metal complex solution with the help of burette as shown in Fig. 3.2. Alginate beads are kept in gelling media overnight with gentle magnetic stirring to allow complete ion-exchange between Na and metal ions. Wet metal alginate beads are separated from solution using stainless steel sieve (5 mm) and washed with several washes of distilled water. Washed beads are dried overnight in convection oven at 90 ˚C. Schematic flow diagram for the synthesis of

metal oxide nanopowders employing Leeds Alginate Process (LAP) is shown in Fig. 3.3. Fig. 3.4 shows the clean wet and dried metal-alginate beads.
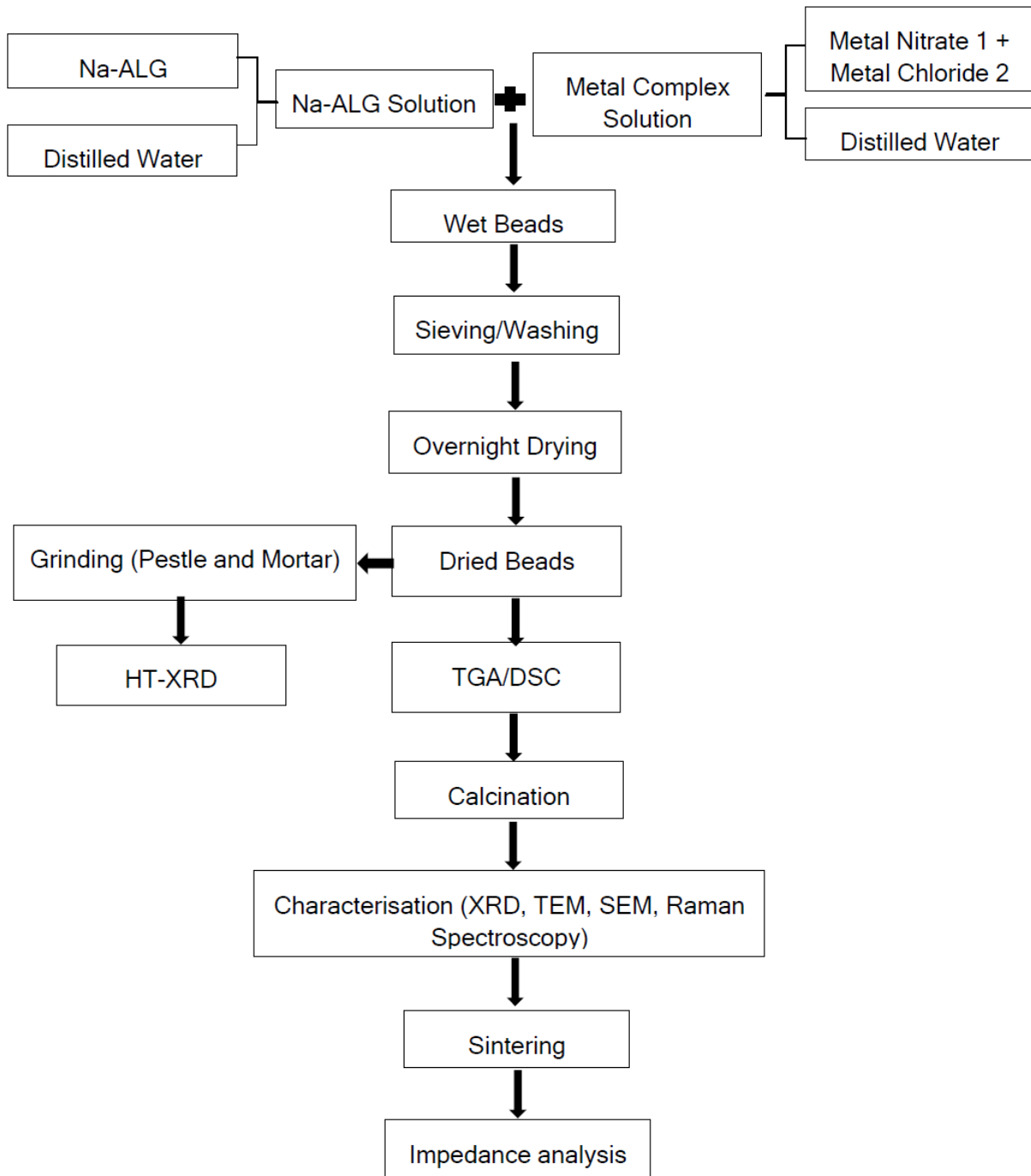
Fig. 3.1: Flow chart of nanoparticles preparation using Na-ALG beads
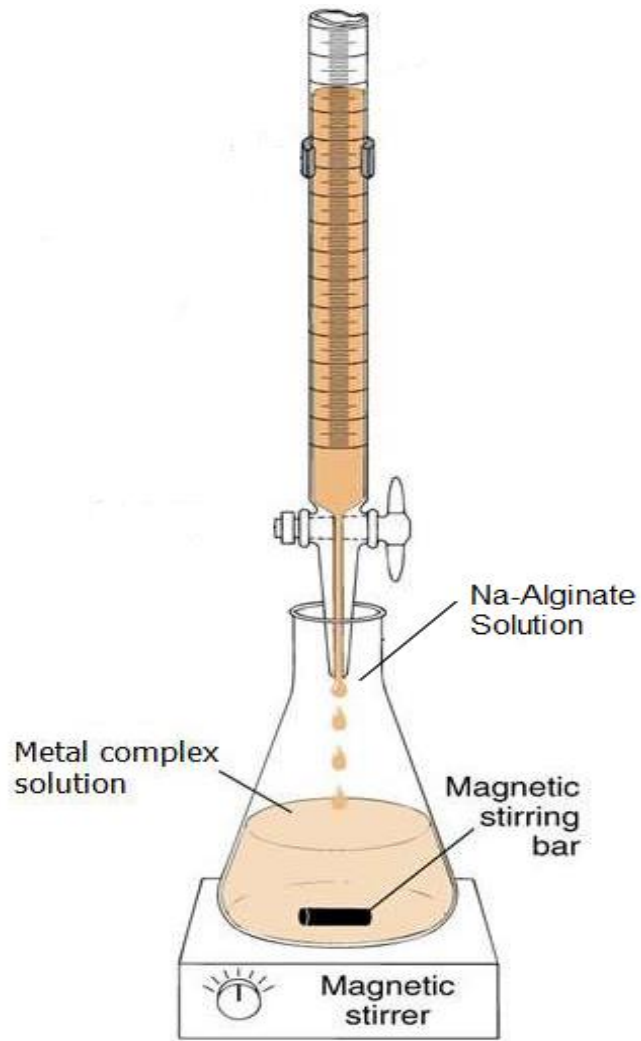
Fig. 3.2: Alginate Sol-gel synthesis
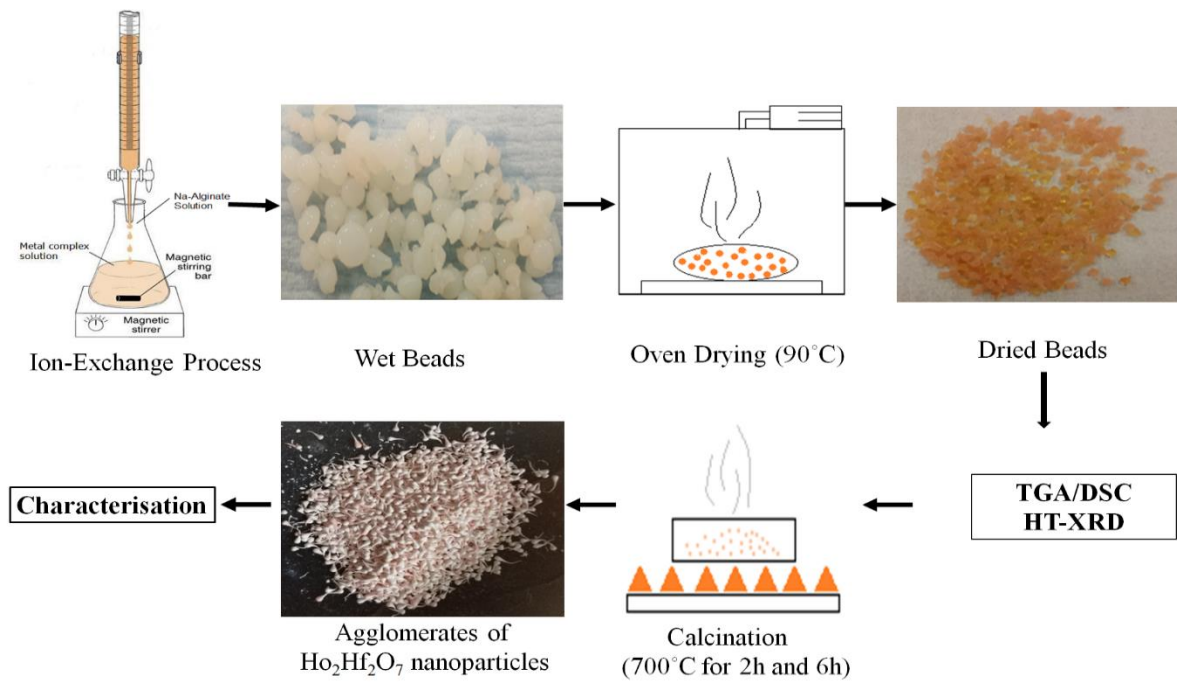
Fig. 3.3: Schematic flow diagram for the synthesis of Ho$_2$Hf$_2$O$_7$ nanopowders employing LAP.
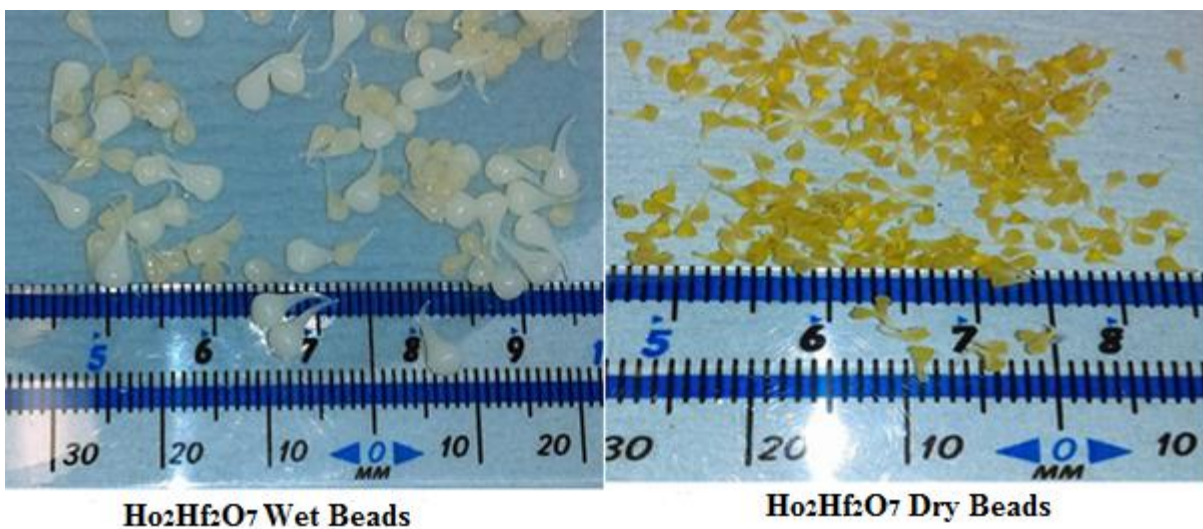
Fig. 3.4: Wet and dried beads of holmium hafnate

3.2.2. Metal complex Nanoparticles Production using Sodium Alginate Granules

Mechanical rotary pan device was used to prepare the granules of sodium alginate. First, sodium alginate powder was introduced in the pan and then sprayed with distilled water while pan is rotating. Granules formed in this process are of different sizes which are then sieved to

obtain uniform sized granules to avoid the final product get affected. Fig. 3.5 shows the granules before and after sieving.

Before Sieving   **After Sieving**
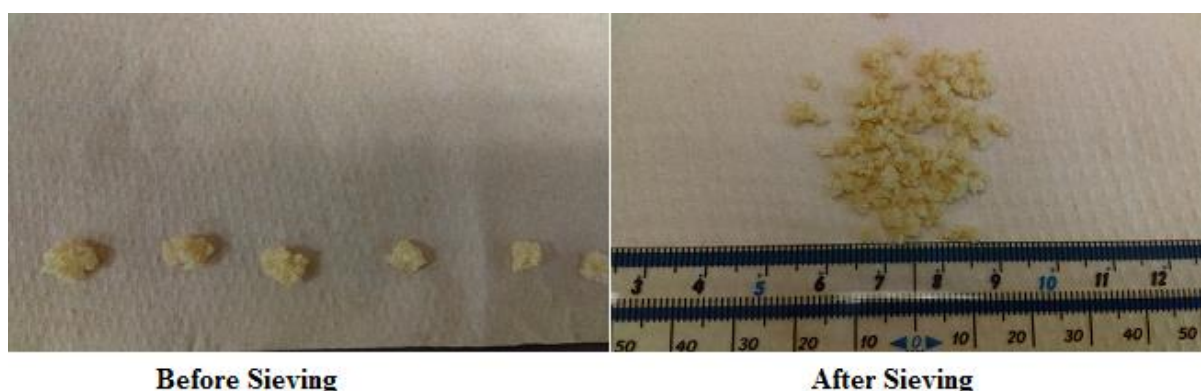
Fig. 3.5: Granules before and after sieving

Metal complex solution was prepared by dissolving appropriate amount of metal nitrates and chlorides salts in the distilled water using magnetic stirrer. Then 10 g of 2 mm sodium alginate granules were introduced and allowed the solution stay overnight with gentle magnetic stirring for ion-exchange. Wet granules removed from the solution using sieve, washed with distilled water and dried in the convection oven at 90 ˚C until constant weight achieved. Fig. 3.6 shows the wet and dry beads.

Wet Granules   **Dry Granules**

Fig. 3.6: Wet and dry granules

3.2.3. Solution Method

Oxide nanoparticles are also prepared using solution method to compare the results with Leeds Alginate Process (LAP). In solution method, appropriate quantity of metal nitrate and chloride salts were dissolved in the distilled water using magnetic stirrer. The solution was subsequently dried on the hot plate at 90 °C while stirring until all the solvent has fully evaporated and only oxide powders left behind. The powder was calcined at similar conditions as in LAP and characterised using different techniques.

3.3. Characterization Techniques

Mechanism of sol-gel process affects the physicochemical properties of final product. These properties are dependent on microstructure, porosity and structural coordination of materials. To understand the properties of synthesised materials monitoring is carried out at various steps and of final product. Different characterization techniques such as TGA/DSC, HT-XRD, XRD, Raman spectroscopy, TEM, SEM and EDX are used to understand the thermal, structural, morphological and spectroscopic properties of the nanopowders. Pellets of nanopowders of different materials were sintered and analysed using AC-Impedance spectroscopy. Principles and measurements of different techniques used are concisely described.

3.3.1. TGA/DSC

3.3.1.1. Principle of Thermal Analysis

A substance can undergo phase transitions or chemical decompositions during the heating process of thermal analysis. Exothermic and endothermic heat effects are involved in phase transitions. In addition to heat effect mass loss can take place if gaseous product forms during chemical decomposition. Thermal analysis methods can be divided in three categories: (i) thermogravimetric analysis (TGA) (ii) differential thermal analysis (DTA) (iii) differential scanning calorimetry (DSC) [105, 108].

3.3.1.2. TG/DTA

Fig. 3.7 shows the schematic representation of TG/DTA system. Main components of apparatus are: (i) sample holder measuring unit (ii) furnace (iii) temperature programmer and recording system.

(i)   Sample holder-measuring unit: High density sintered alumina crucibles are used as sample and reference holders. Thermocouples are used for sample temperature measurement in measuring unit (chromel-alumel thermocouple shows better result below 850˚C and platinum-rhodium thermocouple for above 850˚C). Sample holder forms the part of one arm of thermobalance.

(ii) Furnace: Source of heat with large and uniform temperature zones

(iii) Temperature programmer and recording system: Device which executes the rate of change of temperature on furnace

During heating or cooling cycle, system allows the gas or vapour flow at controlled rate.

3.3.1.3. Thermogravimetric Analysis (TGA)

In TGA mass of sample is measured precisely while it is subject to predetermined cooling or heating. At a fixed temperature sample can be maintained isothermally. In present generation thermogravimetric system, the thermobalance is sensitive to the range of μg. Result of TGA measurement can be influenced by different factors like sample preparation, method parameters, humidity control, choice of crucible, instrumental effect, furnace temperature and inhomogeneity of sample.

3.3.1.4. Differential Thermal Analysis (DTA)

Here difference in temperature between sample cell, Ts, and thermally inert reference, Tr is measured. The behaviour of sample whether exothermic and endothermicis determined by reading the difference (Ts-Tr) as function of temperature. In DTA curve upward deflection is plotted for exothermic process and downward for endothermic [108].

3.3.1.5. Differential Scanning Calorimetry (DSC)

DSC measures the required energy to maintain zero temperature difference between inert reference material and substance. DSC has two types based on its function; power compensation and heat flux as shown in Fig. 3.8.
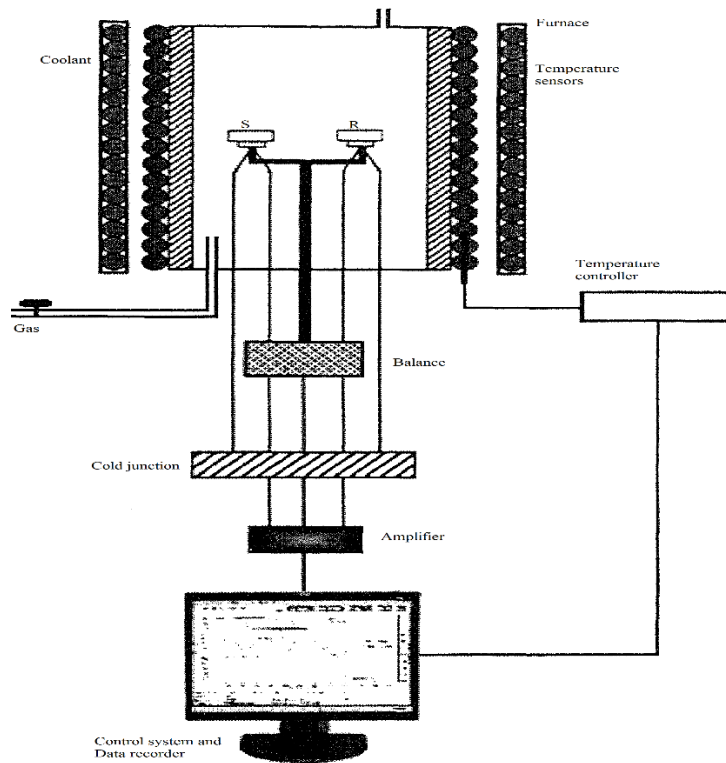
Fig. 3.7: Schematic representation of TG/DTA
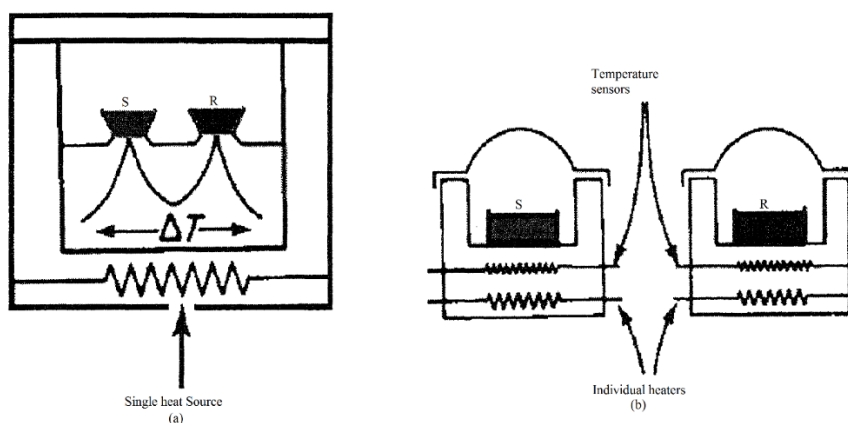
Fig. 3.8: (a) Heat flux DSC (b) Power compensation DSC

Temperature of reference and test sample are independently controlled using separate identical furnaces in power compensation DSC. Uniformity of sample and reference temperature is made by controlling the power input to two furnaces. In case of heat flux both reference and sample are in single furnace. Change in enthalpy or heat capacity of sample cause a relative temperature difference. Difference in energy required to maintain them at nearly identical temperature is provided by heat changes in sample [108].

3.3.1.6. Characterization by TG/DTA and DSC

Dried beads were characterized by thermal analysis to study their thermal behaviour. Thermal analysis is carried out to find the ignition temperature of precursors. For this both TG and DTA techniques were used to characterize thermal and mass loss events on heating the precursors using TG/DTA simultaneously of Mettler Toledo STAR^e System (Leicester, UK). Approximately 10 mg of precursors were taken as sample and TG/DTA study was carried out from room temperature to 1000 ˚C with heating rate of 10 ˚C/min in flowing air at the rate of 10 ml/min. DSC measurement for precursor is also carried out.

3.3.2. High Temperature X-Ray Diffraction (HT-XRD)

The dried metal alginate beads were milled by employing Retsch Shaker Mill at the frequency of 30 Hz using steel ball to obtain fine powder for High Temperature X-ray diffraction (HT-XRD) analysis, employing CuKα radiation (λ= 1.5418A˚) (Anton Paar HTK-1200, Almelo, The Netherlands) at 40 kV and 40 mA. The temperature program was set to increase the sample temperature from room temperature to 1000 °C with the interval of 25 °C at the heating rate of 10 °C/min in static air condition. Dwell time of 30 mins was provided at each temperature to allow the attainment of complete thermal equilibration of the sample. Scan for HT-XRD was performed over a 2θ ranges from 20-80° with the step size of 0.03°. To obtain the information of phases present a total scan time of 20 min was provided. This system employs the

X'cellerator multi-detector which causes surd (irrational) in step size. Programmable divergence and antiscatter slits were used for generating constant irradiation length on the sample to improve the data collection statistics at higher angles and reducing the effect of air scattering at low angles which has been known to influence the background of X-ray diffraction patterns. The data were converted from automatic to fixed slit to make it suitable for structural analysis. Resultant data were analysed using software package X'Pert High Score plus (P'Analytical, The Netherlands).

3.3.3. X-Ray Powder Diffraction (XRD):

XRD is one of the important techniques of characterizing samples. Its effective use is for phase analysis, deduction of an order/disorder phenomenon, structural determination, detection of preferred orientation and determination of crystallite size of powder sample [108].To identify the structure, phase transformation of material, position and intensities of peaks are used [109].

3.3.3.1. Principle of XRD

Parallel monochromatic X-ray beams with the wavelength of λ falling on successive plane of the crystal at an angle of θ as shown in Fig. 3.9. Constructive interference of reflected rays from two successive planes occurs, only the path difference between two rays fulfils the Bragg's law,

$$n \lambda = 2d \sin \theta$$

where 'n' is an integer, 'd' is inter planar distance, 'θ' angle between the atomic plane and incident X-ray beam and 'λ' is wavelength [108, 109]
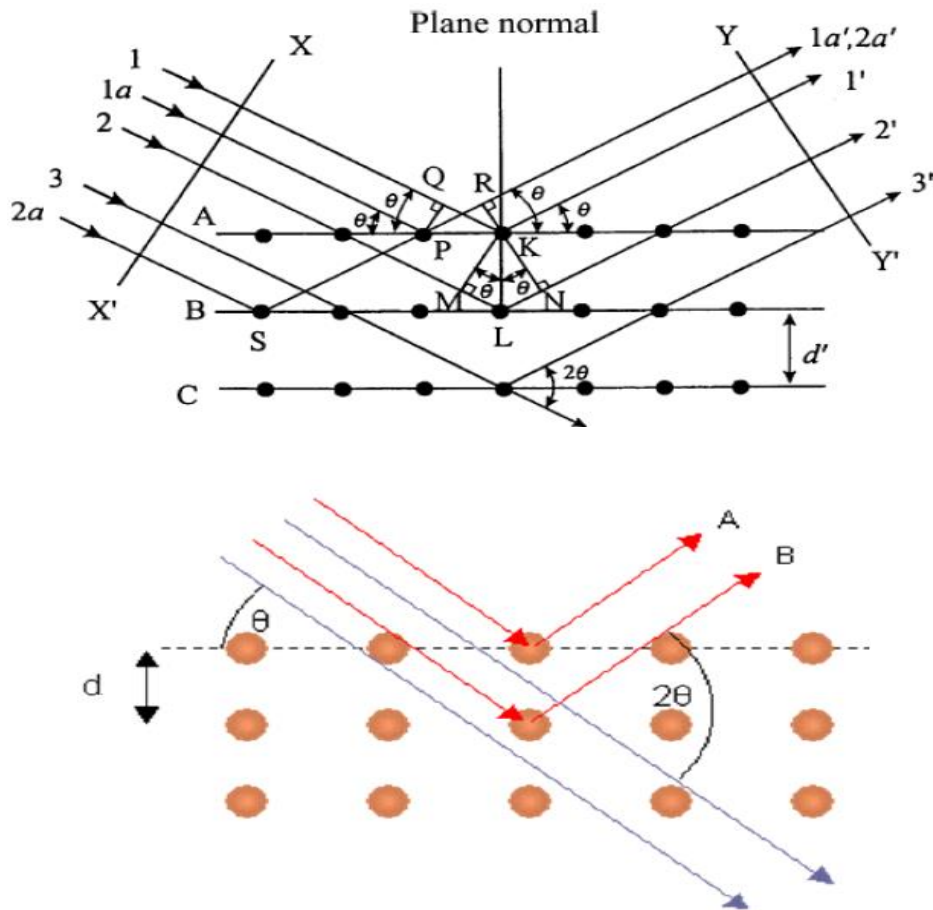
Fig. 3.9: Different sets of parallel crystal planes

3.3.3.2. Crystallite Size Calculation

Crystallite size of particles can be calculated by doing suitable analysis of X-ray line broadening. In XRD, diffracted lines are not always sharp and may be broadened due to nature of specimen (crystallite size), strain or instrumental factors. For small particles lines are broader than usual. Decrease in crystallite size increase in broadening. Scherrer's formula is used to determine crystallite size of sample [110, 111]. Equation 3.1 is Scherrer formula

$$B(2\theta) = K\lambda / L \cos\theta \qquad (3.1)$$

Where 'L' is crystallite size, 'B' is peak width at half maximum in radian of 2θ, 'K' is Scherrer constant and 'θ' is angle which exactly satisfies the Bragg's law.

Peak width (B) is inversely proportional to crystallite size (L). 'K' depends on shape of crystal, size distribution and how the width is determined.

'K' actually varies from 0.62 to 2.08. Most common values for K are:

- 0.94 for full width at half maximum (FWHM) of spherical crystal with cubic symmetry

- 0.89 for integral breadth of spherical crystals with cubic symmetry

- 1, because 0.94 and 0.89 both round up to 1

Different factors contribute to peak profile. Peak broadening can be due to:

- Crystallite size

- Instrumental profile

- Microstrain

- Solid solution inhomogeneity and temperature factors

XRD can be used to determine:

- Phase composition of a sample (Single phase or Multiphase)

  o Quantitative Phase Analysis-determine relative amounts of phases in a mixture with reference to relative peak intensities

- Unit cell lattice parameters and symmetry

  o Index peak positions

  o Lattice parameters can vary as function of and provide information about doping, alloying, strains and solid solutions

- Residual strain (macrostrain)

- Crystal structure

  o By Rietveld refinement of entire diffraction pattern

- Crystallite size and Microstrain

  o Indicated by peak broadening

o   Analysis of peak shapes and width measure the other defects like stacking faults

- Epitaxy/Texture/Orientation

3.3.3.3. Characterization

It is important to have sample with smooth plane surface. Sample is generally ground to particles of 0.002 to 0.005 mm cross section. Ideal sample is homogeneous and crystallites are randomly distributed. Sample is pressed in sample holder to obtain smooth flat surface. Rock the sample through glancing angle (θ) to produce all possible reflections. Powders are mounted in stainless steel sample holder and analysed using X-ray diffraction (Bruker D8 Advance XRD, Germany) using Cu Kα radiation (λ= 1.5418A$\degree$). Scans are usually performed over range of 20 – 80° with step size of 0.04^{o}/s at room temperature. Obtained patterns were compared with the database of International Centre for Diffraction Data (ICDD). A software X'Pert High Score plus (P'Analytical, The Netherlands) was used to perform Rietveld refinement on resultant XRD data.

3.3.4. Transmission Electron Microscope (TEM)

Transmission electron microscope is one of the powerful tools in the field of nanoscience for the direct imaging of lattice structure of solids. TEM is versatile and comprehensive tool to characterize chemical and electronic structure at nanoscale with the help of electron energy loss spectroscopy (EELS) and energy dispersive X-ray spectroscopy (EDS). Details on internal structure of sample such as phase composition, crystal structure, atomic arrangement and defects can be obtained by collecting the transmitted or diffracted electrons, TEM-EDS and selected area electron diffraction (SAED) patterns.

3.3.4.1. Principle of TEM

TEM works on basic principle of light microscope but instead of light it uses electrons. It is possible to obtain a thousand times better resolution than light microscope with lower

wavelength of electrons. Small details of different materials down near to atomic levels can be studied. With the possibility of high magnification TEM is valuable tool for nanomaterials, biological and medical research [112].

Electrons emitted by the electron gun at the top of TEM, travels through column of microscope under high vacuum. Electromagnetic lenses are used to focus the electrons into a thin beam. Electron beam travels through the thin specimen which is dispersed in holey carbon coated grid. Some of the electrons disappear and scatter from the beam depending on the density of material present. An unscattered electron hit the fluorescent screen at the bottom of microscope it generates an image of specimen displayed in varied darkness according to the density. For further analysis image can be recorded digitally or as photograph [113]. Fig. 3.10 shows the schematic of TEM.
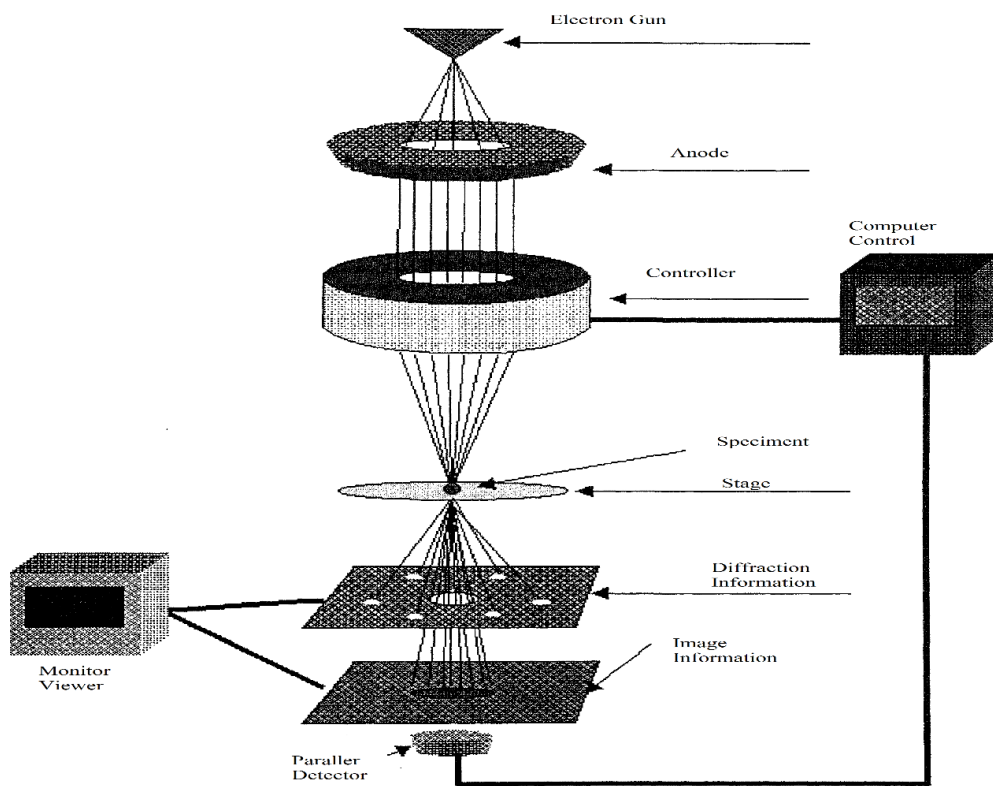
Fig. 3.10: Schematic representation of TEM

3.3.4.2. Characterization

EDS is used to obtain the chemical composition of sample. To determine the lattice image and phase formation at nanometre scale high resolution TEM is used. Sample is dispersed in acetone and drops of it deposited to holey carbon coated commercial copper grid which is specifically for TEM use. Prior to conducting experiment sample is dried and stored in small clean black box. Dried copper grid was further used for TEM analysis.

In this study, transmission electron microscope (FEI Tecnai TF20 FEG-TEM, Eindhoven, The Netherlands) has been used to analyse the particle size and distribution of nanopowder. Dark-field image and selected area electron diffraction (SAED) patterns were used to obtain the interplanar spacing.

3.3.5. Raman Spectroscopy

Raman spectroscopy is form of molecular spectroscopy which involves the scattering of electromagnetic radiation by molecules or atoms. It probes the vibrational, rotational and low frequency modes of molecules, and Raman signal is observed as inelastically scattered light.

Raman spectroscopy has several advantages: [114]

- It is a non-destructive technique

- Involves little or no sample preparation

- Analysis can be performed directly through transparent containers

- Can be used for both qualitative and quantitative analysis

- Highly selective technique; can differentiate molecules in chemical species that are very similar.

- Fast analysis time

Two types of Raman Scattering are: Stokes scattering and anti-Stokes scattering. When energy of the incident photon is not large enough to excite molecule from ground state to lowest

electronic state then molecule will be excited to virtual state between the two states. In the excited molecules electrons cannot stay long at that state so return back to original state immediately then emitted photon has same wavelength as the incident light photon. This is called Rayleigh scattering.

There is possibility that electron fall to any other virtual state different from where it is excited from then there will be energy difference between the emitted and incident photons therefore a shift in wavelength occurs (energy shift) for the emitted photon as compared to incident photon. This is called Raman scattering. Stokes scattering is observed when the emitted photon has lower energy (longer wavelength) than incident photon. If the emitted photon has higher energy than the incident photon then there is anti-Stokes scattering. Fig. 3.11 illustrates difference between scatterings.

$hv = hv_0$
Rayleigh scattering

$hv = hv_0 - hv_k$
Stokes scattering

$hv = hv_0 + hv_k$
Anti-Stokes scattering
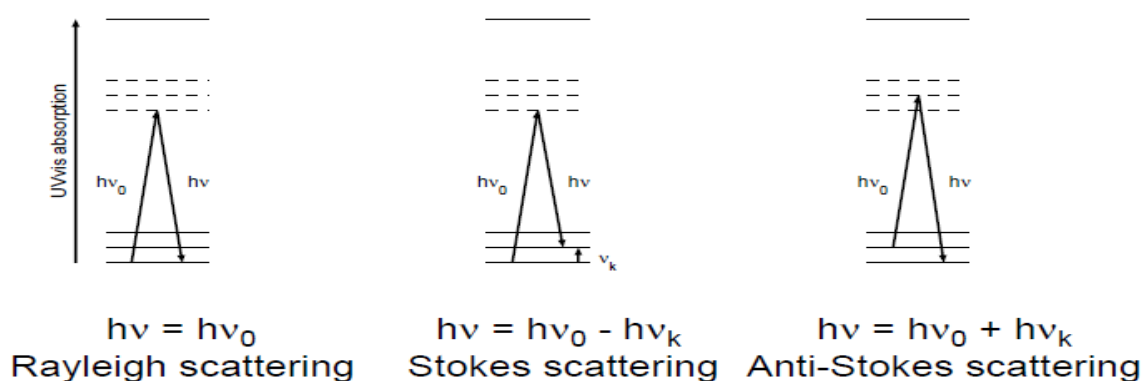
Fig. 3.11: Raleigh scattering, Stokes scattering and anti-Stokes scattering

Numerically, Raman shift in wavenumbers (cm^{-1}) is calculated using equation 3.2.

$$\nu = \frac{1}{\lambda_{incident}} - \frac{1}{\lambda_{scattered}} \qquad (3.2)$$

Here, λs are the wavelengths of incident and Raman scattered photons.

Basically Raman spectrum is recording of frequency and intensity of inelastically scattered photons. Every atom and molecule has its own Raman spectrum which can be used to identify its structure which will relate to the elements and compounds present in the sample.

Raman spectrum is plotted in terms of energy shift and with respect to exciting line rather than by absolute wavelength as energy of this shift is significant [115].

3.4. Sintering and Densification

3.4.1. Pelletizing

Nanopowders are compressed in the form of specific dimensions in a uniaxial stainless steel die pellets using hydraulic press before sintering. Pump handle is used to build the pressure upto 5 tons and then pressure is released by turning the pressure release handle anticlockwise.

3.4.2. Single Step Sintering (SSS)

Sintering is the process in which interparticle pores in a granular material are eliminated by atomic diffusion driven by capillary forces. This is preferred manufacturing method for industrial ceramics. Normal sintering practice for Y_2O_3 is to heat the powder compact at a certain rate and to achieve the maximum density hold it at highest temperature. Fig. 3.12 shows that the grain size of Y_2O_3 sample increases continuously with the density. Final grain size varies between 200-600 nm depending on the composition, most of the variations occur when density exceeds 80 % of theoretical value. Data in Fig. 3.12 below is in line with common sintering experience; accelerated grain growth accompanies final stage sintering. Even with fine starting powder (30 nm), final grain size of dense ceramic is well over 200 nm [116].
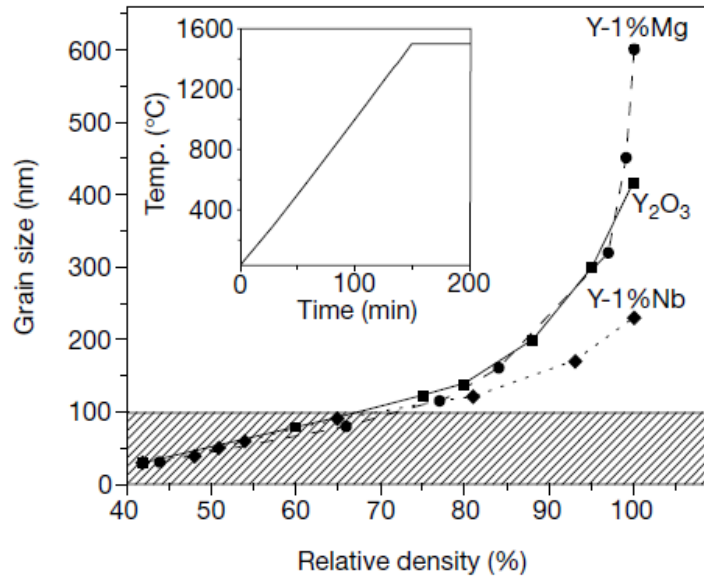
Fig. 3.12: Increasing the grain size of Y$_2$O$_3$ with density in normal sintering. Inset is heating schedule [116]

3.4.3. Two Step Sintering (TSS)

Here sintering method used two steps in heating schedule. First sample is heated to a higher temperature to obtain an intermediate density, then cooled down and held at lower temperature until fully dense. Initially pure Y$_2$O$_3$ is heated to 1310 °C to achieve full density and then holding at 1150 °C for 20h during which there was no grain growth as shown in Fig. 3.13. Another example is heating first at 1250 °C and full densification without grain growth was achieved after holding at 1150 °C for 20 h. Grain size remains constant in second step sintering despite density improvement to 100 % of theoretical value. Sintering has not resulted in grain growth and results are different from Fig. 3.12. Densities higher than 75 % were adequate for subsequent two step sintering [116].
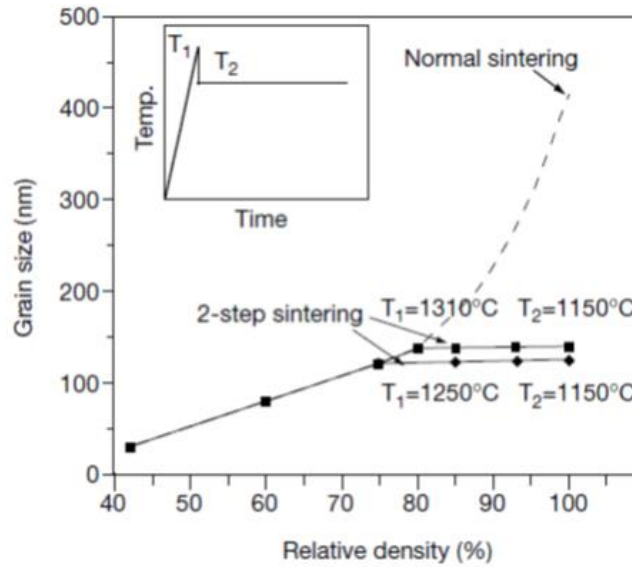
Fig. 3.13: Grain size of Y₂O₃ in two-step sintering. Inset is heating schedule [116]

3.5. Microstructural Study

3.5.1. Grinding, Polishing and Thermal Etching

Sintered pellets of all materials were ground, polished and thermally etched before doing SEM analysis. Pellets were ground to remove the top layer and then polished down to 3 um diamond paste to achieve the smooth surface subsequently for thermal etching all the pellets were heat treated for 1 hr at the temperature 50 °C below their sintering temperature i.e. if sintering is at 1300 °C then thermal etching is at 1250 °C. With thermal etching clear grain boundary are revealed in the microstructure.

3.5.2. Scanning Electron Microscope (SEM)

Scanning Electron Microscope is widely used to investigate the morphology and microstructure of sintered pellets. In this technique sample surface images are captured using electron beam. Deflected electron beam is used to produce images [117].

3.5.2.1. Principle of SEM

A beam of electron is generated from electron gun located at the top of microscope. Beam is condensed by the condenser lens and attracted towards the anode, then objective lens focuses

it at very fine point on the specimen. Primary electrons are inelastically scattered by the atoms in specimen as they strike the surface, which are collected by secondary or backscatter detector, converted to a voltage and amplified. SEM equipped with Energy Dispersive X-ray Spectrometer (EDS) can detect the X-rays produced by interacting the electrons with sample [118]. Local charge on the sample can be either positive or negative. But negative charge causes more serious problem as it repels the incident electron and reflects the scanning probe resulting in image distortion and fluctuation in image intensity [119]. To overcome this problem, sample are coated with gold or carbon using Ion sputter coater. Micrographs are taken at different magnification level from micrometre to nanometre [120].

Characteristic information obtained from SEM images are:

- Grain size

- Surface roughness

- Porosity

- Particle size distributions

- Material homogeneity

- SEM-EDX for elemental composition analysis

3.6. Electrical Properties

3.6.1. Coating of Pellets

To measure the electrical properties of the materials before carrying out impedance measurement all the high density sintered pellets were coated with silver paste and heated at 800 °C for 1 hr so that paste bonds to the pellets strongly and any organic binding material present can be removed.

3.6.2. Impedance Measurement

Electrical conductivity of the materials has been measured using Solartron SI1260 frequency response analyser (FRA) supplied by AMETEK Advanced Measurement Technology, Farnborough, UK. Construction of an impedance plot from the impedance measured of a cell over the wide range of frequency gives more information of conduction mechanism than a DC or single frequency AC measurement.

Electrochemical impedance is usually measured by applying a small AC potential to an electrochemical cell and measuring the current through the cell. The AC excitation voltage should be less than the thermal activation energy to obtain pseudo-linear system. Generally, the AC excitation voltage is set to be less than 10 mV.

The results of EIS investigation can be recorded as Nyquist or Cole-Cole plots of $Z_{imaginary}$ vs Z_{real} and proprietary software of ZView (Scribner Inc, USA) is used to produce the equivalent circuits for a given electrolytes as shown in Fig. 3.14. The peak angular frequency attributed to bulk and grain boundary relaxation processes are denoted by $f_{b(max)}$ and $f_{gb(max)}$, respectively. Values of the resistance R_b, R_{gb} and R_e which represent the bulk, grain boundary and equivalent resistance respectively can be obtained from the intercept of semicircles with abscissa (Z_{real}).

Equations 3.3 to 3.5 are used for resistance (R), capacitance (C) and conductivity (σ):

$$RC = 1/2\pi f \qquad (3.3)$$

$$R = \rho\ L/A \qquad (3.4)$$

$$\sigma = 1/\rho \qquad (3.5)$$

Where:

- R is resistance (Ω)

- C is capacitance (F)

- f_{max} is maximum frequency in one semi-circle (Hz)

- ρ is resistivity (Ωm)

- L is thickness of the pellet (cm)

- A is the electrode area of the pellet (cm^2)

The activation energy (Ea) for ionic conduction can be obtained using Arrhenius equations 3.6 and 3.7:

$$\sigma T = \sigma_0 \, exp \, (-Ea/RT) \tag{3.6}$$

$$ln\sigma T = ln\sigma_0 + (-Ea/R) \, 1/T \tag{3.7}$$

Where:

- σ_0 is pre-exponential conductivity

- Ea is activation energy (J mol^{-1})

- R is gas constant (8.314 J mol^{-1}K^{-1})

By plotting the $ln\sigma T$ against $1/T$ the value of activation energy for ionic conduction of the process can be obtained.
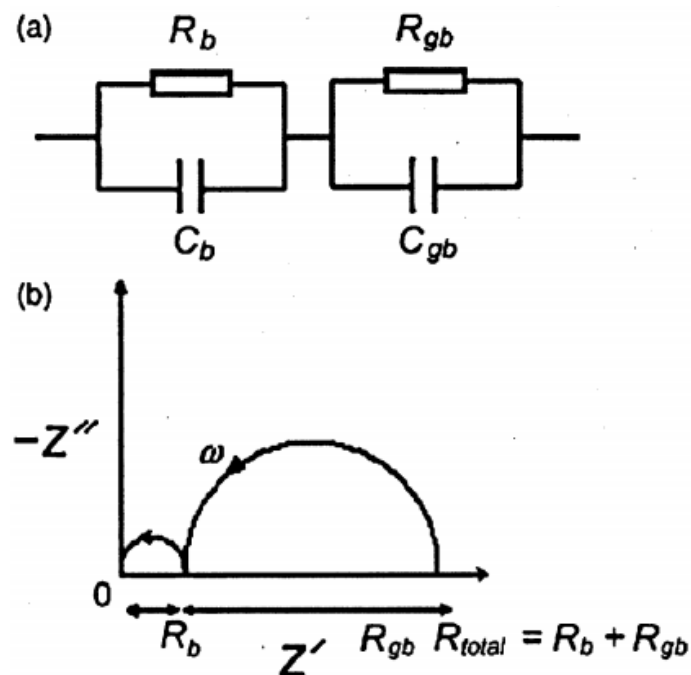
Fig. 3.14: Simulated complex impedance response of polycrystalline ceramic with corresponding equivalent circuit; (a) RC circuit (b) impedance plane plot [121]

The Warburg impedance is used in the equivalent circuit model where semi-infinite linear diffusion affects an electrochemical system by kinetic and diffusion control. The circuit model and Nyquist plot is shown in Fig. 3.15. The Warburg impedance in Fig. 3.15 (b) appears as a straight line with a 45 slope under semi-infinite conditions and one dimensional diffusion that is bound only by a large planar electrode on one side [122].
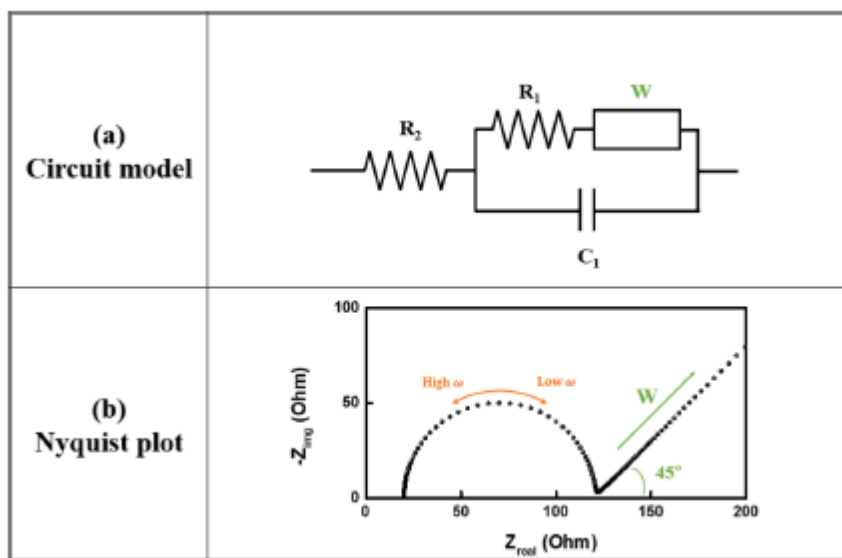
Fig. 3.15: (a) Equivalent circuit (b) Nyquist plot of a Randles cell model [123]

The conductivity of samples were measured in the frequency range of 100 mHz to 100 MHz at different temperature range in ambient air atmosphere using computer-controlled Solartron SI1260. Silver paste acts as electrodes on both sides of the pellets. The pellets are mounted in a spring-loaded quartz rig with electrical contact being made by means of Pt gauze spot welded to Pt wires.

This whole assembly is placed in a stainless steel tube acting as a Faraday cage which is located in a horizontal tube Lenton furnace. A K type thermocouple is placed close to the sample for monitoring temperature adjacent to the rig. At each temperature measurements are performed after at least 30 mins stabilization in both heating and cooling cycles.

3.7. Process Characterisation

3.7.1. Thermoanalytical measurements for Evolved Gas Analysis (EGA)

Coupled TGA/MS (Mass spectroscopy) technique is used to determine the thermal characteristics of the sample and identification of components released during heat treatment. TGA/MS experiments were performed on the TGA coupled with MS. Samples were loaded in Al_2O_3 crucible and mass loss was measured form 30 °C to 1400 °C at the rate of 10 °C/min in oxygen atmosphere at the rate of 10 ml/min. Evolved gases were transferred to the MS instrument for the analyses. A continuous nitrogen flow was supplied at the rate of 40 ml/min during transfer. Intensities of emitted gases were firstly analysed by evolution curves obtained through a preliminary scan from 1 to 64 mass to charge (m/z) value. After scanning, selected compounds were detected and recorded using multiple ion detection (MID) mode.

3.7.2. Processing of spent solution of LAP

Spent solution was processed to know its composition. First, it was heated on hot plate at 98 °C to remove all the water. The dried material was then calcined at 700 °C for 2h. Powder obtained after the calcination was analysed using powder X-ray diffraction (XRD Bruker D8) employing Cu*K*α radiation (λ= 1.5418A˚) at ambient conditions. Scan was performed over a 2θ ranges from 20-80° with the step size of 0.03°. A Rietveld size/strain structural refinement was performed on the data obtained from XRD. P'Analytical X'Pert High Score plus software package was used for Rietveld refinement.

3.7.3. Kinetic Study of Leeds Alginate Process

An appropriate quantity of sodium alginate powder (Sigma Aldrich Company Ltd. Birmingham, UK) was dissolved in distilled water to obtain a 4 wt% solution. The solution was dripped in 1 M HCl solution to produce alginic acid beads. After allowing sufficient time for completion of the ion exchange, the beads were removed from the solution using stainless

steel sieve and washed three times with distilled water to remove any unreacted sodium ion. These beads are used as the feed material for the study of diffusion of metal ions. The beads are dropped into metal nitrate salts solution and the temporal change in the salt solution in monitored to determine the rate of mass transfer.

Commercially available holmium (III) nitrate pentahydrate, Ho $(NO_3)_3.5H_2O$ (purity 99.9%) and hafnium (IV) tetrachloride, $HfCl_4$ (purity 99.9%) (Alfa Aesar, Heysham, UK) were dissolved in distilled water to obtain equimolar ratio of Ho^{3+}/Hf^{4+} [124]. Beads were immersed and kept in a fully mixed state in aliquots of the metal salt solution for set time periods of 2 min, 4 min, 6 min, 10 min, 20 min, 30 min, 1h, 3h, 5h and 7h. The beads were then separated from the solutions, which has been analysed with UV-Vis Spectroscopy to determine the depletion of metal ions in the spent solution and hence their uptake by the beads.

The beads were very uniform in size and their size has measured for 10 beads by image analysis using ImageJ and an average bead diameter has used in the calculation of diffusion coefficients. The entire ion exchange process was carried out at ambient temperature of 20°C.

Chapter 4

Results and Discussions

This chapter provides the results and detailed discussion and analysis of the research findings for both binary and ternary metal oxides. The chapter comprises of ternary metal oxides ($Ho_2Hf_2O_7$, $Ho_2Zr_2O_7$, $La_2Hf_2O_7$ and $La_2Zr_2O_7$) and binary metal oxides (Ho_2O_3, HfO_2, La_2O_3 and ZrO_2) synthesised using Leeds Alginate Process (LAP).

4.1. Holmium Hafnate ($Ho_2Hf_2O_7$)

Nanopowders of holmium hafnate were prepared using Leeds Alginate Process (LAP) and its thermal, structural and morphological characterisation has already reported [124].

4.1.1. Thermal and Structural Characterisation

Thermal analysis of oven dried beads was carried out using TGA/DSC for the determination of calcination temperature to obtain the nanoparticles and the result of the analysis is shown in Fig. 4.1 along with Differential Thermogravimetric (DTG) trace. Thermal decomposition of dried beads involved six stages of phase transformation. These six thermal decomposition stages were identified to be in the range 40 °C to 120 °C, 150 °C to 210 °C, 217 °C-375 °C, 375 °C-485 °C, 485 °C-535 °C and 535 °C-565 °C, respectively. In TGA/DTG profile decomposition steps agreed well with DSC curve as shown in Fig. 4.1. In DSC profile two small endothermic peaks were observed in the range 41 °C-108 °C and 160 °C-178 °C which is due to the loss of water during heat treatment. In TGA curve weight losses of 10 % was observed in the first stage due to the removal of adsorbed water. Evaporation of bound water and dissociation of alginate structure (GG-O-MM, MM-O-GM) along with evolution of bridging oxygen [125] were observed in the range 150 °C-210 °C with corresponding weight loss of 17 %. A weight loss of 23 % was observed in the range 217 °C-375 °C due to further loss of bridging oxygen and partially reacting with some of carbon atoms in the chain to form

CO_2. In DSC profile an exothermic band was observed from 205 °C-365 °C due to this partial reaction and splitting of weaker linkages (G-G, G-M and M-M) in the alginate polysaccharide molecule [125]. Two exothermic peaks were observed in DSC profile in the ranges 372 °C-485 °C and 485 °C-573 °C. These peaks were the result of oxidative decomposition of metal-alginate beads. Weight loss of 21 % was observed from 375 °C to 485 °C due to the bulk oxidation of alginate to form CO_2. Complete decomposition of β-D-mannuronic acid (M) and α-L-guluronic acid (G) residues [125] was observed with weight loss of 3 % and formation of binary metal oxides in the range 485 °C-535 °C. In the DSC curve a shoulder in second exothermic peak was observed at 535 °C. Formation of tertiary oxides was observed in the range 535 °C-565 °C with minor weight loss of 1 %. Based on TGA/DTG/DSC analysis the calcination temperature of 700 °C was determined to be the safe optimum temperature for the formation of phase pure $Ho_2Hf_2O_7$ which is the lowest temperature reported in literature for the formation of this compound.
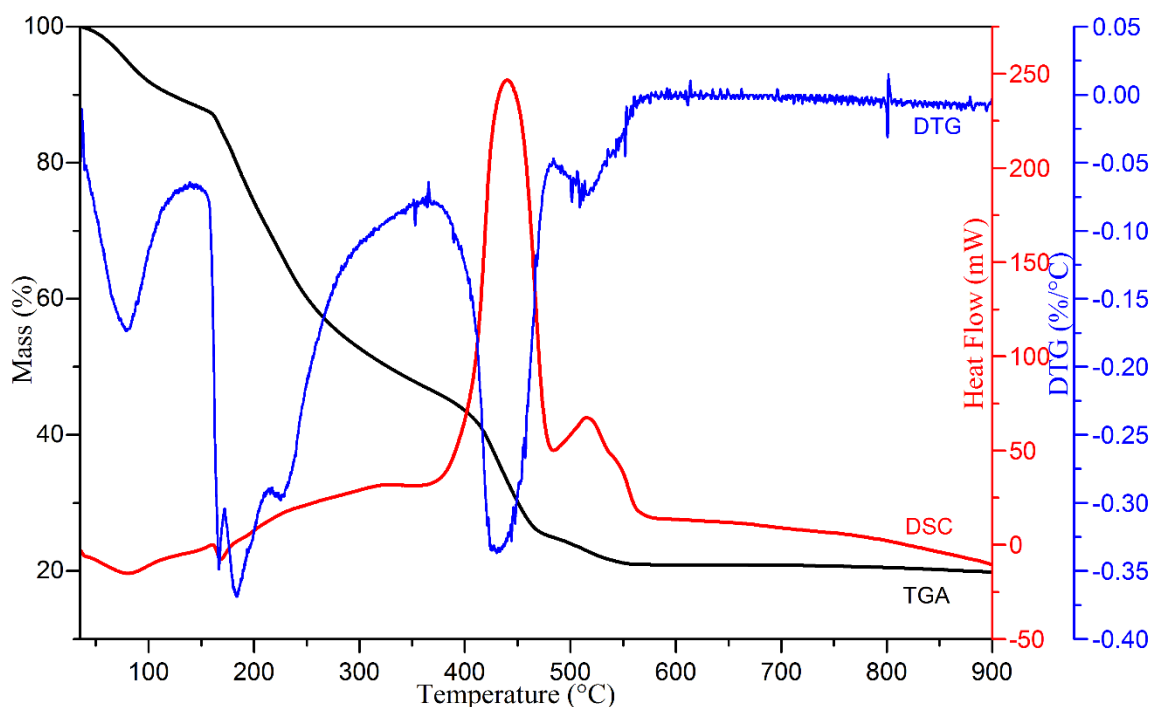
Fig. 4.1: TGA/DSC/DTG analysis of dry beads

74

HT-XRD was performed on milled beads from room temperature to 1000 °C at the rate of 10 °C/min in stationary air on α-Al_2O_3 sample holder.

Fig. 4.2 shows the HT-XRD patterns of oven dried metal alginate beads after eliminating α-Al_2O_3 peaks by refining the observed data. At temperature 400 °C-500 °C peaks of holmium hafnate started appearing along with sample holder peaks. Clearly a single phase cubic defect-fluorite $Ho_2Hf_2O_7$ pattern appeared to have evolved from alginate matrix at 500 °C. At 600 °C, single phase holmium hafnate pattern with high purity was clearly seen after complete thermal decomposition followed by crystallisation of metal-alginate beads which is in good agreement with transformation temperature observed in TGA/DSC analysis. It is apparent that the onset of decomposition occurred at 400 °C and ended at 600 °C with the formation of high purity nanoparticles of $Ho_2Hf_2O_7$. Further increase in temperature from 700 °C-1000 °C results in the XRD peaks becoming narrower, sharper and more intense due to the growth in crystal size [125].

Inset of Fig. 4.2 shows observed HT-XRD patterns of dried metal-alginate beads at selected temperatures of 100 °C, 700 °C and 1000 °C. α-Al_2O_3 peaks were observed throughout the scan from 25-1000 °C as some of the X-rays penetrated through metal alginate sample to the surface of sample holder. Apart from α-Al_2O_3 sample holder peaks, no peaks of any other unexpected material were observed above 400 °C which confirms the formation of high purity $Ho_2Hf_2O_7$ employing the alginate synthesis method (LAP).

Results of TGA/DSC and HT-XRD are in good agreement with each other showing complete thermal decomposition of dried metal alginate beads leading to the formation of nanocrystalline $Ho_2Hf_2O_7$ at 600 °C. Based on the Hess's law of heat summation it can be concluded from the results of TGA/DTG/DSC traces shown in Fig. 4.1 and HT-XRD patterns shown in Fig. 4.2 that the enthalpy change for the thermal decomposition of metal-alginate (Ho^{3+}/Hf^{4+} — ALG) into $Ho_2Hf_2O_7$, $CO_{2\ (g)}$ and $H_2O_{\ (g)}$ is -6834 ± 683J/g.

The net enthalpy change is calculated from the algebraic sum of the area under each peak in the DSC trace divided by the change in weight of the corresponding peak in TGA trace. The net enthalpy change of -6834J/g (±10%) shows that over all decomposition process is exothermic in nature. It can be envisaged that in a continuous manufacturing process the evolved heat can be utilized for the drying and calcination process of beads or stored if it is produced in excess of the requirements thereby making the process either fully or partially self-sustainable.
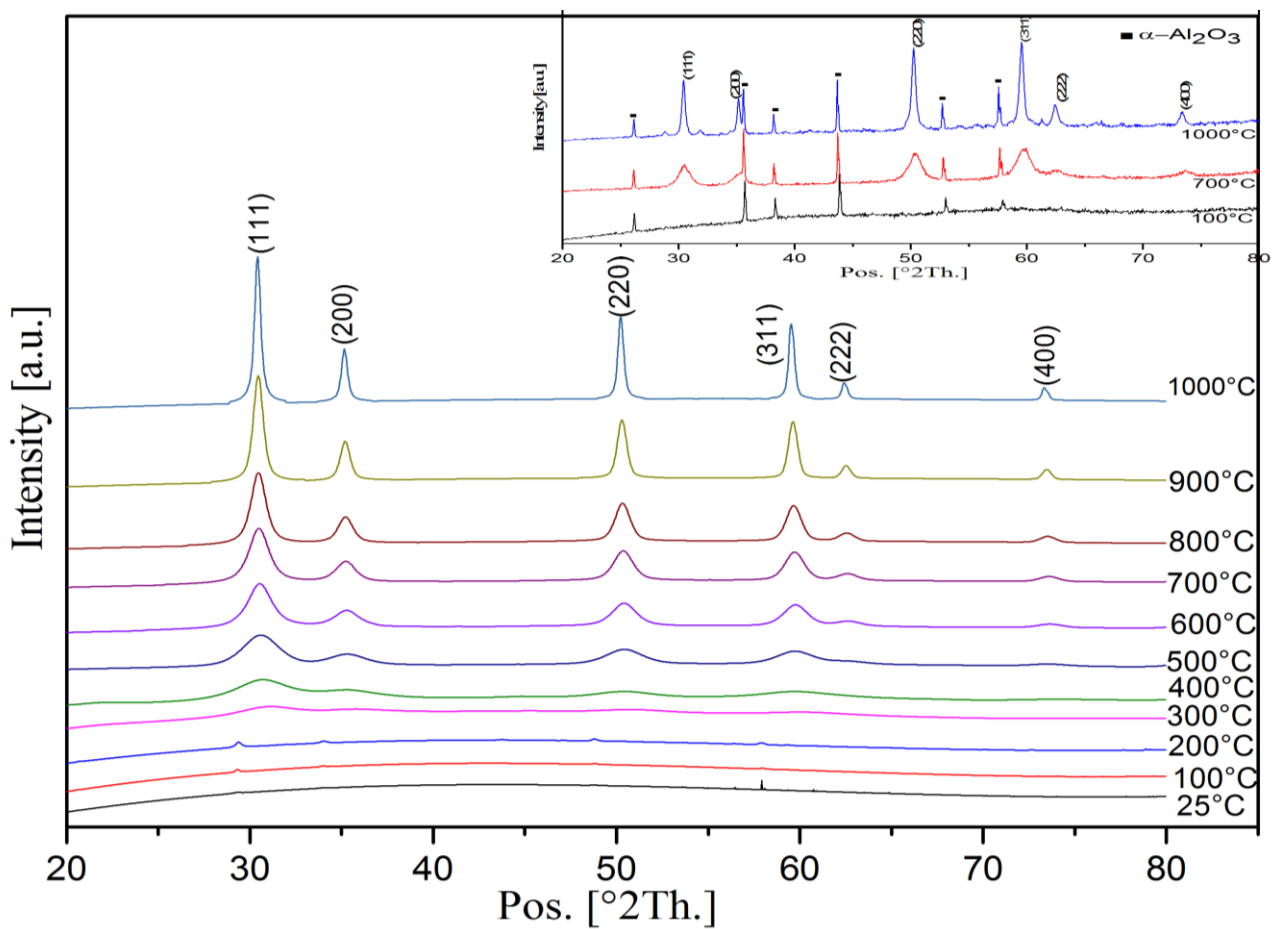
Fig. 4.2: HT-XRD patterns of metal alginate beads from 25-1000°C, sample holder (α-Al$_2$O$_3$) peaks were digitally eliminated for clarity. The patterns are indexed by ICDD, 00-024-0473 with miller indices of crystal planes of cubic Ho$_2$Hf$_2$O$_7$ shown at the top of the peaks. Inset shows the HT-XRD of dried metal-alginate beads at 100°C, 700°C and

1000°C. Inset also shows the positions 'filled squares' of α-Al₂O₃ peaks from sample holder.

Nanopowders of $Ho_2Hf_2O_7$ for further characterisation were obtained from dried beads calcined at 700 °C for 2 h and 6 h in stationary air. During calcination the rate of 10 °C min⁻¹ was maintained for both heating and cooling cycles. Thermal decomposition of the precursor formed the weakly-bonded agglomerates of $Ho_2Hf_2O_7$ nanoparticles which were converted into fine particles using mortar and pestle.

XRD analysis was performed of the nanopowders of $Ho_2Hf_2O_7$ after calcining at 700 °C for 2 h and 6 h respectively. The observed data for different annealing time corresponded with the single phase cubic defect fluorite structure of $Ho_2Hf_2O_7$ as shown in Fig. 4.3. The broadening of the peak is mainly due to the nano-sized crystallites, which is the characteristic of the materials synthesized by Leeds Alginate Process (LAP) [126]. Furthermore, as the calcination duration increases from 2h to 6h coarsening takes place due to thermally assisted enhanced mass transport within the nanocrystals resulting into sharper and narrower XRD peaks.

Table 4.1 below shows the effect of calcination duration on crystallite size. Growth in crystallite size is because of Ostwald ripening in which crystal size increases with time at elevated temperature due to enhanced cationic ionic diffusion as large crystals are formed at the expense of smaller crystals. For longer calcination duration grain growth results in stable structure. The process will continue resulting in the growth of larger particles and correspondingly disappearance of smaller particles [125] [127].
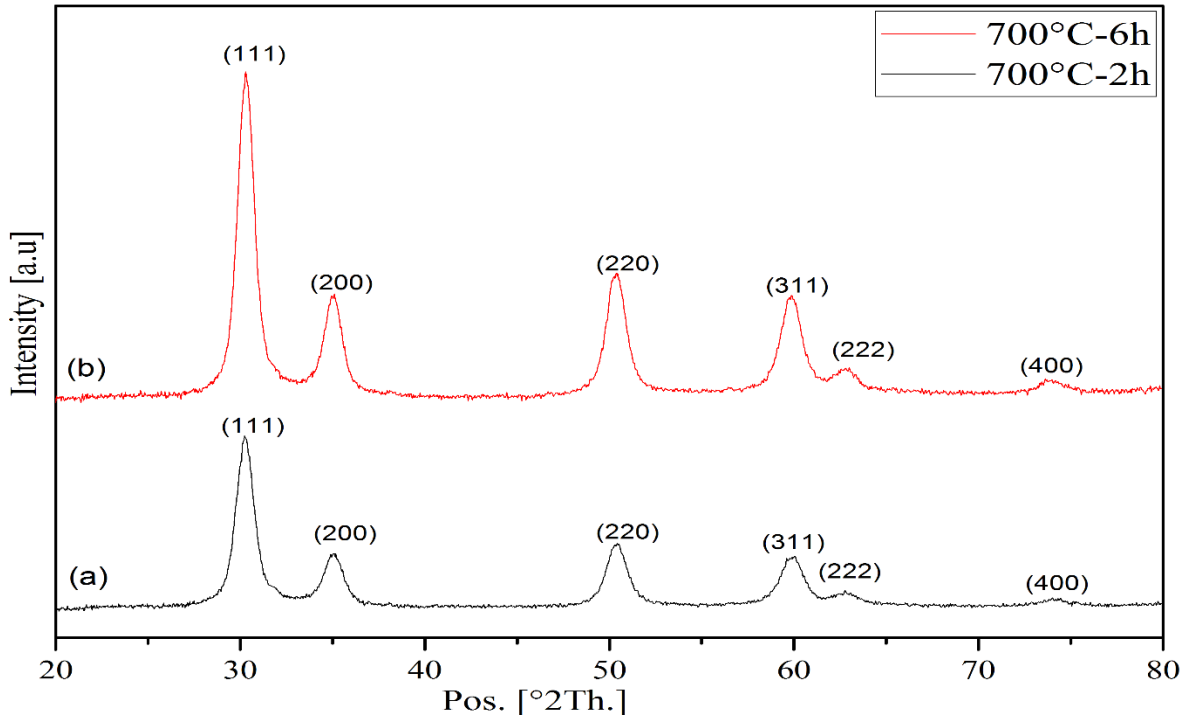
Fig. 4.3: XRD patterns of Ho₂Hf₂O₇ nanoparticles calcined at 700°C for (a) 2h and (b) 6h. Patterns are indexed by ICDD, 00-024-0473 indicating the miller indices of Ho₂Hf₂O₇ shown at the top of the peaks.

Table 4.1: Structural parameters of Ho₂Hf₂O₇

Sample	Rietveld Refined Size Strain Analysis					
Heat Treatment	Avg. Crystallite Size (nm)	Micro Strain (%)	R_{wp} (%)	R_{exp} (%)	GOF	Lattice Parameters (A˚)
700˚C-2h	5.40	2.237	3.4	3.27	1.04	5.1280
700˚C-6h	6.10	1.18	2.84	2.45	1.34	5.1308

Rietveld refinement of the XRD pattern of holmium hafnate (Ho₂Hf₂O₇) calcined at 700 ˚C for 6h is shown in Fig. 4.4. The observed and calculated patterns matched with each other and peaks are also indexed with the XRD reference pattern (ICDD, 00-024-0473). The observed

78

and calculated patterns are in excellent agreement with each other as seen from the value of goodness of fit (GOF) close to unity in Table 4.1.

Crystallite size of sample was calculated applying the Scherrer's equation to the XRD pattern shown in Fig. 4.3. Crystallite size was obtained after eliminating instrument broadening and stress-strain broadening. The observed data and refined model are in good agreement as the sample shows approximately 3% weighted residual (Rwp) from refinement. Coarsening increased with increase in annealing time, and correspondingly the micro-strain decreased. With the rise in annealing time the particles aggregate and resultantly increase in particle size was observed. The lattice parameters of metallic nanoparticles contract with decrease in particle size in an inverse function of the diameters of nanoparticles [128].

The peaks were assigned with their Miller indices using reference pattern. Unit cell parameters of holmium hafnate lattice were modified during Rietveld refinement to best fit the experimental XRD pattern and compared well with reference pattern.

Stable defect fluorite structured nanopowder of $Ho_2Hf_2O_7$ with unit cell lattice parameters a = b = c = 5.1308 A° and α = β = γ = 90° were prepared employing LAP which is in excellent agreement with the corresponding values reported in literature of $Ho_2Hf_2O_7$ obtained mechanochemically [129, 106] and thermodynamically [130].
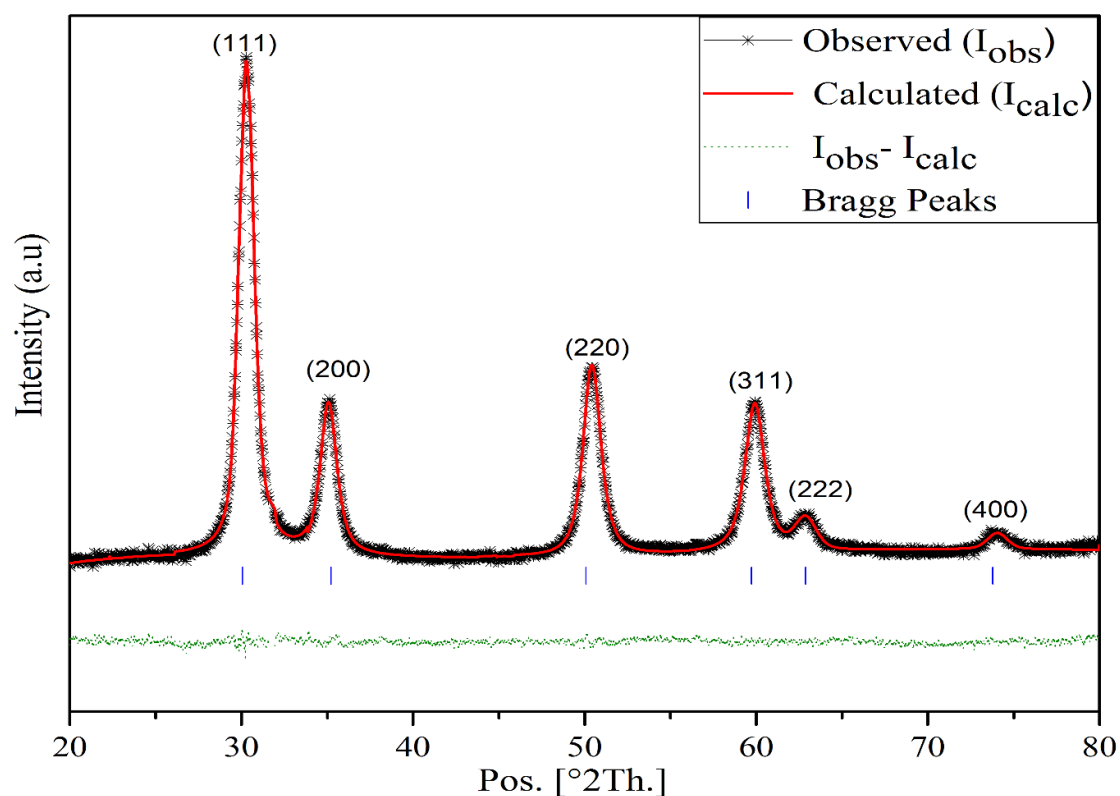
Fig. 4.4: Rietveld refined ambient XRD patterns of $Ho_2Hf_2O_7$ nanoparticles calcined at 700°C for 6h with Miller indices representing fluorite structure.

As XRD techniques are not sufficient to analyse the structural features of light atoms such as oxygen, Raman spectroscopy was used to support these inferences. Peaks identified in Raman spectra were fitted using suitable logarithmic functions to understand true Raman features. Raman peaks were fitted using Lorentz function which is suitable fitting technique for crystallised phases [131]. Lorentz function can be used to obtain wavenumber, area, height and FWHM (full width at half maximum) from a single Raman peak which provide distinct information about the material. Wavenumber (Raman shift) from Raman peak is distinctive to differentiate materials as each ionic group has unique wavenumber under laser excitation [132]. FWHM is relevant to the degree of crystallisation of materials [133]; increase in width suggests less crystallinity. Remaining two features are related to quantitative information of material; peak height and peak area [134]. Raman spectroscopy was employed to understand the material formed. Peaks in the Raman spectra were analysed using Origin Pro software.

Pyrochlore oxides have six theoretical Raman active modes [72, 130, 135-142]

$$\Gamma_{Raman} = A_{1g} + E_g + 4F_{2g} \tag{4.1}$$

These Raman active modes represent the vibrations of <Ln-O> and <Hf-O> bonds [129, 137-145]. Raman spectroscopy is more suitable to study anion disorder in pyrochlores as these modes involve motion of oxygen atoms. Five modes ($A_{1g} + E_g + 3F_{2g}$) contribute to O_{48f} vibrations and O_{8b} vibrations yield a single F_{2g} mode [137, 146]. Raman spectra of $Ho_2Hf_2O_7$ nanopowder is shown in Fig. 4.5 acquired using 473 nm excitation wavelength. Raman modes observed at 571, 657, 885 cm^{-1} correspond to Ho−O stretch. Weak band around 1047 cm^{-1} resulted due to stretching of Hf−O. Spectra in Fig. 4.5 shows some initial pyrochlore type short range ordering of cation and oxygen vacancies [72, 133, 134]. Broad band from 350-450 cm^{-1} can be associated to compositional substitution by atoms with mismatched atomic radii and valencies [147]. Here Raman spectra confirms the defect-fluorite structure of holmium hafnate as the band around ~750 cm^{-1} is breathing mode attributed to distortions in HfO_6 octahedra which strictly should not be present in perfect pyrochlore structure [72]. A band around 530cm^{-1} can be explicitly assigned to the A_{1g} mode of pyrochlore phase [148], which is also absent in Fig. 4.5.

Inset of Fig. 4.5 shows the photoluminescence (PL) spectra of $Ho_2Hf_2O_7$ with excitation wavelengths of 473 nm (blue), 514 nm (green) and 633 nm (Red). Raman spectra shown in Fig. 4.5 was observed below 800 nm. It is known that with the change in excitation wavelength the Raman bands shift the same amount correspondingly while the PL lines stay on the same wavenumber [145]. With 473 nm and 633 nm, $^5F_4/^5S_2 \rightarrow ^5I_7$ transition [149] bands were seen at around wavelength of 850-890 nm showing the PL nature of this band by staying on the same position. The corresponding excitation energy range with this band is ~1.37-1.43 eV. It is quite evident that under the excitation wavelength of 514nm the PL lines from $^5F_4/^5S_2 \rightarrow ^5I_8$ transition [149] are so intense that they suppressed the traditional Raman spectra of holmium hafnate.

Equivalent wavelength and excitation energy range with this band is 810-830 nm and ~1.50-1.54 eV respectively (Luminescence spectra #1 in Fig. 4.5). An important finding from the above analysis is that Raman scattering and PL under 473 nm excitation wavelength can occur simultaneously as two separate optical processes for $Ho_2Hf_2O_7$ nanopowders. The selection of appropriate wavelength is an important factor for Raman study.
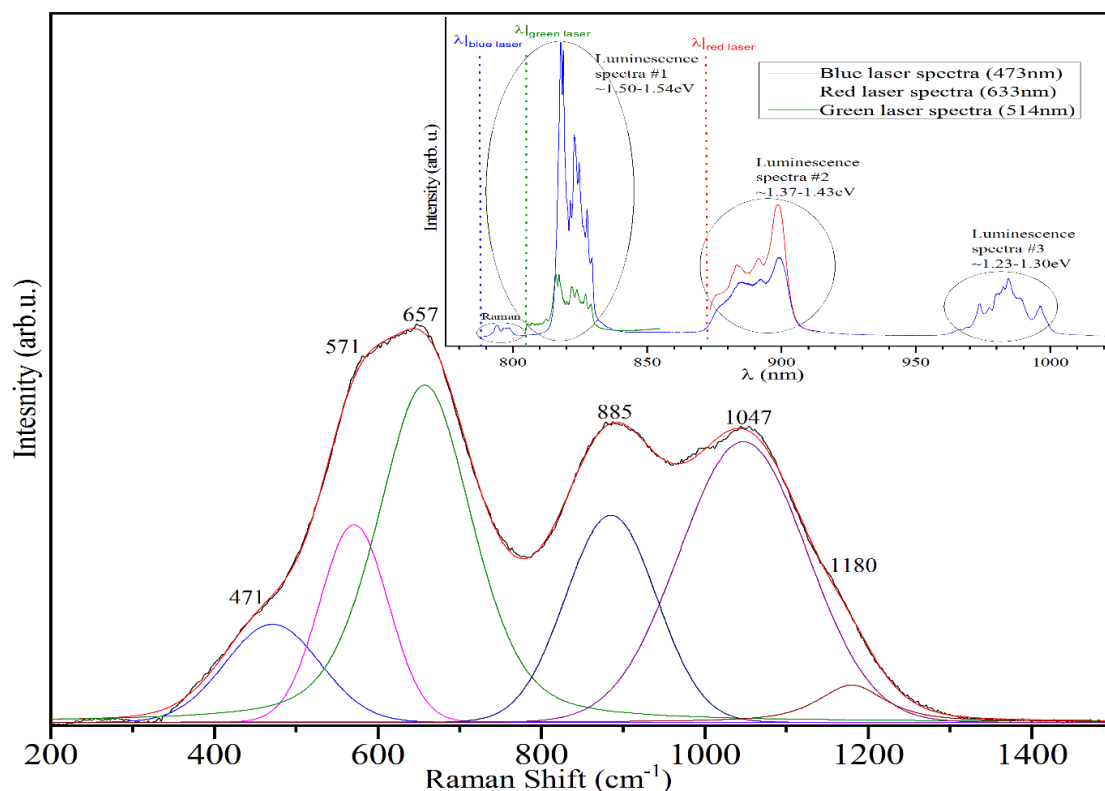
Fig. 4.5: Raman Spectra of $Ho_2Hf_2O_7$ nanopowder with excitation wavelength of 473nm and fitted peaks. Inset shows the luminescence spectra with laser wavelengths of 473nm, 514nm and 633nm.

The morphology of obtained nanopowder of $Ho_2Hf_2O_7$ was investigated using Transmission Electron Microscope (FEI Tecnai TF20 FEG-TEM). Gatan Microscopy Suite (GMS) software was used for the analysis of TEM images and Selected Area Electron Diffraction (SAED) patterns. TEM images and SAED pattern of $Ho_2Hf_2O_7$ nanopowder calcined at 700 °C for 2 h are shown in Fig. 4.6. Inset shows the area enclosed with red circle for SAED pattern. Holmium hafnate nanoparticles are of uniform shape with narrow size distribution and crystalline in

nature (Table 4.3). Results from TEM confirmed the XRD analysis. XRD peak broadening and less sharp SAED rings indicate smaller crystallite size for annealing time of 2 h.
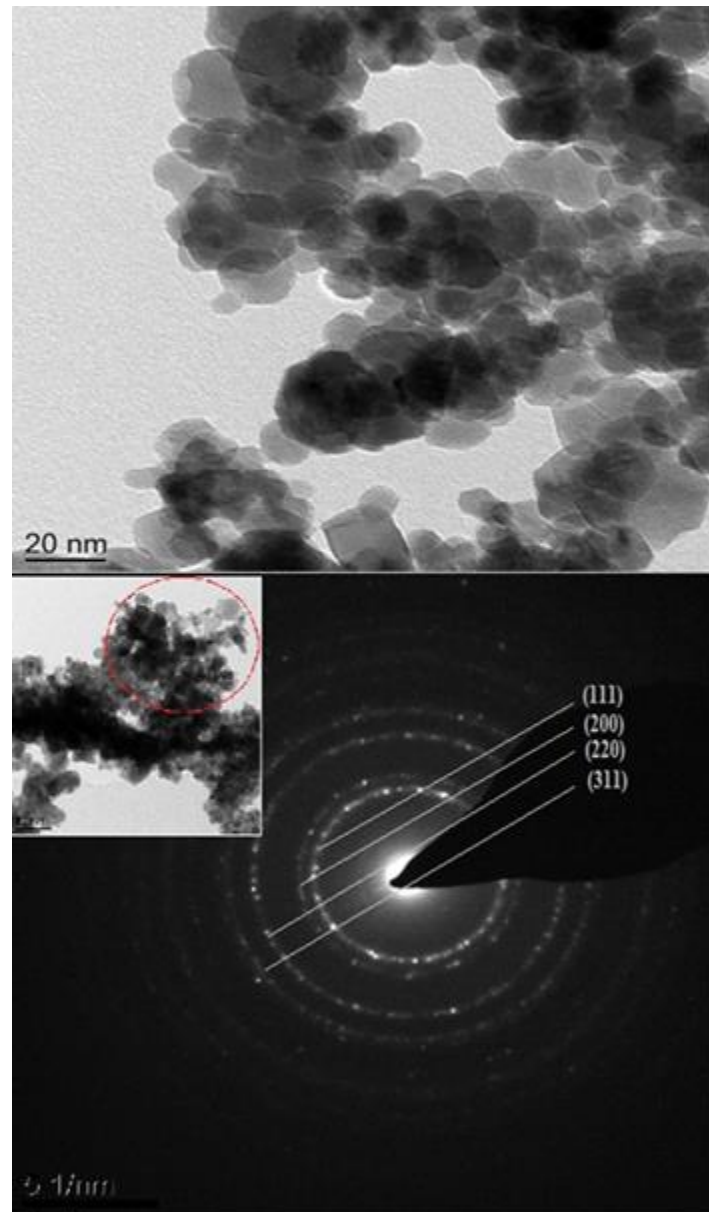
Fig. 4.6: TEM images with SAED pattern of Ho$_2$Hf$_2$O$_7$ calcined at 700˚C for 2h

TEM images of holmium hafnate nanoparticles calcined at 700 ˚C for 6 h are shown in Fig. 4.7. Inset shows the area encircled red for SAED pattern. SAED rings and XRD patterns were compared and all the values of Miller indices (hkl) are in good agreement with XRD reference pattern (ICDD, 00-024-0473). Table 4.2 shows the d-spacing calculated from TEM and XRD

data for different crystal planes. Interplanar spacing (d-spacing) agreed well in case of XRD, TEM (SAED) and reference pattern (Table 4.2).

More spots appearing in the ring pattern in Fig. 4.7 compared with Fig. 4.6 indicate the relatively larger crystallite size of $Ho_2Hf_2O_7$ nanoparticles of sample calcined for 6 h at 700 ˚C. This is in agreement with the results of XRD and TEM analysis shown in Table 4.1 & 4.2.
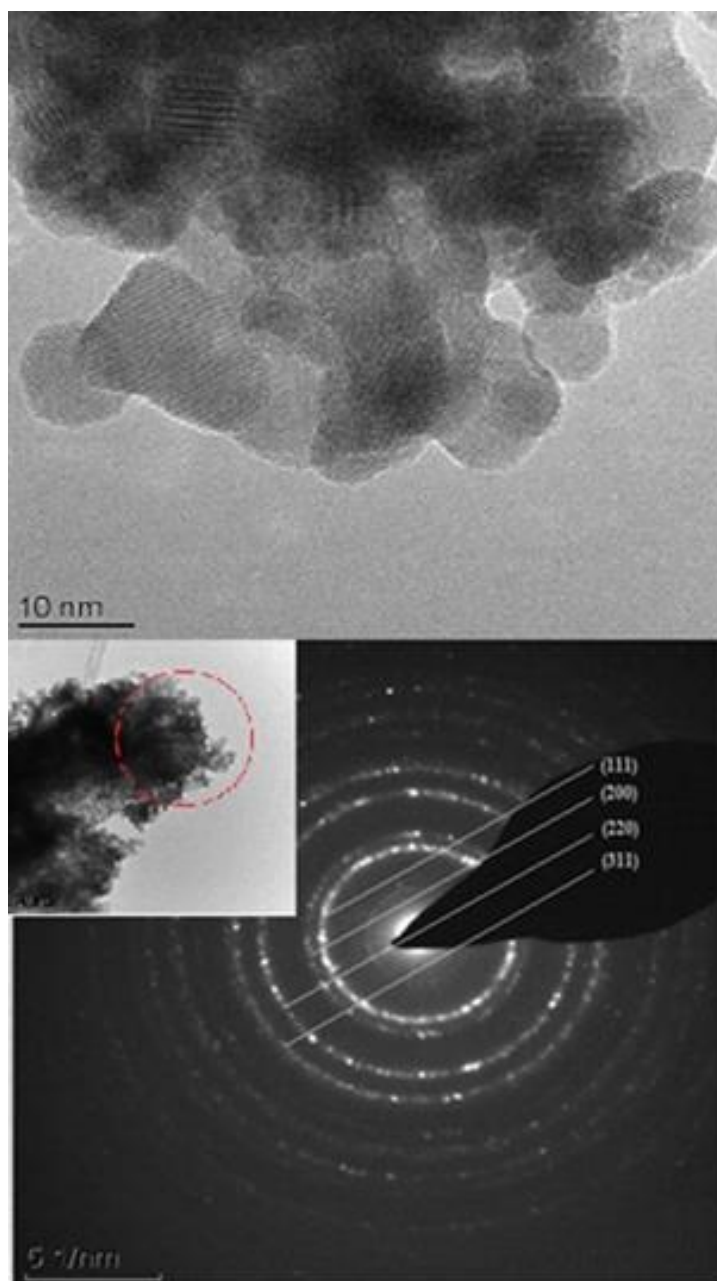
Fig. 4.7: TEM images with SAED pattern of $Ho_2Hf_2O_7$ calcined at 700˚C for 6h

Table 4.2: Comparison of d-spacing of Holmium Hafnate from TEM and XRD Rietveld Refinement

H	k	l	Ref. (ICDD-00-024-0473) d, A˚	XRD d, A˚		TEM d, A˚	
				700˚C-2h	700˚C-6h	700˚C-2h	700˚C-6h
1	1	1	3.00600	2.95158	2.95049	3.00	2.94
2	0	0	2.60400	2.55749	2.55665	2.54	2.52
2	2	0	1.84100	1.81032	1.80979	1.79	1.78
3	1	1	1.57000	1.54445	1.54402	1.53	1.51

Grain sizes from Figs. 4.6 & 4.7 were calculated using ImageJ and are shown in Table 4.3. Holmium hafnate nanoparticles show narrow size distribution and with the increase in calcination duration grain size increases.

Table 4.3: Grain size analysis of Holmium Hafnate nanopowders from TEM images

	Size Range, nm	Avg. Grain Size, nm
700˚C-2h	8.5-12.5	10.3
700˚C-6h	14-18	17.36

Energy Dispersive X-ray (EDX) spectroscopy was used to study the composition of holmium hafnate nanoparticles. Fig. 4.8 shows the EDX analysis of Fig. 4.7 and it confirms the presence of Ho, Hf and O in the same ratio as in the stoichiometry of the material. Peaks due to C and Cu are attributed to the holey carbon copper mesh grid used for TEM-EDX analysis. The inset in Fig. 4.8 shows the atomic percent of elements obtained from EDX analysis which agrees very well with the theoretical values of 18.2at.% for Ho, 18.2at.% for Hf and 63.6at.% for O indicating that the compound exhibit negligible non-stoichiometry.

Element	Atomic%
O	63.2 ± 7
Ho	18.3 ± 5
Hf	18.5 ± 5
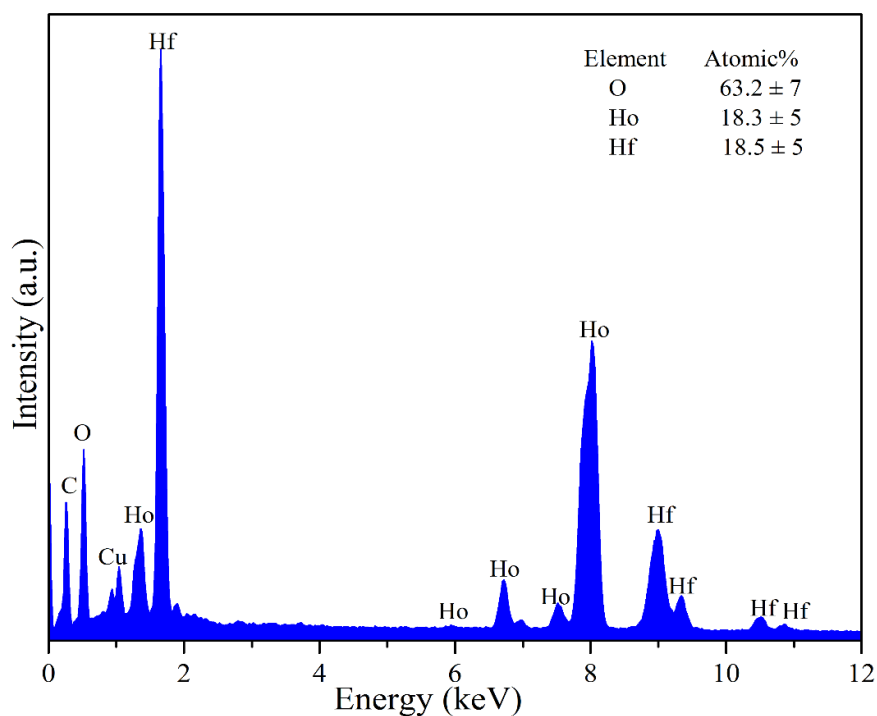
Fig. 4.8: EDX analysis of Ho$_2$Hf$_2$O$_7$ nanopowders calcined at 700˚C for 6h

A HR-TEM image of Ho$_2$Hf$_2$O$_7$ nanopowder calcined at 700 ˚C for 6 h is shown in Fig. 4.9. Lattice planes can be easily seen and indexed as (311). Nanoparticles of Ho$_2$Hf$_2$O$_7$ showed the crystalline phase formation with cubic structure and interplanar distance of 1.51 A˚ which correspond to the (311) plane. HR-TEM image of holmium hafnate powder prepared by solid state reaction through mechanical milling was reported in literature [106]. The interplanar distance calculated by Shojan et al. [106] is 2.60 A˚ for (X00) plane is in good agreement for (200) plane as shown in Table 4.2. Using high purity feed material nanoparticles of Ho$_2$Hf$_2$O$_7$ can be successfully prepared by employing novel Leeds Alginate Process (LAP) at significantly low temperature (~ 600 °C) and in an energy efficient manner compared with other processes [106, 129, 130].
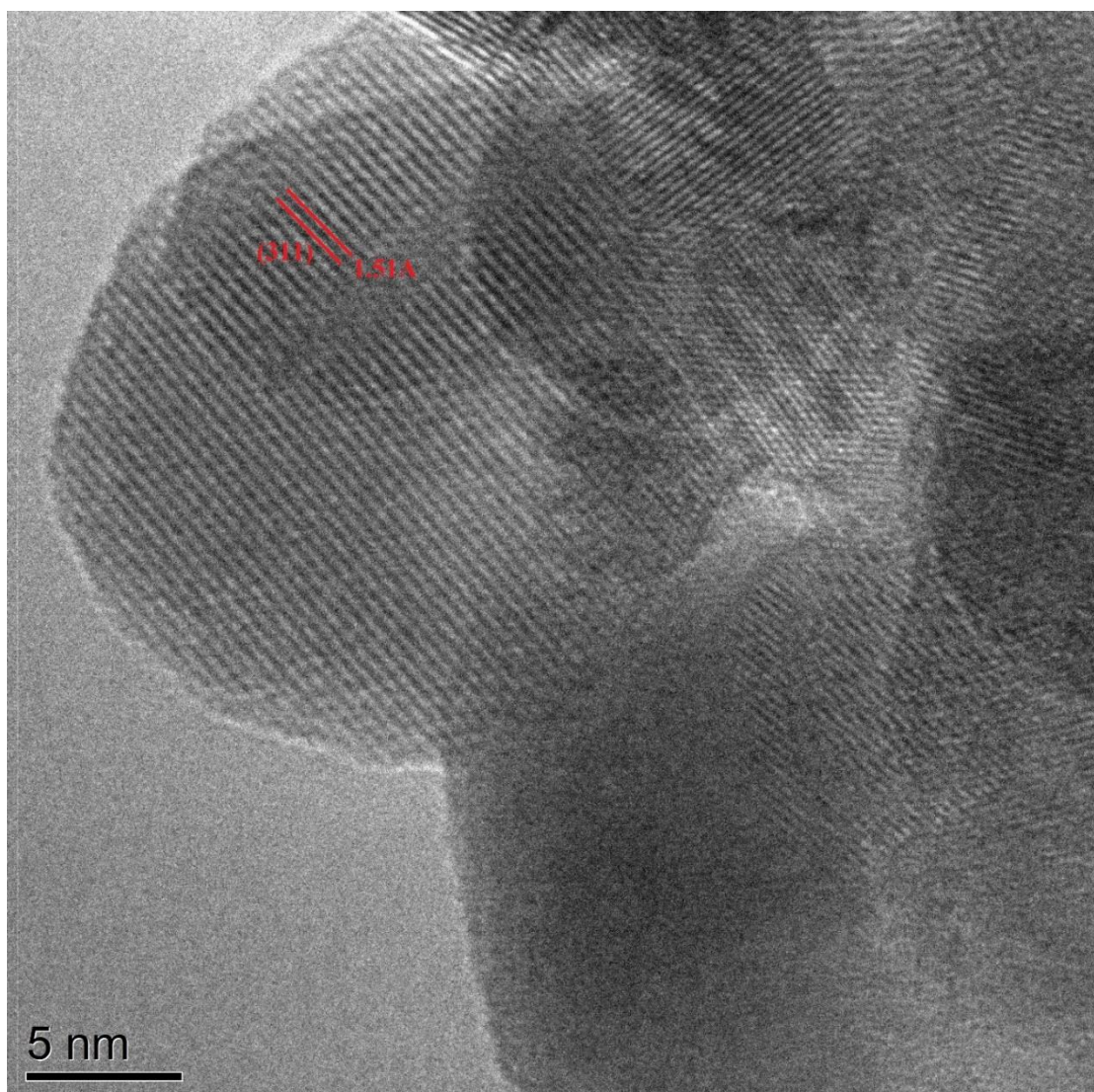
Fig. 4.9: HR-TEM image of Ho₂Hf₂O₇ powder with defect-fluorite structure and interplanar spacing of 1.51A° along the (311) direction.

4.1.2. Thermoresponsive Behaviour

X-ray Diffraction (XRD) analysis was performed on the sintered pellets of holmium hafnate. Fig. 4.10 shows the XRD patterns of Ho₂Hf₂O₇ nanopowders obtained after calcination at 700 °C and pellets sintered from 1100-1500 °C. Nanopowder of holmium hafnate adopts the fluorite structure. This material showed the fluorite structure with some super structural peaks of pyrochlore structure when sintered from 1100-1300 °C. XRD scans in this range have (311) and (321) peaks which are superstructure reflections of $Ho_2Hf_2O_7$ and $Ho_{1.61}Hf_{0.31}O_3$,

respectively. At 1300 °C the scan shows more small reflections of pyrochlore structure but the characteristic peaks of pyrochlore structure are absent. Pyrochlores are superstructure of an anion-deficient fluorite like atomic arrangement, its diffraction pattern have set of superstructure reflections in addition to characteristic peaks of fluorite like substructure [150]. Factors which affect the intensities of superstructure reflections are degree of ordering, distribution of oxygen vacancies and the difference of average scattering factors of elements involved [129]. At 1400-1500 °C clean XRD pattern of holmium hafnate with stable fluorite structure was obtained. At these temperatures no superstructure reflection of pyrochlore was observed. Here the sharp peaks without any superstructure pyrochlore reflection are assigned to their miller indices with fluorite structured holmium hafnate.

Table 4.4 shows the effect of temperature on the intensity of pyrochlore superstructure reflections. It is noted that an increase in sintering temperature from 1100 °C to 1200 °C leads to the increase in intensity of superstructure reflections. Increase in intensity of (311) and (321) reflections is 1.33 to 2.27 % and 1.66 to 2.97 respectively, which is in percentage of intensity of major peak (111). With further rise in temperature to 1300 °C the intensity of superstructure reflections decreased to 1.79 % (311) and 2.49 % (321) and became almost negligible at 1400-1500 °C. Higher energy input is required for superstructure ordering of cations to form pyrochlore structure as compared to the amorphous phase ordering to fluorite structure, therefore for pyrochlore phase formation higher temperatures are required [151].
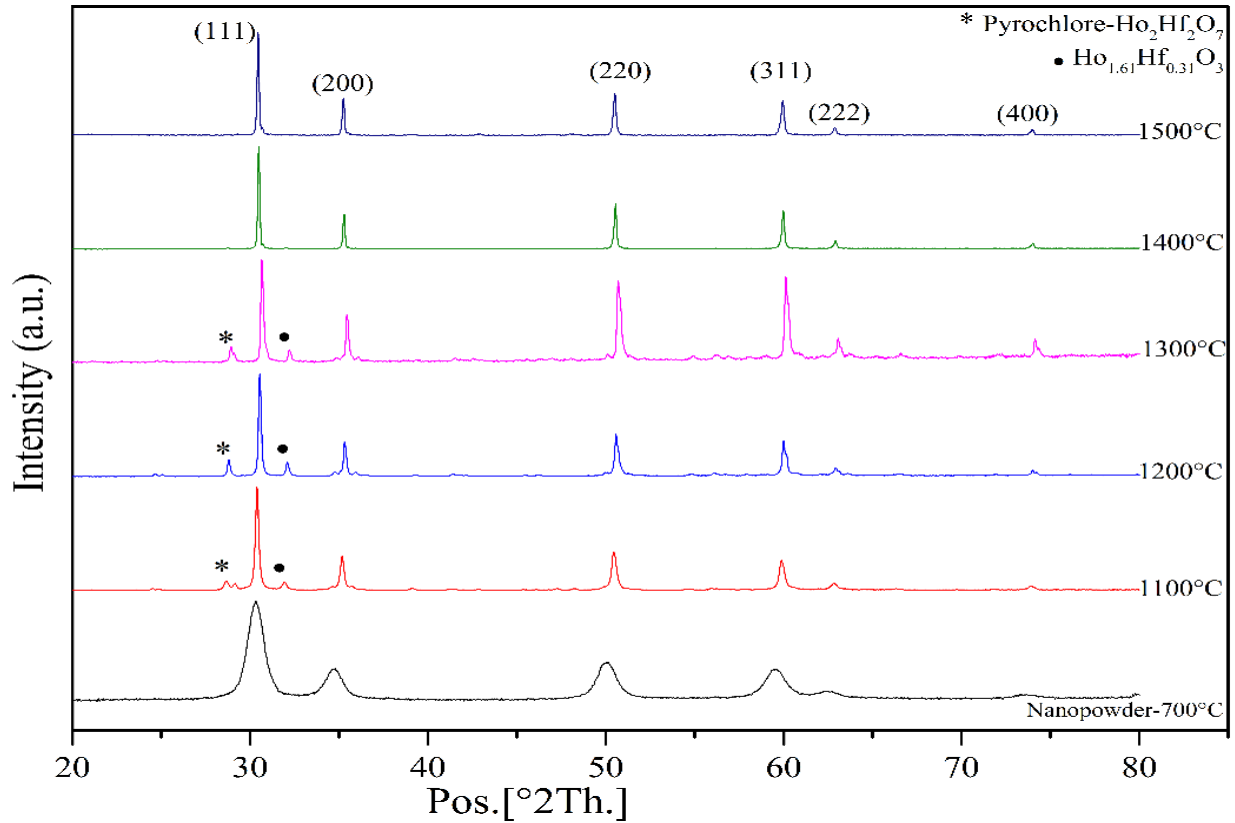
Fig. 4.10: XRD patterns of sintered holmium hafnate pellets. The patterns from 700-1500°C are indexed by ICDD, 00-024-0473 with defect fluorite cubic Ho$_2$Hf$_2$O$_7$ shown at the top of the peaks. Tick marks 'asterisks' for Ho$_2$Hf$_2$O$_7$ and 'filled circles' for Ho$_{1.61}$Hf$_{0.31}$O$_3$ pyrochlore reflections.

Table 4.4: Effect of temperature on the intensity of pyrochlore superstructure reflections (311) and (321)

	700°C	1100°C	1200°C	1300°C	1400°C	1500°C
(311)-Ho$_2$Hf$_2$O$_7$	0	1.33	2.27	1.79	0.05	0
(321)-Ho$_{1.61}$Hf$_{0.31}$O$_3$	0	1.66	2.97	2.49	0.01	0

Table 4.5 shows the effect of temperature increase in crystallite size and unit cell parameters of holmium hafnate. With the increase in temperature the crystallite size increased throughout

the range from 6 nm to 109 nm and corresponding decrease in microstrain was observed as shown in Fig. 4.11. Increasing in sintering temperature results in narrowing of diffraction peaks which is due to growth in crystallite size. Unit cell parameters also increased with the increase in temperature from ~5.131-5.148 A˚ and they are in conformation of fluorite phase. But at 1400°C a minor decrease in unit cell parameters was observed as shown in Fig. 4.12. These results show that $Ho_2Hf_2O_7$ maintains stable fluorite structure over the wide temperature range. The absence of pyrochlore phase in $Ho_2Hf_2O_7$ can be attributed to the low radius ratio (r_{Ho}/r_{Hf} =1.315) [130].
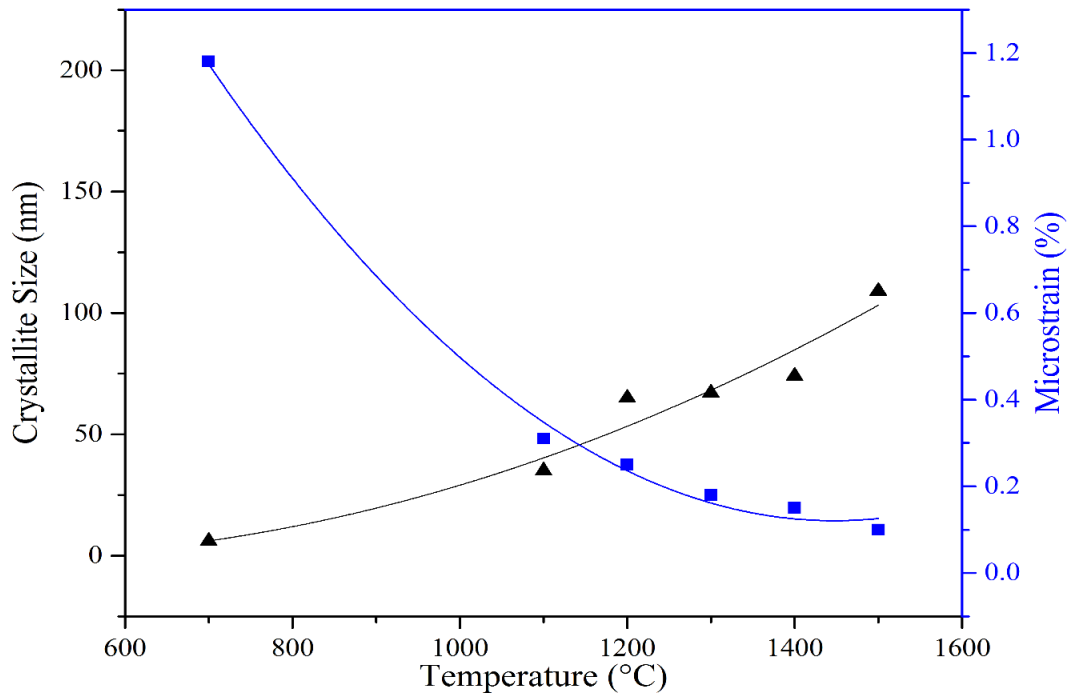
Fig. 4.11: Effect of temperature on crystallite size and microstrain of holmium hafnate nanopowder (700°C) and sintered pellets (1100-1500°C)
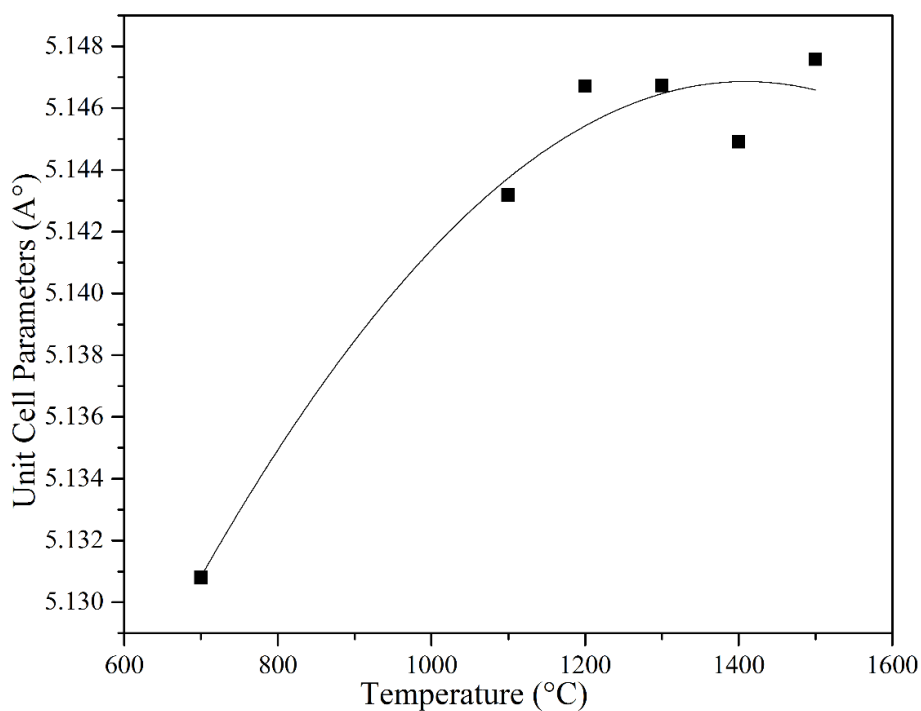
Fig. 4.12: Change in unit cell parameters with rise in temperature.

Table 4.5: Effect of temperature on crystallographic data and structural refinement parameters of holmium hafnate pellets

Temperature, °C	700- Nanopowder	1100	1200	1300	1400	1500
Phase	Defect-Fluorite	Defect-Fluorite	Defect-Fluorite	Defect-Fluorite	Defect-Fluorite	Defect-Fluorite
Space group	$Fm\bar{3}m$	$Fm\bar{3}m$	$Fm\bar{3}m$	$Fm\bar{3}m$	$Fm\bar{3}m$	$Fm\bar{3}m$
Lattice constant, A° a=b=c	5.131	5.143	5.147	5.147	5.145	5.148
R_p, %	2.09	12.7	15.6	36.0	9.4	11.9

R_{wp}, %	2.84	18.9	23.0	50.9	12.9	15.2
R_{exp}, %	2.45	8.4	10.37	19	8.4	11.2
GOF, x^2	1.34	5.0	4.94	6.9	2.34	1.84
Crystallite Size, nm	6.0	35	65	67	74	109
Micro Strain, %	1.18	0.31	0.25	0.18	0.15	0.10

Table 4.5 shows some of the structural parameters of $Ho_2Hf_2O_7$ pellets obtained after refinement. The values of R_{wp} and Goodness of Fit (GOF) relative to temperature are tabulated. Goodness of Fit (x^2) is ratio of squares of R_{wp} and R_{exp}, $x^2 = R_{wp}^2 / R_{exp}^2$ and its value must be less than 10 [152, 153]. Lower values at 700 ℃, 1400 ℃ and 1500 ℃ show the excellent agreement between observed and calculated pattern during Rietveld refinement. From 1100-1300 ℃ comparatively higher values show more residual data after refinement which is due to the appearance of superstructure reflections.
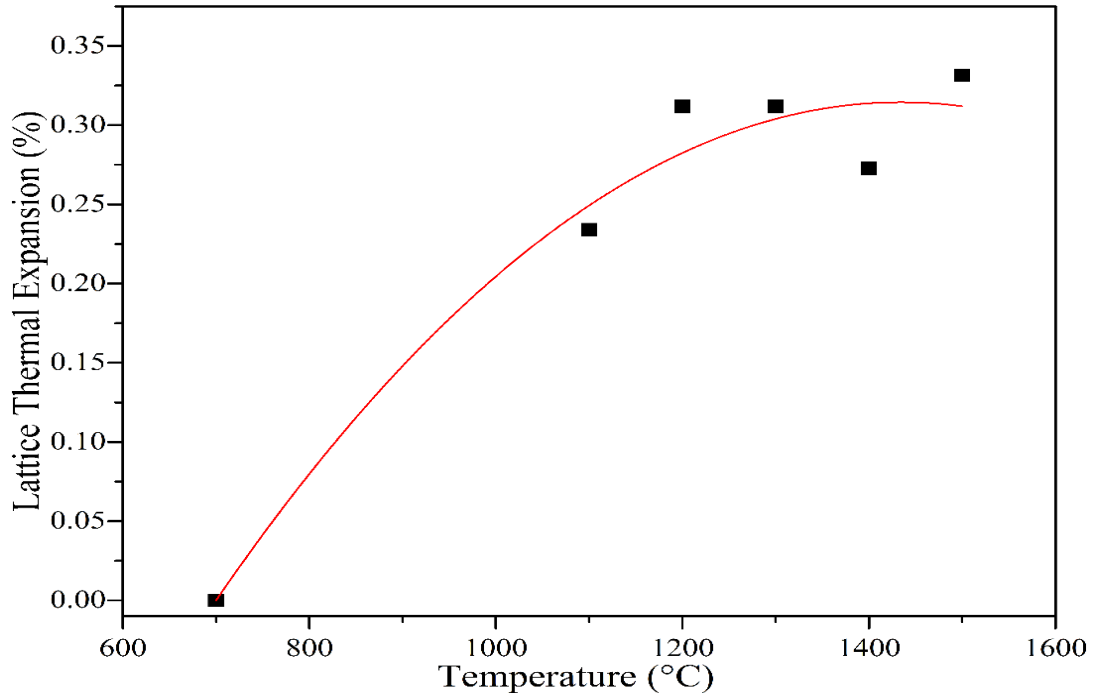
Fig. 4.13: Percent lattice thermal expansion of $Ho_2Hf_2O_7$ with temperature

Fig. 4.13 shows the shift in the % lattice thermal expansion (% LTE) as the function of temperature. Using the equation 4.2 % LTE was calculated where α_T and α_{298K} are the values of the cell parameters at the selected temperature and room temperature, respectively [154].

$$\% \text{ LTE} = 100 \frac{(\alpha_T - \alpha_{298K})}{\alpha_{298K}} \tag{4.2}$$

In Fig. 4.13 the variation in % LTE with temperature is non-linear and calculated from the lattice parameters obtained after refinements of diffraction data at different temperatures. Coefficient of thermal expansion (CTE) was calculated at highest temperature using equation 4.3.

$$\text{CTE } (T) = \frac{1}{\alpha_{298K}} \times \frac{(\alpha_T - \alpha_{298K})}{\alpha_{298K}} \tag{4.3}$$

The value of CTE of $Ho_2Hf_2O_7$ at 1500 °C calculated from the present data is 4.142×10^{-6} °C^{-1}

Disorder within the pyrochlore structure arises from vacancies and defects that disrupt the translational symmetry and can impact the appearance of the Raman spectra [72]. Five modes (A_{1g} + E_g + 3F_{2g}) contribute to O_{48f} vibrations and O_{8b} vibrations yield a single F_{2g} mode [137, 146]. Fig. 4.14 shows the Raman spectra of holmium hafnate nanopowder at 700 °C and sintered pellets over the range of 1100-1500 °C. Inset of Fig. 4.14 shows the luminescence spectra of all the samples. Here some sharp band of pyrochlore superstructure were observed from 1100-1300 °C. The sharp band at 500 cm^{-1} is due to pyrochlore superstructure reflection as literature says the band around 530 cm^{-1} can be unambiguously assigned to the A_{1g} mode of pyrochlore phase [148]. Intensity of peaks at 110 cm^{-1} and 500 cm^{-1} increase with temperature from 1100 °C to 1200 °C due to structural disorder due to pyrochlore reflections [106]. Significant feature of Raman spectra is growth of F_{2g} bands near 400 cm^{-1} and 600 cm^{-1} (here, 580 cm^{-1}) in lanthanide based pyrochlore oxides [72]. From 1100-1300 °C Raman spectra confirms the structural transformation of holmium hafnate as the band around ~750 cm^{-1} (here, 735 cm^{-1}) is breathing mode attributed to distortions in HfO_6 octahedra which strictly should not be present in perfect pyrochlore structure [155]. With increase in temperature the disorder increases and hence at 1400-1500 °C the Raman spectra is of defect-fluorite structure with minor softening due to rise in temperature. Individual modes are indistinguishable in fully disordered defect-fluorite [72, 130, 154]. Disorder in pyrochlores results as an increase in line broadening in Raman spectra [72], such broadening has observed in Raman spectra of holmium hafnate at 1400 °C and 1500 °C. This shows the fluorite structure of holmium hafnate with change in temperature. Raman spectra over the temperature range is in excellent agreement with XRD scans. Holmium hafnate persists as fluorite even at 1500 °C which is in agreement with the cationic radius ratio criteria and previous findings [106, 129, 130].
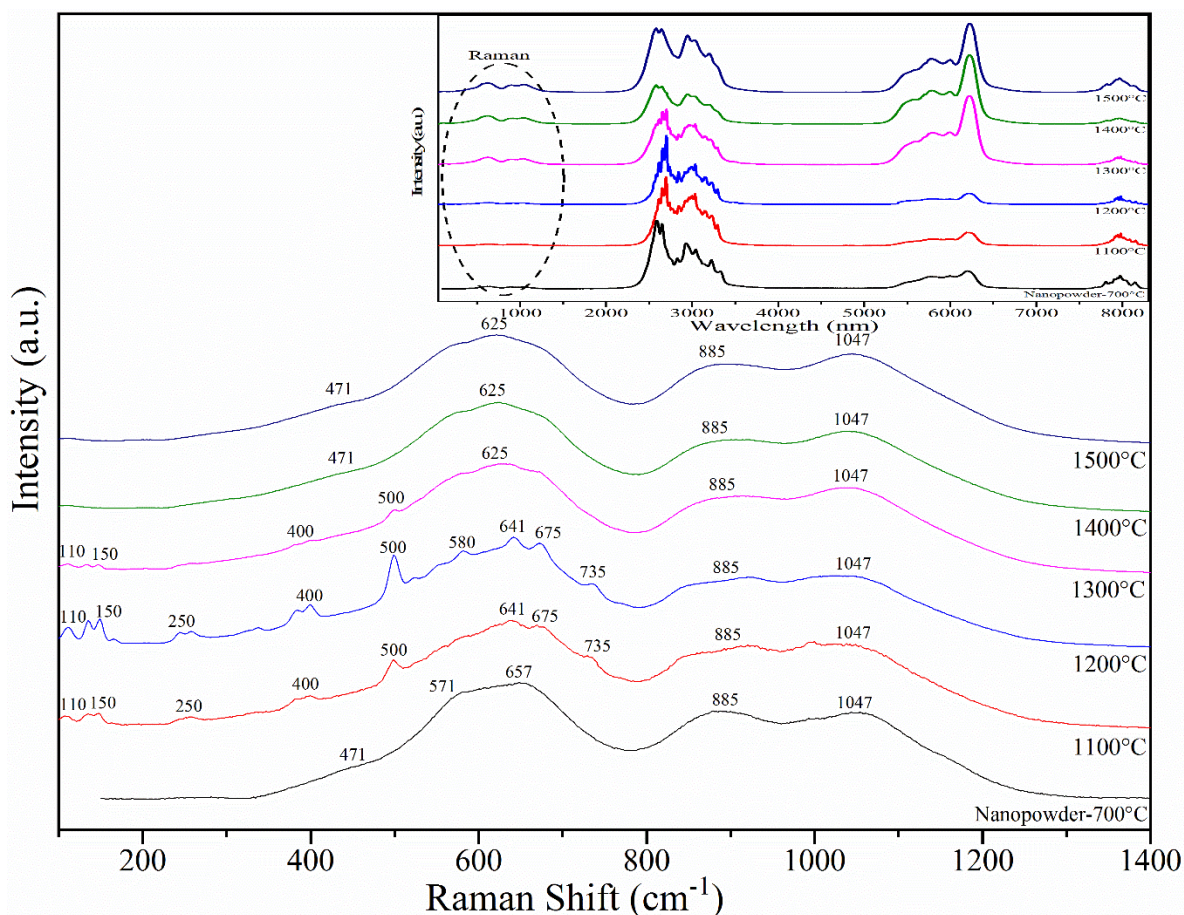
Fig. 4.14: Raman Spectra of Ho₂Hf₂O₇ nanopowder and pellets sintered from 1100-1500°C. Inset shows the luminescence spectra of all the samples.

Diffraction and spectroscopic investigation of $Ho_2Hf_2O_7$ structure with the rise in temperature is matching well with the phase diagram of Ho_2O_3 and HfO_2. This diagram shows the cubic fluorite structure of holmium hafnate till 2200 °C with ionic radii of holmium and hafnium 1.015 A° and 0.71 A°, respectively [156]. According to the ionic radii provided in this article [156] the cationic radius ratio is $r_{Ho}/r_{Hf} = 1.43$ which is close to the fluorite to pyrochlore phase transition (Fluorite < 1.46 < Pyrochlore). In this study appearance of some superstructure reflections of pyrochlore can be due to $Ho_2Hf_2O_7$ cationic radius ratio which is near to the boundary of fluorite to pyrochlore phase transition.

4.1.3. Sintering and Microstructure

Nanopowders of holmium hafnate were pressed into pellets and heat treated to get the highly dense ceramic compacts. Pellets were sintered using conventional sintering technique of heating them to a specific temperature and then holding at that temperature for some time. The process of conventional sintering which is also called single step sintering (SSS) process was first used to sinter the pellets from 1100 °C to1500 °C with the interval of 100°C and holding them at each temperature for 2 h at ambient pressure. Archimedes' method was used to measure the density of pellets at each temperature and then relative density was calculated with respect to theoretical density obtained from crystallographic data. Relative density was found in the range of 74 (±0.5)% to 93 (0.5)% from 1100 °C to 1500 °C with SSS process as shown in Fig. 4.15. There is just 1.2 % increase in relative density when sintered from 1400 °C to 1500 °C. There is an increase of 0.8 % in the relative density with the increase in sintering duration from 2 h to 6 h at 1500 °C as clearly seen in Fig. 4.15. Densification of $Ho_2Hf_2O_7$ pellets achieved at 1500 °C for 2 h is significantly higher than that of mechanochemically obtained holmium hafnate sintered at 1500 °C for 12 h (84.23%) [129].

Two step sintering (TSS) process was used to achieve the highly dense ceramic pellets at low temperature. In TSS process the pellets were first sintered to high temperature for short time to achieve intermediate density and then subsequently held at lower temperature for longer duration to achieve highly dense compacts of $Ho_2Hf_2O_7$. In first trial of TSS process, pellets were sintered in two steps (I) –1500 °C for 5 min, (II) – 1200 °C for 24 h as densities higher than 75 % were adequate for second step sintering [116]. The relative densities achieved in second step for 24 h and 72 h were 84 (±0.5)% and 92 (±0.2)%, respectively. Here the relative densities achieved are even less than that achieved at 1500 °C for SSS process. Later, pellets were sintered using TSS process at (I) –1500 °C for 5 min, (II) – 1300 °C for 72 h and a significant rise in relative density was noticed. The sintering duration in the second step was increased to 96 h to achieve maximum density and relative density of 98 (±0.1)% was found

which is quite good for solid electrolyte applications. The corresponding residual porosity of pellets were reduced from 25 (±0.5)% to 6 (±0.5)% in the SSS process and goes down to 2 (±0.1)% in TSS process as shown in Fig. 4.15.
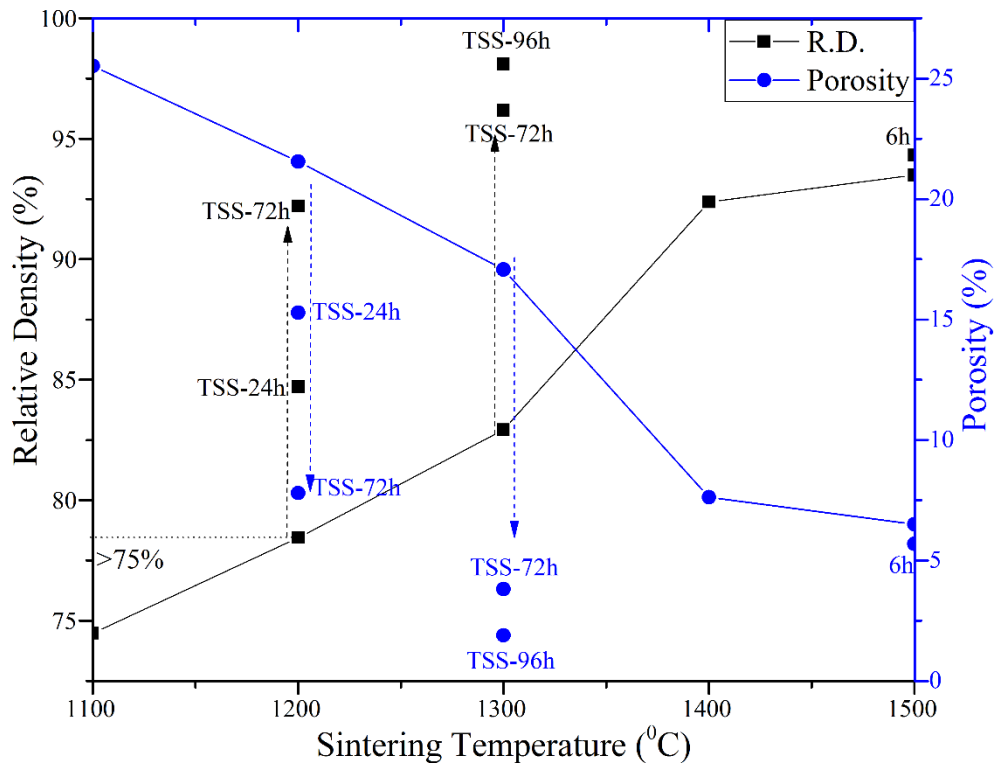
Fig. 4.15: Effect of sintering temperature on the relative density and porosity of holmium hafnate pellets. Two step sintering (TSS): (I) - 1500°C for 5min, (II) -1 300°C for 96h. Arrows showing increase in relative density and decrease in porosity with TSS process.

Microstructures of pellets sintered using SSS process from 1100 °C to 1500 °C and TSS process (I) –1500 °C for 5 min, (II) – 1300 °C for 96 h were analysed using scanning electron microscope (SEM). Fig. 4.16 shows the SEM micrographs of sintered pellets. Effect of sintering temperature on relative density and grain size is shown in Table 4.6. Grain size was calculated from SEM mircrographs and it is found that with the increase in temperature from 1100 °C to 1500 °C for SSS process the grain size is increasing and reached to 1.6 (±0.02)µm at 1500 °C as shown in Table 4.6 while the corresponding relative density was 93 %.

Pellets sintered using TSS process achieved higher density of 98 % and grain size of 0.77 ($\pm$0.02)μm. There substantial increase in densification with TSS process but an increase of 0.18 ($\pm$0.02)μm in grain size was noticed as compared to the one found at 1300 °C with SSS process. The increase in grain size with TSS process was mainly due to the coarsening in first step sintering [116]. It is observed that in the second step of TSS process densification proceeds with the constant grain size which means grain boundary diffusion is active and grain boundary migration is suppressed [116].

TSS process for sintering of $Ho_2Hf_2O_7$ pellets has found itself more favourable to achieve the desired densification and even the grain growth is far less than that of SSS process where the densification is very low.
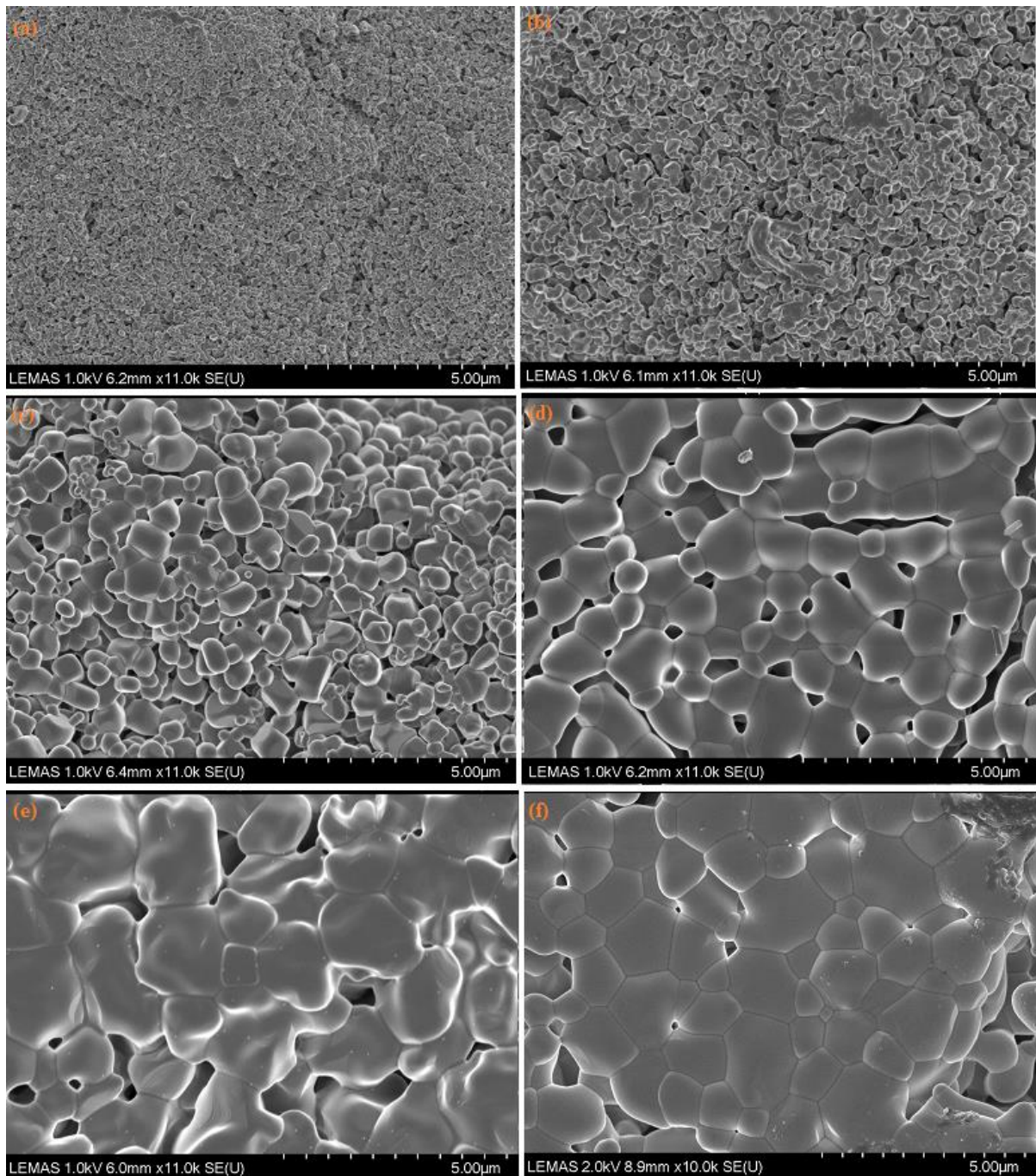
Fig. 4.16: SEM micrographs of sintered Ho$_2$Hf$_2$O$_7$ pellets. From (a) to (e) are the micrographs of the pellets after single step sintering (SSS) for 2h at (a) 1100°C (b) 1200°C (c) 1300°C (d) 1400°C (e) 1500°C and (f) after two step sintering (TSS): (I) - 1500°C for 5min, (II) - 1300°C for 96h.

99

Table 4.6: Variation of grain size and relative density as a function of sintering temperature of $Ho_2Hf_2O_7$ pellet samples

Sintering Temperature (°C)	Relative Density (%)	Grain Size (μm)
1100	74.48	0.122
1200	78.44	0.218
1300	82.93	0.590
1400	92.37	1.011
1500	93.50	1.591
TSS	98.10	0.770

4.1.4. AC Impedance Spectroscopy

Impedance spectroscopy of $Ho_2Hf_2O_7$ pellets sintered with SSS were carried out over the temperature range of 340 °C to 750 °C in the frequency range of 100 mHz to 100 MHz for both heating and cooling cycles. Selected Nyquist plots are shown in the Fig. 4.17 which is used to study relaxation phenomena such as contribution of bulk, grain boundary and material electrode interface effect. At 340 °C a single semicircle was observed for both heating and cooling cycles as shown in Fig. 4.17 (a) which is an indication of bulk contribution. From low to high frequency all the contribution is due to grain resistance.

On the contrary at 550 °C two semi-circles were recorded for both heating and cooling cycles as shown in Fig. 4.17 (b). The first high frequency semi-circle was attributed to the bulk or grain interior response whereas the second low frequency semi-circle attributed to the grain boundary response. The contribution of the grain boundary to the total resistance increased with the increase in temperature from 340 °C to 750 °C.
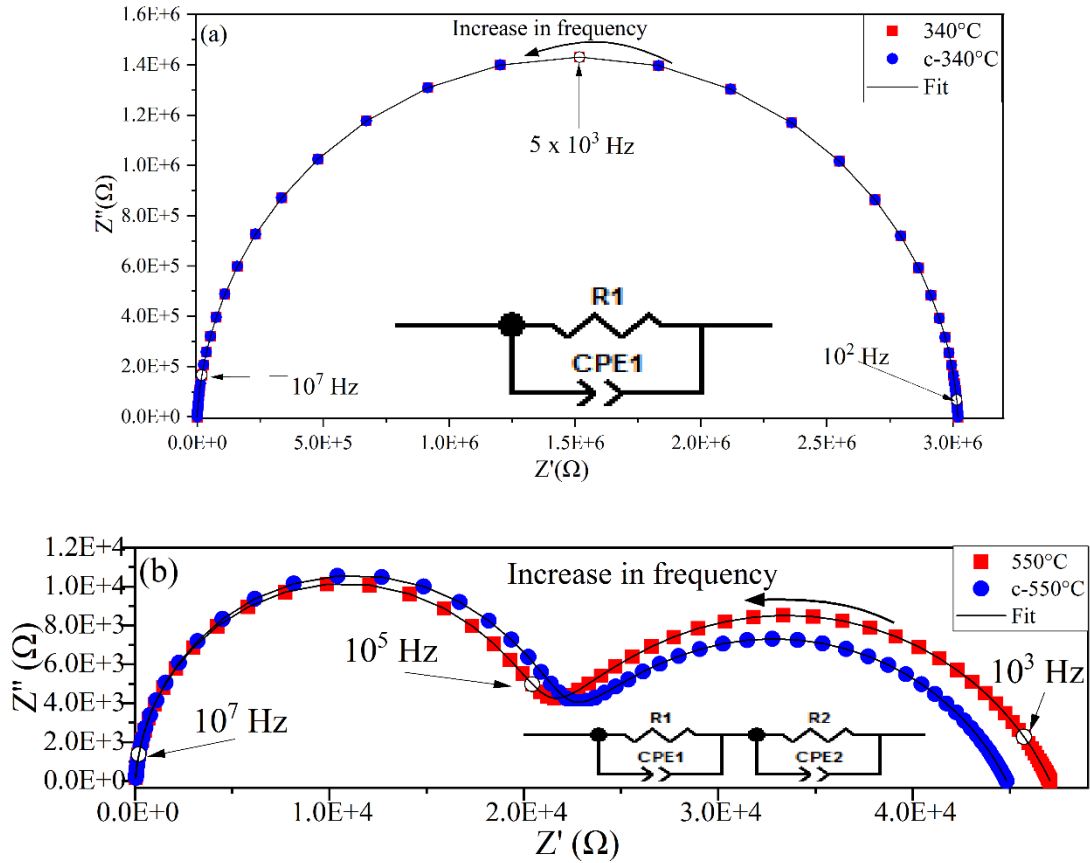
Fig. 4.17: Complex impedance plots for Ho₂Hf₂O₇ sintered at 1500°C for 2h measured in heating cycle at (a) 340°C and (b) 550°C, (c-340°C and c-550°C for cooling cycle).

The temperature dependence of the electrical conductivity (σT) was analysed using an Arrhenius expression of the form

$$\sigma T = \sigma_0 \, exp \, (-Ea/kT) \tag{4.4}$$

where σ_0 is pre-exponential factor related to the effective number of mobile charge carriers, T is the absolute temperature, k is Boltzmann constant and Ea is the activation energy for oxide ion migration. The value of activation energy for ionic conduction in Ho₂Hf₂O₇ has been obtained by plotting $ln\sigma T$ against $1/T$ as shown in Fig. 4.18 for bulk and grain boundary of single step sintered Ho₂Hf₂O₇ pellet measured over the temperature range of 340 °C to 750 °C and frequency range of 100 mHz to 100 MHz for both heating and cooling cycles. The straight lines in the graph represents the experimental data least square best fit to an Arrhenius expression confirming that the ionic diffusion in the sample is thermally activated. Activation

101

energies and conductivities for both bulk and grain boundary diffusion can be easily calculated from the slopes and intercepts, respectively, of such linear fits.

According to calculations, [157, 158] the energetically preferred pathway for oxide on migration in $A_2B_2O_7$ pyrochlore consists of $O_{48f} \rightarrow O_{48f}$ sequential jumps, along the shortest edge of the BO_6 polyhedra such as HfO_6; activation energies calculated for this oxygen ion diffusion mechanism are in general ≤ 1 eV. Activation energies found for the bulk and grain boundary conductivity of SSS processed $Ho_2Hf_2O_7$ pellet are 1.24 (± 0.01)eV and 1.55 (± 0.01)eV, respectively. The values of bulk and grain boundary conductivities found at 725°C are 1.8×10^{-4} S.cm^{-1} and 9.0×10^{-5} S.cm^{-1}, respectively. The magnitude of activation energy for ionic conduction has been found to be far lower than that reported in literature [129] for $Ho_2Hf_2O_7$ (1.395 eV). Conductivity of $Ho_2Hf_2O_7$ was also reported at 750°C is 5.01×10^{-4} S.cm^{-1} [129].
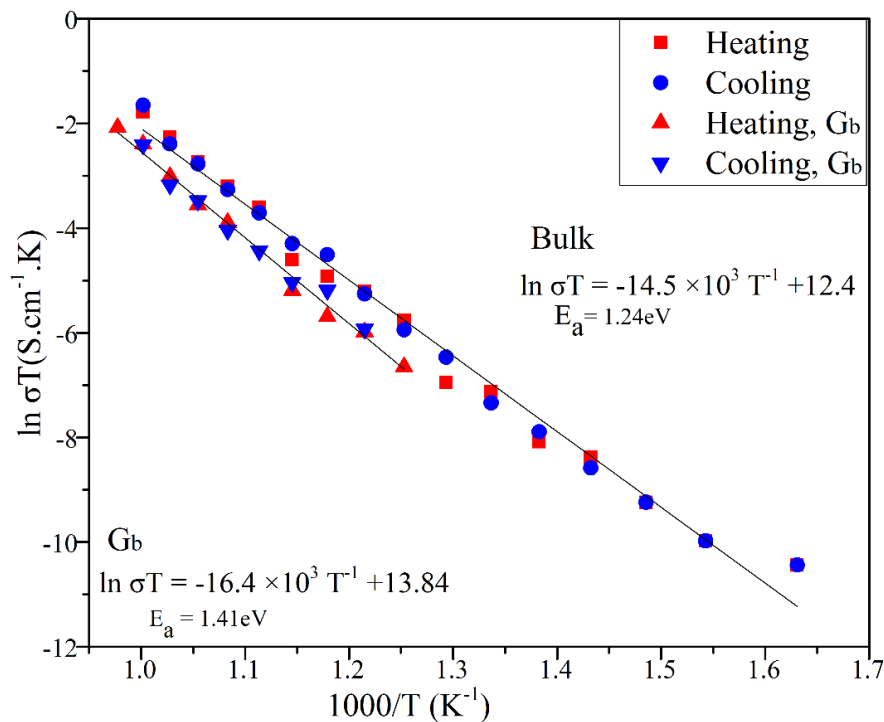
Fig. 4.18: Temperature dependence Arrhenius plots of bulk and grain boundary conductivity in heating and cooling cycles of holmium hafnate pellets sintered at 1500°C for 2h using SSS process.

Frequency dependence of the real components of conductivity for SSS $Ho_2Hf_2O_7$ material (log-log representation) for both heating and cooling cycles are shown in Fig. 4.19 (a & b). Bulk and grain boundary contribution for conductivity and their dependence on frequency can be clearly seen in Fig. 4.19. Another important characteristic feature of ion conducting solids is blocking effect which is also evident in this type of log-log representation. At lower temperature there is decrease in conductivity at lower frequencies. In Fig. 4.19 (a) there are three regions; lower frequency, plateau and higher frequency. Plateau is showing dispersion and separating the two frequency regions. The plateau developing at lower frequency above 340 °C is due to the grain boundary contribution to the conductivity whereas at higher frequencies is because of bulk contribution. The frequency dispersive region separating low frequency and high frequency plateaus shifts towards higher frequencies with increase in temperature and leads above 700 °C to a regime where conductivity is almost frequency independent as shown in Fig. 4.19 (a) & (b). The regimes are consistent with heating and cooling cycles.
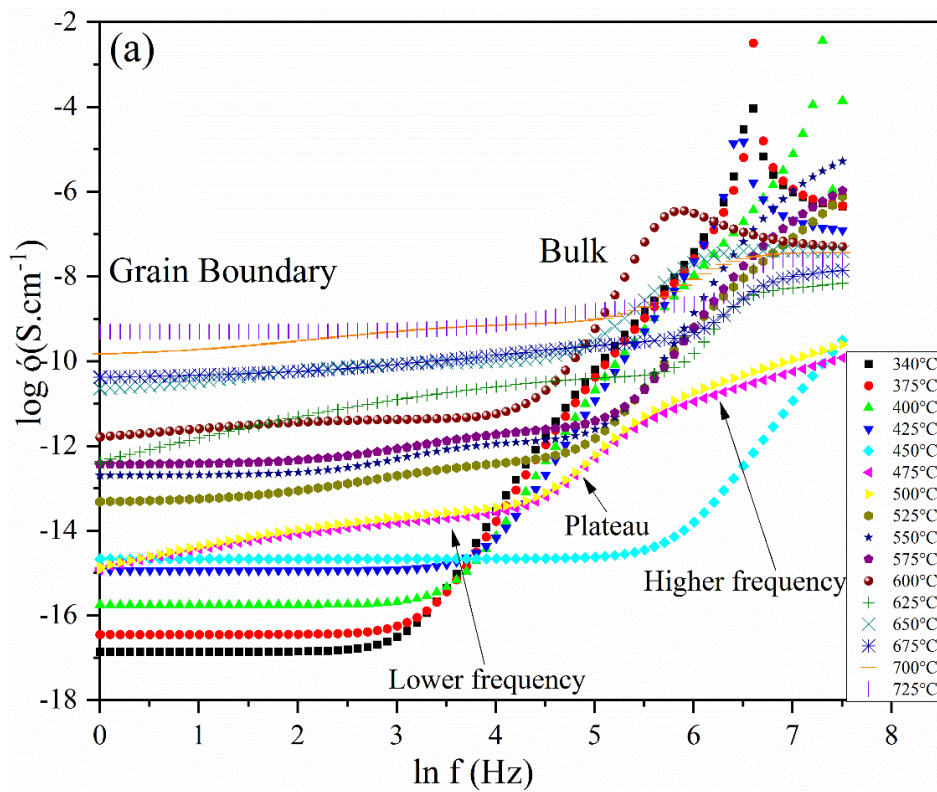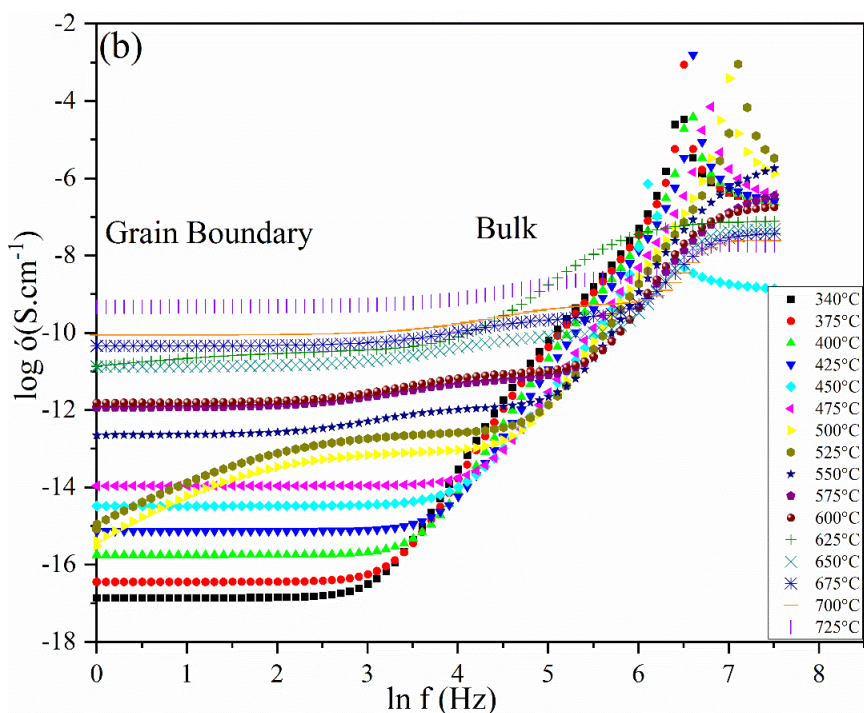
Fig. 4.19: Frequency and temperature dependence of the real parts of Ho₂Hf₂O₇ conductivity (a) heating (b) cooling

Impedance spectroscopy results at 350 °C and 550 °C of $Ho_2Hf_2O_7$ pellets sintered using TSS process are sown in Fig. 4.20. Squares represent the heating cycle while circles are for cooling cycle in Fig. 4.20. At 350 °C the conductivity of the sample is entirely due to bulk contribution and no sign of grain boundary contribution is present here. The increase in frequency is from left to right which can be clearly seen in the Fig. 4.20 (a). There appears with the increase in temperature the grain resistance is decreasing as shown in Fig. 4.20 (b) at 550 °C.

The heating and cooling cycles in the impedance plots of $Ho_2Hf_2O_7$ pellets sintered with SSS and TSS processes show the consistent results over the entire temperature range from 340 °C to 750 °C (SSS) and 350 °C to 700 °C (TSS). This indicates that the holmium hafnate solid electrolyte respond reversibly in the temperature range of measurement which is an important behaviour of solid electrolytes as they are subject to temperature variation when used in an electrochemical device [159].
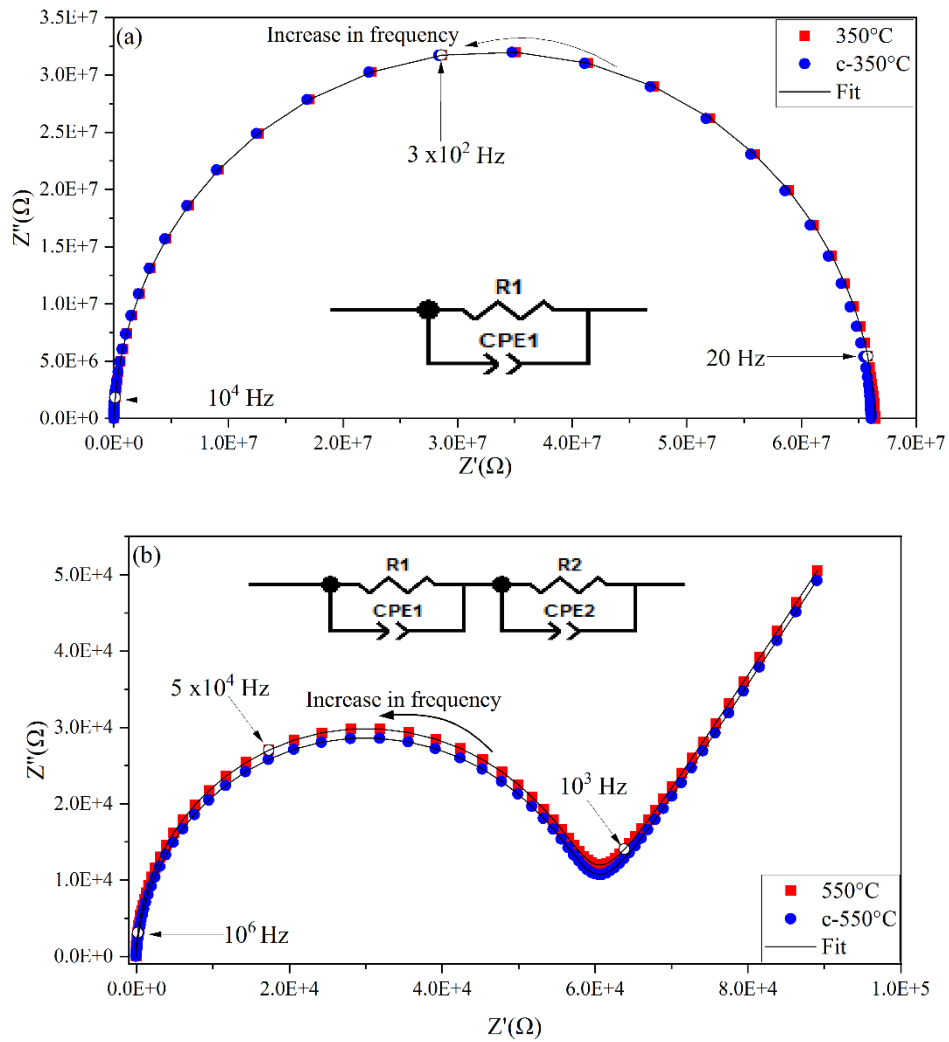
Fig. 4.20: Complex impedance plots for Ho₂Hf₂O₇ with two step sintering; (I) - 1500°C for 5min, (II) - 1300°C for 96h measured in heating cycle at (a) 350°C and (b) 550°C, (c-350°C and c-550°C for cooling cycle).

Temperature dependence Arrhenius plots of bulk and grain boundary (Gb) conductivities for both heating and cooling cycles of holmium hafnate prepared using TSS process are shown in Fig. 4.21. All the contribution to the total conductivity from 350 °C to 550 °C is due to the bulk conductivity. A noticeable deviation in the conductivity plot was observed at 550 °C which indicates the decrease in bulk conductivity and after that grain boundary contribution was observed. Grain boundary contribution to the total conductivity started from 575 °C as seen from the grain boundary (Gb) plot in Fig. 4.21. The values of activation energies for bulk and

grain boundary have been found quite close to each other; 1.32 (±0.01)eV and 1.30 (±0.01)eV, respectively. There has not been found significant difference in the bulk and grain boundary conductivity for the $Ho_2Hf_2O_7$ sample sintered with TSS process.
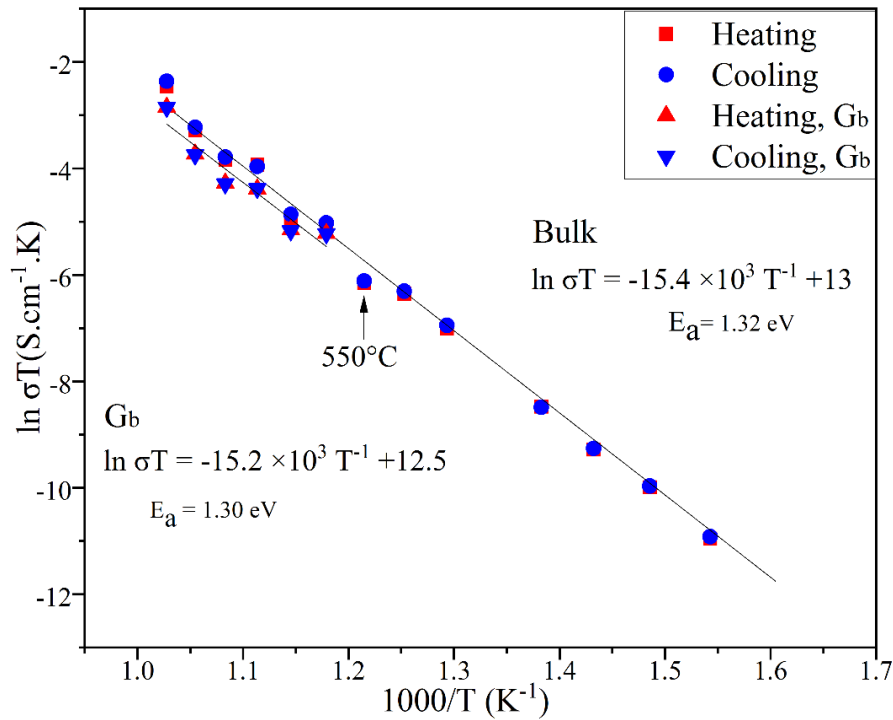
Fig. 4.21: Temperature dependence Arrhenius plots of bulk and grain boundary (Gb) conductivity for both heating and cooling cycles of holmium hafnate prepared using TSS process.

Frequency dependence of the real components of conductivity for TSS $Ho_2Hf_2O_7$ are shown in Fig. 4.22 (a) & (b) for both heating and cooling cycles, respectively. Bulk and grain boundary contribution and their dependence on frequency in the form of log-log representation are shown in Fig. 4.22. Three regions are observed in the frequency dependent conductivity plots are: lower frequency dispersive region, plateau and higher frequency dispersive region. At lower frequency region there is decrease in conductivity at low temperatures. The plateau developing at temperatures ≤ 550 °C at lower frequency regions are due to grain boundary contribution and at higher frequency regions is mainly bulk contribution. With the increase in temperature

this plateau is shifting to the higher frequency region and develops a regime above 675 °C where conductivity is not much affected by frequency as shown in Figs. 4.22 (a) & (b). The results for both heating and cooling cycles are well consistent throughout the temperature range of 350-700 °C.

The results of frequency dependence conductivity obtained from TSS $Ho_2Hf_2O_7$ are showing similar trends for SSS $Ho_2Hf_2O_7$ at temperature below 500 °C but at higher temperatures these trends are varying.
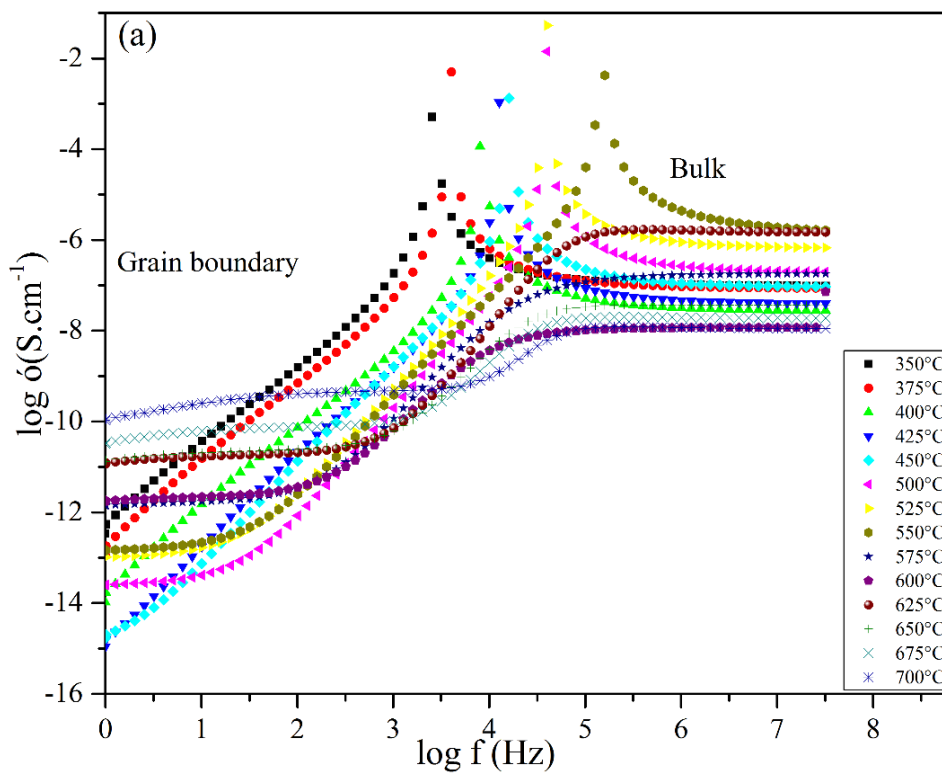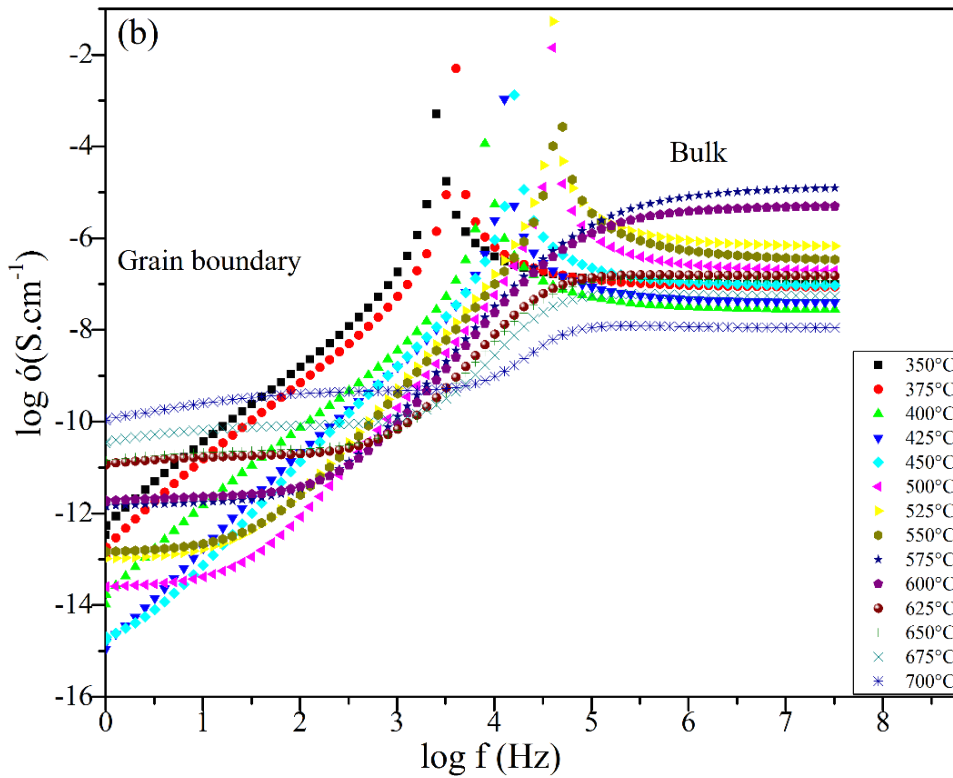
Fig. 4.22: Frequency and temperature dependence of the real parts of $Ho_2Hf_2O_7$ conductivity (a) heating (b) cooling

Table 4.7: Corresponding activation energies and conductivity values of SSS and TSS processed $Ho_2Hf_2O_7$

Sample	Activation Energy (eV)	R^2 value	Conductivity at 575 °C S.cm^{-1}	Conductivity at 700 °C S.cm^{-1}
SSS-Bulk	1.24	0.98918	1.08×10^{-5}	1.00×10^{-4}
SSS-Gb	1.41	0.99474	5.28×10^{-6}	4.66×10^{-5}
TSS-Bulk	1.32	0.99246	7.58×10^{-6}	9.19×10^{-5}
TSS-Gb	1.30	0.93209	6.34×10^{-6}	5.94×10^{-5}

The Arrhenius plots for bulk conductivity of $Ho_2Hf_2O_7$ pellets sintered using the SSS and TSS processes are compared in Fig. 4.23 (a). The magnitude of activation energy for the samples

108

sintered by SSS process is lower in the case of bulk and higher for grain boundary than that of the samples prepared by TSS process. There is noticeable variation in the bulk conductivity plots. The values of the bulk conductivity for the SSS process is 1 order of magnitude higher than that of the TSS process at the lower temperature end but the gap closes with the rise in temperature and at higher temperature end they differ by about 0.5 order of magnitude, which is clearly seen in Fig. 4.23 (a) and Table 4.7.

Fig. 4.23 (b) shows the comparison of Arrhenius plots of grain boundary conductivity of SSS processed $Ho_2Hf_2O_7$ samples and TSS processed samples. There appears to be an abrupt variation of grain boundary conductivity over the temperature range for TSS processed sample resulting in the decrease in R^2 value for linear fit as shown in Table 4.7. The values of grain boundary conductivity of the TSS processed sample are found to be similar to the SSS processed sample up to 600 °C but from 650 °C onwards the linear fit of TSS processed plot shows minor deviation from the SSS processed plot and yields the magnitude of activation energy for TSS processed sample (1.30 eV) lower than that of the SSS processed sample (1.41 eV) as shown in Fig. 4.23 (b). The trend of grain boundary conductivity plots and corresponding values of activation energies for SSS and TSS processed samples are found contrary to the trends of the bulk conductivity plots and corresponding activation energy values.
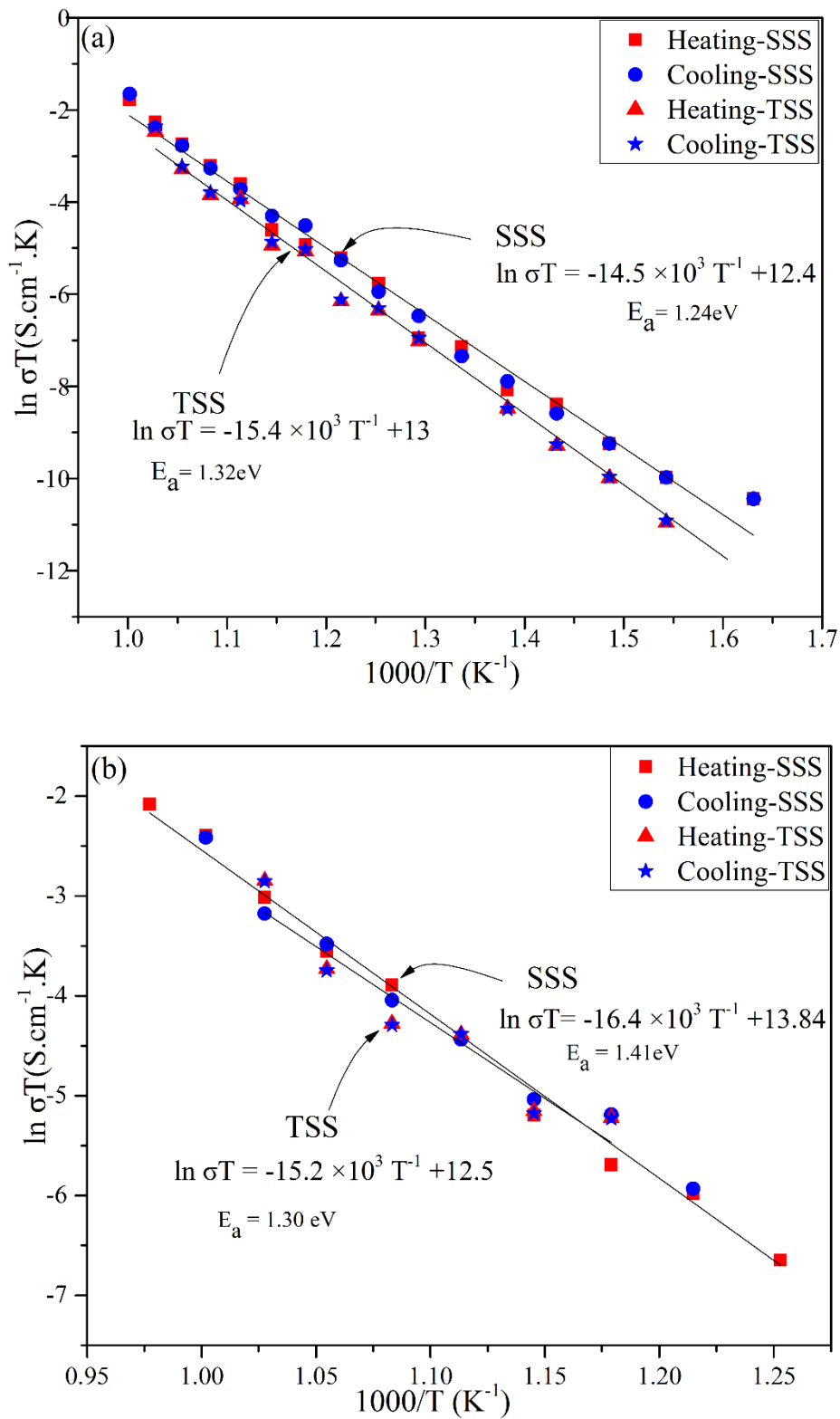
Fig. 4.23: Comparison of temperature dependence Arrhenius plots of (a) bulk and (b) grain boundary (Gb) conductivity for both heating and cooling cycles of holmium hafnate prepared using SSS and TSS processes.

Above comparison suggests that although SSS processed $Ho_2Hf_2O_7$ sample exhibits better results than that of TSS processed sample but there is not as much difference in the results has found as in case of $Ho_2Zr_2O_7$ samples [160] synthesised and processed with similar techniques.

4.2. Holmium Zirconate ($Ho_2Zr_2O_7$)

Nanopowders of $Ho_2Zr_2O_7$ used to study the structural and morphological properties were obtained using Leeds Alginate Process developed and its thermal and structural characterisation has already reported [161].

4.2.1. Thermal and Structural Characterisation

Metal-alginate dried beads were thermally analysed using simultaneous TGA/DTG/DSC in flowing air and the result are shown in Fig. 4.24. Thermal decomposition of metal-alginate beads can be divided into seven steps as shown in Table 4.8. TGA and DSC profile are in good agreement with each other. In the first step, the mass loss is due to the removal of adsorbed water from beads. The twin exothermic peaks were observed in step 2 & 3 which are due to the first stage of partial combustion of organic matrix. More weight loss is involved with the main peak and less with the shouldered end as shown in the inset (a) of Fig. 4.24. First three steps accompanied with weight loss of 23 %. Inset (b) of Fig. 4.24 shows the data from 150-1000 °C to elaborate the DTG curve by reducing its scale. In step 4 and 5 total weight loss is around 25 % which is due to the evolution of oxygen resulting from the cleavage of weaker linkage (G-G, G-M, and M-M) in the alginate structure. In steps 4 and 5 onsets of two minor exothermic peaks appears at 247 °C and 350 °C resulting from the second stage of combustion of organic matrix. The exothermic peak in step 6 is due to the final stage of oxidative decomposition of remainder organic and inorganic matrix resulting into approximately 11 % weight loss. Pyrolysis of the organometallic precursor was complete with the endset of major exothermic peak at about 615 °C. A small weight loss of about 0.9 % can still be observed between 833-900 °C which may be due to the loss of excess oxygen from the lattice of

Ho$_2$Zr$_2$O$_{7+\delta}$ that manifests a small endothermic peak in DSC trace. This allows us to estimate an excess oxygen of about ±0.025 % in Ho$_2$Zr$_2$O$_{7+\delta}$. Based on these results, a calcination temperature of 700 °C was selected for further processing of dried alginate beads. These results are in agreement with the Ho$_2$Zr$_2$O$_7$ prepared by Polymerized-Complex Method (PCM) [162].
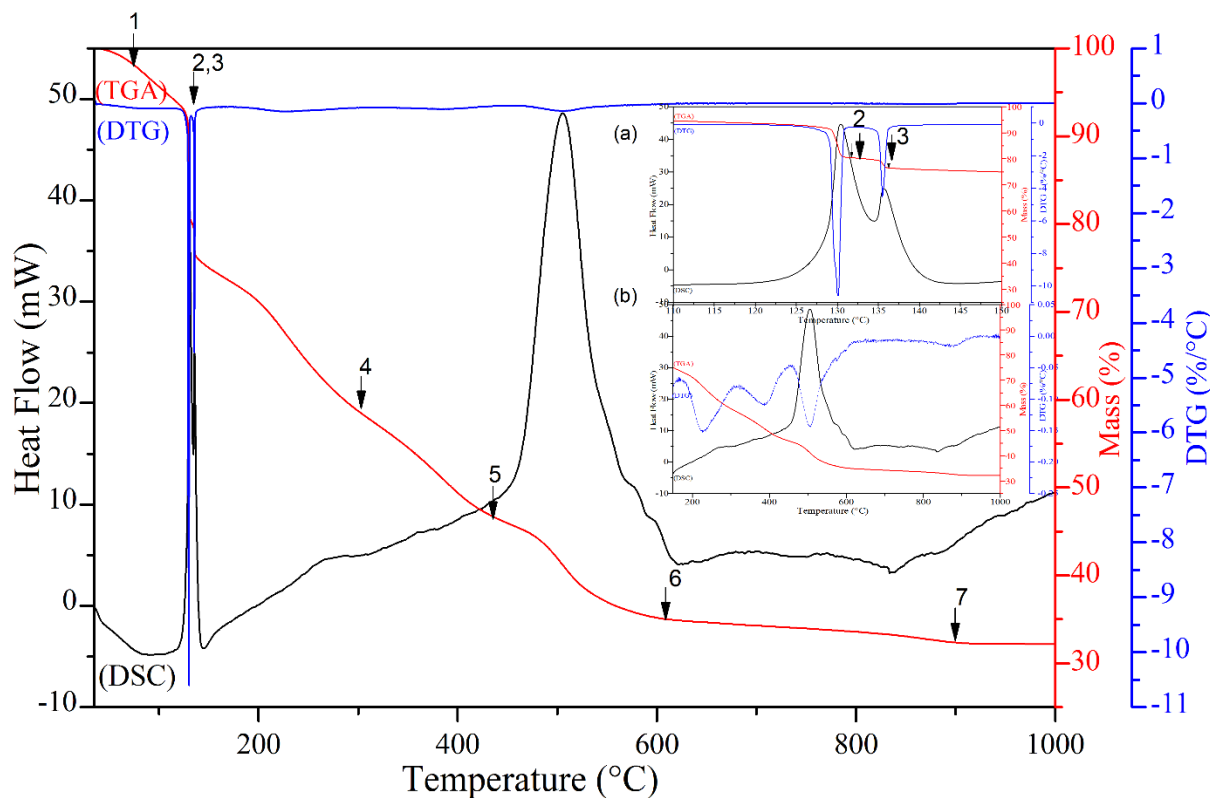
Fig. 4.24. Thermal analysis of dried beads. Marked arrows show numbered steps.

Table 4.8: TGA/DSC analysis of dried beads

% Weight Loss in TGA curve		
Steps	Temp. Range, ˚C	Wt. loss, %
1	RT- 127	7.5
2	127-131	11.9
3	134-137	3.5
4	180-306	14.7

5	327-440	10
6	457-614	10.7
7	833-900	0.9
Peaks in DSC curve		
Peak 1	RT-116	Endothermic
Peak 2	116-134	Exothermic
Peak 3	134-145	Exothermic
Peak 4	247-302	Exothermic
Peak 5	350-380	Exothermic
Peak 6	437-616	Exothermic
Peak 7	815-865	Endothermic

Fig. 4.25 (a) shows the results of HT-XRD patterns of oven dried metal alginate beads from room temperature to 1000 °C. No diffraction peaks are observed between 25 °C to 300 °C as the decomposition of metal-alginate beads has not yet commenced. At 400 °C some minor undulation in the baseline were observed at the position close to the diffraction peaks of crystalline $Ho_2Zr_2O_7$. At 600 °C, thermal decomposition of beads has completed according to Fig. 4.24 and high purity single phase holmium zirconate peaks were observed. These results are in excellent agreement with TGA/DSC analysis. A few minor peaks from $\alpha-Al_2O_3$ sample holder were also noticed along with holmium zirconate peaks as shown in Fig. 4.25 (a).

Fig. 4.25 (b) shows the refined HT-XRD pattern from 400-1000 °C. Here the data is refined to digitally eliminate $\alpha-Al_2O_3$ sample holder peaks. It is clearly evident that the decomposition started at 400 °C and ended at 600 °C yielding a high purity nanoparticles of holmium zirconate. With further increase in temperature from 700-1000 °C crystal size increased and sharpness of peaks also increased as a result of crystal growth [125].

Results of thermal decomposition of dried metal alginate beads using TGA/DSC and HT-XRD show high degree of internal consistency with respect to the decomposition temperature of metal alginate beads and also onset and endset of holmium zirconate formation.

Results of TGA/DSC and HT-XRD are in good agreement with each other showing complete thermal decomposition of dried metal alginate beads at 600 °C. Based on the results of TGA/DSC/DTG and HT-XRD it can be concluded that the enthalpy change for the decomposition of metal alginate (Ho^{3+}/Zr^{4+}-ALG) into $Ho_2Zr_2O_7$, $CO_{2\ (g)}$ and $H_2O_{\ (g)}$ is -3826 ± 383 J/g based on the Hess's law of heat summation.

The net enthalpy change of the decomposition process is calculated from the algebraic sum of the area under each peak in the DSC trace divided by the change in weight of the corresponding peak in the TGA trace. The net enthalpy change of -3826 J/g (±10%) suggests that the overall decomposition process is exothermic in nature. It can be envisaged that the evolved heat can be utilized for the drying and calcination process of beads in a continuous manufacturing process or stored if it is produced in excess of the requirements.
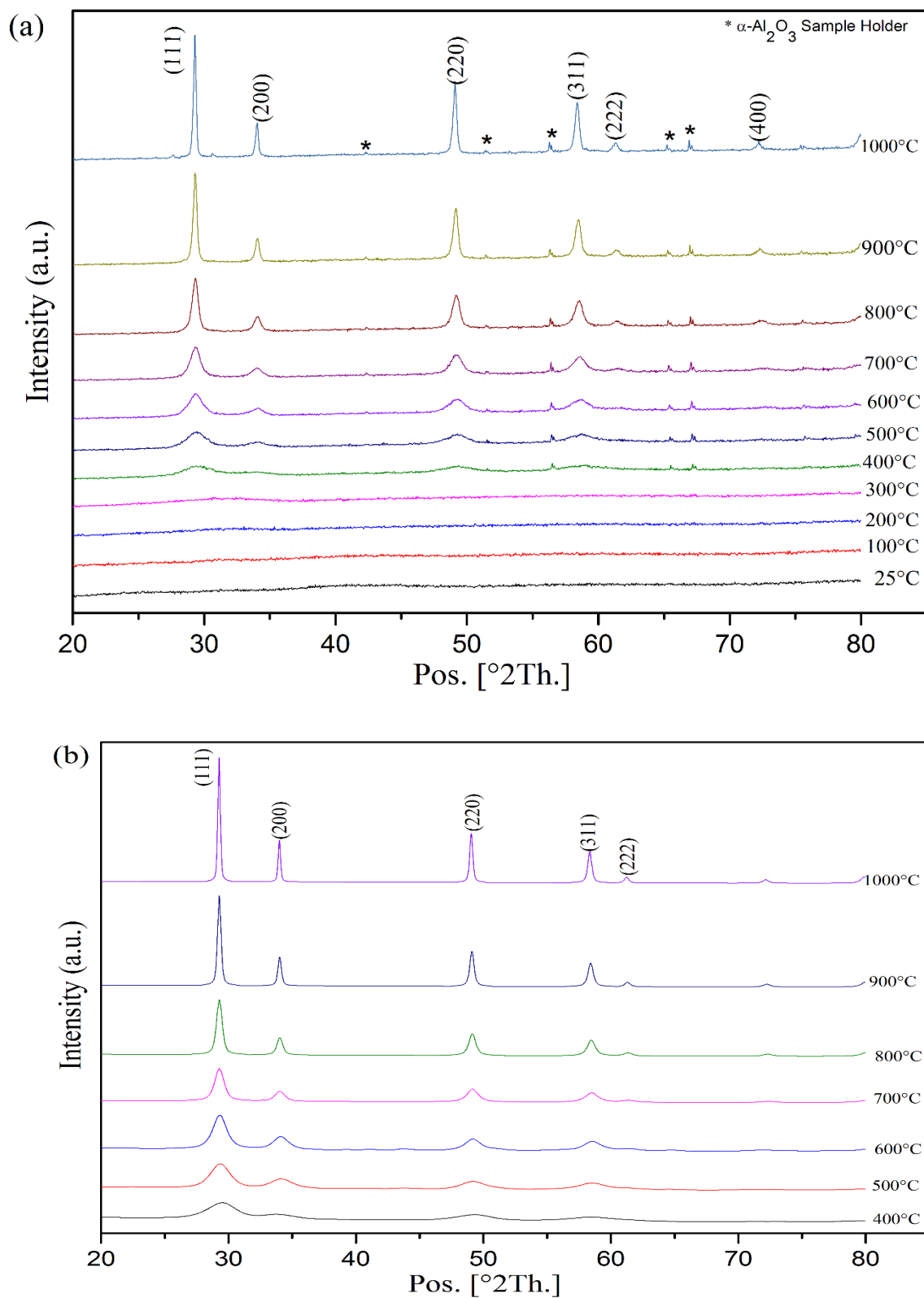
Fig. 4.25: (a) HT-XRD patterns of dried metal alginate beads from 25-1000°C. The patterns are indexed by ICDD, 01-080-7723 with cubic Ho₂Zr₂O₇ shown at the top of the

115

peaks. Tick marks '*' for α-Al₂O₃ peaks. (b) Refined HT-XRD patterns from 400-1000°C, sample holder (α-Al₂O₃) peaks were digitally removed.

Fig. 4.26 shows the XRD pattern of nanopowders obtained after calcination of dried beads at 700 °C for 2 h and 6 h. The observed data for different calcination durations yielded single phase $Ho_2Zr_2O_7$ having cubic defect fluorite structure. XRD pattern of material calcined for 2 h shows broader peaks compared with that of 6h. Broadening of peak is one of the indicator of presence of nano-sized crystallites.

Effect of calcination duration on crystallite size is shown in Table 4.9. Crystallite size increased with the increase in annealing time. This phenomenon is known as Ostwald ripening in which inhomogeneous structure changes over time and larger crystals are formed at the expense of small ones to yield relatively more stable structure [127] also commonly observed during the powder sintering processes.
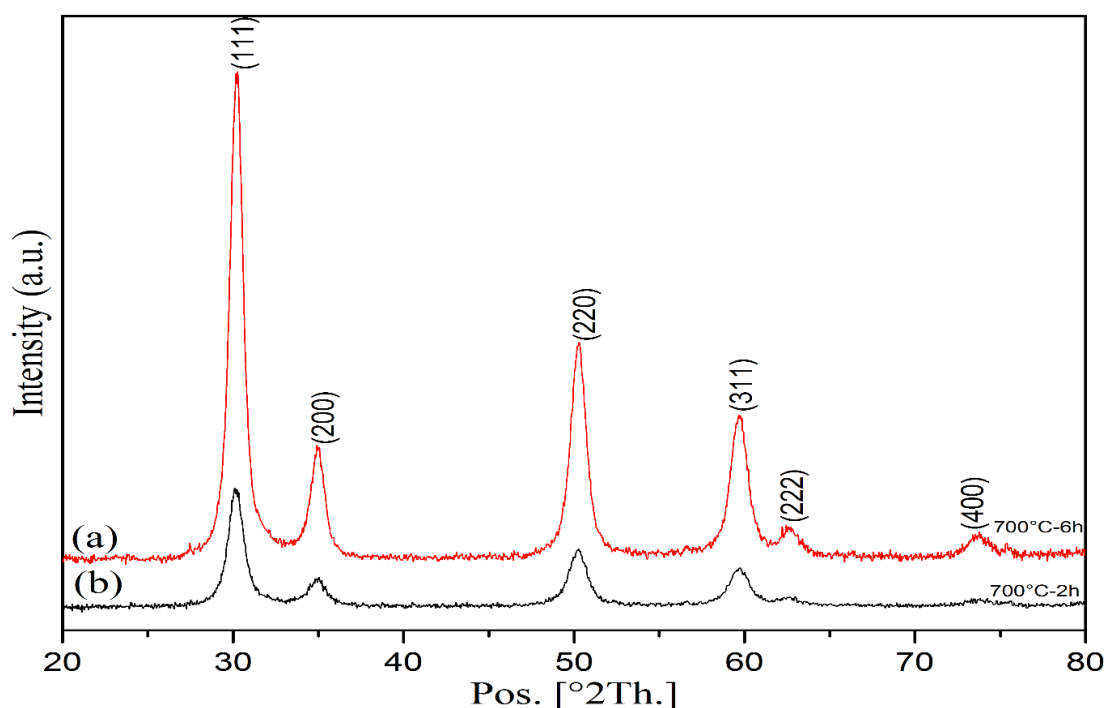
Fig. 4.26: XRD patterns of $Ho_2Zr_2O_7$ nanoparticles obtained after calcination at 700°C for (a) 6h and (b) 2h. Patterns are indexed by ICDD, 01-080-7723 at the top of the peaks.

The Rietveld refinement of XRD pattern of holmium zirconate ($Ho_2Zr_2O_7$) calcined at 700 °C for 6 h is shown in Fig. 4.27. The observed and calculated patterns matched with each other and peaks could also be indexed with the XRD reference pattern (ICDD, 01-080-7723). The value of goodness of fit (GOF) is close to 5% as seen in Table 4.9.

Crystallite size was obtained from XRD pattern using Scherrer equation after eliminating instrument broadening and stress-strain broadening. The original data and refined model are in excellent agreement with each other and the value of weighted residual (Rwp) from refinement is 7 %. With the increase in annealing time from 2 h to 6 h, particle coarsening occurred and correspondingly micro-strain decreased as anticipated. Coarsening resulted in crystal growth from approximately 6 nm to 8 nm. The unit cell parameters of the nanopowder of $Ho_2Zr_2O_7$ having defect fluorite structure (a = b = c = 5.148 A° and α = β = Γ = 90°) prepared through ion-exchange based sol-gel method in this study is in excellent agreement with the data obtained through Polymerized-Complex Method (PCM) [162] and gel combustion technique followed by high temperature sintering [163].
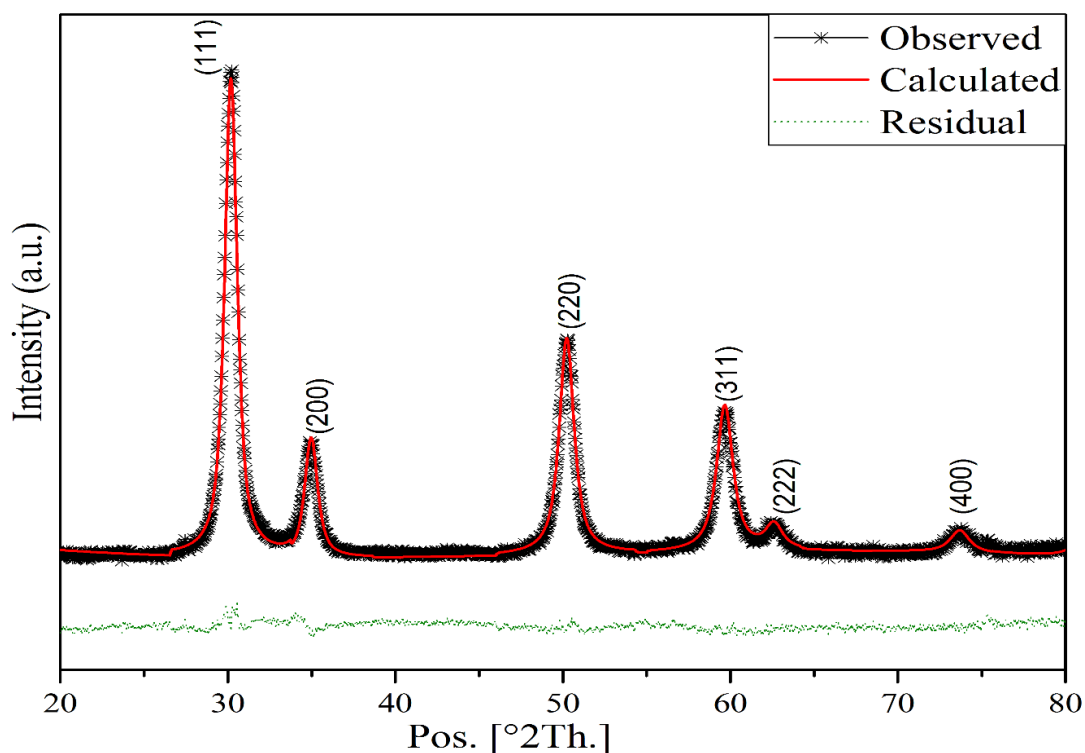
Fig. 4.27: Rietveld refinement of XRD patterns of Ho$_2$Zr$_2$O$_7$ nanoparticles obtained after calcination at 700 °C for 6h. Miller indices representing fluorite structure are shown on the top of the peaks.

Table 4.9: Structural properties of Ho$_2$Zr$_2$O$_7$

Sample	Rietveld Refined Size Strain Analysis					
	Avg. Crystallite Size (nm)	Micro Strain (%)	R$_{wp}$ (%)	R$_{exp}$ (%)	GOF $=(R_{wp})^2/(R_{exp})^2$	Lattice Parameters (A°)
700°C-2h	6.27	2.478	5.843	5.276	1.226	5.149734
700°C-6h	7.85	2.042	6.971	3.037	5.266	5.147994

Fig. 4.28 shows the comparison between the XRD patterns of holmium hafnate (Ho$_2$Hf$_2$O$_7$) [124] and holmium zirconate (Ho$_2$Zr$_2$O$_7$) synthesised through alginate based sol gel method. In many aspects Hf is considered chemically identical to Zr, since they belong to the same group of the periodic table. Hf^{+4} and Zr^{+4} have ionic radii of 0.71A° and 0.72A° for six fold coordination respectively [164]. Cation with larger ionic radius (Zr^{+4}) shows that the fluorite peaks have shifted slightly to the lower angle as seen in the insets of Fig. 4.28 which is in agreement with the larger unit cell parameter of Ho$_2$Zr$_2$O$_7$ compared with Ho$_2$Hf$_2$O$_7$ [124] by approximately 5%.
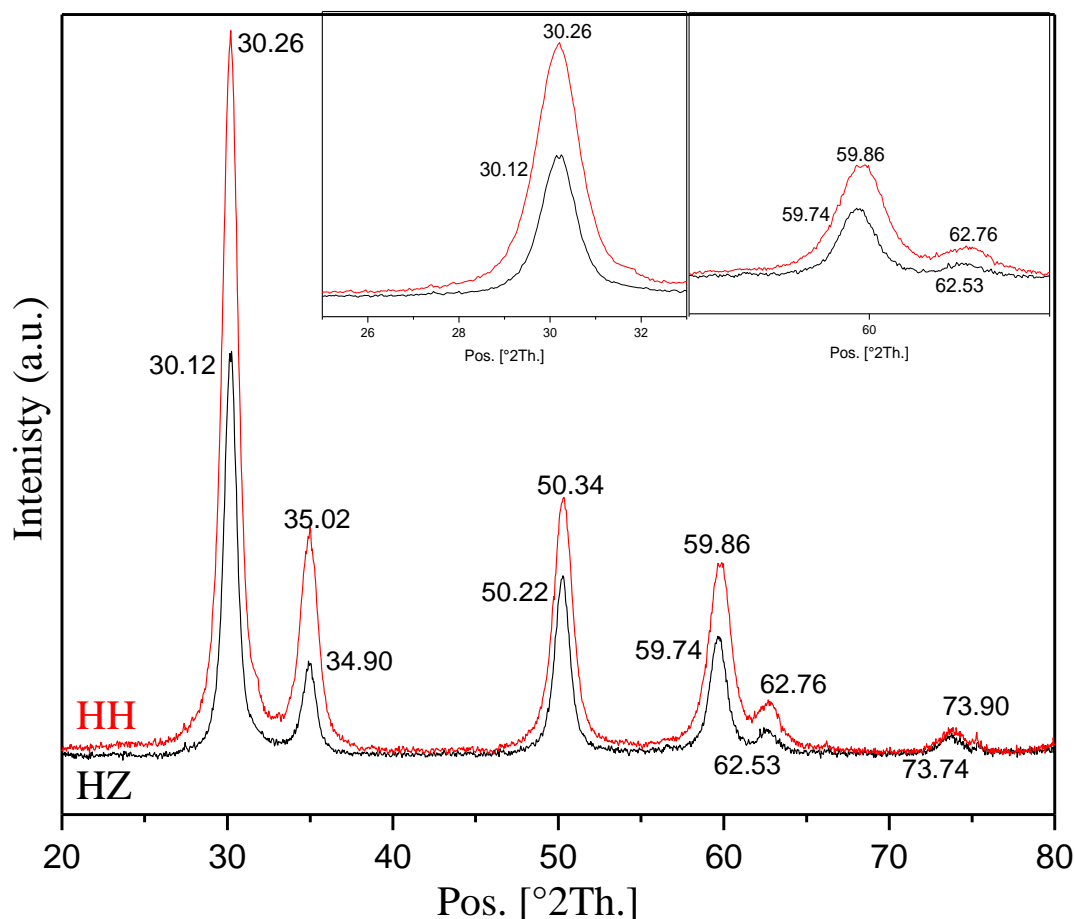
Fig. 4.28: XRD patterns of holmium hafnate (HH) and holmium zirconate (HZ) synthesised through alginate method. Insets show the shifting of peak positions.

XRD technique is more restrained to disorder in cation sub-lattice rather than in anion sub-lattice since the scattering power of X-rays for oxygen is much lower than rare-earth and transition metal cations. On the other hand, Raman spectroscopy is sensitive to metal-oxygen vibrations compared with metal-metal vibrations in oxides. Hence, Raman spectroscopy is an excellent technique to analyse the extent of disorder in pyrochlore oxides and differentiate between the pyrochlore and defect fluorite structures [93]. Factor group analysis predicted that there are a total of six Raman active modes in pyrochlore oxides as mentioned in equation 4.1 [165].

Raman spectra of $Ho_2Zr_2O_7$ nanopowder obtained after calcination at 700˚C for 6h is shown in Fig. 4.29. Individual modes are indistinguishable in fully disordered defect-fluorite [72, 135,

136] structure, the spectra here shows some initial pyrochlore type short range ordering of cation and oxygen vacancies [72, 135, 136] and appearance of weak bands is due to partial ordering of fluorite structure [163]. Bands around 270 and 590cm^{-1} correspond to the Zr−O vibrations. The band at 590 cm^{-1} is assigned to F$_{2g}$ mode due to Zr−O stretch [163]. Bands around 665 and 883cm^{-1} correspond to the Ho−O vibrations. The vibrations corresponding to Ho−O and Zr−O appear in band 1060 cm^{-1}. Band around 491cm^{-1} clearly indicates the presence of disordered defect fluorite structure. The transformation from ordered pyrochlore structure to disordered defect fluorite structure shows the broad hump around 350-400 cm^{-1} [163] is not noticed since the compound is single phase fluorite. A band around 531cm^{-1} is also absent here which is strictly assigned to the A$_{1g}$ mode of pyrochlore phase [141].
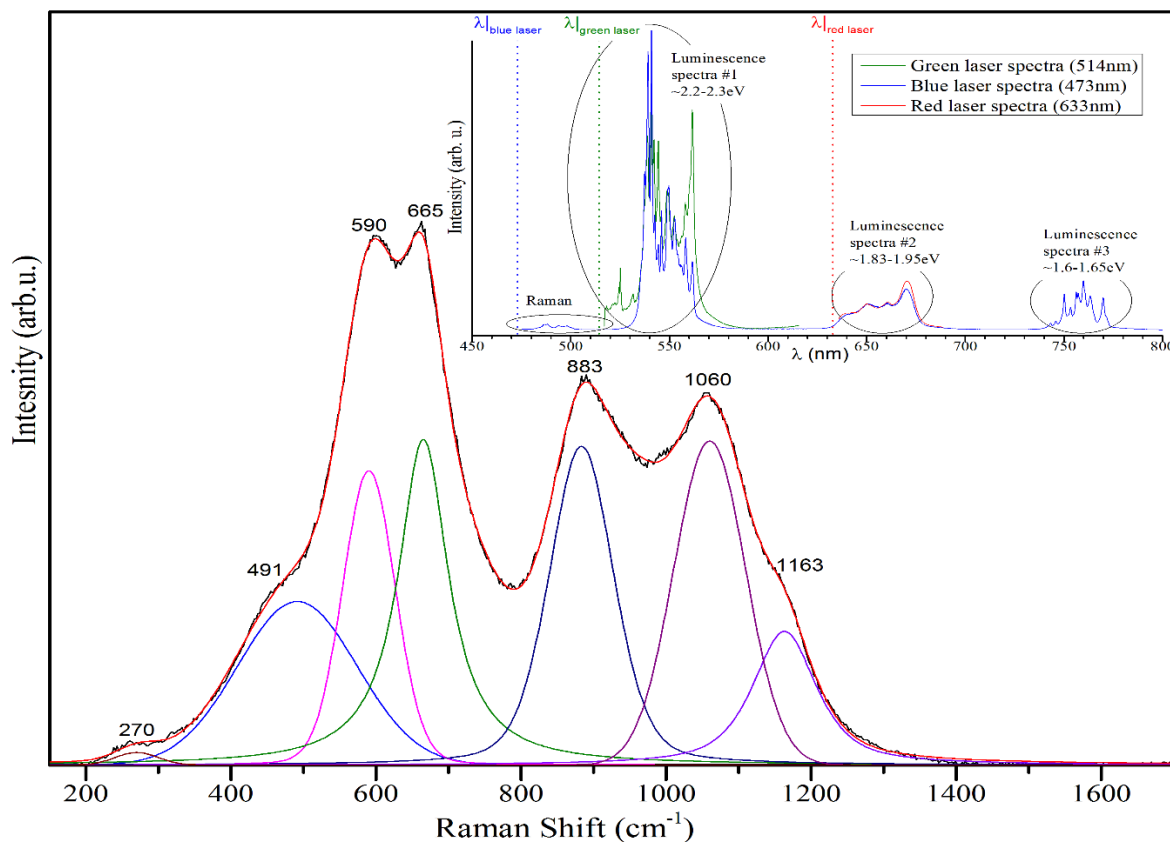
Fig. 4.29: Raman spectra of Ho$_2$Zr$_2$O$_7$ nanopowder obtained after calcination at 700°C for 6h. Spectrum with laser wavelength of 473nm along with peaks fitting. Black curve

is original Raman spectrum and red is fitted one. Inset shows the luminescence spectra for three different lasers blue-473nm, green-514nm and red-633nm.

Inset in Fig. 4.29 shows the luminescence spectra of $Ho_2Zr_2O_7$ nanopowders at different wavelengths. First luminescence spectra with excitation wavelength of 514nm appeared at the range of 520 to 560 nm. Second luminescence spectra using excitation wavelength of 633 nm appeared at wavelength from 635 to 680 nm. Third one with 473 nm blue laser was observed from 740 to 770 nm.

TEM images and SAED pattern of $Ho_2Zr_2O_7$ nanopowder obtained after calcining at 700 ˚C for 6 h are shown in Fig. 4.30. Holmium zirconate nanoparticles were of uniform shape with narrow size distribution and crystalline in nature. The interplanar spacing of nanocrystalline $Ho_2Zr_2O_7$ were calculated from the SAED pattern and were assigned unique Miller indices. The Miller indices (hkl) of all the crystal planes of $Ho_2Zr_2O_7$ obtained from SAED pattern are in good agreement with XRD reference pattern (ICDD, 01-080-7723) and the XRD pattern shown in Fig. 4.26 & 4.27. Table 4.10 shows the d-spacing calculated from TEM and XRD data for different planes. Interplanar spacing (d-spacing) calculated from the XRD and TEM (SAED) are in excellent agreement with each other and reference pattern as shown in Table 4.10.

TEM is one of the few techniques that allows real space visualisation of nanoparticles [166] Average particle size of $Ho_2Zr_2O_7$ obtained from TEM image analysis is 9±1nm and average crystallite size from XRD is 8 nm (Table 4.9). The particle size determined by TEM analysis and the crystallite size calculated from refinement of XRD data are in excellent agreement with each other in spite of the fact that the particle dimensions obtained from these two complimentary analytical techniques corresponds to the dissimilar orientation of the nanopowders [167].

Table 4.10: Comparison of d-spacing of Holmium Zirconate from TEM, XRD Rietveld refinement and XRD reference pattern

h	k	l	Ref. (ICDD, 01-080-7723) d, A˚	XRD d, A˚ 700˚C-6h	TEM d, A˚ 700˚C-6h
1	1	1	3.01450	2.959	3.01
2	0	0	2.61060	2.566	2.61
2	2	2	1.84600	1.819	1.82
3	1	1	1.57430	1.550	1.55
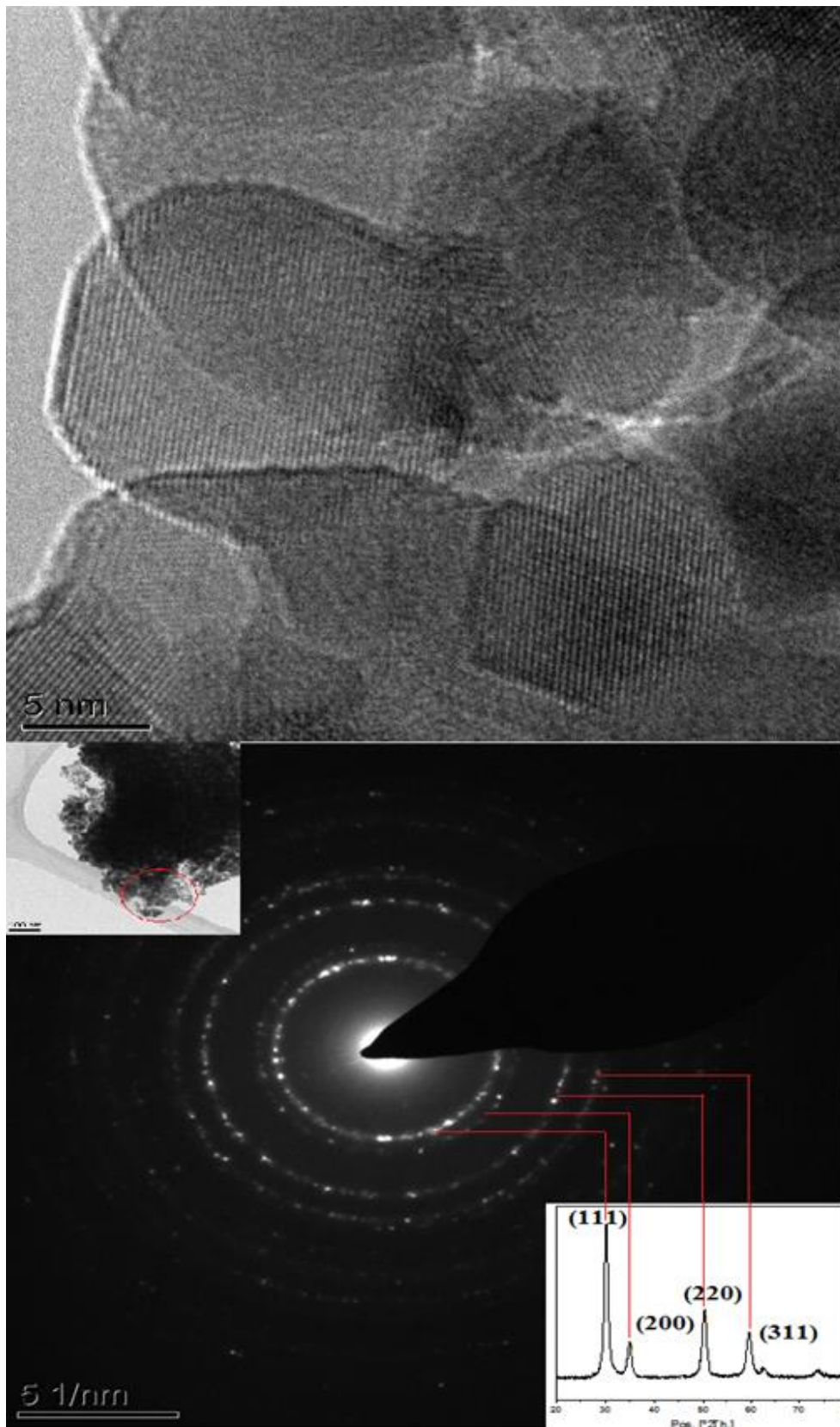
Fig. 4.30: TEM images with SAED pattern of Ho₂Zr₂O₇ calcined at 700°C for 6h. SAED pattern indexed with XRD peaks

Fig. 4.31 shows the TEM-EDX spectrum of nanopowder of holmium zirconate. To further confirm the composition of the synthesised material EDX analysis was performed. $Ho_2Zr_2O_7$ nanocrystals are composed of holmium, zirconium and oxygen with an atomic ratio of 2 : 2 : 7. The peaks due to Cu and C in the spectrum are attributed to the holey carbon mesh grid used for TEM analysis. The Inset in Fig. 4.31 shows the atomic % of elements obtained from EDX and stoichiometry with error bars. This agrees well with the theoretical values of 18.2% for Ho, 18.2% for Zr and 63.6% for O indicating that compound exhibit negligible non-stoichiometry. The percentage error in the elemental analysis is less than 0.2%.
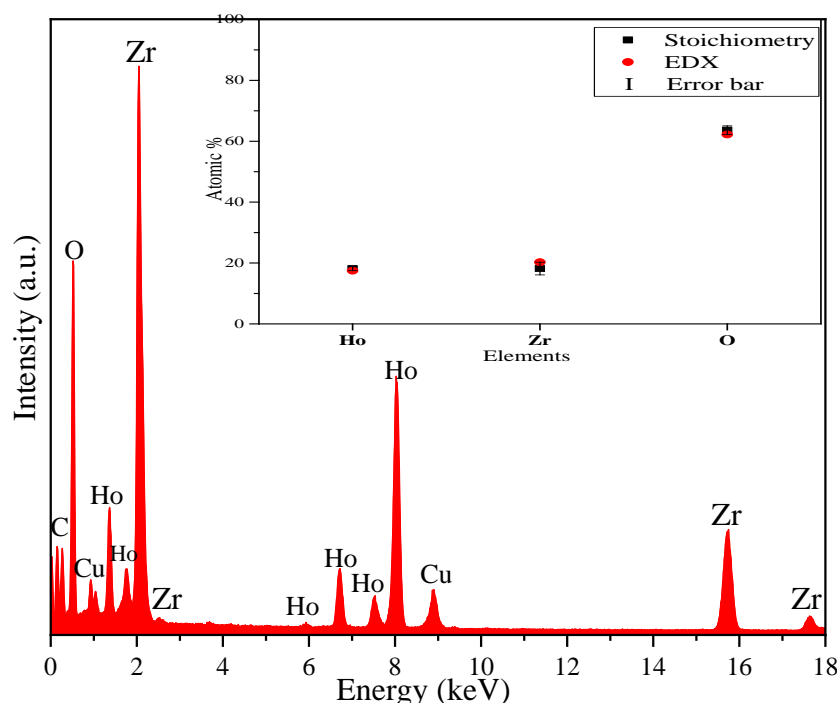
Fig. 4.31: TEM-EDX spectrum of $Ho_2Zr_2O_7$ calcined at 700˚C for 6h. Inset compares the atomic % of elements with the stoichiometry.

Fig. 4.32 shows the surface profile imaging of $Ho_2Zr_2O_7$ nanopowder calcined at 700 ˚C for 6 h using High Resolution TEM (HRTEM) which is capable of showing the unidirectional images of the top surface layer, i.e. a profile view [168]. The main advantage of HRTEM is to allow examination of crystal phases in an overlapping nanopowder sample [169].

Lattice planes can be easily seen and indexed as (111) and (222) in Fig. 4.32. Nanoparticles of $Ho_2Zr_2O_7$ showed the crystalline phase formation with cubic structure and interplanar distance of 3.0 A˚ and 1.82 A˚ for (111) and (222) planes, respectively. Using high purity feed material nanoparticles of $Ho_2Zr_2O_7$ can be successfully prepared using Leeds Alginate Process (LAP).
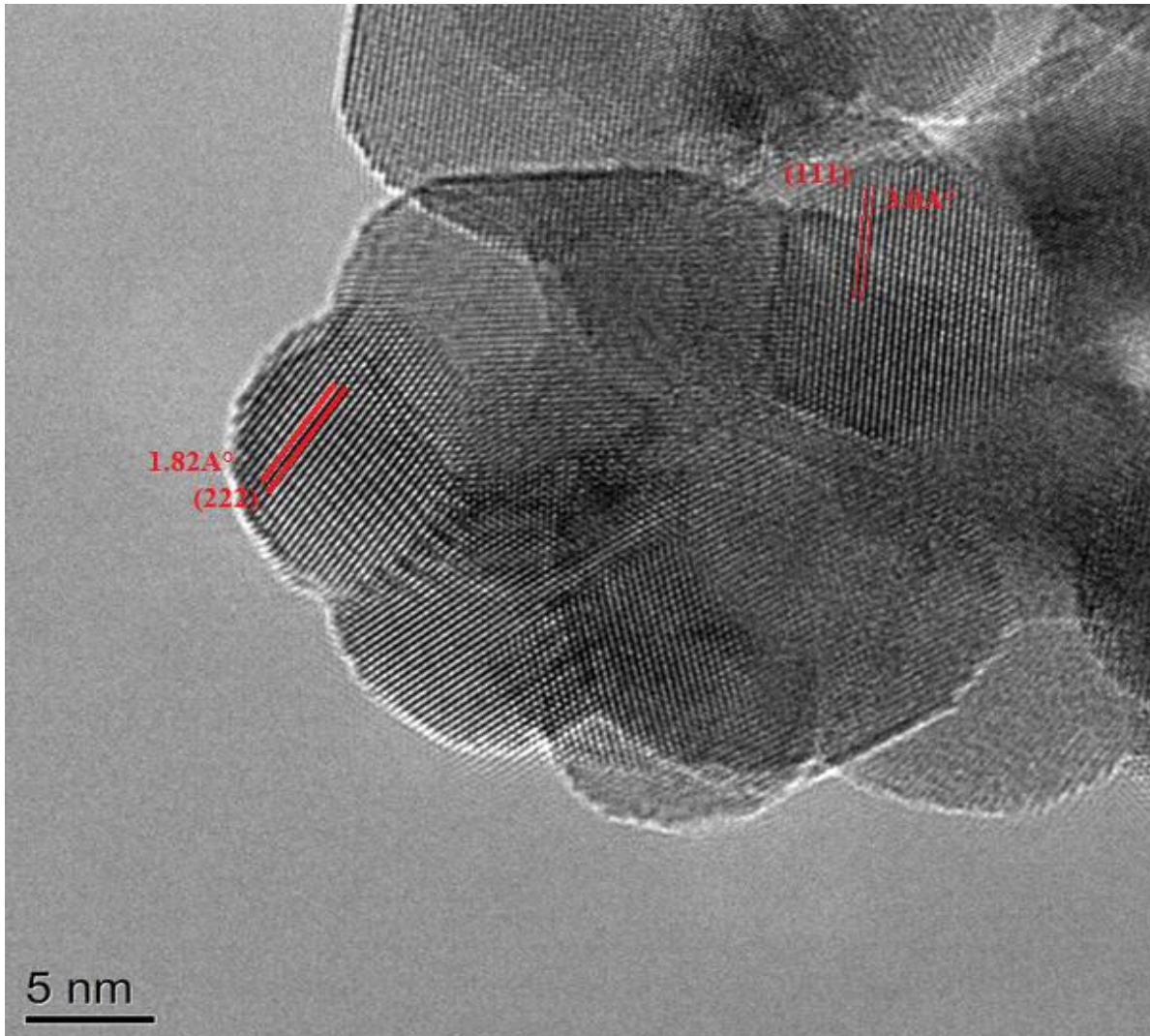
Fig. 4.32: HR-TEM image of $Ho_2Zr_2O_7$ nanopowder with defect fluorite structure and interplanar spacing of 3.0 A˚ and 1.82 A˚ along the (111) and (222) planes respectively.

4.2.2. Thermoresponsive Behaviour of Sintered Pellets

Pellets of holmium zirconate were sintered and analysed using XRD. Fig. 4.33 shows the XRD scans of $Ho_2Zr_2O_7$ nanopowder and pellets sintered over the temperature range 1100-1500 °C.

XRD scans of nanopowder of holmium zirconate and the pellets sintered at 1100-1500 °C showed the cubic defect-fluorite structure and peaks are indexed accordingly. At 1300 °C pellet of this material has shown the minor superstructural reflection of pyrochlore. The defect fluorite structure was completely recovered when pellet of $Ho_2Zr_2O_7$ was sintered at 1400 °C. Here the material got the cubic fluorite structure which is in agreement with the previous finding around this temperature [163] and continue till 1500 °C.

Effect of temperature on crystallite size and crystallographic data of holmium zirconate is shown in Table 4.11. Continuous increase in the crystallite size from 8 nm to 97 nm was observed with the rise in temperature as shown in Fig. 4.34. Intensity of XRD peaks is enhanced with increase in structural disorder due to rise in temperature [106]. Increasing the crystallite size and corresponding decrease of microstrain with temperature (Fig. 4.34) result in sharpness of XRD peaks. The intensification of diffraction peaks and increase in crystallite size may be due to internal strains resulting from thermal energy provided and forms the larger grains at higher temperature [170]. For the pellets with fluorite structure the unit cell parameters are increasing until 1300 °C as there appears some superstructure reflection of pyrochlore structure which later on recovers at 1400 °C and 1500 °C as shown in Fig. 4.35. These results confirm the stable fluorite structure of $Ho_2Zr_2O_7$ over the entire temperature range which is also in agreement with the cationic radius ratio, $r_{Ho}/r_{Zr} = 1.41$.
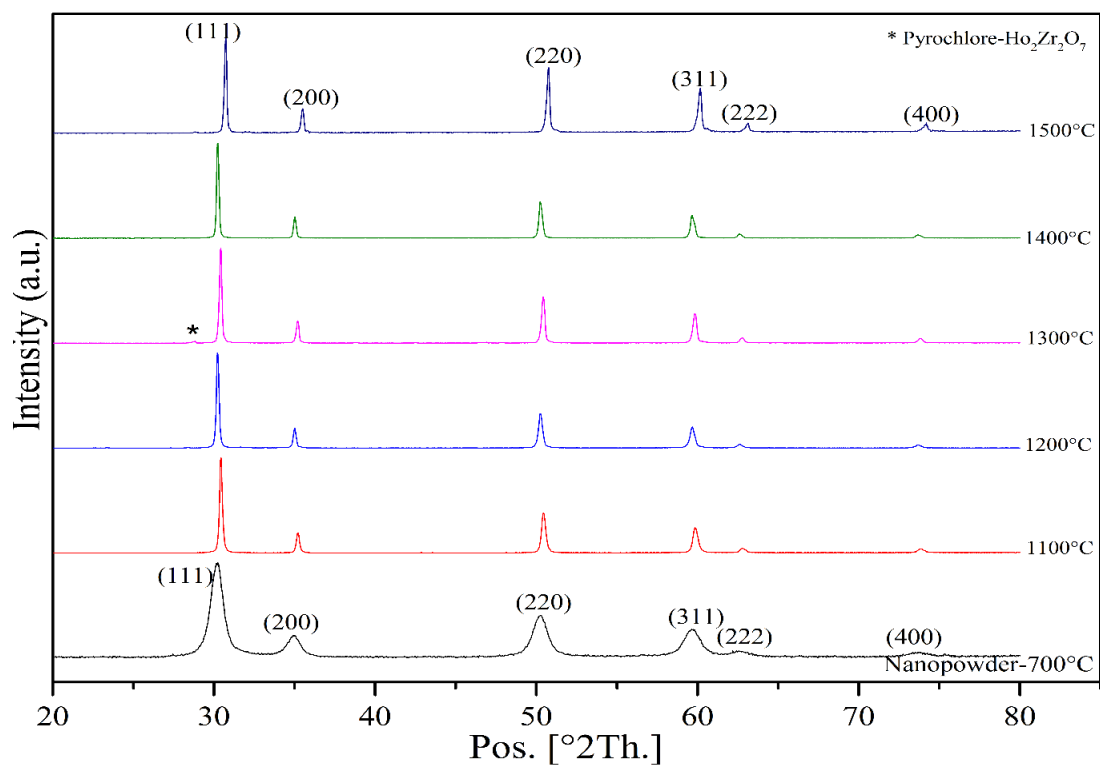
Fig. 4.33: XRD patterns of sintered holmium zirconate pellets. The patterns from 700-1500°C are indexed by ICDD, 01-080-7723 with defect fluorite cubic $Ho_2Zr_2O_7$ shown at the top of the peaks. Asterisk at 1300°C is pyrochlore reflection of $Ho_2Zr_2O_7$.
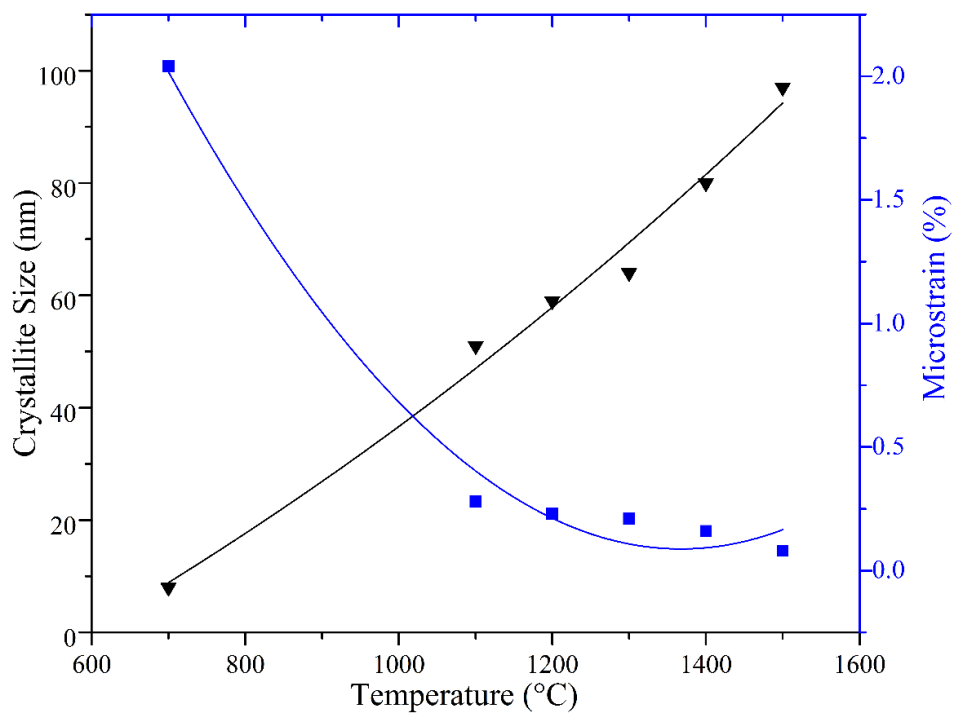
Fig. 4.34: Effect of temperature on crystallite size and microstrain of holmium zirconate nanopowder (700°C) and sintered pellets (1100-1500°C)
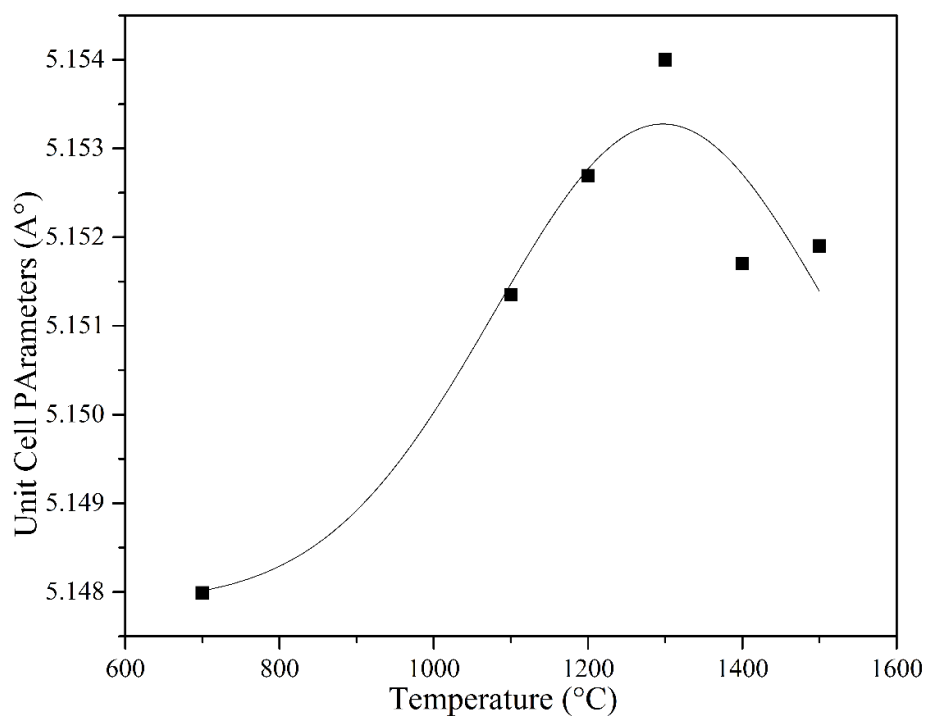
Fig. 4.35: Change in unit cell parameters with rise in temperature

Table 4.11: Effect of temperature on crystallographic data and structural refinement parameters of holmium zirconate pellets

Temperature, °C	700-Nanopowder	1100	1200	1300	1400	1500
Phase	Cubic Fluorite	Cubic Fluorite	Cubic Fluorite	Cubic Fluorite	Cubic Fluorite	Cubic Fluorite
Space group	$Fm\bar{3}m$	$Fm\bar{3}m$	$Fm\bar{3}m$	$Fm\bar{3}m$	$Fm\bar{3}m$	$Fm\bar{3}m$
Lattice constant, A° a=b=c	5.148	5.151	5.153	5.154	5.1517	5.152

R_p, %	4.64	12.28	10.87	27.74	11.19	19.50
R_{wp}, %	6.97	16.40	15.50	33.97	16.20	24.28
R_{exp}, %	3.03	4.62	3.52	7.94	3.64	8.16
x^2	5.27	12.62	19.30	18.28	19.78	8.84
Crystallite Size, nm	8	51	59	64	80	97
Micro Strain, %	2.04	0.28	0.23	0.21	0.16	0.08

Raman spectra of holmium zirconate nanopowder and pellets sintered from 1100-1500 °C are shown in Fig. 4.36. Inset of Fig. 4.36 shows the photoluminescence spectra of holmium zirconate at all temperatures using blue light with wavelength of 473 nm. Encircled in inset is the Raman spectra of the material. When the holmium zirconate pellets were sintered at 1100-1500 °C Raman bands started broadening as compared to the nanopowder at 700 °C [161]. Band observed around 350-500 cm^{-1} which indicates the fluorite structure [163]. A very minor change in the Raman bands was observed from 550-700 cm^{-1} at temperature 1300 °C which is due to the superstructure reflection of pyrochlore holmium zirconate and agrees well with the XRD data. Spectra of holmium zirconate observed at 1400 °C and 1500 °C is almost same and restored to the cubic fluorite structure without any pyrochlore reflections. In pyrochlore oxides broadening of Raman bands results in an increase in disorder [72], which has observed in the Raman spectra of holmium zirconate over the entire temperature range 1100-1500 °C. Results obtained from XRD scans and Raman spectra are in excellent agreement with each other and shows that holmium zirconate persists cubic fluorite structure at higher temperatures.

Phase diagram of Ho_2O_3 and ZrO_2 found in literature covers the temperature above 1700 °C. Ionic radii of holmium and zirconium are 1.015 A° and 0.72 A°, respectively [156]. The cationic radius ratio is $r_{Ho}/r_{Zr} = 1.41$ which lies in the region of cubic pyrochlore formed by order-disorder transformation [96].
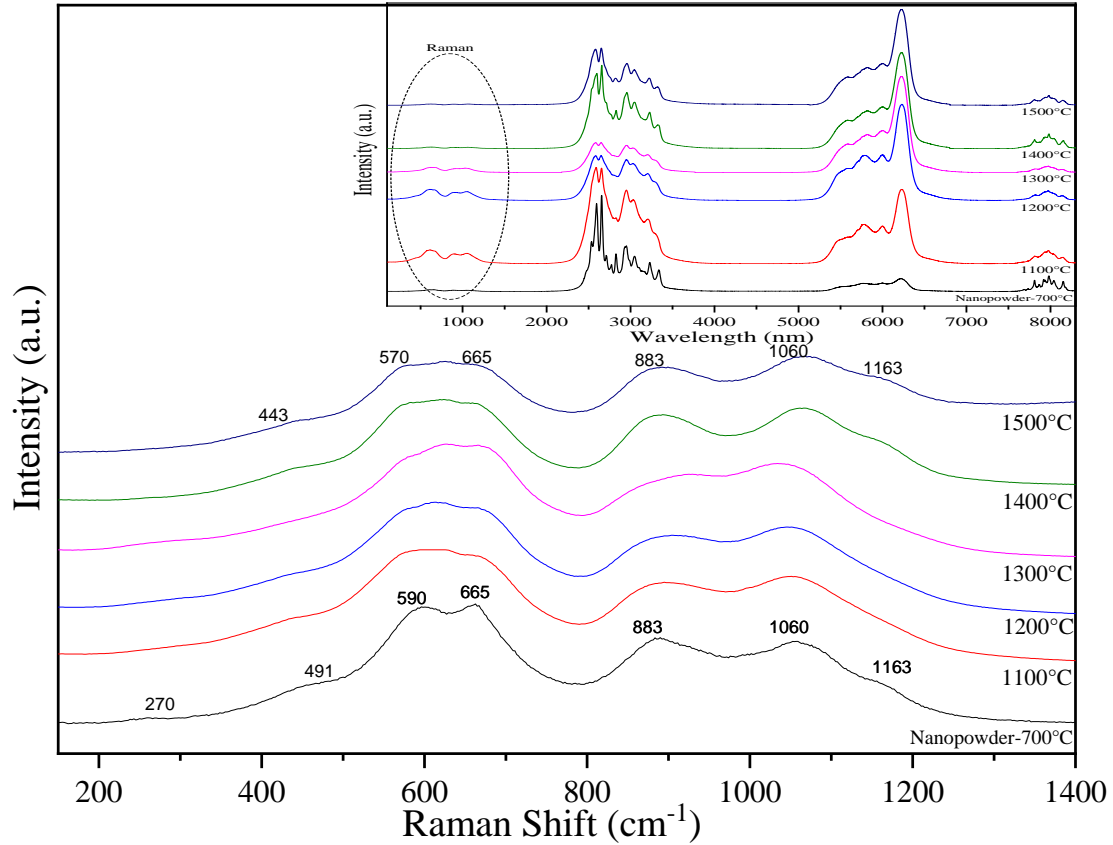
Fig. 4.36: Raman Spectra of $Ho_2Zr_2O_7$ nanopowder and pellets sintered from 1100-1500°C. Inset shows the photoluminescence spectra of holmium zirconate at all temperatures.

4.2.3. Densification of Sintered Pellets with Single Step Sintering (SSS) and Two Step Sintering (TSS)

Microstructural and ionic conductivities properties of $Ho_2Zr_2O_7$ sintered using SSS and TSS processes have already reported [160].

4.2.3.1. Density and Microstructure

Pellets of holmium zirconate ($Ho_2Zr_2O_7$) were sintered using single step sintering (SSS) and two step sintering (TSS) processes. The variation of percentage relative density and percentage residual porosity of the sintered pellets as a function of sintering temperature using SSS and TSS is shown in Fig. 4.37. It can be clearly seen in Fig. 4.37 that the relative density of $Ho_2Zr_2O_7$ pellets sintered using SSS process is increasing systematically and correspondingly the porosity is decreasing with increase in sintering temperature. The relative density of samples sintered at 1500 °C using SSS process was found to be 92 ($\pm$0.4) % and corresponding porosity decrease to 8 ($\pm$0.6) %.

In a TSS process, the sample is first heated to a temperature corresponding to highest relative density as obtained by the SSS process to attain an intermediate density and then held at lower temperature corresponding to 75 % of the theoretical density for a prolonged duration [116]. In this investigation samples are heated in the first step to 1500 °C for 5 min to achieve the intermediate density and in the subsequent step the samples are held at 1300 °C, corresponding to greater than 75 % theoretical density for 96 h to achieve maximum density. It can be seen in Fig. 4.37 that the samples held for 72 h in the second step were only 83 % dense. It should be noted that for the second step of TSS process the temperature chosen is 1300 °C as the relative density achieved at this temperature during SSS process is greater than 75 % and as mentioned in literatures [116, 171] the intermediate densities greater than 75 % are adequate for second step of sintering, at which the pores in the sample became subcritical and unstable against shrinkage. Hence, as seen in Fig. 4.37 the relative density achieved in this study is 98 ($\pm$0.3) % for $Ho_2Zr_2O_7$.
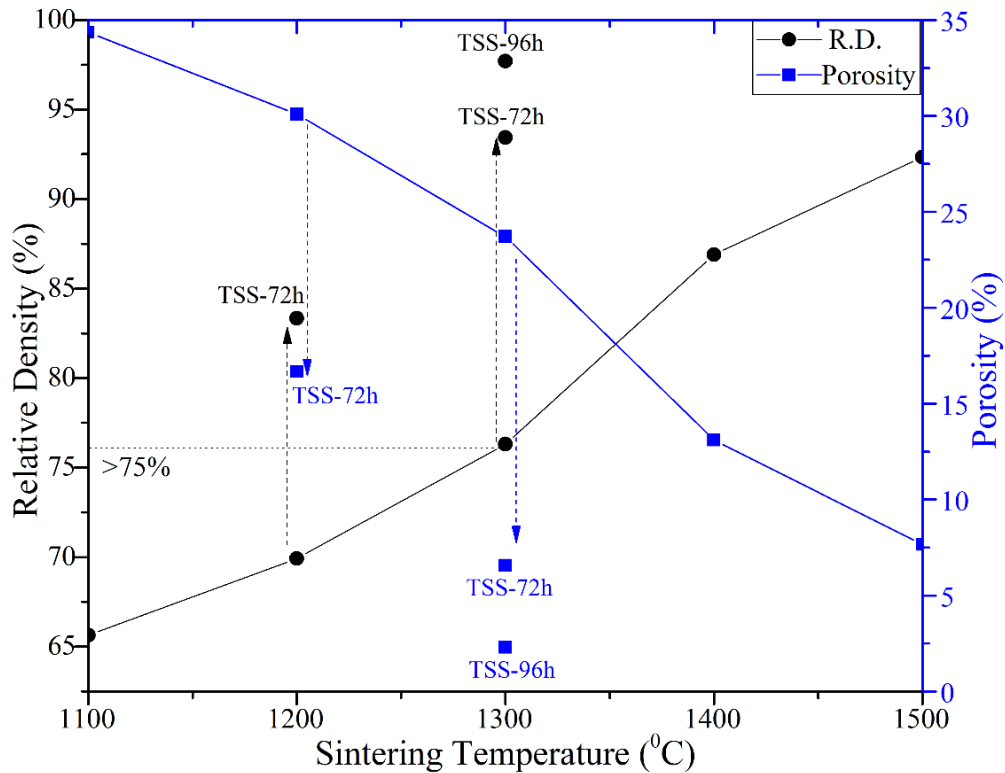
Fig. 4.37: Effect of sintering temperature on the relative density and porosity of holmium zirconate pellets. Two step sintering (TSS): (I) - 1500°C for 5min, (II) -1 300°C for 96h.

The variation of grain size of thermally etched pellet samples of $Ho_2Zr_2O_7$ as a function of the relative density of the samples sintered using SSS and TSS process respectively is shown in Fig. 4.38. The grain size was calculated from the SEM micrographs of the thermally etched polished sample using ImageJ. It can be seen in Fig. 4.38 that with the increase in relative density there is increase in grain size for samples sintered from 1100 °C to 1500 °C using the SSS process. Furthermore, Fig. 4.38 shows that as the sintering temperature approaches 1300 °C the relative density and grain size increases sharply suggesting that this is the critical temperature for the sudden enhancement in mass transfer rate in $Ho_2Zr_2O_7$ which leads to enhanced grain growth. However, interestingly for samples sintered using the TSS process at 1300 °C, the grain size remains almost unchanged at about 1.29 (±0.1) μm whereas the relative density reaches a maximum of 98 %, nearly 6 % greater than the samples sintered using SSS

132

at 1500 °C. The variation in density of $Ho_2Zr_2O_7$ samples sintered using SSS and TSS process is in good agreement with the microstructure of samples shown in Fig. 4.39. Hence, the TSS process is a better approach to achieve greater densification of nanopowder ceramic samples and supressing the grain growth as second sintering step proceeds with a frozen microstructure and has slower diffusion kinetics that is sufficient to achieve maximum density [116]. Micrographs from (a) to (e) in Fig. 4.39 represent those of the samples sintered using SSS process and (f) is for the one using TSS process. Thermal etching of all the polished pellets helped to reveal the clear grain boundary in SEM micrographs. Smaller grain size of oxide with higher density is likely to enhance the fracture toughness and improve the tolerance limit of solid electrolytes again thermal shock in SOFC [171]. Similar results were obtained in our earlier investigation of cerium gadolinium oxide (CGO) [172].
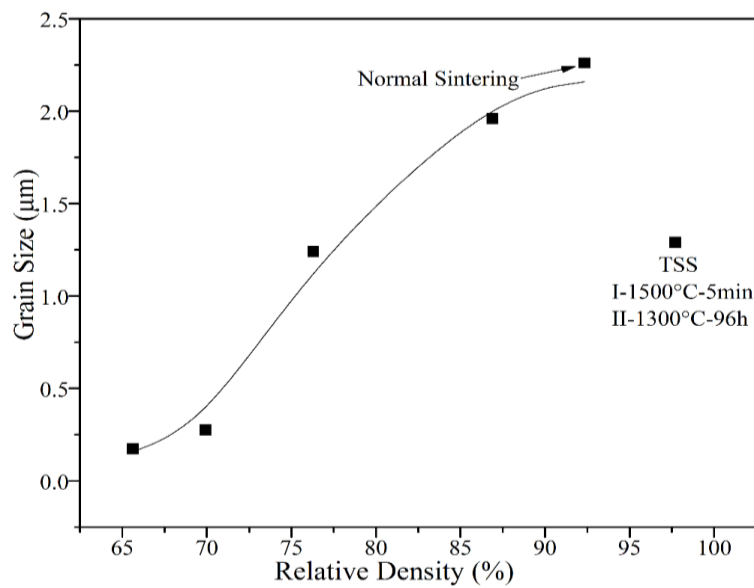
Fig. 4.38: Variation of grain size and relative density as a function of sintering temperature of Ho₂Zr₂O₇ pellet samples
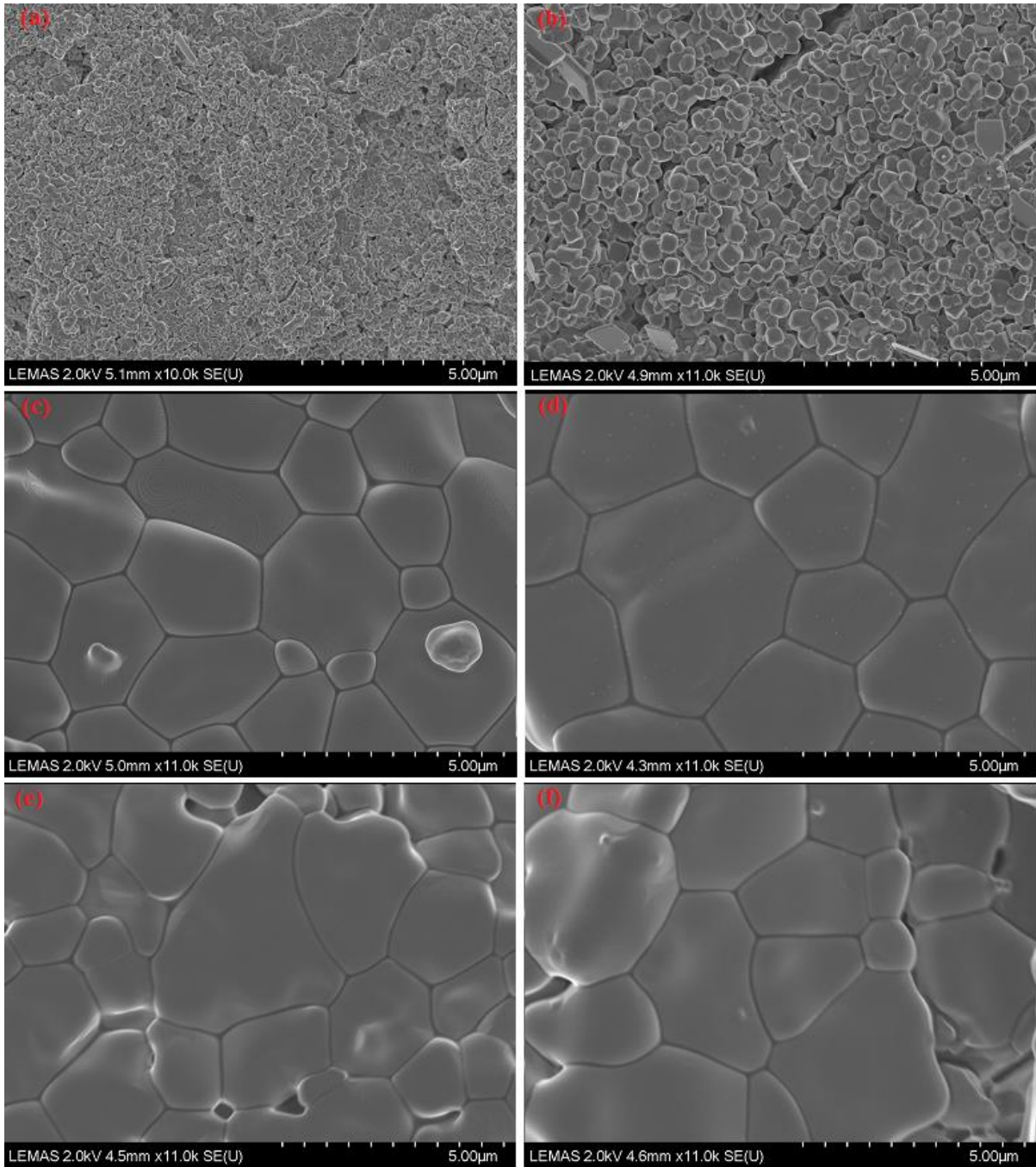
Fig. 4.39: SEM micrographs of sintered Ho$_2$Zr$_2$O$_7$ pellets. From (a) to (e) are the micrographs of the pellets after single step sintering (SSS) for 2h at (a) 1100°C (b) 1200°C (c) 1300°C (d) 1400°C (e) 1500°C and (f) after two step sintering (TSS): (I) - 1500°C for 5min, (II) - 1300°C for 96h.

4.2.4. AC Impedance Spectroscopy

The Nyquist plots of $Ho_2Zr_2O_7$ sintered at 1500 °C for 2 h using SSS process measured at 350 °C and 550 °C are shown in Fig. 4.40 for both heating and cooling cycles. At 350 °C only a single semicircle response was recorded which corresponds to the bulk contribution as shown in Fig. 4.40 (a) suggesting that grain boundary contribution is negligible. On the contrary two semicircles in the complex impedance plane were recorded at 550 °C as shown in Fig. 4.40 (b) that correspond to the bulk contribution at higher frequency and grain boundary effects at lower frequency. The radius of semicircles decreases with the increase in temperature indicating the presence of thermally activated bulk conduction process [173]. The results of heating and cooling cycles have been found to be almost identical throughout the temperature range of measurement from 350 °C – 750 °C akin to those shown in Fig. 4.40 (a and b) at 350 °C and 550 °C. This indicates that the $Ho_2Zr_2O_7$ solid electrolyte respond reversibly in the temperature range of measurement, which is an important behaviour of solid electrolytes as they are subject to temperature variation when used in an electrochemical device [159].
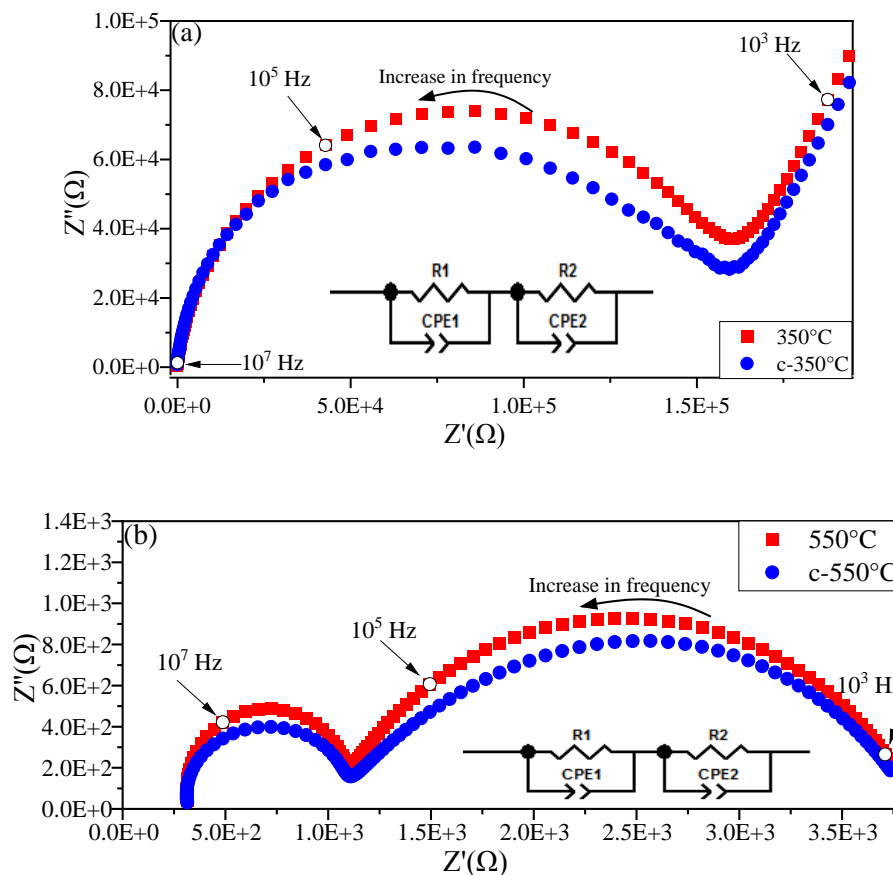
Fig. 4.40: Complex impedance plots for Ho$_2$Zr$_2$O$_7$ sintered at 1500°C for 2h measured in heating cycle at (a) 350°C and (b) 550°C, (c-350°C and c-550°C for cooling cycle).

The temperature dependence of the electrical conductivity (σT) was analysed using an Arrhenius expression mentioned in equation 4.4.

The value of activation energy for ionic conduction in Ho$_2$Zr$_2$O$_7$ has obtained by plotting *lnσT* against *1/T* as shown in Fig. 4.41 for bulk and grain boundary of single step sintered Ho$_2$Zr$_2$O$_7$ pellet measured over the range of 350°C - 750°C and frequency range of 100 mH to 100 MHz for both heating and cooling cycles.

The ionic conductivity of Ho$_2$Zr$_2$O$_7$ has been found to increase with increase in temperature following the Arrhenius behaviour thereby confirming that ionic diffusion in the material is thermally activated. The average value of activation energies for bulk ionic conduction has been found to be 0.99 ($\pm$0.01)eV by combining data for both heating and cooling cycles. These values are comparable with activation energy of ionic conductivity of CGO pellets prepared by SSS [172] process. The magnitude of activation energy for ionic conduction of Ho$_2$Zr$_2$O$_7$ has been found to be better than that for the conventional solid electrolytes Yttria Stabilized Zirconia-YSZ (1.01 eV) and comparable with Gadolinium Doped Ceria (GDC) (0.9 eV) [174].

Fig. 4.41 also shows the Arrhenius plot of grain boundary conductivity for both heating and cooling cycles. The effect of grain boundary started appearing at temperature greater than 527 °C. The combined average value of activation energy for grain boundary conductivity for both heating and cooling cycles has been found to be 1.54($\pm$0.02)eV. The grain boundary conductivity in samples prepared by SSS process has been 1.3×10^{-2} S.cm^{-1} order of magnitude lower than that of bulk over the entire temperature range reflecting the defective nature of grain boundary compared with the bulk of grains.
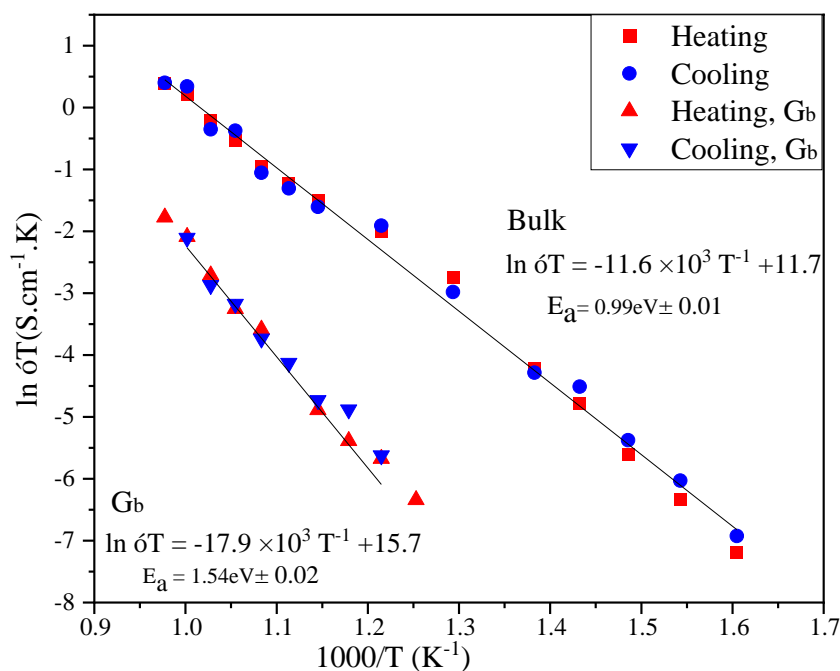
Fig. 4.41: Temperature dependence Arrhenius plots of bulk and grain boundary conductivity in heating and cooling cycles of holmium zirconate pellets sintered at 1500°C for 2h using SSS process.

Figs. 4.42 (a) & (b) illustrate the frequency dependence of the real components of conductivity for SSS $Ho_2Zr_2O_7$ material (log-log representation) for both heating and cooling cycles. Bulk and grain boundary contribution for conductivity and their dependence on frequency are shown in Fig. 4.42. Another important characteristic feature of ion conducting solids is blocking effect which is also evident in this type of log-log representation. At lower temperature there is decrease in conductivity at lower frequencies. In Fig. 4.42 (a) there are three regions; lower frequency, plateau and higher frequency. Plateau is showing dispersion and separating the two frequency regions. The plateau developing at lower frequency above 350 °C is due to the grain boundary contribution to the conductivity whereas at higher frequencies is because of bulk contribution. The frequency dispersive region separating low frequency and high frequency plateaus shifts towards higher frequencies with increase in temperature and leads above 700

137

°C to a regime where conductivity is almost frequency independent as shown in Figs. 4.42 (a) & (b). The regimes are consistent with heating and cooling cycles.

Bode plots explicitly shows frequency information so the behaviour at lower frequency suggests the transport process of ions
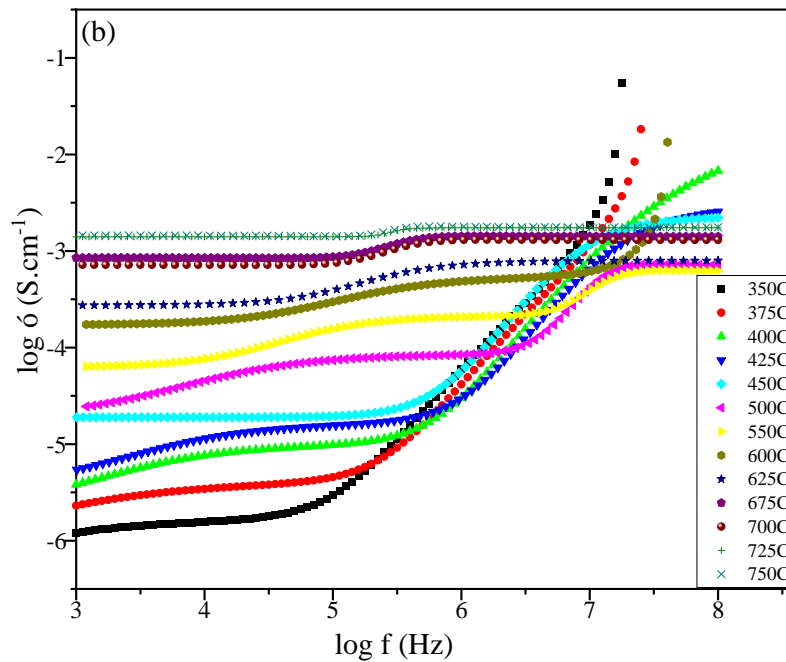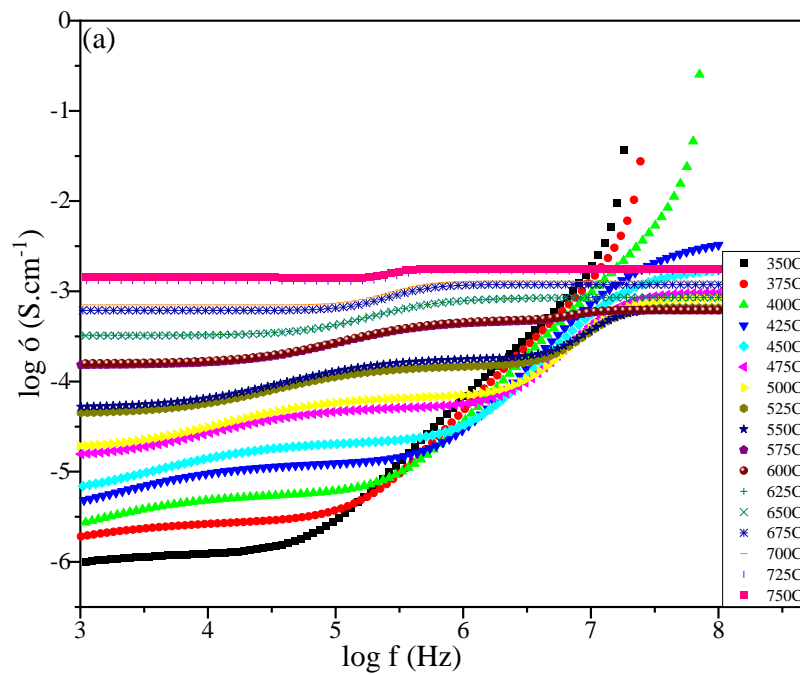
Fig. 4.42: Frequency and temperature dependence of the real parts of Ho$_2$Zr$_2$O$_7$ conductivity (a) heating (b) cooling

Fig. 4.43 shows the results of the impedance spectroscopy measurements at 350 °C and 550 °C of holmium zirconate pellets sintered using the two step sintering (TSS) process. Unlike in the samples prepared using SSS process complex impedance of bulk Ho$_2$Zr$_2$O$_7$ measured at 350 °C and 550 °C for both heating and cooling cycles shown in Fig. 4.43 (a and b) is in good agreement with each other whereas that for the grain boundary component is in reasonable agreement. At 350 °C the conductivity of the sample is entirely due to the bulk contribution and there is no sign of grain boundary contribution as shown in Fig. 4.43 (a). With the increase in temperature there appears two semicircles which suggests that there is a significant contribution of bulk and grain boundary towards the conductivity as shown in Fig. 4.43 (b).
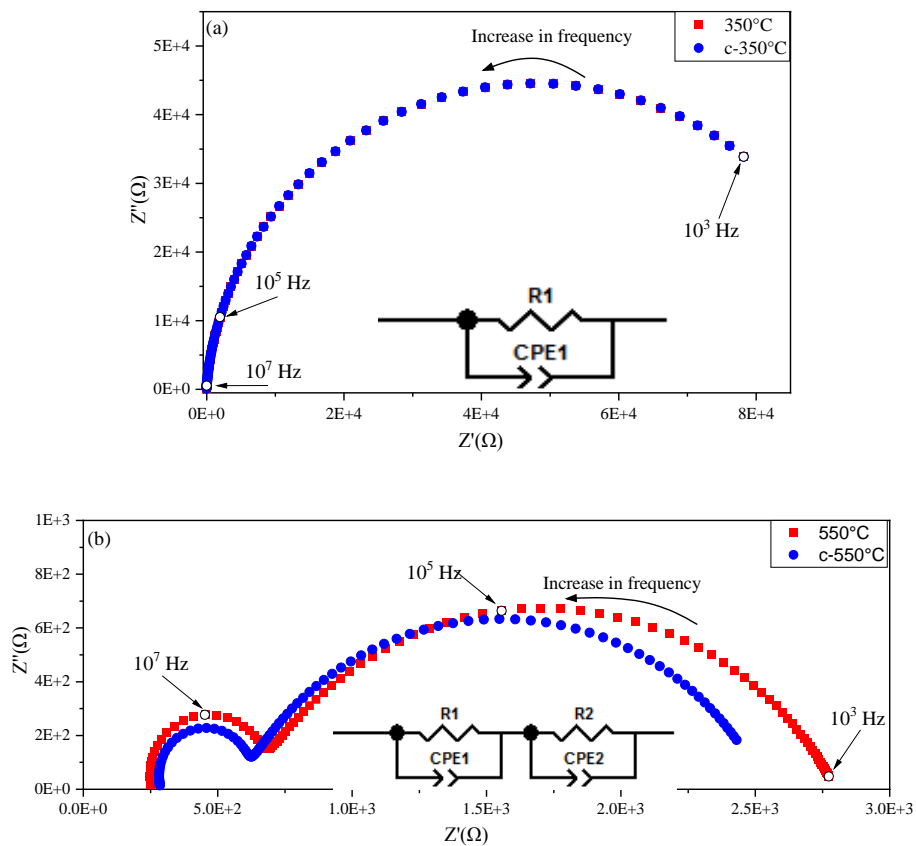
Fig. 4.43: Complex impedance plots for Ho₂Zr₂O₇ with two step sintering; (I) - 1500°C for 5min, (II) - 1300°C for 96h measured in heating cycle at (a) 350°C and (b) 550°C, (c-350°C and c-550°C for cooling cycle).

Temperature dependence of bulk and grain boundary conductivity of Ho₂Zr₂O₇ pellets sintered using TSS process in both heating and cooling cycles, calculated from the data of impedance measurement are shown in Fig. 4.44 as Arrhenius plots. The average values of activation energies for bulk and grain boundary conductivity are 0.99 (±0.009)eV and 1.40 (±0.004)eV obtained from the heating and cooling cycles, respectively.
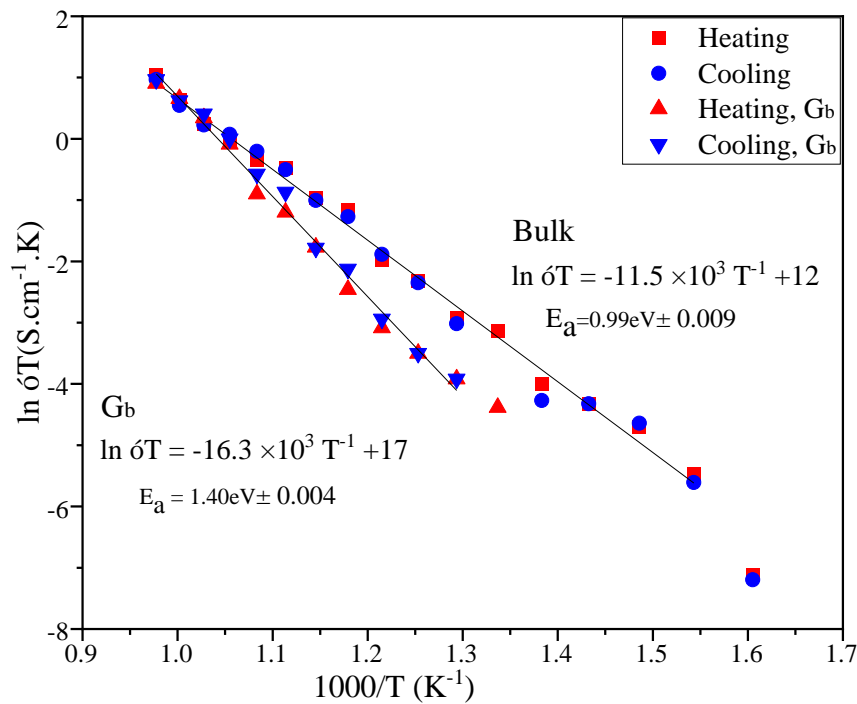
Fig. 4.44: Temperature dependence Arrhenius plots of bulk and grain boundary (Gb) conductivity for both heating and cooling cycles of holmium zirconate prepared using TSS process.

Frequency dependence of the real components of conductivity for TSS Ho₂Zr₂O₇ are shown in Fig. 4.45 (a) & (b) for both heating and cooling cycles, respectively. Bulk and grain boundary contribution and their dependence on frequency in the form of log-log representation are shown

in Fig. 4.45. Three regions are observed in the frequency dependent conductivity plots are: lower frequency dispersive region, plateau and higher frequency dispersive region. At lower frequency region there is decrease in conductivity at low temperatures. The plateau developing at lower temperatures $\leq$ 450 °C at lower frequency regions are due to grain boundary contribution and at higher frequency regions is mainly bulk contribution. With the increase in temperature this plateau is shifting to the higher frequency region and develops a regime above 700 °C where conductivity is almost frequency independent as shown in Figs. 4.45 (a) & (b). The results for both heating and cooling cycles are well consistent throughout the temperature range of 350-750 °C.

The results of frequency dependence conductivity obtained from TSS $Ho_2Zr_2O_7$ are showing similar trends for SSS $Ho_2Zr_2O_7$.
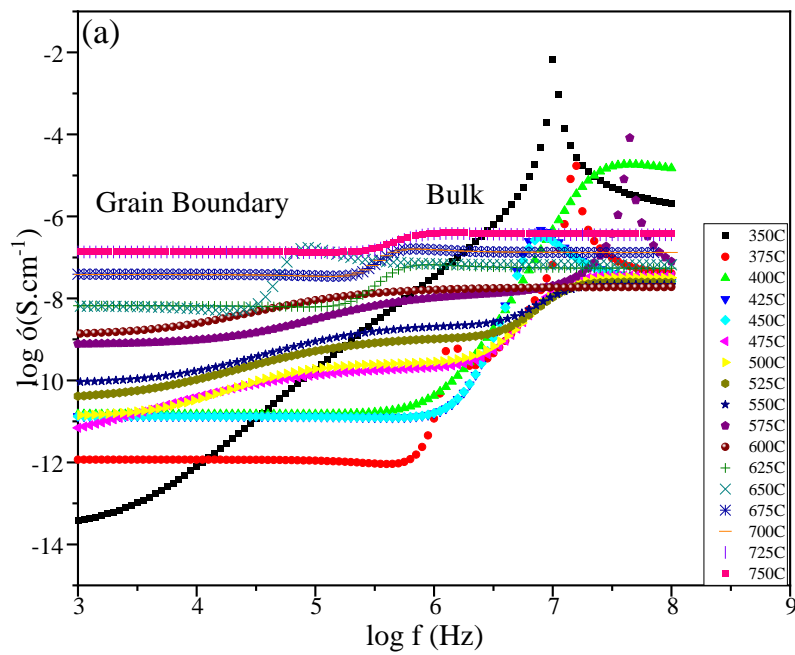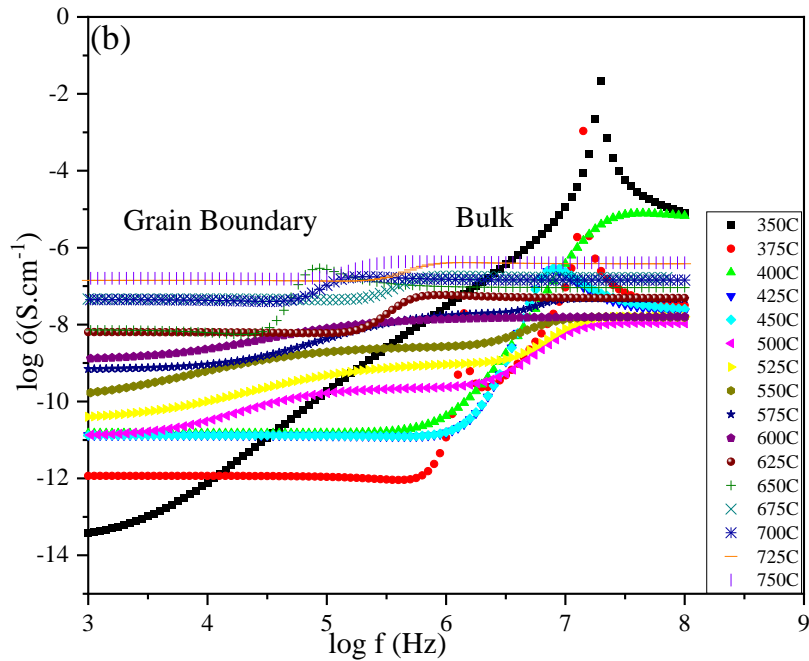
Fig. 4.45: Frequency and temperature dependence of the real parts of Ho₂Zr₂O₇ conductivity (a) heating (b) cooling

The values of bulk conductivity of $Ho_2Zr_2O_7$ samples sintered using TSS process 2.67×10^{-3} S.cm⁻¹ has been found to be greater than $Ho_2Zr_2O_7$ prepared using SSS process 1.46×10^{-3} S.cm⁻¹ at 750 °C as shown in Table 4.12. Similar comparison with grain boundary conductivity revealed that the grain boundary conductivity of samples sintered by TSS process is greater than that of SSS process sample by nearly 3 order of magnitude. This is clearly seen in Fig. 4.46 (a & b), respectively. This clearly suggests that the samples of $Ho_2Zr_2O_7$ prepared by TSS process has significantly fewer grain boundary defects compared to those processed by SSS process. Clearly, TSS process is capable of producing nearly perfect sample for further applications in solid state devices. Similar results were reported in our study of CGO [172].
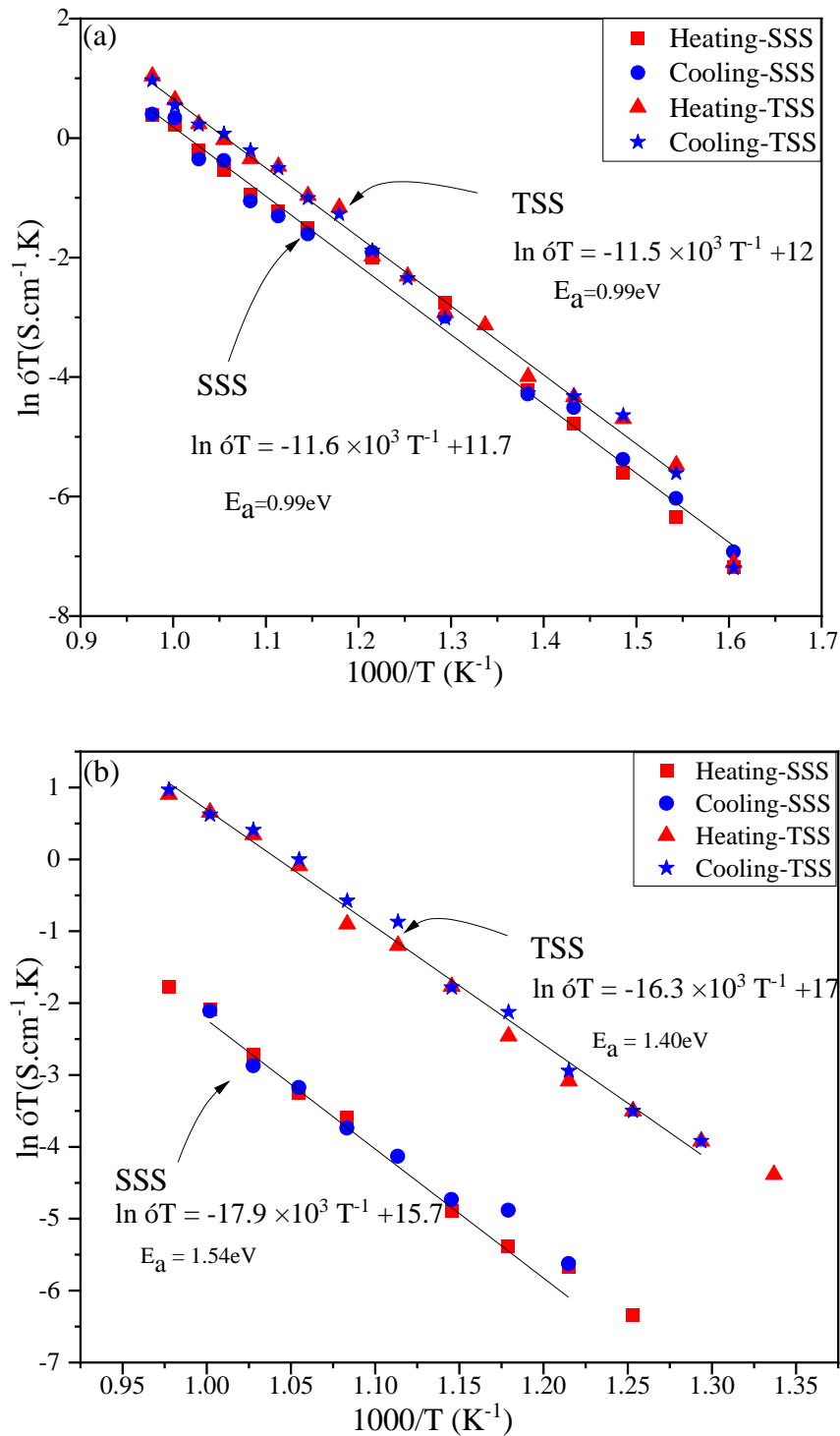
Fig. 4.46: Comparison of temperature dependence Arrhenius plots of (a) bulk and (b) grain boundary (Gb) conductivity for both heating and cooling cycles of holmium zirconate prepared using SSS and TSS processes.

Table 4.12: Corresponding activation energies and conductivity values of SSS and TSS processed Ho$_2$Zr$_2$O$_7$

Sample	Activation Energy (eV)	R^2 value	Conductivity at 550°C S.cm^{-1}	Conductivity at 750°C S.cm^{-1}
SSS-Bulk	0.99	0.99448	1.94×10^{-4}	1.46×10^{-3}
SSS-Gb	1.54	0.98864	4.28×10^{-6}	1.66×10^{-4}
TSS-Bulk	0.99	0.99048	1.76×10^{-4}	2.67×10^{-3}
TSS-Gb	1.40	0.99433	5.99×10^{-5}	2.50×10^{-3}

Fig. 4.47 compares the conductivities of fluorite structured holmium hafnate and holmium zirconate with the established electrolytes; YSZ and GDC [174].
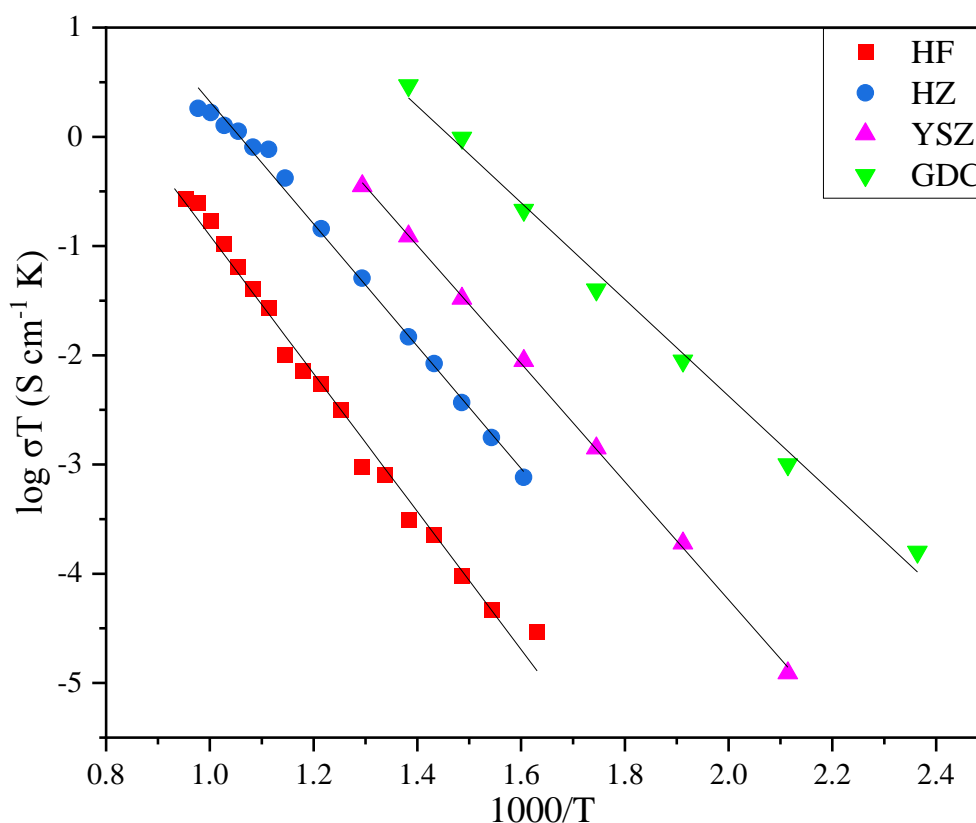
Fig. 4.47: Comparison of temperature dependence Arrhenius plots of holmium hafnate (HH), holmium zirconate (HZ), yttria stabilized zirconia (YSZ) and gadolinium doped ceria (GDC).

4.3. Lanthanum Hafnate (La$_2$Hf$_2$O$_7$)

4.3.1. Thermal and Structural Characterisation

Firstly, the thermal analysis was performed on the dried metal alginate beads to understand the thermal behaviour to find the calcination temperature to gain the nanopowders of lanthanum hafnate (La$_2$Hf$_2$O$_7$). Simultaneous TGA /DSC analysis of dried metal alginate beads in flowing air is shown in Fig. 4.48. At the start of the experiment an endothermic hook was observed in the DSC curve from room temperature (RT) to 95 °C which is due to the difference in the heat capacity of the sample and the reference pan [175]. DTG is the first derivative of TGA curve. Six endothermic peaks were observed in the DTG curve along with an obvious weight loss within the corresponding temperature range in the TGA curve. Six steps in TGA curve were observed according to the endothermic peaks in DTG curve. In first step, from RT to 140 °C the weight loss of 16 % was observed with an exothermic peak from 95 °C to 140 °C in DSC curve which can be due to the removal of any bonded water present in the beads. Weight loss of 6.5 % and 9 % were recorded in second (140 °C to 190 °C) and third (310 °C to 440 °C) steps, respectively, with a joint exothermic and endothermic peaks in the DSC curve from 150 °C to 193 °C. Evolving of oxygen due to the disassociation of the weaker linkage (G-G, G-M, M-M) of alginate structure [161] is the main cause of weight loss in second and third steps. A minor weight loss of 1.4 % was also observed from 440 °C to 470 °C as a minor endothermic kink in the DTG curve was noticed which can be due to the starting of decomposition of alginate structure. A major weight loss of 8 % was observed in the TGA curve from 475 °C to 580 °C which is purely attributed to the major oxidative decomposition of organic matrix in alginate and the corresponding exothermic peaks from 440 °C to 590 °C in the DSC curve shows the formation of binary oxides (La$_2$O$_3$ and HfO$_2$) after the decomposition. In the last step of TGA/DTG curves, a weight loss of 1.7 % was observed from 815 °C to 900 °C with a corresponding exothermic bend from 830 °C to 870 °C in the DSC curve which is due to the

combining of binary oxides into the ternary oxide ($La_2Hf_2O_7$) and removal of any excess oxygen present in the structure. Keeping in view the completion of major oxidation of beads and crystallizing into nanopowders below 650 °C, a temperature of 700 °C was determined for calcination.
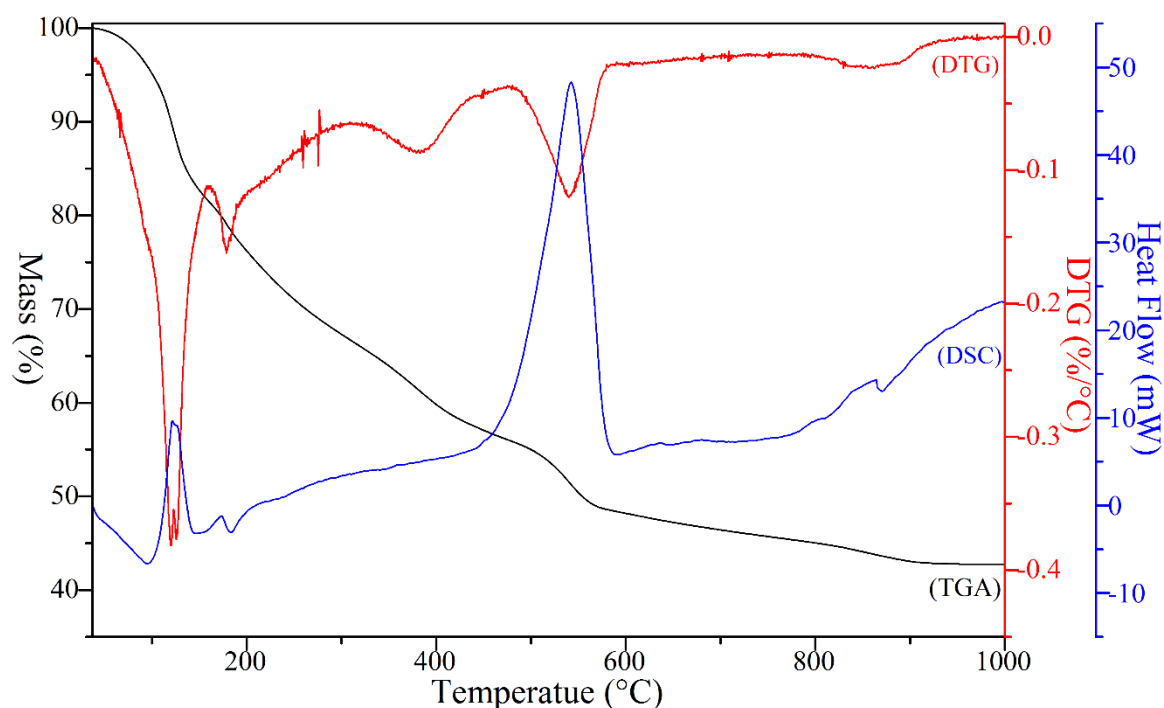
Fig. 4.48: TGA/DSC/DTG analysis of dry metal alginate beads

Results of HTXRD pattern of oven dried beads of metal alginate from room temperature to 1000 °C are shown in Fig. 4.49. A minor bend was observed at 400 °C close to the point where diffraction peak of crystalline $La_2Hf_2O_7$. No diffraction peaks were observed from room temperature to below 400 °C. Below 700 °C thermal decomposition of beads was completed according to Fig. 4.48 so some of the peaks of crystalline $La_2Hf_2O_7$ were observed at 700 °C. Peaks observed at 700 °C are at the positions characterised for fluorite structure but with the increase in temperature the peaks are moving towards the left of horizontal axis as clearly seen along the dotted line in Fig. 4.49. The major peak has significantly moved to the left from 700 °C to 1000 °C. High purity single phase lanthanum hafnate peaks were observed at 900 °C which is in excellent agreement with the results obtained from the TGA/DSC in Fig. 4.48.

146

Sharpness of $La_2Hf_2O_7$ diffraction peaks increased with the increase in temperature from 900 °C to 1000 °C owing to crystal growth [125]. Thermal behaviour of metal alginate beads studied using TGA/DSC/DTG and HTXRD are in good agreement with respect to the thermal decomposition of metal alginate beads and formation of crystalline nanopowders of $La_2Hf_2O_7$. Fig. 4.48 and Fig. 4.49 show the complete thermal decomposition of metal alginate beads is below 700 °C. It can be concluded from the thermal analysis that the enthalpy change for the decomposition of metal alginate (La^{3+}/Hf^{4+} -ALG) into $La_2Hf_2O_7$, $CO_{2\ (g)}$ and $H_2O_{\ (g)}$ is -2231 J/g ($\pm$10%) based on the Hess's law of heat summation which suggest that overall decomposition process is exothermic in nature.
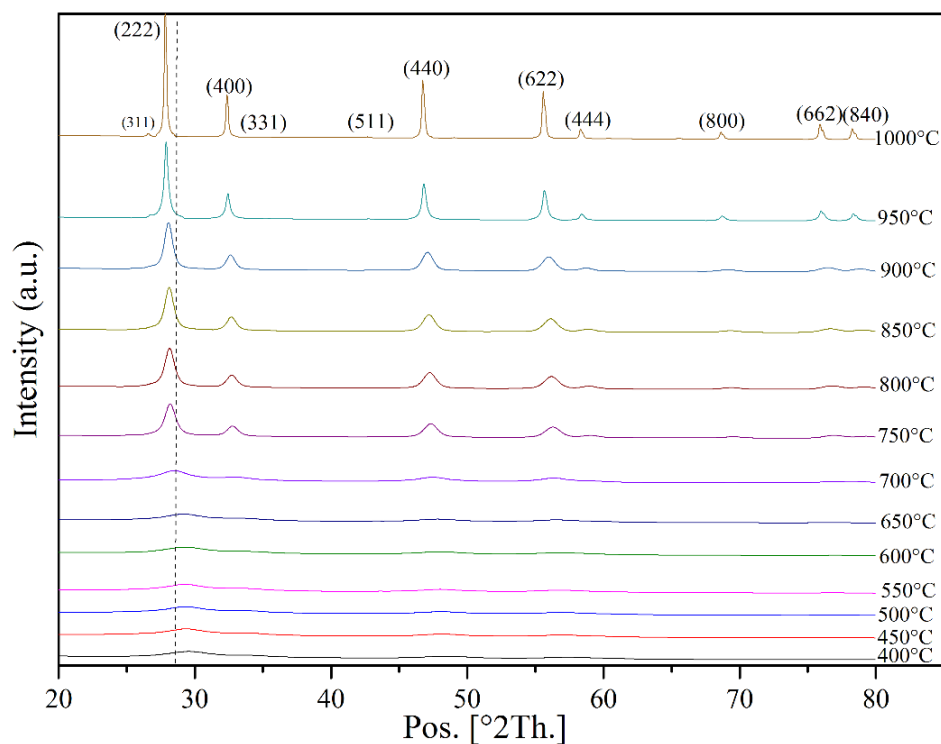
Fig. 4.49: HT-XRD patterns of metal alginate beads from 400-1000°C. The patterns are indexed by ICDD, 01-078-5592 with miller indices of crystal planes of cubic $La_2Hf_2O_7$ shown at the top of the peaks.

XRD patterns of the nanopowders obtained after calcining for 6 h at 700 °C and 900 °C are shown in Fig. 4.50. At first, dried metal alginate beads were calcined at 700 °C for 6 h to

147

obtain the nanopowders at comparatively low temperature as the thermal decomposition has completed below this point in Fig. 4.48 and Fig. 4.49. Another reason of choosing 700 °C as calcination temperature, is successfully obtaining the nanopowders of $Ho_2Hf_2O_7$ [124] and $Ho_2Zr_2O_7$ [161] at this temperature synthesised through similar route. XRD pattern of the nanopowders obtained after calcining the beads at 700 °C is showing the split peaks and presence of some extra peaks. Some of the peaks are not at the positions characterised for the powdered $La_2Hf_2O_7$ [176]. This pattern shows the complete decomposition of metal alginate beads but not the complete formation of $La_2Hf_2O_7$ nanopowders. Later, the dried metal alginate beads were heat treated at 900 °C for 6 h and clean XRD pattern of the nanopowders obtained is shown in Fig. 4.50. The observed XRD pattern yielded single phase $La_2Hf_2O_7$ with cubic pyrochlore structure. Crystallite size was obtained from XRD pattern using Scherrer equation after eliminating instrument broadening and stress-strain broadening. Average crystallite size increased from 4 nm to 20 nm with the increase in calcination temperature from 700 °C to 900 °C as shown in Table 4.13 which is due to the Ostwald ripening [127].

148
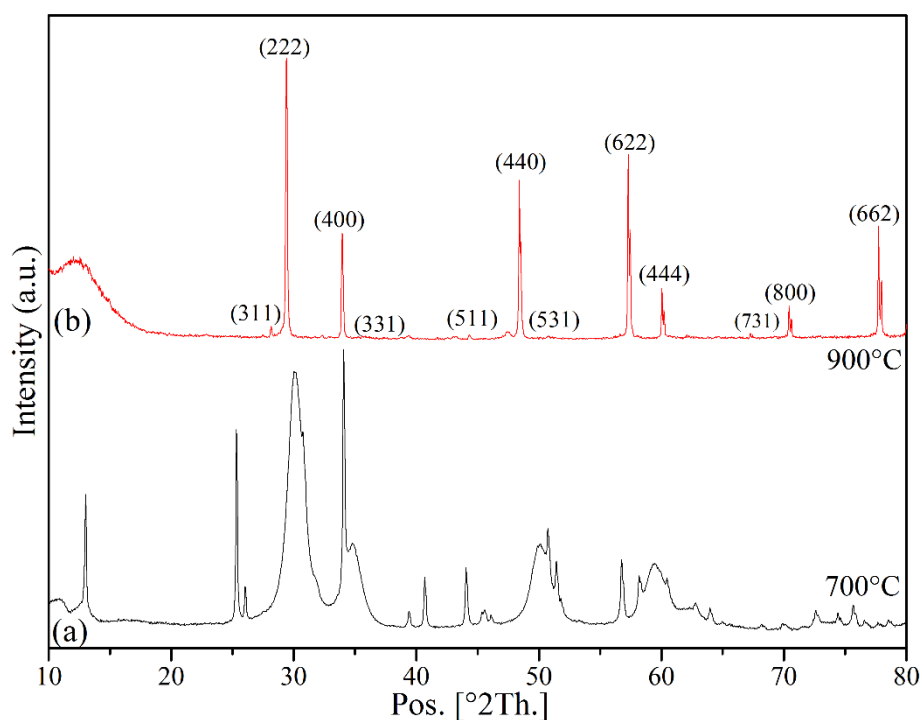
Fig. 4.50: XRD patterns of La₂Hf₂O₇ nanoparticles calcined for 6h at (a) 700°C (b) 900°C. Pattern is indexed by ICDD, 01-078-5592 indicating the miller indices of La₂Hf₂O₇ shown at the top of the peaks.

Fig. 4.51 shows the Rietveld refined XRD pattern of La$_2$Hf$_2$O$_7$ calcined at 900 °C for 6 h. The observed and calculated patterns are in good agreement with each other and the peaks could be indexed with XRD reference pattern of ICDD, 01-078-5592. Structural parameters obtained after the Rietveld refinement of XRD pattern can be seen in Table 4.13. The values of goodness of fit (GOF) and weighted residual (Rwp) from refinement are not very satisfactory which is due to the high value of residual as clearly seen in the Fig. 4.51. Sharpness of peaks in the observed data is higher than that in the calculated one which results in the high value of residual and refinement parameters. Particle coarsening increased with the increase in the calcination temperature and corresponding decrease in the micro strain as shown in the Table 1. The unit cell parameters of nanopowders of La$_2$Hf$_2$O$_7$ have found to be (a = b = c = 10.7726 A° and α = β = Γ = 90°) which indicates the cubic pyrochlore structure of La$_2$Hf$_2$O$_7$ as the values are doubled than that obtained for the defect fluorite structured Ho$_2$Hf$_2$O$_7$ and Ho$_2$Zr$_2$O$_7$ [161]. The XRD pattern and the value of unit cell parameters of La$_2$Hf$_2$O$_7$ nanopowders prepared through Leeds Alginate Process (LAP) are in excellent agreement with the one prepared through milling and calcination [177] and close to the one reported in literature [178].
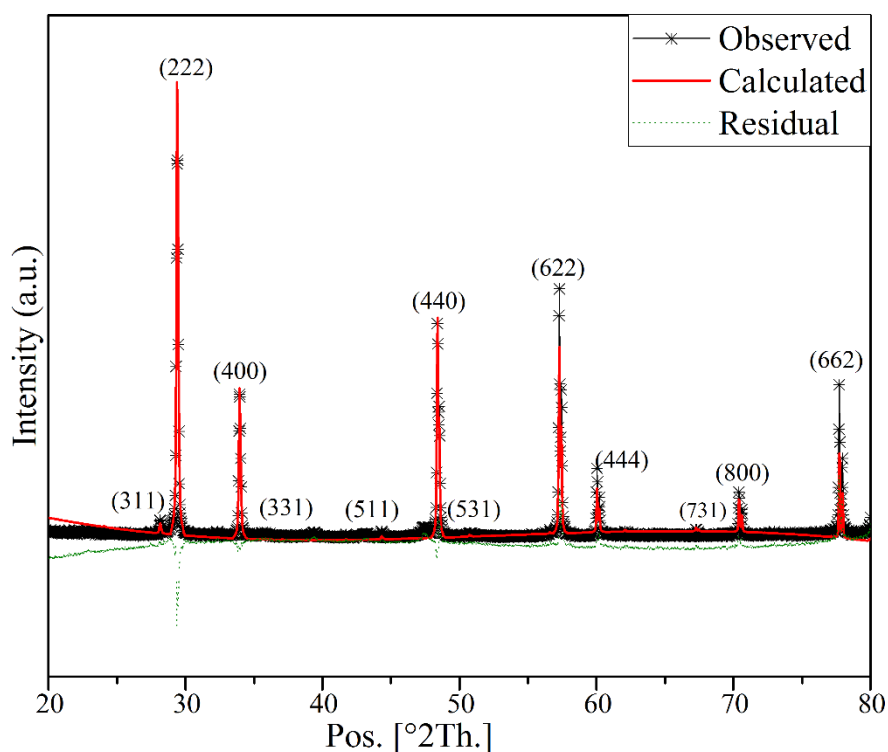
Fig. 4.51: Rietveld refined ambient XRD patterns of La₂Hf₂O₇ nanoparticles calcined at 900°C for 6h with Miller indices representing cubic pyrochlore structure.

Table 4.13: Structural parameters of La₂Hf₂O₇

Sample Heat Treatment	Rietveld Refined Size Strain Analysis					
	Avg. Crystallite Size (nm)	Micro Strain (%)	R_{wp} (%)	R_{exp} (%)	GOF	Lattice Parameters (A°)
700°C-6h	4.3	3.63	20.63	1.48	194	10.3468
900°C-6h	20.8	0.78	22.9	4.28	28.6	10.7726

Fig. 4.52 shows the TEM images and SAED pattern of the powder obtained after calcining metal alginate beads at 700 °C for 6 h. Nanoparticles of the powder obtained are crystalline and in narrow size distribution. The interplanar spacing are calculated from the SAED pattern and shown in Table 4.14. It is clear from the Fig. 4.52 and Fig. 4.50 that nanoparticles obtained after calcining at 700 °C do not fully form lanthanum hafnate rather some of the peaks are missing or overlapped.

150
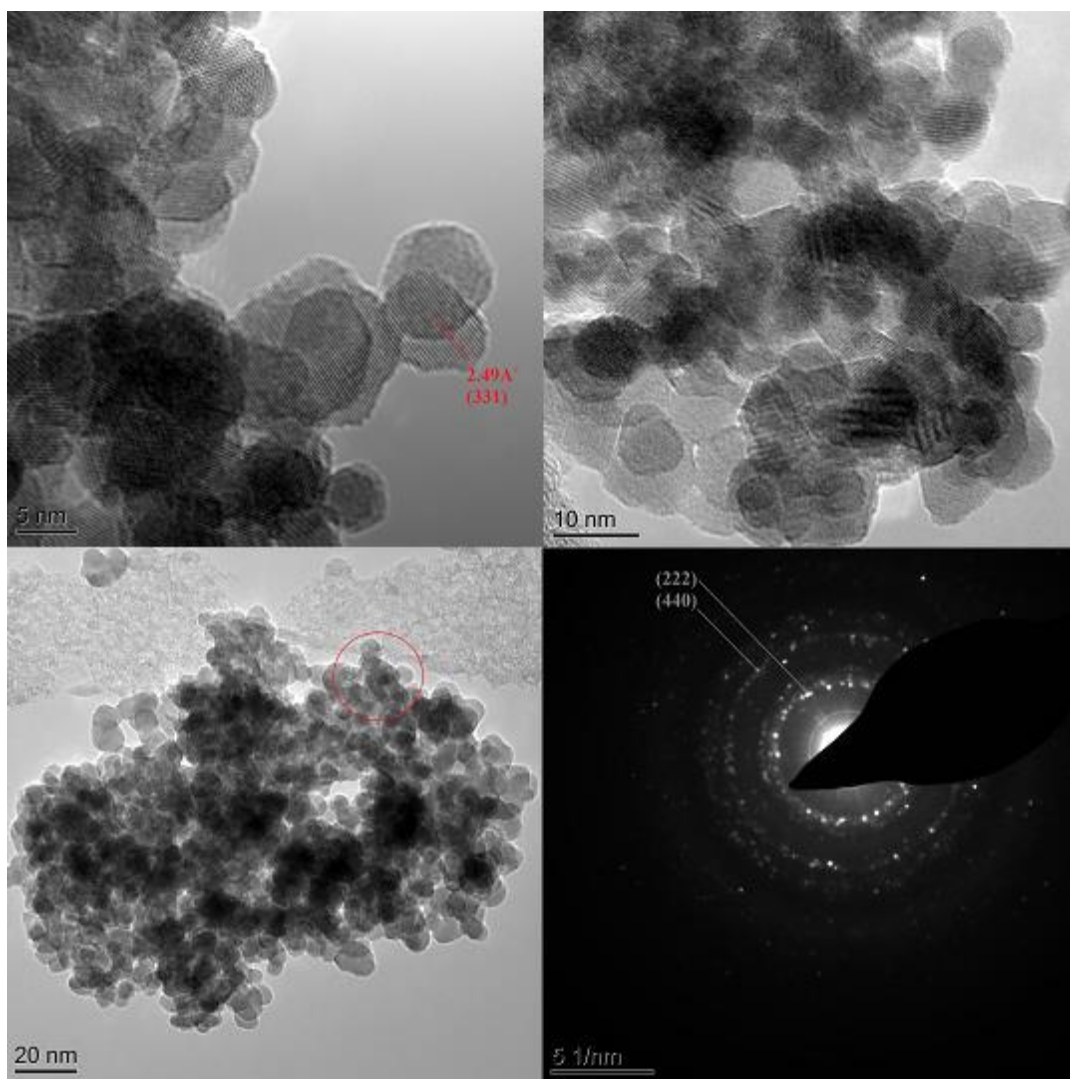
Fig. 4.52: TEM images with SAED pattern of La₂Hf₂O₇ calcined at 700˚C for 6h

TEM images and SAED pattern of La₂Hf₂O₇ nanoparticles obtained after calcining metal alginate beads at 900 ˚C for 6h are shown in Fig. 4.53. Crystallite size increased with the increase in calcination temperature and SAED pattern shows brighter rings. More rings in the SAED pattern as compared to the one in Fig. 4.52 indicates the formation of all the characterised peaks for La₂Hf₂O₇ nanopowders. SAED pattern was used to calculate the interplanar spacing and were assigned unique miller indices (hkl). The Miller indices of all the crystal planes obtained from SAED pattern are in excellent agreement with the XRD pattern in Fig. 4.50 as well as XRD reference pattern (ICDD, 01-078-5592).
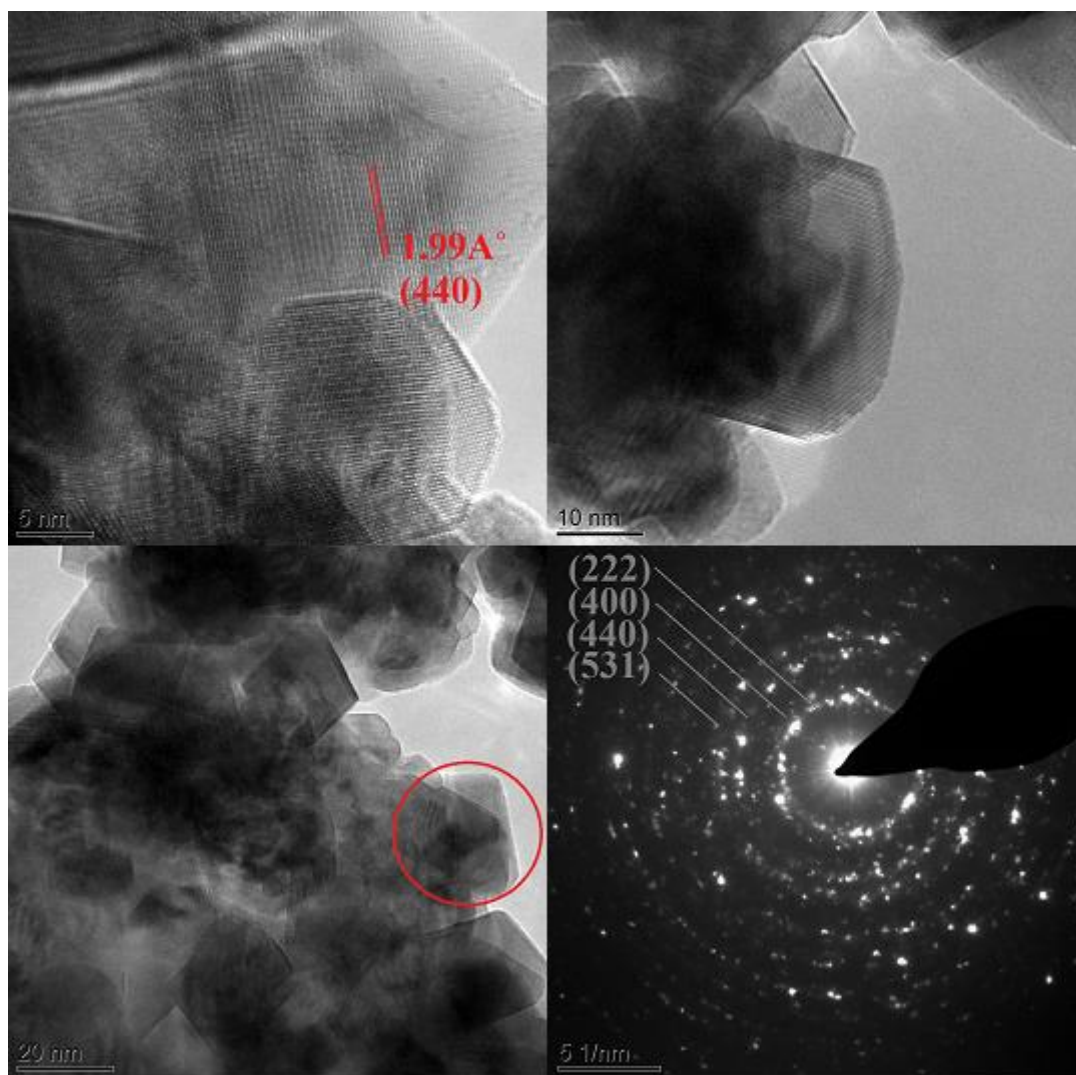
Fig. 4.53: TEM images with SAED pattern of La₂Hf₂O₇ calcined at 900˚C for 6h

Table 4.14 shows the comparison of d-spacing of powder obtained after calcination at different temperatures from TEM-SAED and XRD rietveld refinement. The powder obtained at 700 ˚C is showing some missing peaks in XRD data and TEM results. The d-spacing related to major peak observed in the XRD pattern are in good agreement with TEM result and with the XRD reference pattern. Interplanar spacing of lanthanum hafnate nanopowders obtained at 900 ˚C calculated from XRD and TEM-SAED corroborates well along with XRD reference pattern as shown in Table 4.14.

Table 4.14: Comparison of d-spacing of Lanthanum Hafnate from TEM and XRD

Rietveld Refinement

h	k	l	Ref. (ICDD, 01-078-5592) d, A˚	XRD d, A˚		TEM d, A˚	
				700˚C-6h	900˚C-6h	700˚C-6h	900˚C-6h
2	2	2	3.1108	3.0887	3.1015	3.17	3.16
4	0	0	2.6940	Not formed	2.6867	Not formed	2.76
3	3	1	2.4722	Not formed	2.4658	2.49	2.45
4	4	0	1.9050	Not formed	1.9007	1.99	1.99

TEM-EDX was performed on the nanopowders of $La_2Hf_2O_7$ to confirm the composition of synthesised material. The atomic % of elements found from the EDX analysis are in good agreement with the chemical formula of the lanthanum hafnate. The average composition of lanthanum hafnate found after the analysis is $La_{2.04}Hf_{1.96}O_7$. The results are within error of TEM-EDX analyses.

4.3.2. Sintering and Microstructural Characterisation

Nanopowders of lanthanum hafnate obtained after calcining at 900 ˚C were pressed into pellets and sintered over the temperature range of 1100 ˚C to 1500 ˚C. These pellets are then analysed with XRD to study the stability of the synthesised material with the increase in temperature. Fig. 4.54 shows the XRD scans of $La_2Hf_2O_7$ nanopowder and pellets sintered over the temperature range of 1100 °C to 1500 °C. XRD patterns of nanopowders and sintered pellets of lanthanum hafnate shows the stable cubic pyrochlore structure of $La_2Hf_2O_7$ with the space group of $Fd\bar{3}m$ over the entire range of heat treatment from 1100 °C to 1500 °C. These results confirm the stable pyrochlore structure of $La_2Hf_2O_7$ over the entire temperature range which is also in agreement with the cationic radius ratio, $r_{La}/r_{Hf} = 1.6$, as suitable ionic radii for the formation of the pyrochlore structure is $1.8 \geq (r_A/r_B) \geq 1.46$ [9].

La$_2$Hf$_2$O$_7$ nanopowders with stable pyrochlore structure was synthesised using Leeds Alginate Process at low temperature of 900 °C as compared to the others using solution combustion followed by pressureless sintering method at 1600 °C [176], through milling and calcination of metal oxides at 1500 °C [177] and with glycerol-citrate method at 1200 °C [179].
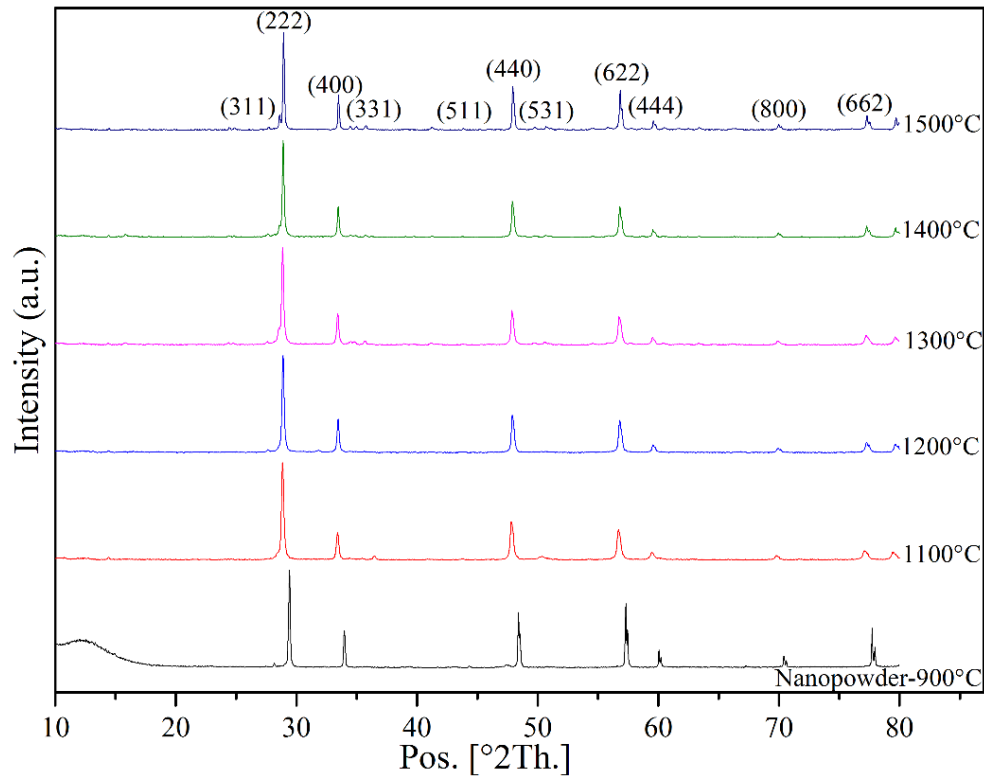
Fig. 4.54: XRD patterns of sintered lanthanum hafnate pellets. The patterns from 900°C to 1500°C are indexed by ICDD, 01-078-5592 with cubic pyrochlore La$_2$Hf$_2$O$_7$ shown at the top of the peaks.

Nanopowders of La$_2$Hf$_2$O$_7$ were pressed into pellets and sintered using conventional and non-conventional sintering technique at ambient pressure. Conventional technique also called single step sintering (SSS) means heating the pellets for 2 h at each temperature from 1100 °C to 1500 °C with the heating and cooling rate of 3 °C /min. Non-conventional technique involves the two step sintering (TSS) process; (I) – 1500 °C for 5 min, (II) -1300 °C for 96 h. Relative density and porosity of lanthanum hafnate pellets as a function of sintering temperature is shown in Fig. 4.55, sintered with both SSS and TSS processes. Relative density curve shows

the linear increase from 1100 °C to 1300 °C with density enhancement of 22 % and the corresponding decrease in porosity. There is a slight decrease in densification was observed at 1400 °C and 1500 °C and relative density reached to 91 % with the improvement of 15 %. The phenomenon of slightly less densification at higher temperatures can be explained by 'microstructural coarsening' including pore and grain growth which retards densification [180].

In the TSS process, the pellet is first heated to 1500 °C corresponding to the highest relative density point obtained in SSS process so that intermediate density can be attained and then held for the prolonged duration at lower temperature of 1300 °C corresponding to the 75% of relative density. The dotted line in the Fig. 4.55 is showing that relative density achieved at 1300 °C is above 75 %. The upward and downward arrows are pointing to the increase in relative density
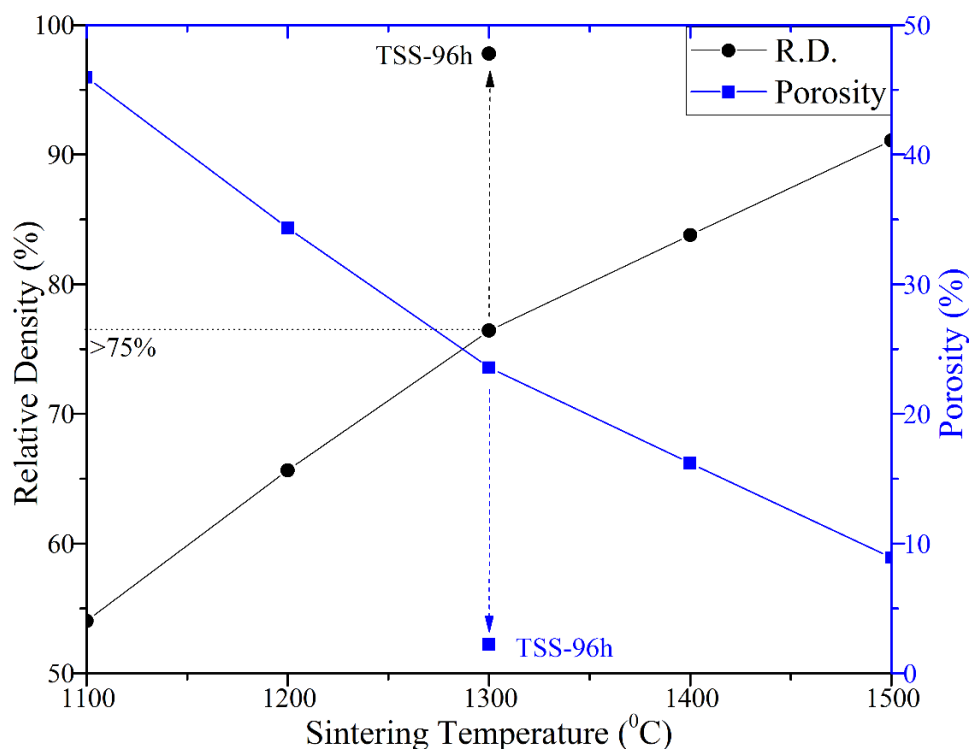
Fig. 4.55: Effect of sintering temperature on the relative density and porosity of lanthanum hafnate pellets. Two step sintering (TSS): (I) - 1500°C for 5min, (II) -1

300°C for 96h. Arrows showing increase in relative density and decrease in porosity with TSS process.

and corresponding decrease in porosity for the $La_2Hf_2O_7$ pellets sintered using TSS process. The relative density has reached to 98 (±0.2)% in TSS processed sample and corresponding porosity decreased to 2 (±0.2)% .

Fig. 4.57 shows the variation in grain size and relative density as a function of sintering temperature for $La_2Hf_2O_7$ pellets sintered using SSS and TSS processes. Grain size was calculated from the SEM micrographs of the pellets shown in the Fig. 4.56. It is quite evident from the SEM micrographs that with the increase in sintering temperature for SSS process relative density is increasing along with grain size (Fig. 4.57). It is noticed that increase in grain size is < 0.7 μm even though there is 22 % increase in relative density from 1100 °C to 1300 °C. This can be explained as the dispersed open pores can pin the grain boundaries and hinder the grain boundary migration which results in supressed grain growth [181, 182]. A slight decrease in density at higher temperature was noticed with the sharp increase in grain size from 0.5 to 1.45 μm at 1500 °C (relative density ∼ 91 %). Slight density decrease at higher temperature is due to the insoluble gases entrapped in the pores [183]. The reason of sharp grain growth can be referred to the open pores collapsed to form closed ones and results in significant decrease in pore pinning
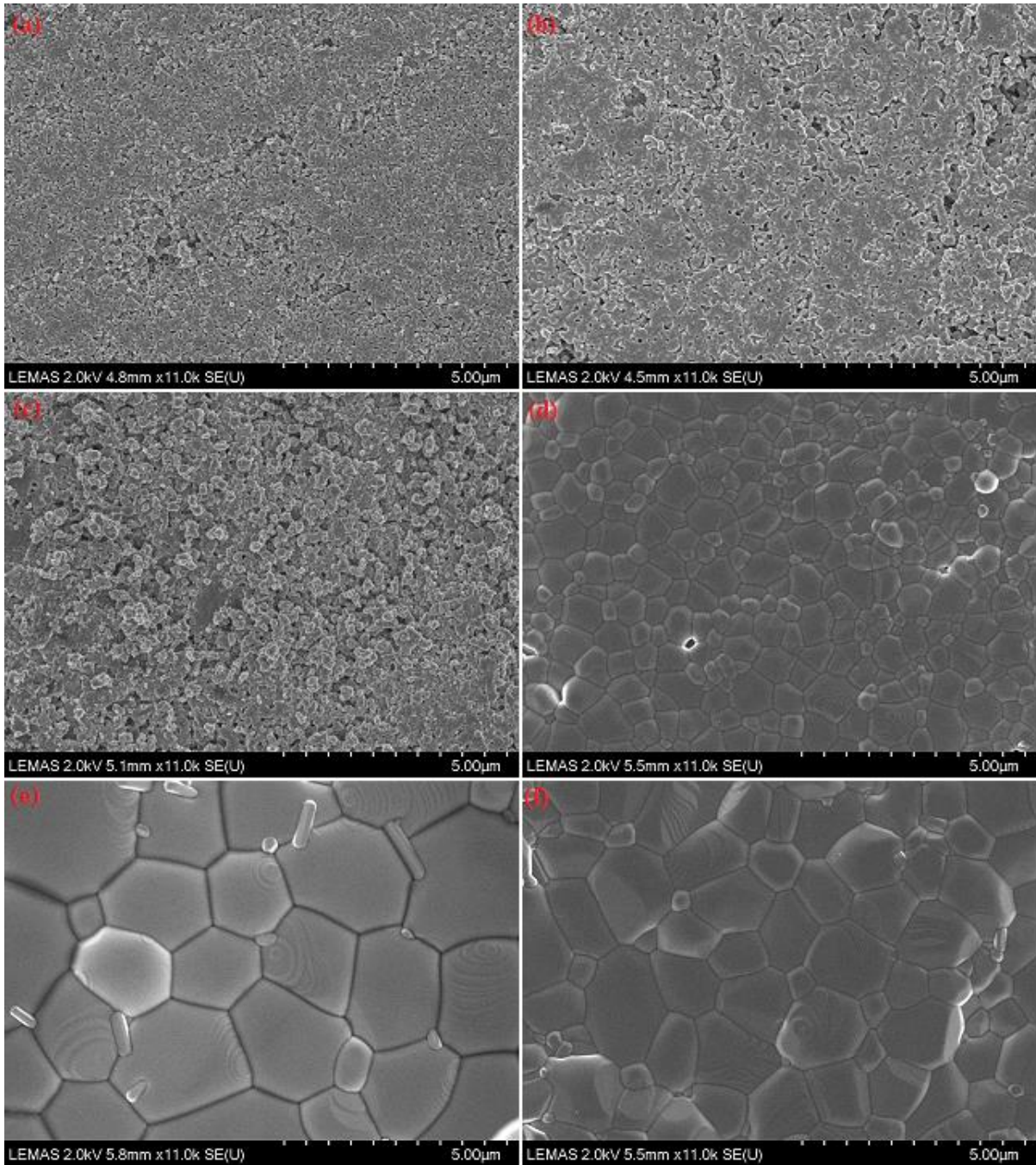
Fig. 4.56: SEM micrographs of sintered La$_2$Hf$_2$O$_7$ pellets. From (a) to (e) are the micrographs of the pellets after single step sintering (SSS) for 2h at (a) 1100°C (b) 1200°C (c) 1300°C (d) 1400°C (e) 1500°C and (f) after two step sintering (TSS): (I) - 1500°C for 5min, (II) - 1300°C for 96h.

which results in accelerated grain growth [182, 184]. In the samples processed with TSS shows the less grain growth (~0.9 μm) whereas the relative density reaches to 98 %, nearly 7 % greater

than the SSS processed sample at 1500°C. Dashed arrow in Fig. 4.56 points to the decrease in grain size with TSS process. Achievement of a better density during the TSS process may also have resulted from the reduced entrapped gas pressure within micropores at a lower temperature (step-II) because the gas pressure decrease may not be able to prohibit the mass transport caused by diffusion mechanisms [185]. The variation in density and grain growth of $La_2Hf_2O_7$ samples sintered with SSS and TSS processes are in good agreement with the micrographs in the Fig. 4.56. Hence, the TSS process has proved to be a better approach to attain greater densification of $La_2Hf_2O_7$ nanopowders ceramic sample with supressed grain growth as second sintering step proceeds with a frozen microstructure and has slower diffusion kinetics that is sufficient to achieve maximum density [116]. Similar results were obtained for the $Ho_2Hf_2O_7$ and $Ho_2Zr_2O_7$ and earlier investigation of the group for cerium gadolinium oxide (CGO) [172].
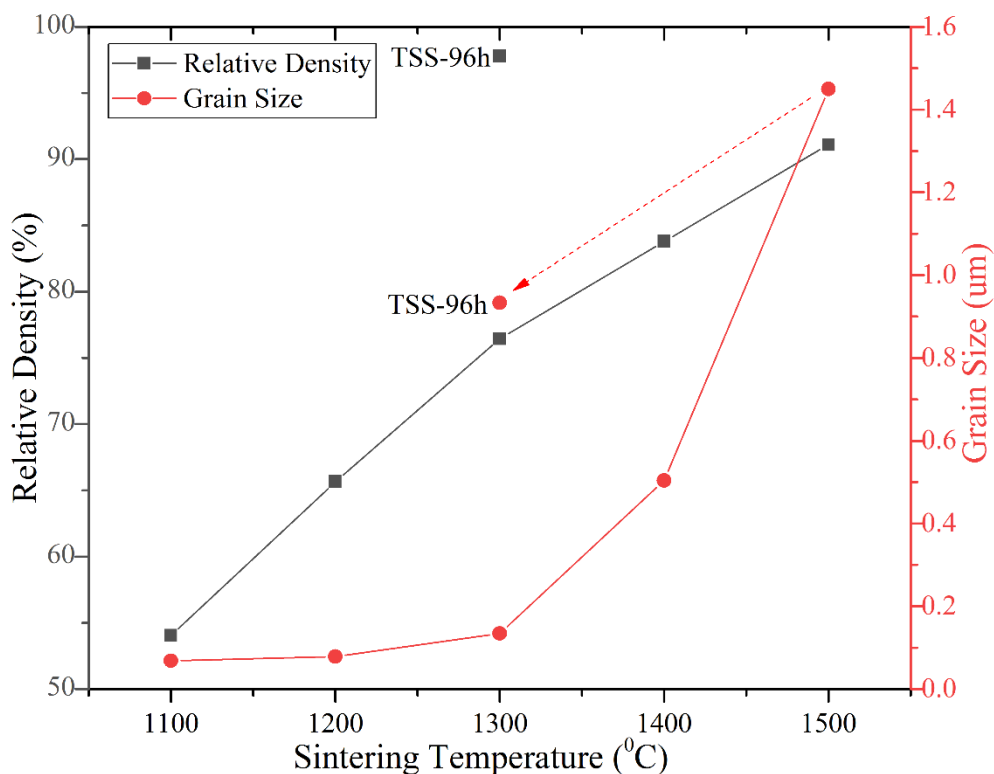
Fig. 4.57: Relative density and grain size of $La_2Hf_2O_7$ ceramics as a function of sintering temperature. TSS-96h shows the grain size for the pellet sintered with TSS process.

4.3.3. AC Impedance Spectroscopy

The Nyquist plots of $La_2Hf_2O_7$ sintered at 1500 °C for 2 h using SSS process measured at 350 °C and 550 °C are shown in Fig. 4.58. The complex impedance plots shows the single semicircle over the entire range of measurement from 350 °C to 800 °C which is the indication of just bulk contribution towards the conductivity. The radius of the semicircle decreased with the increase in measurement temperature indicating the thermally activated conduction mechanism in operation over the studied temperature range [173]. Complex impedance plots in Fig. 4.58 (a & b)
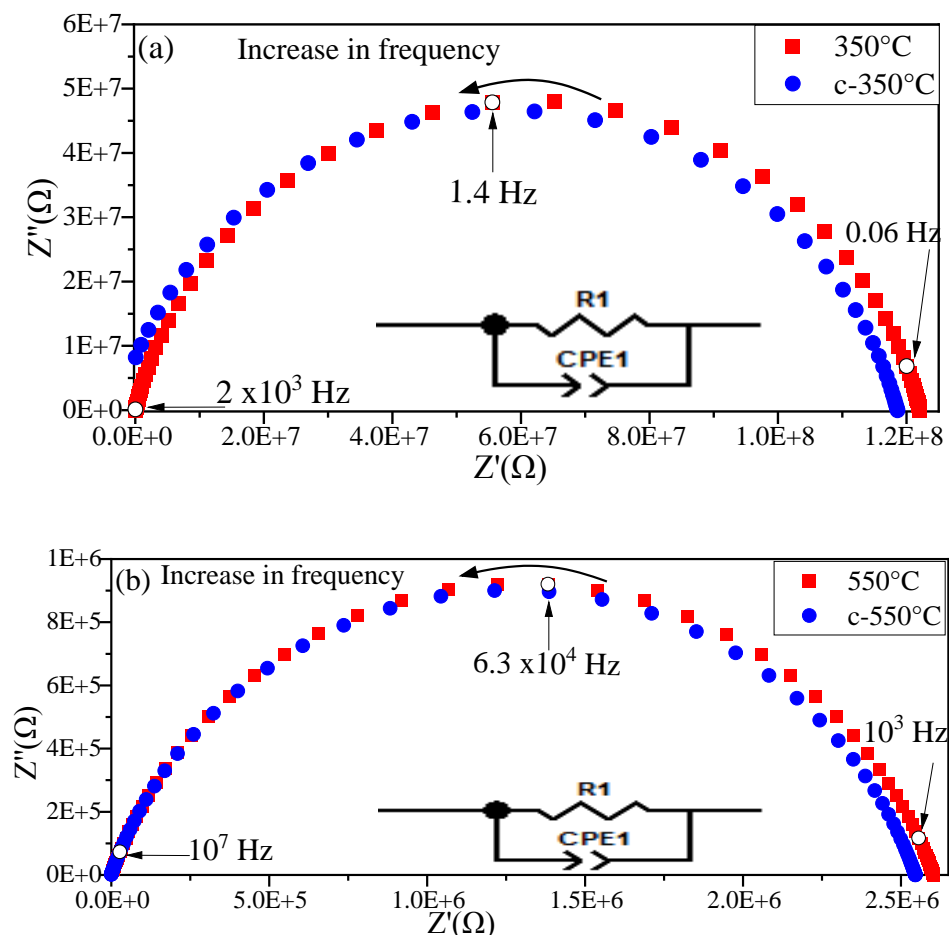
Fig. 4.58: Complex impedance plots for $La_2Hf_2O_7$ sintered at 1500°C for 2h measured in heating cycle at (a) 350°C and (b) 550°C, (c-350°C and c-550°C for cooling cycle).

suggests a single relaxation process as no sign of grain boundary or electrode effects was observed [186]. The reproducible Nyquist plots show consistent results in the heating and cooling cycles over the entire temperature range indicates the reversible response of $La_2Hf_2O_7$ ceramic electrolyte. This behaviour of responding reversibly is very important for the solid electrolytes used to design chemical sensor that is subject to temperature variation [159]. Temperature dependent Arrhenius plot of bulk conductivity of $La_2Hf_2O_7$ ceramic pellet sintered using SSS process is shown in Fig. 4.59 for both heating and cooling cycles. The value of activation energy for ionic conduction in $La_2Hf_2O_7$ has obtained by plotting $ln\sigma T$ against $1/T$ for ionic conductivity of single step sintered pellet measured over the range of 350 °C to 800 °C and frequency range of 100 mHz to 100 MHz for both heating and cooling cycles. The ionic conductivity increased with the increase in temperature as clearly seen from the behaviour of Arrhenius plot in Fig. 4.59 confirming that the ionic conductivity in the material is thermally activated. The rise in ionic conductivity over the temperature range is from 1.3×10^{-9} S.cm^{-1} at 350 °C to 2.6×10^{-6} S.cm^{-1} at 800 °C. The average value of activation energy for bulk ionic
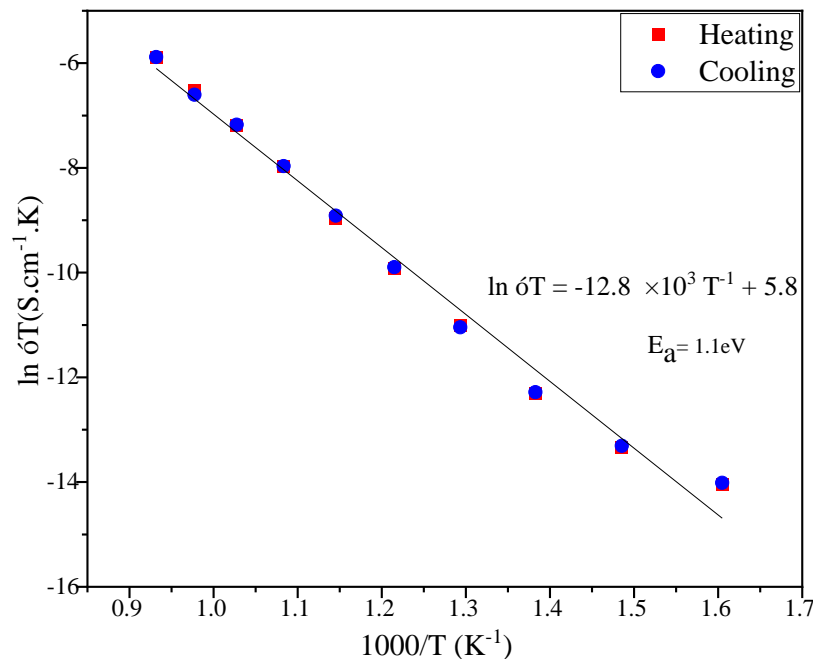
Fig. 4.59: Temperature dependence Arrhenius plot of bulk conductivity in heating and cooling cycles of lanthanum hafnate pellets sintered at 1500°C for 2h using SSS process.

conduction has been found to be 1.1 (±0.01) eV after combining data for heating and cooling cycles. The magnitude of activation energy for $La_2Hf_2O_7$ is higher than that of $Ho_2Zr_2O_7$ (0.99 eV) and less than that of $Ho_2Hf_2O_7$ (1.24 eV) sintered using SSS process, but the values are in acceptable range as the activation energies for oxide ion diffusion mechanism are in general ~ 1 eV [129].

Frequency dependence of the real components of conductivity for SSS processed $La_2Hf_2O_7$ material (log-log representation) for both heating and cooling cycles is shown in Fig. 4.60. Bulk contribution for conductivity and its dependence on frequency is shown in Fig. 4.60 over the temperature range of 350 °C to 800 °C. Another important characteristic feature of ion conducting solids is blocking effect which is also evident in this type of log-log representation. At lower temperature there is decrease in conductivity at lower frequencies. The frequency dispersive region separating low frequency and high frequency zones shifts towards higher frequencies with increase in temperature and leads above 700 °C to a regime where conductivity is almost frequency independent as shown in Fig. 4.60 (a & b). The regimes are consistent with heating and cooling cycles.
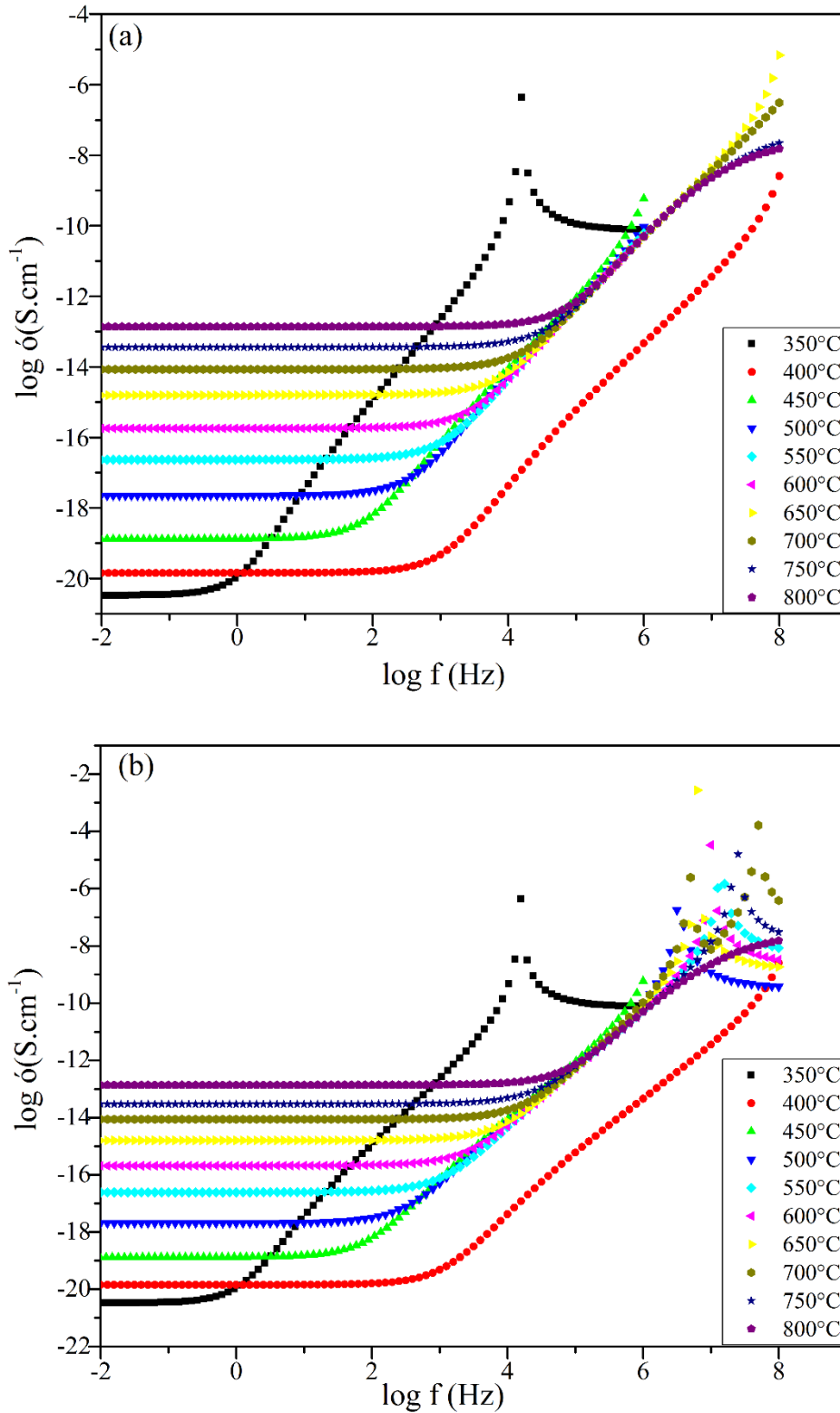
Fig. 4.60: Frequency and temperature dependence of the real parts of La$_2$Hf$_2$O$_7$ conductivity (a) heating (b) cooling sintered using SSS process.

Results of the impedance spectroscopy measurements at 350 °C, 550 °C and 600 °C of La$_2$Hf$_2$O$_7$ ceramic pellets sintered using the two step sintering (TSS) process are shown in the Fig. 4.61.
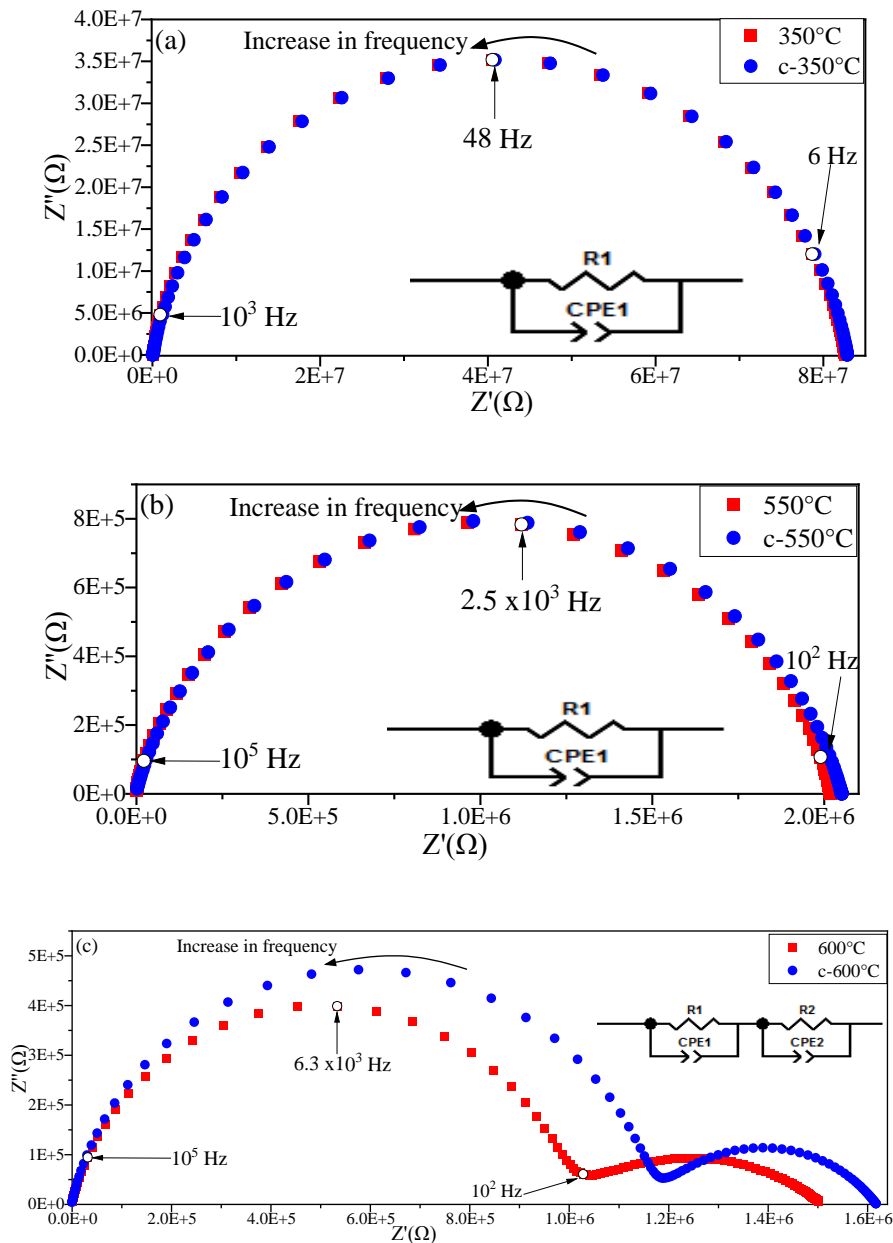
Fig. 4.61: Complex impedance plots for La$_2$Hf$_2$O$_7$ with two step sintering; (I) - 1500°C for 5min, (II) - 1300°C for 96h measured in heating cycle at (a) 350°C (b) 550°C and (c) 600°C (c-350°C, c-550°C and c-600°C for cooling cycle).

Complex impedance plots of lanthanum hafnate at 350 °C and 550 °C show the single semicircle as seen in Fig. 4.61 (a & b) which is the indication of purely bulk contribution towards the ionic conductivity of the material and no sign of grain boundary contribution from 350 °C to 550 °C for both heating and cooling cycles. With the increase in measurement temperature there appear two semicircle at 600 °C as seen in Fig. 4.61 (c), exhibiting both bulk and grain boundary contribution towards the conductivity. Significant gain boundary contribution along with bulk was observed from 600 °C to 800 °C. Fig. 4.61 (c) shows some inconsistencies in the heating and cooling cycles of measurements specifically in lower frequency region.

Temperature dependence of bulk and grain boundary conductivity of $La_2Hf_2O_7$ pellets sintered using TSS process in both heating and cooling cycles, calculated from the data of impedance measurement are shown in Fig. 4.62 as Arrhenius plots. The bulk conductivity is higher than grain boundary conductivity by an order of magnitude as shown in the Table 4.15. The inconsistency in the heating and cooling cycles of grain boundary plot was observed from 600 °C to 800 °C The average values of activation energies for bulk and grain boundary conductivity are 1.24 ($\pm$0.01) eV and 1.12 ($\pm$0.01) eV obtained from the heating and cooling cycles, respectively.
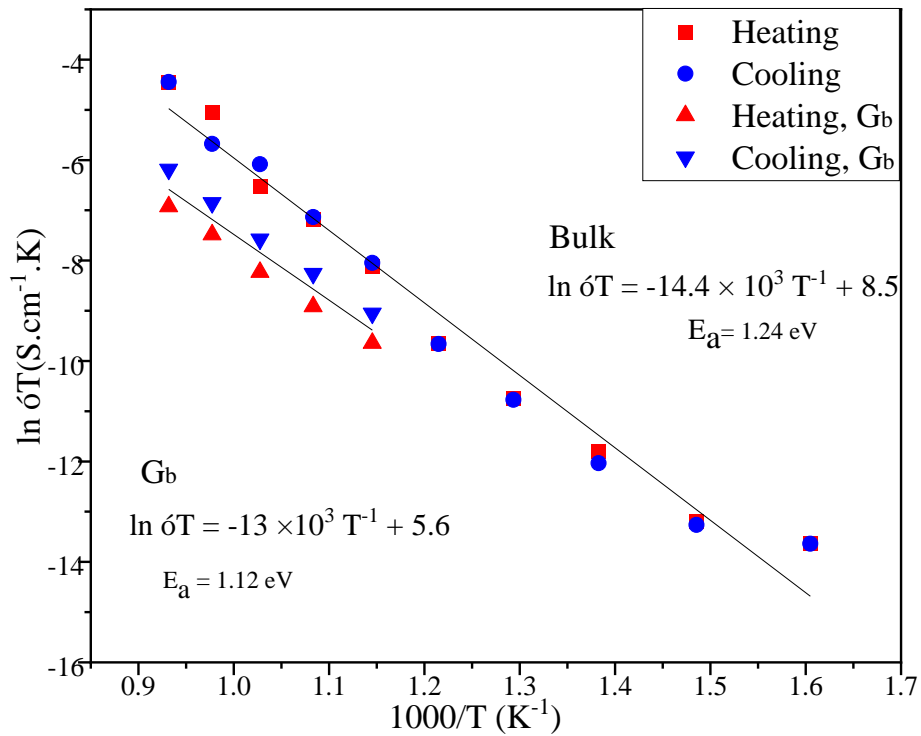
Fig. 4.62: Temperature dependence Arrhenius plots of bulk and grain boundary (Gb) conductivities for both heating and cooling cycles of lanthanum hafnate prepared using TSS process.

Fig. 4.63 shows the frequency dependence of the real components of conductivity for TSS processed $La_2Hf_2O_7$ material (log-log representation) for both heating and cooling cycles. The results are almost consistent for heating and cooling cycles as seen in Fig. 4.63 (a & b). There found a dispersion in the conductivity at low frequencies whereas at higher frequencies the curves converge to the same value.
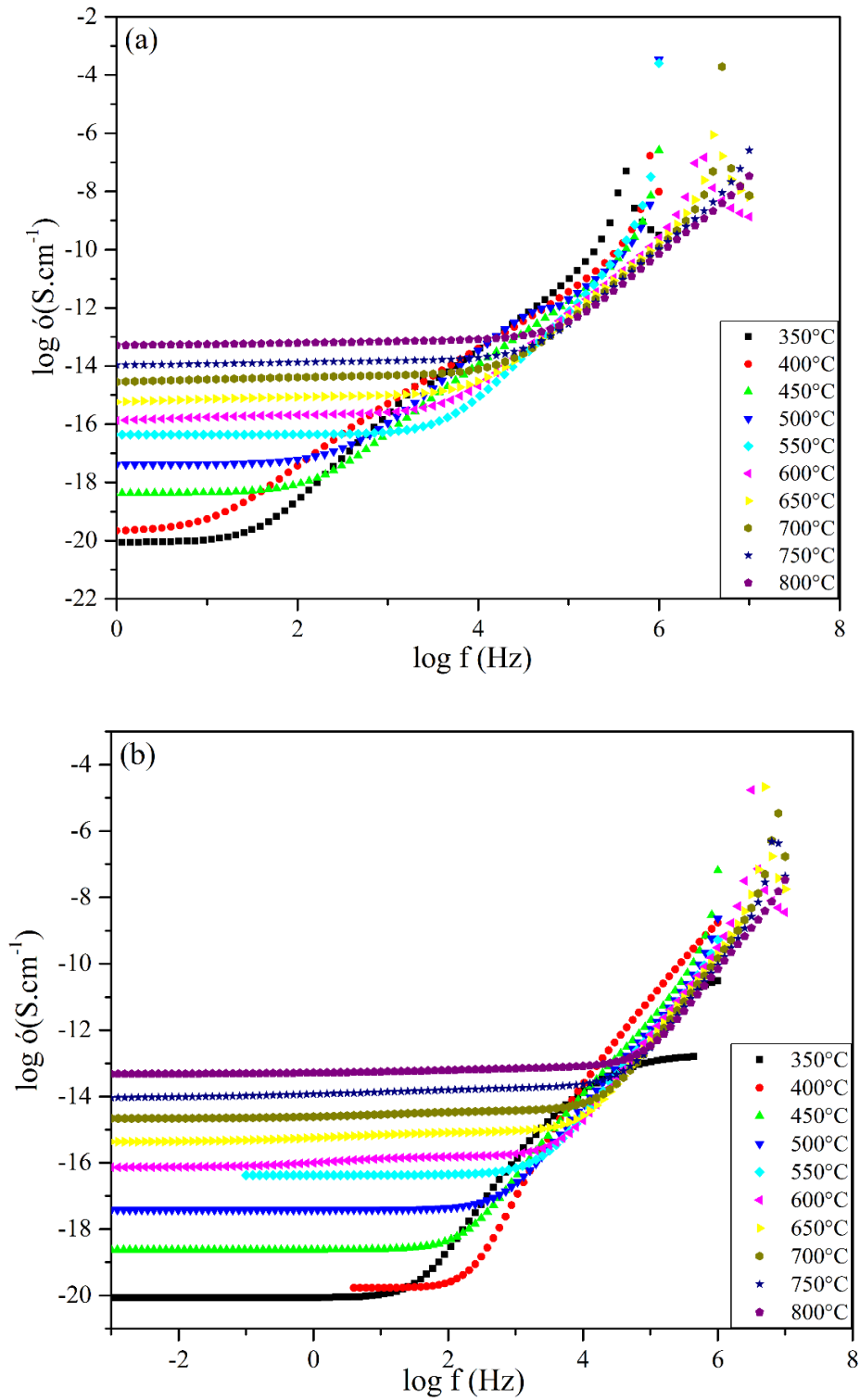
Fig. 4.63: Frequency and temperature dependence of the real parts of La₂Hf₂O₇ conductivity (a) heating (b) cooling sintered using TSS process.

Table 4.15: Corresponding activation energies and conductivity values of SSS and TSS processed La₂Hf₂O₇

Sample	Activation Energy (eV)	R^2 value	Conductivity at 600°C S.cm^{-1}	Conductivity at 800°C S.cm^{-1}
SSS-Bulk	1.10	0.98822	1.5×10^{-7}	2.60×10^{-6}
TSS-Bulk	1.24	0.97538	3.53×10^{-7}	1.09×10^{-5}
TSS-Gb	1.12	0.99865	1.44×10^{-7}	1.92×10^{-6}

Fig. 4.64 compares the Arrhenius plots of bulk conductivity of La$_2$Hf$_2$O$_7$ ceramic pellets sintered using both SSS and TSS processes. The fitted curve shows that at lower temperature the values of ionic conductivity are same for both process but with the increase in temperature the plots are parting and sample sintered with TSS process shows higher ionic conductivity than that of SSS processed sample. This is probably due to the highly dense pellet with smaller grain size obtained with TSS process. The value of activation energy is lower for SSS process than that of TSS process as seen in Table 4.15.
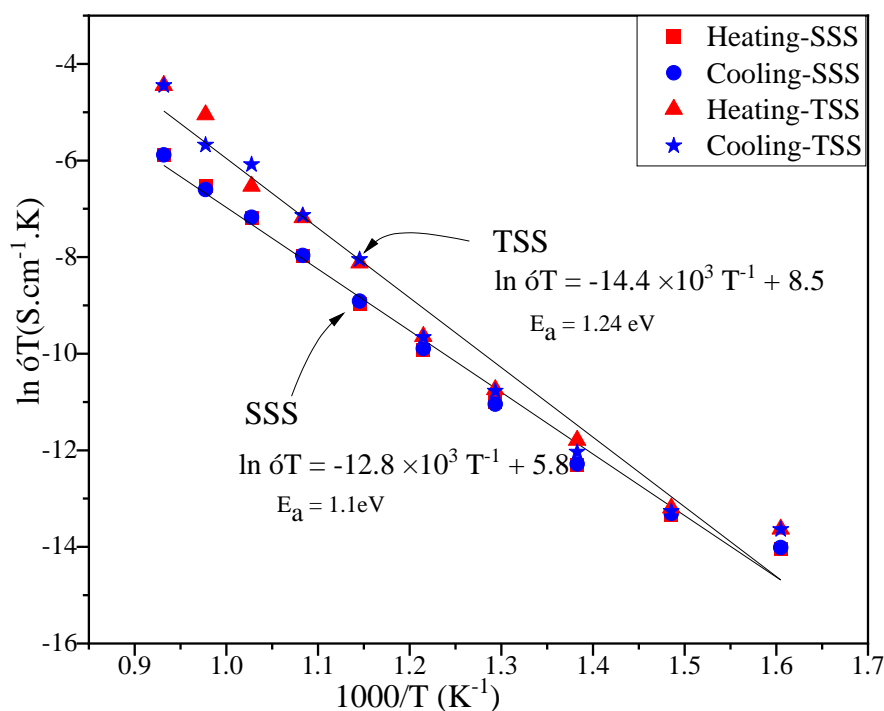
Fig. 4.64: Comparison of temperature dependence Arrhenius plots of bulk conductivity for both heating and cooling cycles of lanthanum hafnate prepared using SSS and TSS processes.

Table 4.15 compares the values of activation energy, R^2 values and ionic conductivity for lanthanum hafnate samples sintered using SSS and TSS processes at 600 °C and 800 °C. In case of SSS processed sample the grain boundary contribution was not noticed throughout the temperature measurement range but for TSS processed the grain boundary contribution appeared at 600 °C. Hence, TSS process is a better sintering route for the lanthanum hafnate ($La_2Hf_2O_7$) as highly dense ceramics with less grain size at low temperature and better ionic conductivity can be obtained than that sintered using SSS process.

The values of ionic conductivities of pyrochlore structured $La_2Hf_2O_7$ ceramic sample have been found significantly less than that of defect fluorite structured $Ho_2Hf_2O_7$ ceramic sample. Although synthesis route of materials and processing of ceramic pellets are same in both cases but even then ionic conductivity for holmium hafnate ceramic sample is more than two order of magnitude higher than that of lanthanum hafnate ceramic sample. This can be explained that the defect fluorite structured holmium hafnate is better ionic conductor due to the presence of oxygen vacancy in the structure. In pyrochlore structures all the cations and anions are ordered with respect to the oxygen atoms, this ordering causes the pyrochlore unit cell to double with respect to that of fluorite and drastically affects ionic and thermal conductivity [187].

4.4. Lanthanum Zirconate ($La_2Zr_2O_7$)

4.4.1. Thermal and Structural characterisation

Dried metal alginate beads were thermally analysed to determine the calcination temperature to obtain the lanthanum zirconate ($La_2Zr_2O_7$) nanopowders. Fig. 4.65 shows the simultaneous TGA/DSC analysis of dried metal alginate beads. DTG curve was obtained from the first

derivative of TGA curve. TGA and DSC curves are in good agreement with each other. The weight loss at different steps corresponding to the temperature range from the TGA/DTG curves are presented in Table 4.16. Peaks in the DSC curve are also tabulated. In first two steps from room temperature (RT) to 165 °C a weight loss of 23 % was observed with two endothermic and exothermic peaks in the DSC curve corresponding to this range. This weight loss is apparently due to the removal of adsorbed water or any bonded water present in the metal alginate beads. A similar trend was noticed at 130 °C with weight loss of 26.6 % in the TGA curve of lanthanum zirconate synthesised through the heat treatment of dried sols of ion-exchanged metal salts. Weight loss in TGA curve was attributed to the removal of physically adsorbed water and hydroxyl group [188]. A weight loss of ∼25 % was observed in the third and fourth steps of TGA with corresponding exothermic bends in the DSC curve. This weight loss can be attributed to the release of oxygen resulting from the cleavage of weaker linkage (G-G, G-M, and M-M) in the alginate structure [161]. The oxidative decomposition of alginate was observed in the fifth and sixth steps of TGA curve with the weight loss of ∼10 % and corresponding major and minor exothermic peaks in the DSC curve. The minor exothermic peaks adjacent to the major one indicates the formation of binary oxides (La_2O_3 and ZrO_2) after the completion of decomposition of alginate structure. In the last step of TGA curve a weight loss of < 2% was observed with corresponding exothermic peak in the DSC curve indicating the formation of ternary oxides ($La_2Zr_2O_7$). As the decomposition of alginate structure completed below 650°C in the sixth step of TGA/DTG a calcination temperature of 700 °C was determined to obtain the nanopowders of lanthanum zirconate.
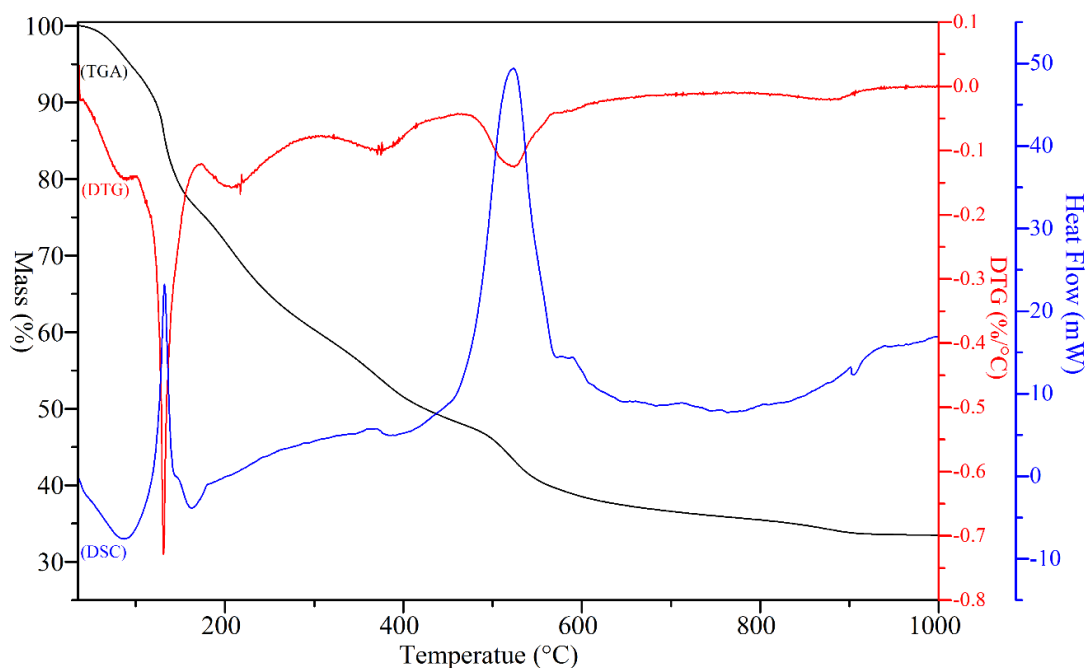
Fig. 4.65: TGA/DSC/DTG analysis of dry metal alginate beads

Table 4.16: TGA/DSC analysis

% Weight Loss in TGA curve			Peaks in DSC curve		
Steps	Temp. Range,°C	Wt. loss, %	No.	Temp. Range,°C	Type of peaks
1	RT- 97	6	Peak 1	RT-90	Endothermic
2	97-165	17	Peak 2	90-165	Exothermic
3	170-275	14	Peak 3	165-200	Exothermic
4	300-425	10.6	Peak 4	345-380	Exothermic
5	460-575	6	Peak 5	380-570	Exothermic
6	575-625	4.5	Peak 6	570-615	Exothermic
7	815-910	1.85	Peak 7	896-910	Exothermic

Metal alginate beads were oven dried and milled using ball mill to carry out the HTXRD scan from room temperature (RT) to 1000 ˚C. The particle size of (10 - 50 μm) is preferred for HTXRD analysis [189]. Fig. 4.66 shows the HTXRD pattern of ball milled metal alginate

beads. There found a lot of extra peaks which are not characterised for lanthanum zirconate, it means ball milling has introduced a new structure [190] which got activated at higher temperature. There appears second phase when the sample was heated above 800 ˚C, superposing of major peak at higher temperature indicating the presence of monoclinic zirconia (m-ZrO$_2$) [190]. The appearance of peaks ~2θ = 30° is due to the contaminated solid solution introduced through ball milling.
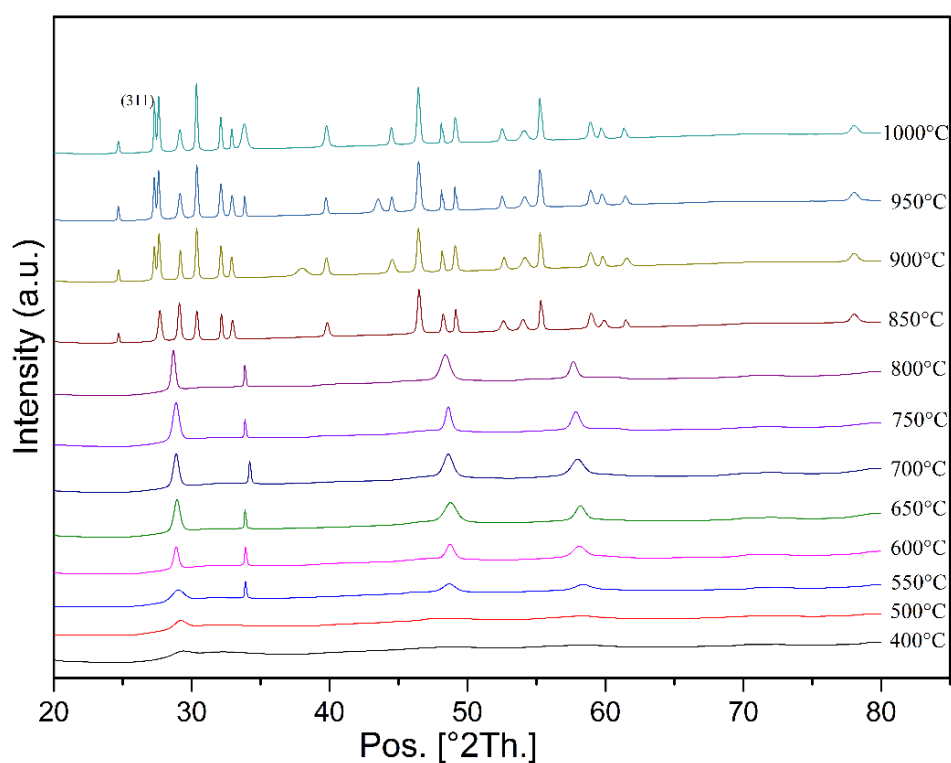
Fig. 4.66: HT-XRD patterns of metal alginate beads from 400-1000°C. Pattern above 800 ˚C are contaminated due to ball milling.

Later on, oven dried metal alginate beads were powdered using pestle and mortar and HTXRD analysis was carried out. Fig. 4.67 shows the HTXRD patterns of powdered metal alginate beads from 400 ˚C to 1000 ˚C. Below 400 ˚C no diffraction peak of any material was observed. As the thermal decomposition of the metal alginate beads completed below 650 ˚C as clearly seen in Fig. 4.64 and some of the kinks in the pattern started appearing at 400 ˚C and formed the peaks at 700 ˚C corresponding to the fluorite structure of La$_2$Zr$_2$O$_7$. The peaks found at 700

171

˚C are characterised for the fluorite structure of $La_2Zr_2O_7$ but with the increase in temperature the major peaks slightly shift to the lower angles along the dotted line which indicates the formation of crystalline $La_2Zr_2O_7$ with pyrochlore structure [191]. The formation of this pyrochlore phase at higher temperature are reported in literature, who observed the formation of this phase after 6 h at 1000 °C from powders obtained by the sol–gel method [192] and also the formation of $La_2Zr_2O_7$ at T ≥ 1100 °C in a system containing Sr, Mn and Y [193]. High purity single phase pyrochlore structured $La_2Zr_2O_7$ peaks were observed at 900 ˚C which is in excellent agreement with the interpretations of Fig. 4.65. Sharpness of $La_2Zr_2O_7$ diffraction peaks increased with the increase in temperature from 900 °C to 1000 °C owing to crystal growth [125]. Comparison of Fig. 4.66 and Fig. 4.67 shows the formation of extra peaks at higher temperature due to the milling of beads using ball mill. So the ball mill is not recommended for converting beads into powders for characterisation as it induce an extra phase in the milled powder. Some of the literature has observed formation of this extra phase even at room temperature [190].

Thermal behaviour of metal alginate beads studied using TGA/DSC/DTG and HTXRD are in good agreement with respect to the thermal decomposition of metal alginate beads and formation of pyrochlore structured crystalline nanopowders of $La_2Zr_2O_7$. Fig. 4.65 and Fig. 4.67 show the complete thermal decomposition of metal alginate beads is below 700°C. It can be concluded from the thermal analysis that the enthalpy change for the decomposition of metal alginate (La^{3+}/Zr^{4+} -ALG) into $La_2Zr_2O_7$, $CO_{2 (g)}$ and $H_2O_{(g)}$ is -2581 J/g (±10%) based on the Hess's law of heat summation which suggest that overall decomposition process is exothermic in nature.
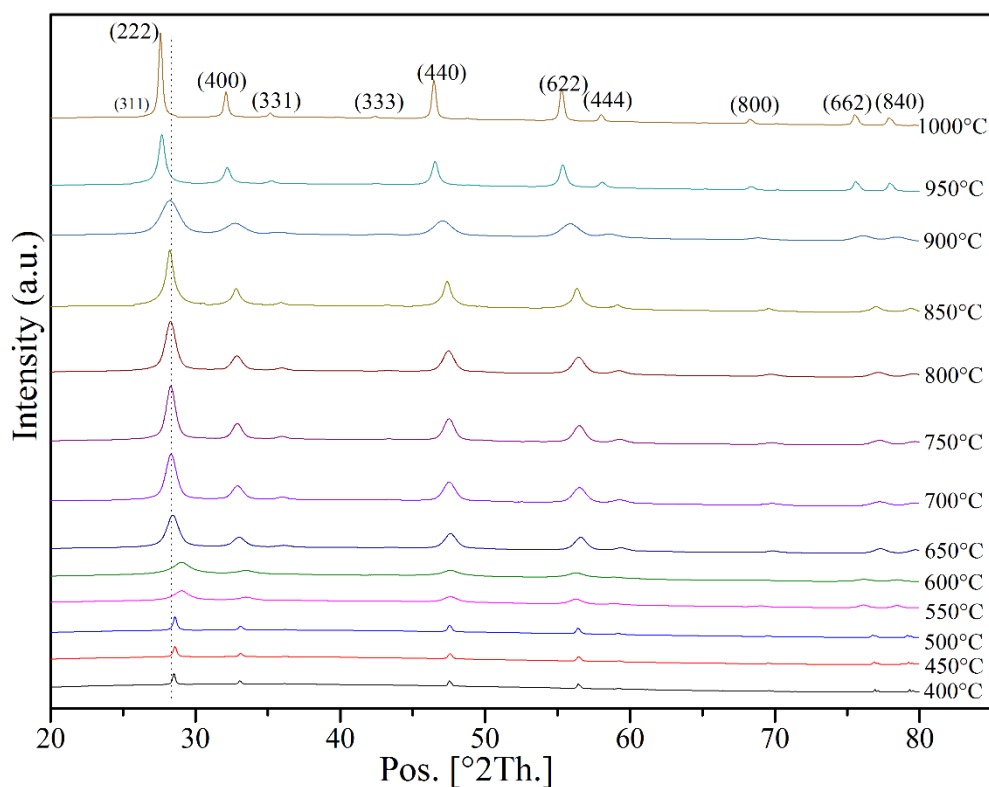
Fig. 4.67: HT-XRD patterns of metal alginate beads from 400-1000°C. The patterns are indexed by ICDD-01-084-2632 with miller indices of crystal planes of cubic La$_2$Zr$_2$O$_7$ shown at the top of the peaks.

Fig. 4.68 shows the XRD patterns of the nanopowders obtained after calcining the metal alginate beads for 6h at 700 °C and 900 °C. In case of HTXRD analysis metal alginate beads anneal at one temperature for 30 mins so it is decided to calcine the beads first at 700 °C for longer time (6 h) to achieve the lanthanum zirconate nanopowders at comparatively low temperature. There observed the split in the major peaks in the XRD pattern obtained after calcining the beads at 700 °C. This pattern is different than that found in HTXRD at 700 °C as some extra peaks were also observed which should not be present in the fluorite structure of La$_2$Zr$_2$O$_7$ [190], here it is more like transformation from fluorite to pyrochlore structure. Clean XRD pattern was obtained for the nanopowders obtained after calcining the metal alginate beads at 900 °C for 6h as seen in the Fig. 4.68. The observed XRD pattern showed the single phase with cubic pyrochlore structure. The peaks observed in the pattern at 900 °C are

173

characterised for the crystalline nanopowders of $La_2Zr_2O_7$ with pyrochlore structure [190-193]. The patterns in Fig. 4.68 confirms the completed decomposition of metal alginate beads below 700 °C and formation of pyrochlore structured $La_2Zr_2O_7$ at 900 °C, which is in excellent agreement with the TGA/DSC results. Crystallite size was obtained from XRD pattern using Scherrer equation after eliminating instrument broadening and stress-strain broadening. Average crystallite size increased from 4 nm to 31 nm with the increase in calcination temperature from 700 °C to 900 °C as shown in Table 4.17 which is due to the Ostwald ripening [127].
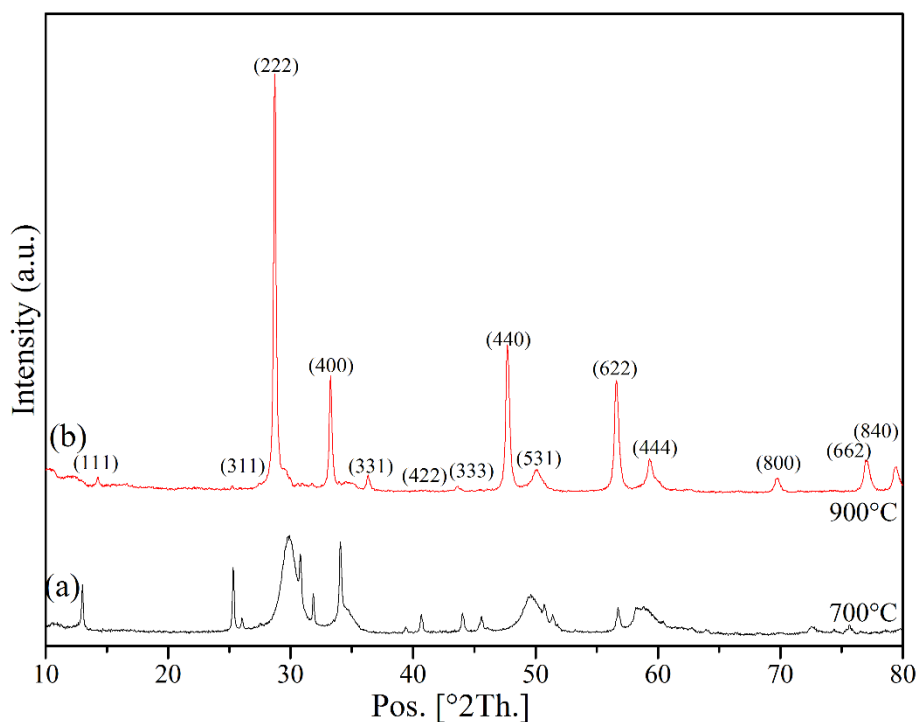
Fig. 4.68: XRD patterns of $La_2Zr_2O_7$ nanoparticles calcined for 6h at (a) 700°C (b) 900°C. Pattern is indexed by ICDD-01-084-2632 indicating the miller indices of $La_2Zr_2O_7$ shown at the top of the peaks.

Rietveld refined XRD pattern of lanthanum zirconate obtained after calcining at 900°C for 6h is shown in Fig. 4.69. The XRD pattern was refined using the XRD reference pattern ICDD, 01-084-2632 and the miller indices of the peaks are shown at the top. The observed and

calculated patterns are in good agreement with each other and residual pattern shows the difference in the sharpness of some of the peaks. Structural parameters obtained after Rietveld refinement are shown in the Table 4.17; the values of goodness of fit (GOF) and weighted residual are not satisfactory due to the sharpness of peaks in the observed pattern obtained after calcining the beads at 900 °C. Coarsening of particles increased with the increase in calcination temperature and corresponding decrease in the micro strain was also observed.

The unit cell parameters of nanopowders obtained after calcining the beads at 700 °C have found to be (a = b = c = 10.4470 A° and $\alpha = \beta = \Gamma = 90°$) which indicates neither pyrochlroe nor fluorite structure of the material formed. The unit cell parameters of nanopowders of $La_2Zr_2O_7$ obtained after calcining the beads at 900 °C have found to be (a = b = c = 10.7960 A° and $\alpha = \beta = \Gamma = 90°$) which indicates the cubic pyrochlore structure of $La_2Zr_2O_7$ with space group $Fd\bar{3}m$, as the values are doubled than that obtained for the defect fluorite structured $Ho_2Zr_2O_7$ [161]. The XRD pattern and the value of unit cell parameters of $La_2Zr_2O_7$ nanopowders prepared through Leeds Alginate Process (LAP) at 900 °C are in excellent agreement with the one prepared through sintering of metal salts at 1500 °C for 24 h [194] and through co-precipitation method and heat treating at 1450 °C [195]. The XRD pattern of lanthanum zirconate nanopowders at 900 °C shows the formation of its pyrochlore structure at comparatively low temperature as compared to the patterns reported in the literature with some minor reflections of pyrochlore structure at this temperature and clean pattern of pyrochlore structured $La_2Zr_2O_7$ obtained at 1100 °C [188].

Table 4.17: Structural parameters of La₂Zr₂O₇

Sample	Rietveld Refined Size Strain Analysis					
Heat Treatment	Avg. Crystallite Size (nm)	Micro Strain (%)	R_{wp} (%)	R_{exp} (%)	GOF	Lattice Parameters (A˚)

700°C-6h	4.6	3.27	19.4	4.07	22.8	10.4470
900°C-6h	30.9	0.50	26.7	5.48	23.7	10.796
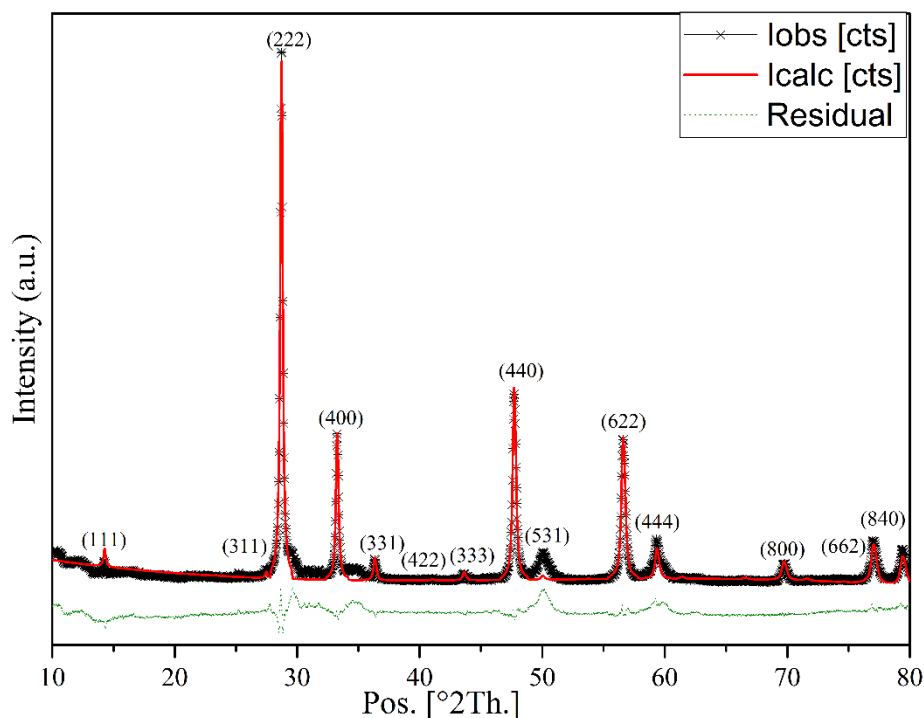
Fig. 4.69: Rietveld refined ambient XRD patterns of La$_2$Zr$_2$O$_7$ nanoparticles calcined at 900°C for 6h with Miller indices representing cubic pyrochlore structure.

Nanopowders of lanthanum zirconate were analysed using Raman spectroscopy in the frequency range of 25 – 1200 cm^{-1} and results are shown in the Fig. 4.70 with three different lasers blue (473 nm), green (514 nm) and red (633 nm). Raman spectroscopy is sensitive to the cation-oxygen vibration and provide clear information to distinguish structural change of pyrochlore and defect-fluorite materials [93]. Based on the group theory the cubic A$_2$B$_2$O$_7$ type pyrochlores belong to the space group $Fd\overline{3}m$ and have six Raman active modes distributed as A$_{1g}$ + E$_g$ + 4F$_{2g}$ [164]. The most intense Raman band at 300 cm^{-1} is mainly due to the Zr-O vibrations of the E$_g$ mode [130]. Raman band at 500 cm^{-1} is assigned to the A$_{1g}$ mode which is related to the O-Zr-O bending vibrations of ZrO$_6$ octahedra [163]. The presence of E$_g$ and A$_{1g}$

176

modes in the Raman spectra in Fig. 4.70 confirms the pyrochlore structure of $La_2Zr_2O_7$ nanoparticles as these modes are strictly assigned to the pyrochlore phase [163]. The Raman bands at around 397, 520, 639 and 750 cm^{-1} can be assigned to the F_{2g} mode which are mostly related to Zr-O stretching with a mixture of La-O stretching and sometimes O-Zr-O bending vibrations [163]. Based on the assignments of all the active modes in the Raman spectra it is apparent that $La_2Zr_2O_7$ formed an ordered pyrochlore structure since all the active modes can be clearly observed in the Fig. 4.69.

Analyses from XRD and Raman spectroscopy are in agreement with each other as they confirm the pyrochlore structure of lanthanum zirconate synthesised from LAP which is also in agreement with the cationic radius ratio. An ordered pyrochlore structure formed if the r_A/r_B ration is in the range of 1.46 to 1.78. Pyrochlore structure will become less ordered with the decrease in cationic radius ratio and ultimately transformed to cubic defect-fluorite phase when this ratio is below 1.46.
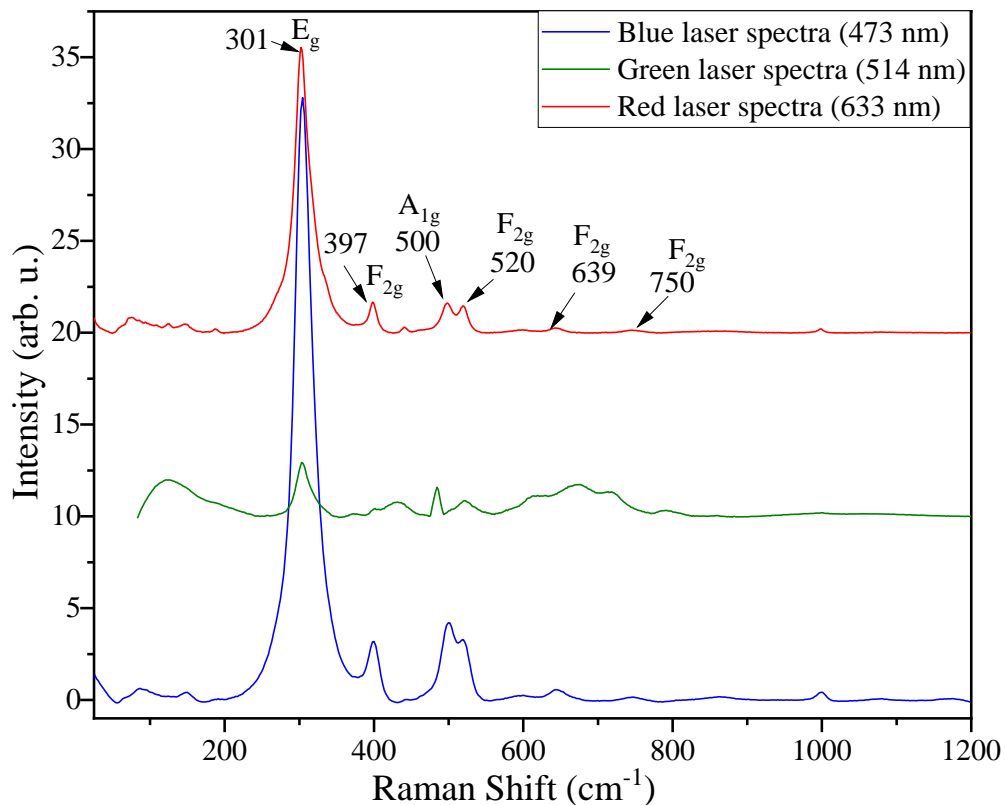
Fig. 4.70: Raman spectra of La$_2$Zr$_2$O$_7$ nanopowder obtained after calcination at 900°C for 6h for three different lasers blue-473nm, green-514nm and red-633nm.

TEM images of the nanopowders obtained after calcining metal alginate beads at 700 °C are shown in the Fig. 4.71. There found the amorphous and crystalline particles as clearly seen in the images. The crystalline nature of the particles is more visible with the increase in the magnification but on the other hand amorphous particles are not showing in crystallinity even in the high resolution image. Nanopowders obtained at 700 °C contained mixed particles both amorphous and crystalline as confirmed by the TEM-SAED patterns in the Fig. 4.72. Bright rings were observed in the SAED pattern for crystalline material as compared to the amorphous one. Fig. 4.72 confirm the XRD pattern of the nanopowders obtained at 700 °C in Fig. 4.68 which shows the combination of sharp and broader peaks and that is the indication of mixture of amorphous and crystalline powder. TEM images found for the amorphous material are quite similar to the one reported in case of dried sol [188].

TEM images and SAED pattern of La$_2$Zr$_2$O$_7$ nanoparticles obtained after calcining metal alginate beads at 900 °C for 6 h are shown in Fig. 4.73. Crystallite size increased with the increase in calcination temperature and SAED pattern shows brighter and more rings as compared to the one found in the Fig. 4.72 for crystalline powder, indicates the formation of all the characterised peaks for pyrochlore structured La$_2$Zr$_2$O$_7$ nanopowders. SAED pattern was used to calculate the interplanar spacing and were assigned unique miller indices (hkl). The Miller
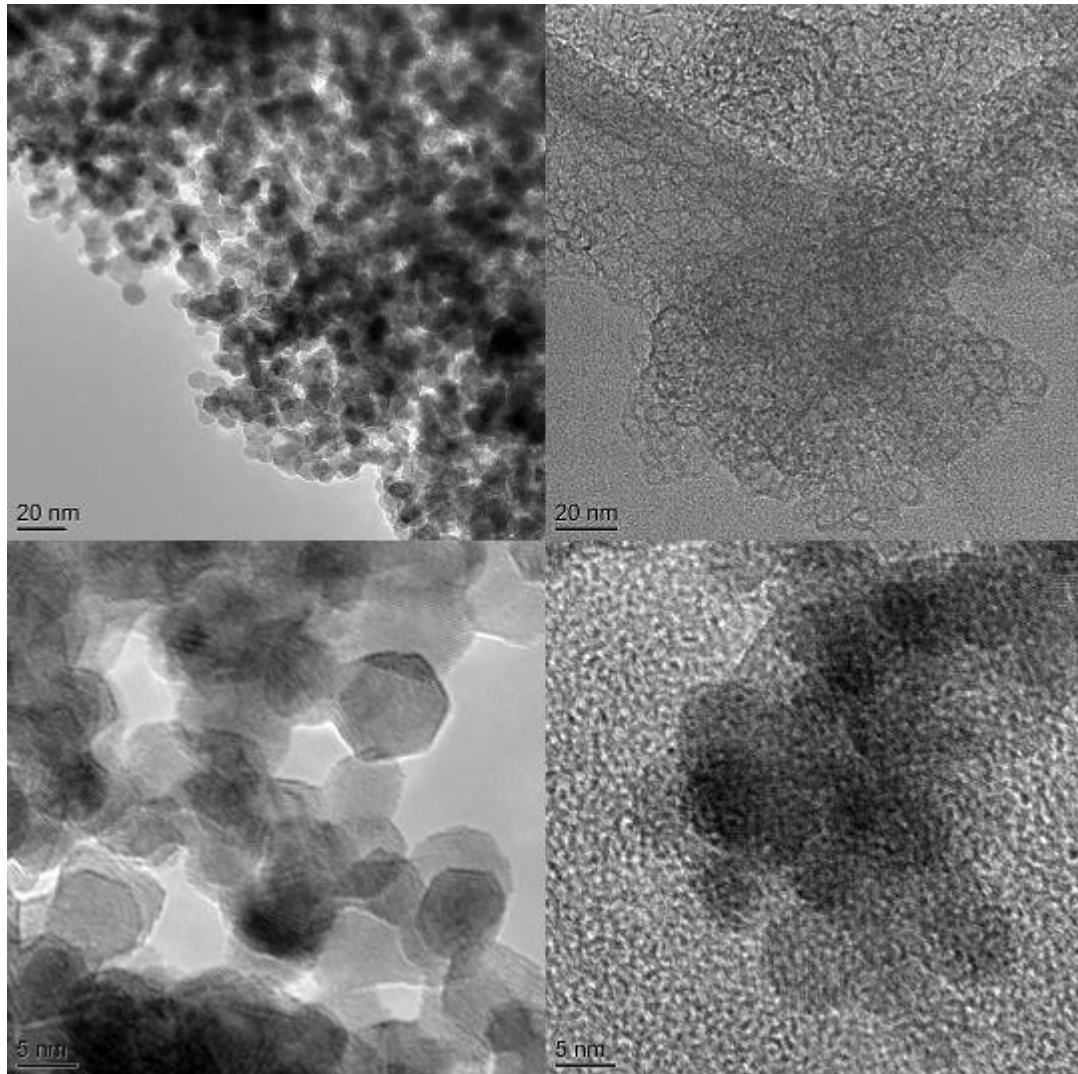
Fig. 4.71: TEM images with of La$_2$Zr$_2$O$_7$ calcined at 700˚C for 6h

indices of all the crystal planes obtained from SAED pattern are in excellent agreement with

the XRD pattern in Fig. 4.68 and Fig. 4.69 as well as XRD reference pattern (ICDD, 01-084-

2632).

Table 4.18 shows the comparison of d-spacing of powder obtained after calcination at different

temperatures from TEM-SAED and XRD Rietveld refinement. The powder obtained at 700 ˚C

is missing the peak (331) in both XRD data and TEM results; which is the characteristic peak

of pyrochlore structured materials. Nanopowders obtained at 900 ˚C indicates the presence of

peak (331) in XRD data as well as TEM results. The d-spacing related to major peaks observed

in the XRD pattern are in good agreement with TEM result and with the XRD reference pattern.

Interplanar spacing of lanthanum zirconate nanopowders obtained at 900 °C calculated from XRD and TEM-SAED agrees well along with XRD reference pattern as shown in Table 4.18.
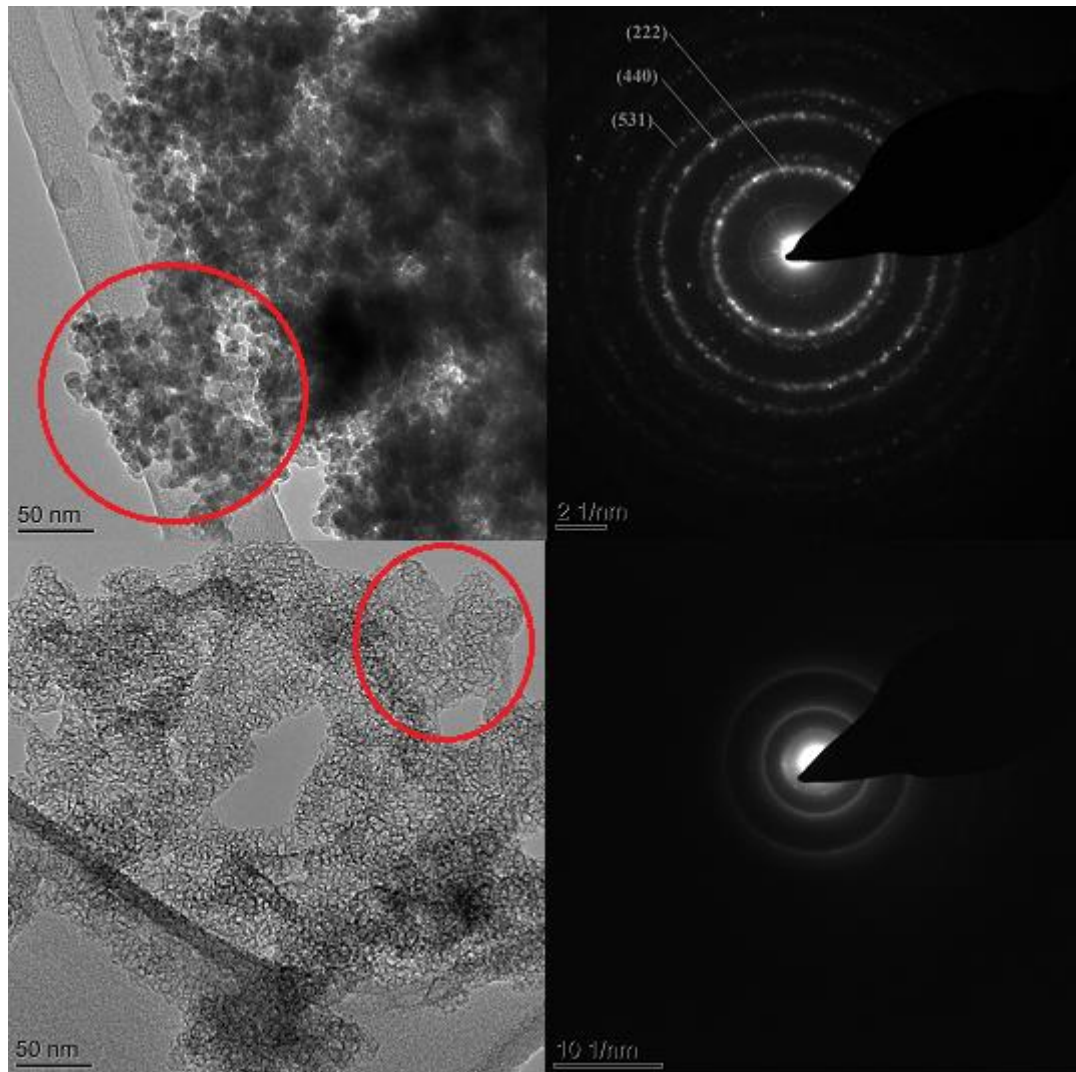
Fig. 4.72: TEM images with SAED pattern of La$_2$Zr$_2$O$_7$ calcined at 700°C for 6h.

Table 4.18: Comparison of d-spacing of Lanthanum Zirconate from TEM and XRD Rietveld Refinement

H	K	l	Ref. (ICDD-01-084-2632) d, A°	XRD d, A°		TEM d, A°	
				700°C-6h	900°C-6h	700°C-6h	900°C-6h
2	2	2	3.1144	3.0056	3.1086	3.24	3.11

4	0	0	2.6972	2.6064	2.6931	2.43	2.75
3	3	1	2.4751	Not formed	2.4718	Not formed	2.49
4	4	0	1.9072	1.8478	1.9056	1.65	1.97
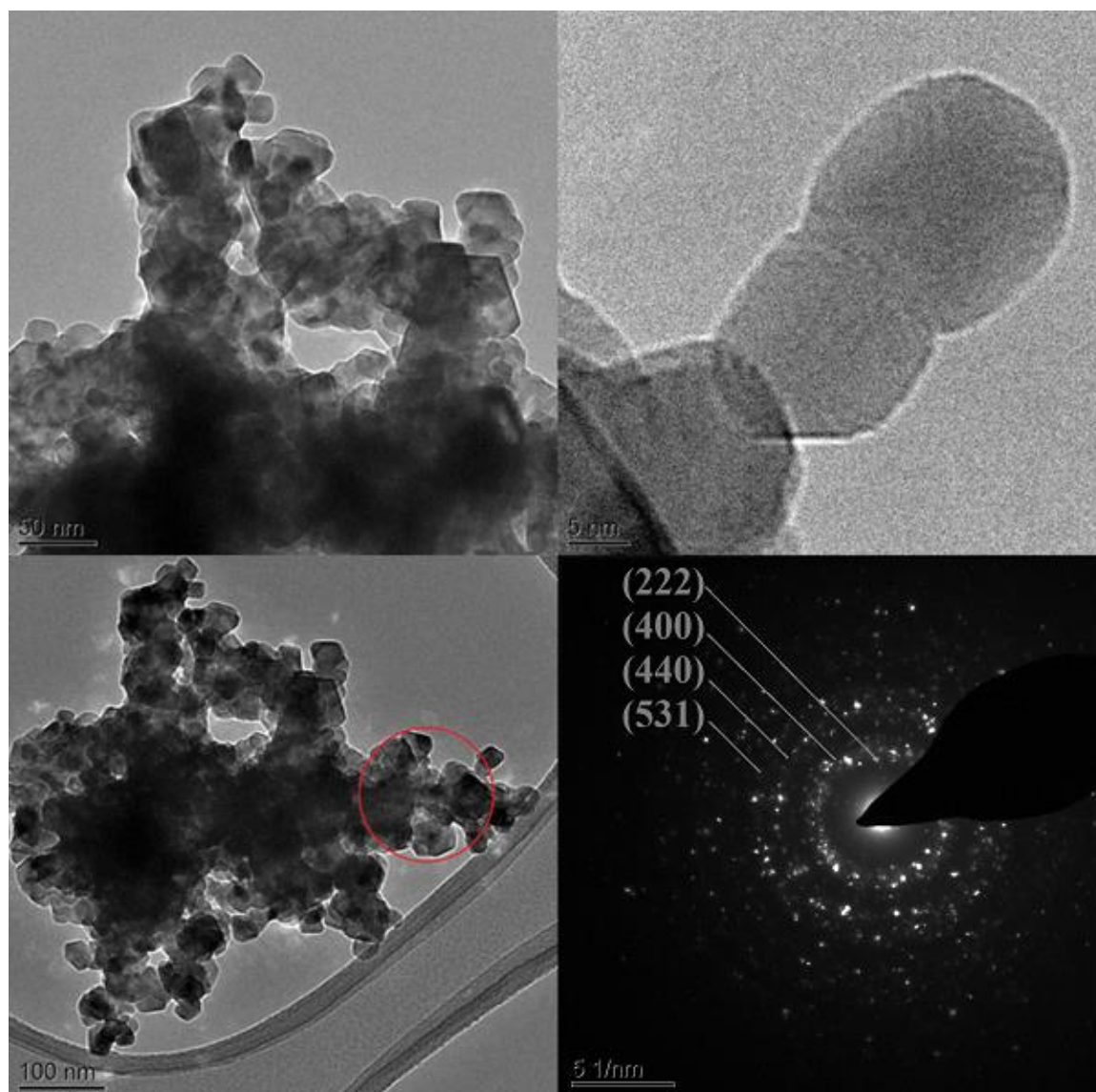
Fig. 4.73: TEM images with SAED pattern of La$_2$Zr$_2$O$_7$ calcined at 900°C for 6h

TEM-EDX was performed on the nanopowders of La$_2$Zr$_2$O$_7$ to confirm the composition of synthesised material. The atomic % of elements found from the EDX analysis are in good agreement with the chemical formula of the lanthanum zirconate. The average composition of

lanthanum zirconate found after the analysis is $La_{1.97}Zr_{2.03}O_7$ and the results are within error of TEM-EDX analyses. Lanthanum zirconate composition found using TEM-EDX is in good agreement with the one measured using calorimetry technique [194]. Fig. 4.73 shows the X ray mapping of lanthanum zirconate nanopowders obtained from SEM-EDX. EDX elemental mapping has obtained from the SEM image in Fig. 4.74 (a). Elemental mapping of lanthanum zirconate is shown in Fig. 4.74 (b, c & d) which show the uniform distribution of lanthanum, zirconium and oxygen in the sample of nanopowders.
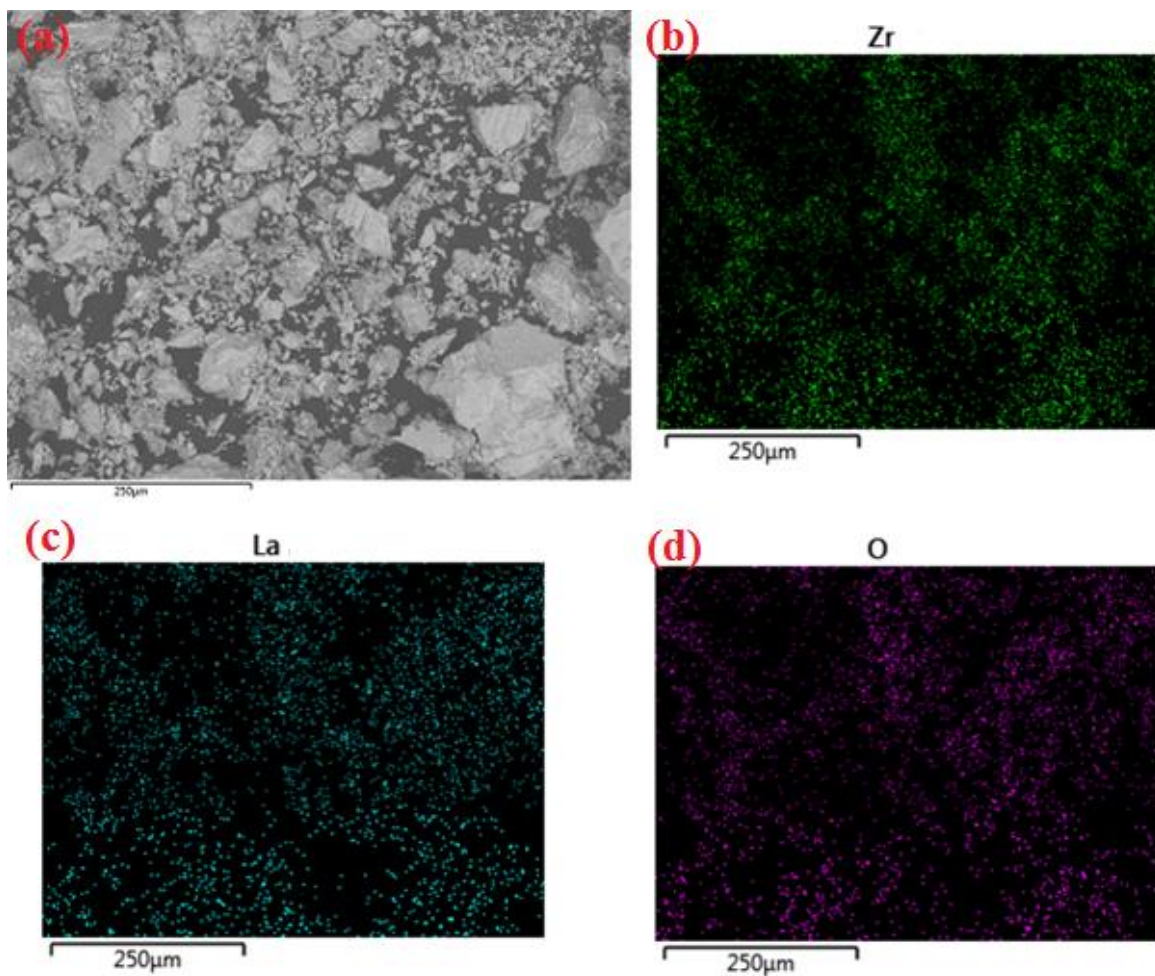
Fig. 4.74: SEM-EDX mapping of lanthanum zirconate nanopowders (a) SEM image of nanopowders (b, c, d) EDX elemental mapping of nanopowders

4.4.2. Sintering and Microstructural Characterisation

Nanopowders of lanthanum zirconate obtained after calcining at 900 ˚C were pressed into pellets and sintered over the temperature range of 1100 ˚C to 1500 ˚C. These pellets are then analysed with XRD to study the stability of the synthesised material with the increase in temperature. Fig. 4.75 shows the XRD scans of $La_2Zr_2O_7$ nanopowder and pellets sintered over the temperature range of 1100 °C to1500 °C. XRD patterns of nanopowders and sintered pellets of lanthanum zirconate shows the stable cubic pyrochlore structure of $La_2Zr_2O_7$ with the space group of $Fd\bar{3}m$ over the entire range of heat treatment from 1100 ˚C to 1500 ˚C. These results confirm the stable pyrochlore structure of $La_2Zr_2O_7$ over the entire temperature range which is also in agreement with the cationic radius ratio, $r_{La}/r_{Zr} = 1.61$, as suitable ionic radii for the formation of the pyrochlore structure of $A_2B_2O_7$ type materials is $1.8 \geq (r_A/r_B) \geq 1.46$ [9].

$La_2Zr_2O_7$ nanopowders prepared through Leeds Alginate Process (LAP) at low temperature (900 °C) as compared to the ones synthesised through sintering of metal salts at 1500 °C for 24 h [194] and through co-precipitation method followed by heat treatment at 1450 °C [195].
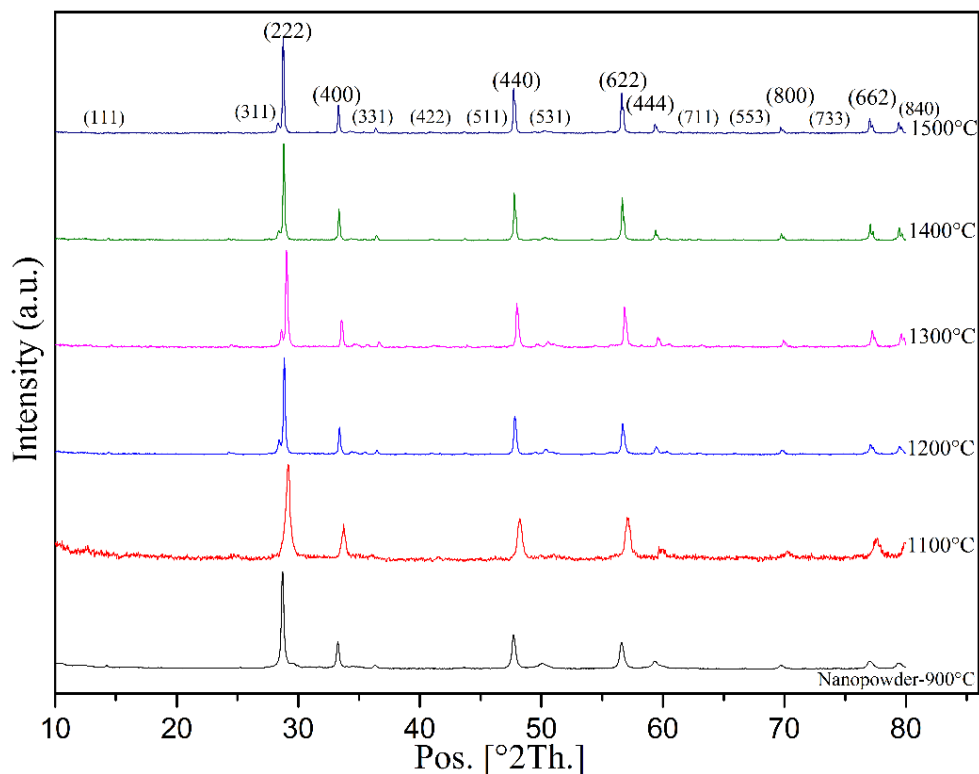
Fig. 4.75: XRD patterns of sintered lanthanum zirconate pellets. The patterns from 900°C to 1500°C are indexed by ICDD-01-084-2632 with cubic pyrochlore La$_2$Zr$_2$O$_7$ shown at the top of the peaks.

Relative density and porosity of lanthanum zirconate pellets as a function of sintering temperature is shown in Fig. 4.76, sintered with both SSS and TSS processes. Relative density curve shows the linear increase from 1100 °C to 1300 °C with density enhancement of 14 % and the corresponding decrease in porosity. There relative density reached to 93 % at 1500 °C with the improvement of ~16 %. In the TSS process, the pellet is first heated to 1500 °C corresponding to the highest relative density point obtained in SSS process so that intermediate density can be attained and then held for the prolonged duration at lower temperature of 1300 °C corresponding to the 75 % of relative density. The dotted line in the Fig. 4.76 is showing that relative density achieved at 1300 °C is above 75 %. The upward and downward arrows are pointing to the increase in relative density and corresponding decrease in porosity for the La$_2$Zr$_2$O$_7$ pellets sintered using TSS process. The relative density has reached to 99 (±0.3)% in TSS processed sample and corresponding porosity decreased to 1.0 (±0.3)%.
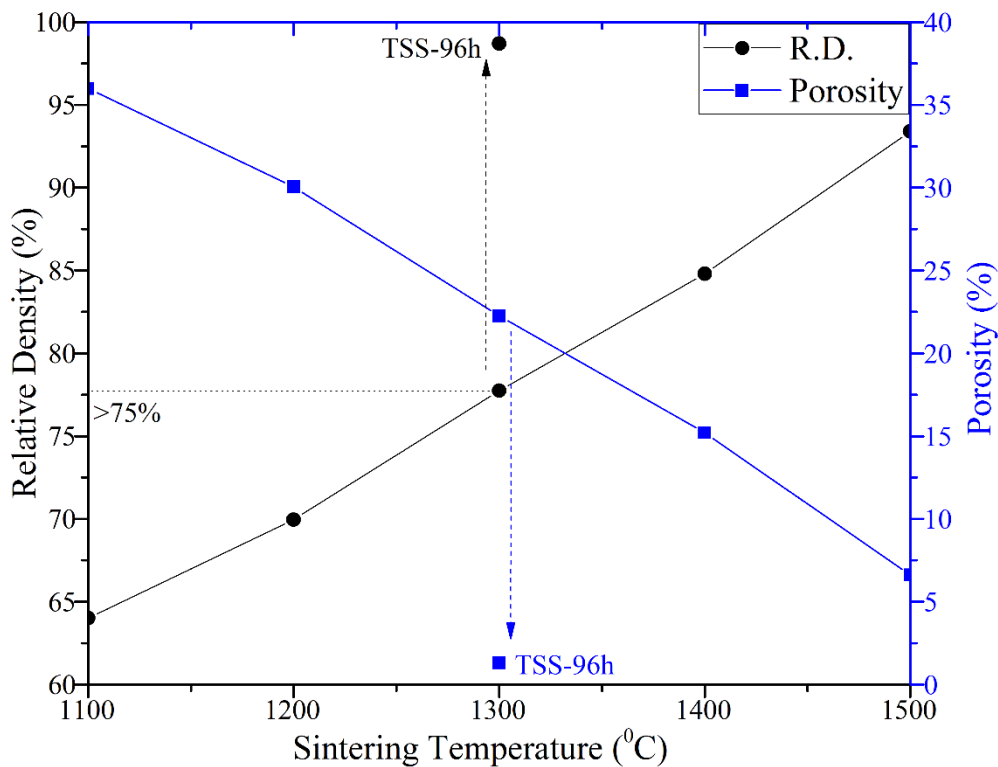
Fig. 4.76: Effect of sintering temperature on the relative density and porosity of lanthanum zirconate pellets. Two step sintering (TSS): (I) - 1500°C for 5min, (II) -1 300°C for 96h. Arrows showing increase in relative density and decrease in porosity with TSS process.

Fig. 4.78 shows the variation in grain size and relative density as a function of sintering temperature for $La_2Zr_2O_7$ pellets sintered using SSS and TSS processes. Grain size was calculated from the SEM micrographs of the pellets shown in the Fig. 4.77. It is quite evident from the SEM micrographs that with the increase in sintering temperature for SSS process relative density is increasing along with grain size (Fig. 4.78). It is noticed that increase in grain size is < 0.4 μm even though there is 14 % increase in relative density from 1100 °C to 1300 °C. This can be explained as the dispersed open pores can pin the grain boundaries and hinder the grain boundary migration which results in supressed grain growth [181, 182]. The sharp increase in grain size from 0.8 to 1.98 μm at 1500 °C (relative density ~ 93%). The reason of sharp grain growth can be referred to the open pores collapsed to form closed ones and results

in significant decrease in pore pinning which results in accelerated grain growth [182, 184]. In the samples processed with TSS shows the less grain growth ($\sim$0.9 μm) whereas the relative density reaches to 99 %, nearly 6 % greater than the SSS processed sample at 1500 °C. Dashed arrow in Fig. 4.78 points to the decrease in grain size with TSS process.
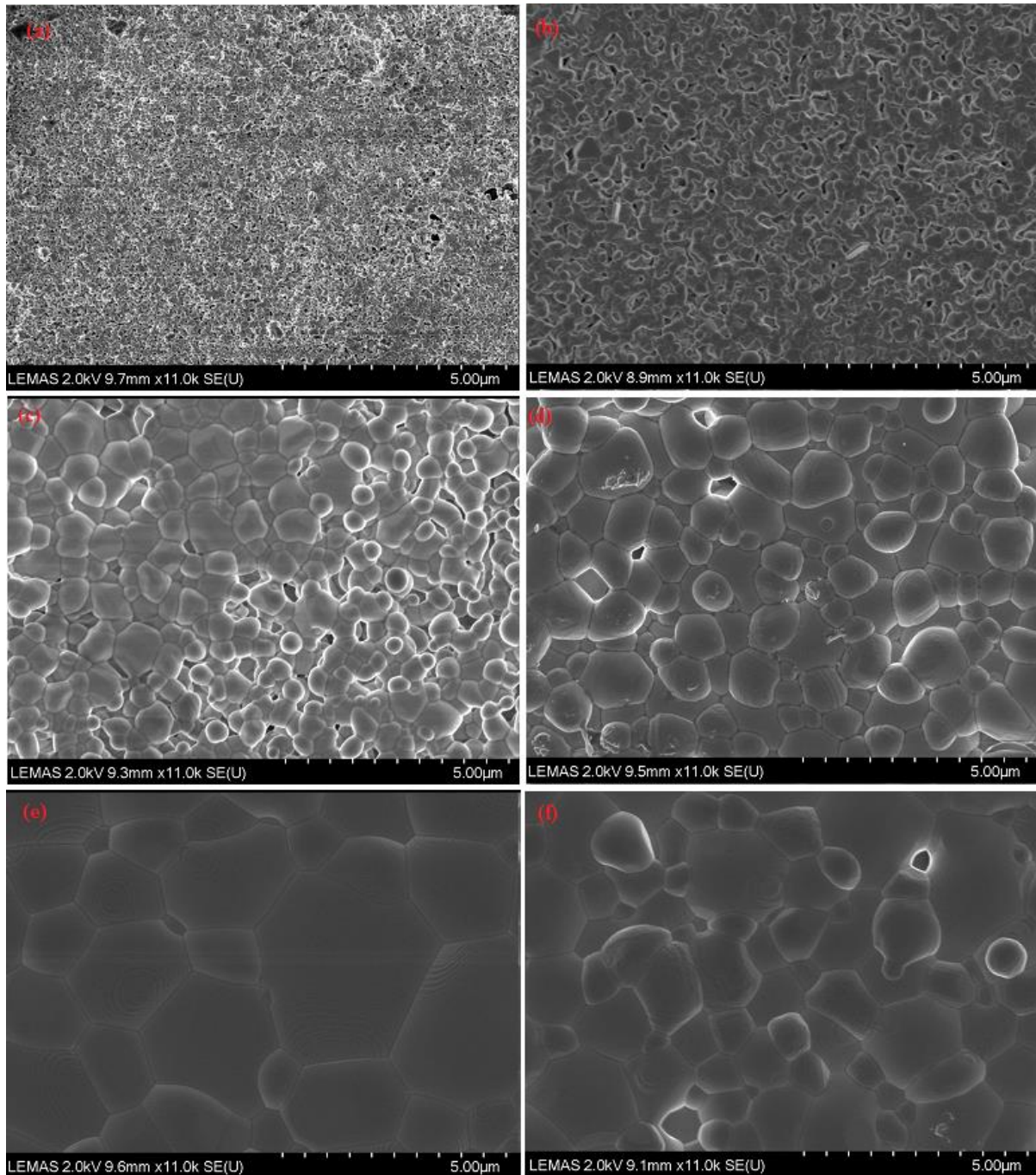
Fig. 4.77: SEM micrographs of sintered La$_2$Zr$_2$O$_7$ pellets. From (a) to (e) are the micrographs of the pellets after single step sintering (SSS) for 2h at (a) 1100 °C (b)

186

1200°C (c) 1300°C (d) 1400°C (e) 1500°C and (f) after two step sintering (TSS): (I) - 1500°C for 5min, (II) - 1300°C for 96h.

Achievement of a better density during the TSS process may also have resulted from the reduced entrapped gas pressure within micropores at a lower temperature (step-II) because the gas pressure decrease may not be able to prohibit the mass transport caused by diffusion mechanisms [185]. The variation in density and grain growth of $La_2Zr_2O_7$ samples sintered with SSS and TSS processes are in good agreement with the micrographs in the Fig. 4.77. Hence, the TSS process has proved to be a better approach to attain greater densification of $La_2Zr_2O_7$ nanopowders ceramic sample with supressed grain growth as second sintering step proceeds with a frozen microstructure and has slower diffusion kinetics that is sufficient to achieve maximum density [116]. Similar results were obtained for the $Ho_2Hf_2O_7$, $Ho_2Zr_2O_7$ and $La_2Hf_2O_7$ and earlier investigation of the group for cerium gadolinium oxide (CGO) [172].
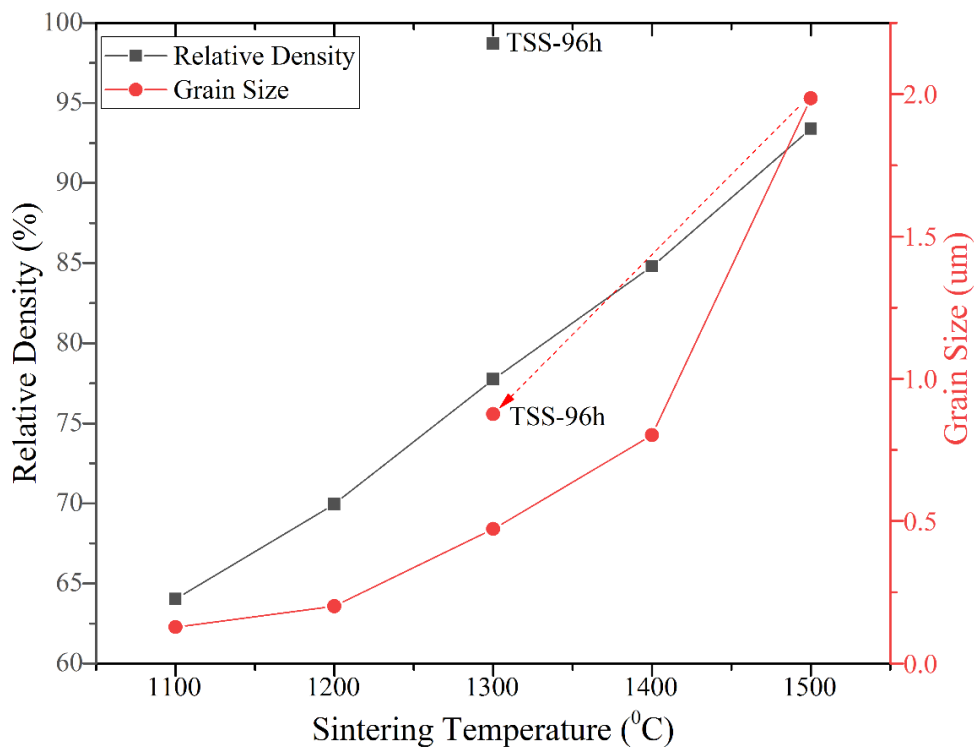
Fig. 4.78: Relative density and grain size of $La_2Zr_2O_7$ ceramics as a function of sintering temperature. TSS-96h shows the grain size for the pellet sintered with TSS process.

4.4.3. AC Impedance Spectroscopy

The Nyquist plots of $La_2Zr_2O_7$ sintered at 1500 °C for 2 h using SSS process measured at 400°C and 550 °C are shown in Fig. 4.79. The complex impedance plots shows the single semicircle over the entire range of measurement from 400 °C to 800 °C which is the indication of just bulk contribution towards the conductivity. The radius of the semicircle decreased with the increase in measurement temperature indicating the thermally activated conduction mechanism in operation over the studied temperature range [173]. Complex impedance plots in Fig. 4.79 (a & b) suggests a single relaxation process as no sign of grain boundary or electrode effects was observed [186]. The reproducible Nyquist plots show consistent results in the heating and cooling cycles over the entire temperature range indicates the reversible response of $La_2Zr_2O_7$ ceramic electrolyte. This behaviour of responding reversibly is very important for the solid electrolytes used to design chemical sensor that is subject to temperature variation [159].
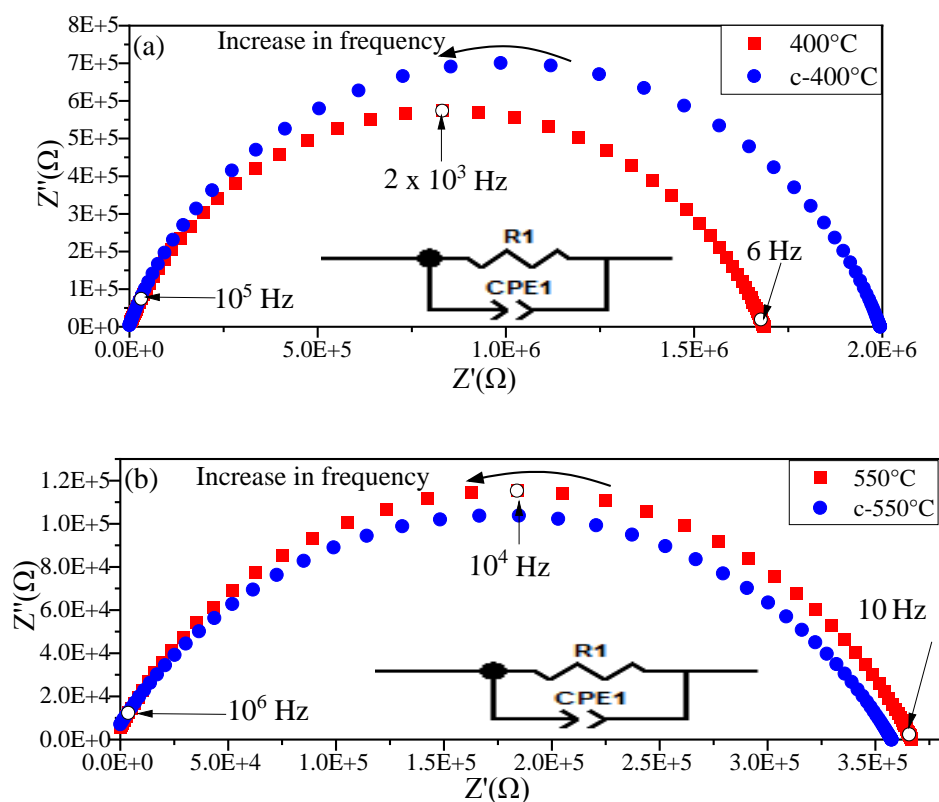
Fig. 4.79: Complex impedance plots for La$_2$Zr$_2$O$_7$ sintered at 1500°C for 2h measured in heating cycle at (a) 400°C and (b) 550°C, (c-400°C and c-550°C for cooling cycle).

Temperature dependent Arrhenius plot of bulk conductivity of La$_2$Zr$_2$O$_7$ ceramic pellet sintered using SSS process is shown in Fig. 4.80 for both heating and cooling cycles. The value of activation energy for ionic conduction in La$_2$Zr$_2$O$_7$ has obtained by plotting $ln\sigma T$ against $1/T$ for ionic conductivity of single step sintered pellet measured over the range of 350 °C to 800 °C and frequency range of 100 mHz to 100 MHz for both heating and cooling cycles. The ionic conductivity increased with the increase in temperature as clearly seen from the behaviour of Arrhenius plot in Fig. 4.80 confirming that the ionic conductivity in the material is thermally activated. The rise in ionic conductivity over the temperature range is from 1.01×10^{-7} S.cm^{-1} at 350 °C to 6.70×10^{-6} S.cm^{-1} at 800 °C. The average value of activation energy for bulk ionic conduction has been found to be 0.62 ($\pm$0.02) eV after combining data for heating and cooling cycles.

Fig. 4.80: Temperature dependence Arrhenius plot of bulk conductivity in heating and cooling cycles of lanthanum zirconate pellets sintered at 1500°C for 2h using SSS process.

Frequency dependence of the real components of conductivity for SSS processed $La_2Zr_2O_7$ material (log-log representation) for both heating and cooling cycles is shown in Fig. 4.81. Bulk contribution for conductivity and its dependence on frequency is shown in Fig. 4.81 over the temperature range of 350°C to 800°C. Another important characteristic feature of ion conducting solids is blocking effect which is also evident in this type of log-log representation. At lower temperature there is decrease in conductivity at lower frequencies. The frequency dispersive region separating low frequency and high frequency zones shifts towards higher frequencies with increase in temperature and leads above 700°C to a regime where conductivity is almost frequency independent as shown in Fig. 4.81 (a & b). The regimes are consistent with heating and cooling cycles.

Frequency dependence of the real components of conductivity for SSS processed $La_2Zr_2O_7$ material (log-log representation) for both heating and cooling cycles is shown in Fig. 4.81. Bulk contribution for conductivity and its dependence on frequency is shown in Fig. 4.81 over the temperature range of 350 °C to 800 °C. Another important characteristic feature of ion conducting solids is blocking effect which is also evident in this type of log-log representation. At lower temperature there is decrease in conductivity at lower frequencies. The frequency dispersive region separating low frequency and high frequency zones shifts towards higher frequencies with increase in temperature. The regimes are consistent with heating and cooling cycles.
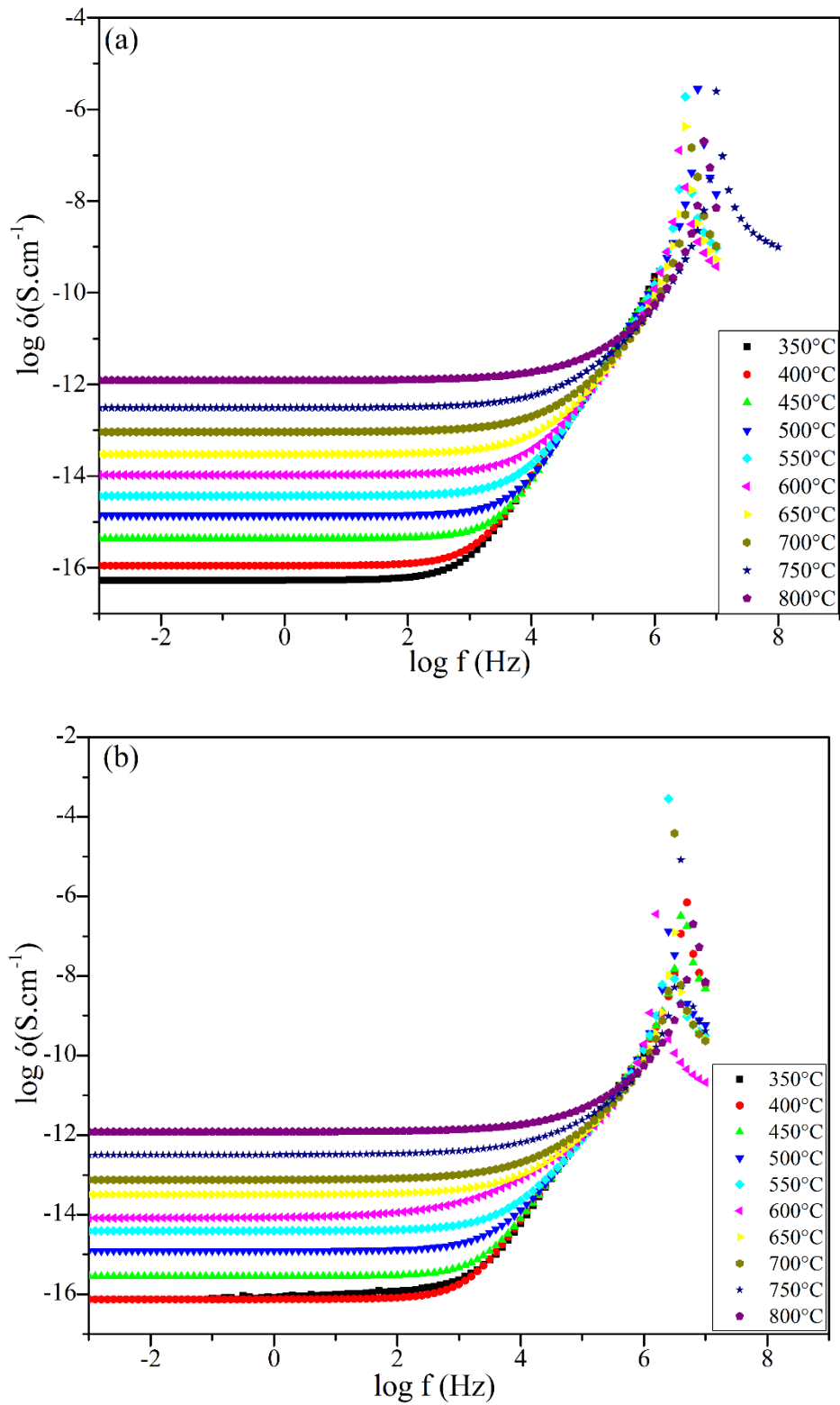
Fig. 4.81: Frequency and temperature dependence of the real parts of La$_2$Zr$_2$O$_7$ conductivity (a) heating (b) cooling sintered using SSS process.

Results of the impedance spectroscopy measurements at 400 °C and 550 °C of $La_2Zr_2O_7$ ceramic pellets sintered using the two step sintering (TSS) process are shown in the Fig. 4.82. Complex impedance plots of lanthanum zirconate at 400 °C and 550 °C show the single semicircle as seen in Fig. 4.82 (a & b) which is the indication of purely bulk contribution towards the ionic conductivity of the material and no sign of grain boundary contribution over the entire temperature range of measurement for both heating and cooling cycles.
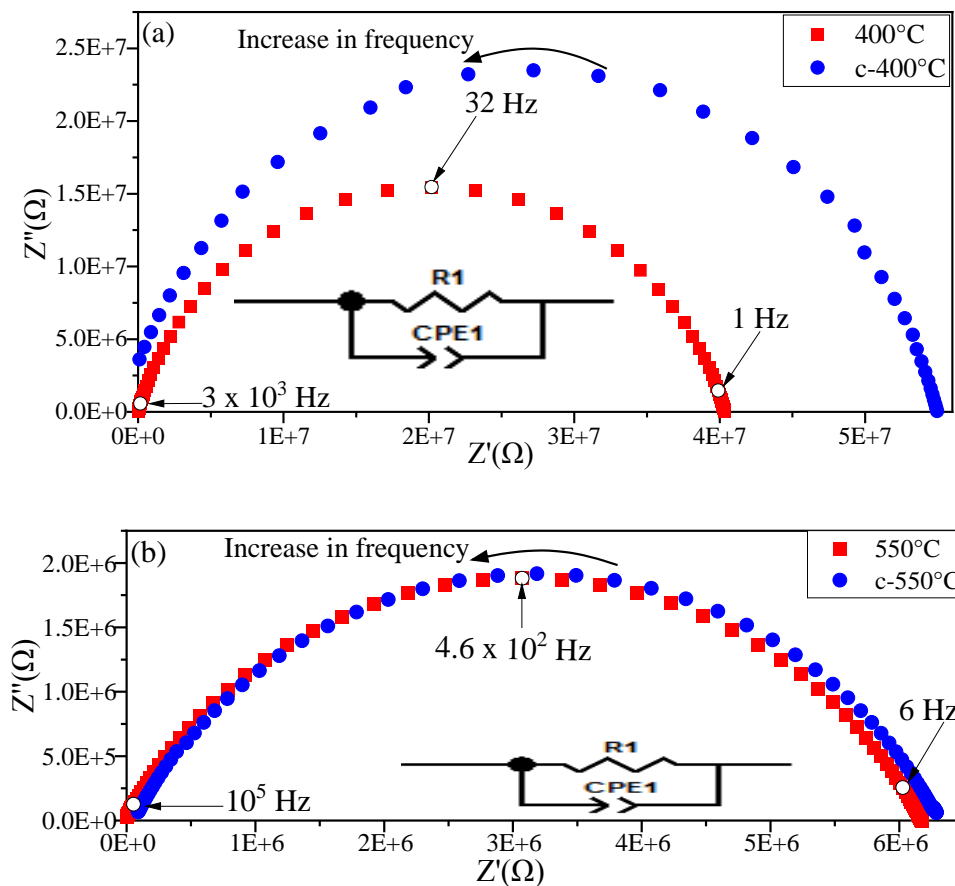
Fig. 4.82: Complex impedance plots for $La_2Zr_2O_7$ with two step sintering; (I) - 1500°C for 5min, (II) - 1300°C for 96h measured in heating cycle at (a) 400°C and (b) 550°C (c-400°C and c-550°C for cooling cycle).

Temperature dependence of bulk and grain boundary conductivity of $La_2Zr_2O_7$ pellets sintered using TSS process in both heating and cooling cycles, calculated from the data of impedance measurement are shown in Fig. 4.83 as Arrhenius plots. The inconsistency in the heating and

cooling cycles of ionic conductivity plot was observed at the start of measurement and bit at the higher temperature. The average value of activation energy for bulk conductivity is 0.81 ($\pm$0.02) eV obtained from the heating and cooling cycles which is higher than that found in case of SSS processed sample of lanthanum zirconate.

The plot shows data with axes labeled $1000/T$ (K^{-1}) on the x-axis and $\ln \sigma T (S.cm^{-1}.K)$ on the y-axis, with Heating (red squares) and Cooling (blue circles) legend entries. Text annotations read:

$$\ln \sigma T = -9.5 \times 10^3\ T^{-1} + 1.23$$

$$E_a = 0.81\ eV$$
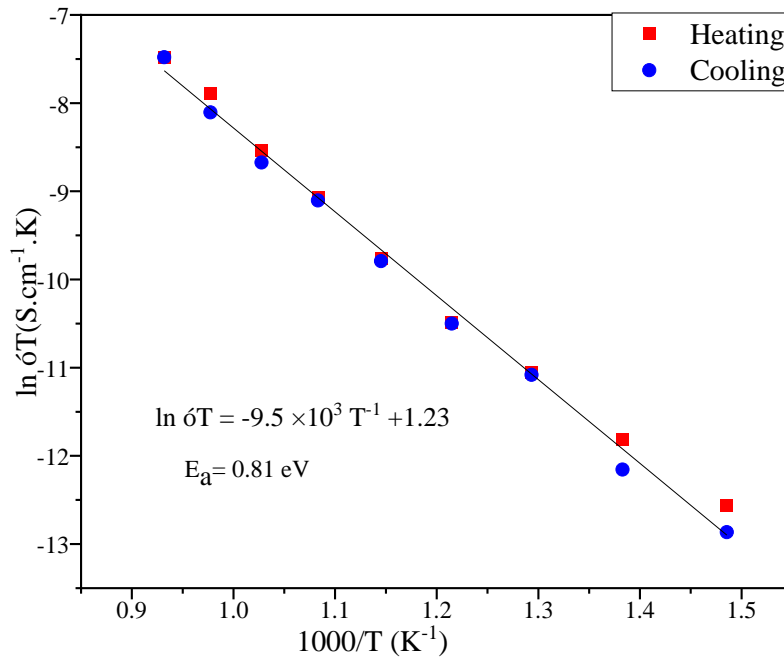
Fig. 4.83: Temperature dependence Arrhenius plots of bulk conductivity for both heating and cooling cycles of lanthanum zirconate prepared using TSS process.

Fig. 4.84 shows the frequency dependence of the real components of conductivity for TSS processed $La_2Zr_2O_7$ material (log-log representation) for both heating and cooling cycles. The results are almost consistent for heating and cooling cycles as seen in Fig. 4.84 (a & b). There found a dispersion in the conductivity at low frequencies whereas at higher frequencies the curves converge to the same value.
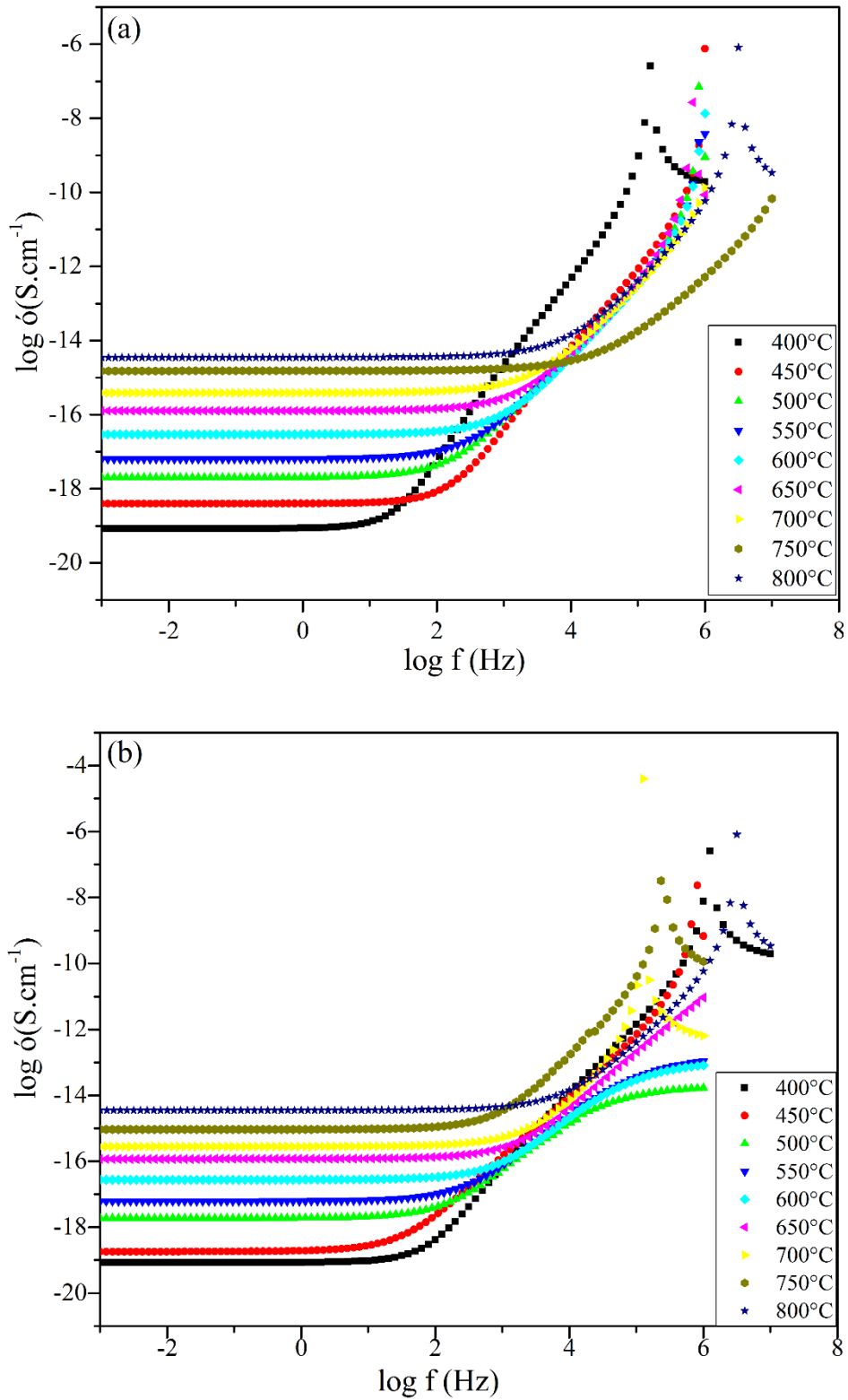
Fig. 4.84: Frequency and temperature dependence of the real parts of La₂Zr₂O₇ conductivity (a) heating (b) cooling sintered using TSS process.

Fig. 4.85 compares the Arrhenius plots of bulk conductivity of $La_2Zr_2O_7$ ceramic pellets sintered using both SSS and TSS processes. The fitted curve shows that at lower temperature the values of ionic conductivity for TSS processed sample are three order of magnitude less than that of SSS processed sample of lanthanum zirconate. The gap is reducing with the increase in temperature and sample sintered with SSS process shows nearly two order of magnitude higher ionic conductivity than that of TSS processed sample. The value of activation energy is lower for SSS process than that of TSS process as seen in Table 4.19. The results of ionic conductivity for SSS and TSS processed sample of lanthanum zirconate are contrary to the one obtained in case of lanthanum hafnate, where TSS processed sample shows higher ionic conductivity than that of SSS processed sample.
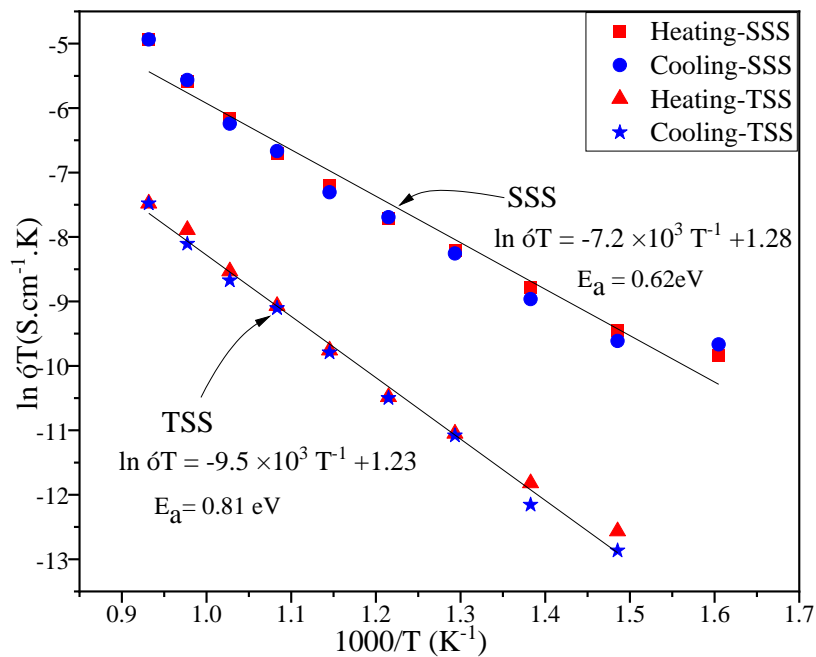
Fig. 4.85: Comparison of temperature dependence Arrhenius plots of bulk conductivity for both heating and cooling cycles of lanthanum zirconate prepared using SSS and TSS processes.

Table 4.19 compares the values of activation energy, R^2 values and ionic conductivity for lanthanum zirconate samples sintered using SSS and TSS processes at 550 °C and 800 °C. The

grain boundary contribution was not noticed throughout the temperature measurement range for both SSS and TSS processed samples.

Table 4.19: Corresponding activation energies and conductivity values of SSS and TSS processed La$_2$Zr$_2$O$_7$

Sample	Activation Energy (eV)	R^2 value	Conductivity at 550°C S.cm^{-1}	Conductivity at 800°C S.cm^{-1}
SSS-Bulk	0.62	0.97011	5.47×10^{-7}	6.70×10^{-6}
TSS-Bulk	0.81	0.99571	3.37×10^{-8}	5.26×10^{-7}

The values of ionic conductivities of pyrochlore structured La$_2$Zr$_2$O$_7$ ceramic sample have been found significantly less than that of defect fluorite structured Ho$_2$Zr$_2$O$_7$ ceramic sample. Although synthesis route of materials and processing of ceramic pellets are same in both cases but even then ionic conductivity for holmium zirconate ceramic sample is more than three order of magnitude higher than that of lanthanum zirconate ceramic sample. This can be explained that the defect fluorite structured holmium zirconate is better ionic conductor due to the presence of oxygen vacancy in the structure. In pyrochlore structures all the cations and anions are ordered with respect to the oxygen atoms, this ordering causes the pyrochlore unit cell to double with respect to that of fluorite and drastically affects ionic and thermal conductivity [187].

4.5. Parent Oxides

Leeds Alginate Process (LAP) was used to successfully synthesise the parent oxides of the pyrochlore materials namely the holmium oxide (Ho$_2$O$_3$), hafnium oxide (HfO$_2$), lanthanum oxide (La$_2$O$_3$) and zirconium oxide (ZrO$_2$). Results from different techniques are in Appendix.

Chapter 5

Comparison of Leeds Alginate Process with Solution Method

5.1. Holmium Hafnate (Ho$_2$Hf$_2$O$_7$)

5.1.1. Structural and Morphological Characterisation

LAP describes the synthesis of holmium hafnate through the thermal decomposition of beads obtained after ion-exchange between metal salts and sodium alginate solutions.

Solution method describes the mixing of two solutions of metal nitrate salts and then evaporating the water to attain powder. The powder then heat treated similarly as beads have been treated to obtain the nanopowders.

Fig. 5.1 compares the XRD scans of powders obtained from solution and beads (LAP) methods after calcination at 700 °C for 6 h. It can be clearly seen from the XRD scan that the powder obtained through solution method is amorphous in nature. The broadness of peaks shows less crystallinity of material as compared to the one obtained from the beads method. Rietveld refined XRD scans of holmium hafnate obtained from solution method is shown in Fig. 5.2.
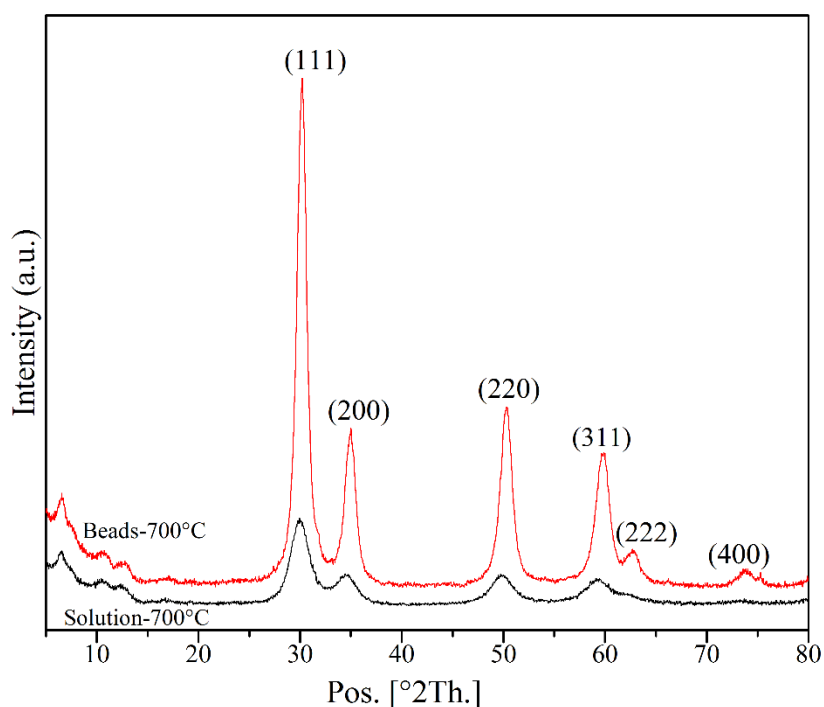
Fig. 5.1: XRD scans of holmium hafnate synthesised using both methods and calcined at 700°C

Structural parameters of holmium hafnate synthesised through both methods are shown in Table 5.1. The lesser crystallite and lesser fitting of observed and calculated pattern for solution method was observed as compared to the beads method. Lattice parameter of solution method is not in agreement with the one obtained through beads method and reported in the literature [106, 129, 130].
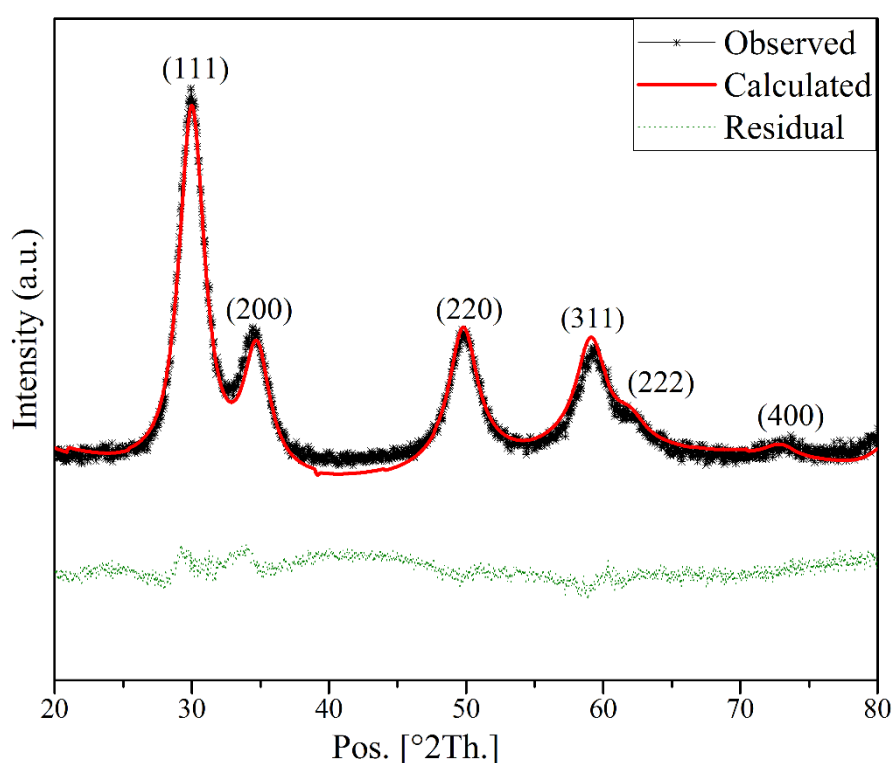
Fig. 5.2: Rietveld refined XRD analysis of holmium hafnate synthesised with solution method and calcined from at 700°C for 6h

Table 5.1: Structural parameters of Ho$_2$Hf$_2$O$_7$ synthesised using Solution method and

Beads alginate method

Sample Type	Rietveld Refined Size Strain Analysis					
	Avg. Crystallite Size (nm)	Micro Strain (%)	R$_{wp}$ (%)	R$_{exp}$ (%)	GOF	Lattice Parameters (A$^\circ$)
Solution-700˚C	2.5	5.10	9.2	3.75	6.0	5.2074
Beads-700˚C	6.10	1.18	2.84	2.45	1.34	5.1308

The holmium hafnate powder obtained from solution method was heat treated at higher temperature to figure out the point where the crystallinity in the material is similar to the one obtained from the beads method. Fig. 5.3 shows the comparison of XRD scans of powder obtained from the solution method heat treated at 1100 °C and from beads method at 700 °C for 6 h. Here, the pattern of solution method is showing the crystallinity similar to the one obtained from the beads method. Fig. 5.3 shows the XRD scans of powder heat treated from 700 °C to 1300 °C in comparison to nanopowder obtained from the beads method at 700 °C. Structural parameters of holmium hafnate obtained after rietveld refined size strain analysis are shown in Table 5.2. Increase in average crystallite size was observed with the increase in calcination temperature from 700 °C to 1300 °C due to sharpness of peaks as seen in Fig. 5.3. Observed and calculated pattern are in best agreement at 1100 °C as the GOF found is 3.62. Lattice parameters found at 1100 °C is closest to the one found in the literature for holmium hafnate. No improvement in the lattice parameters and GOF was observed at 1300 °C.
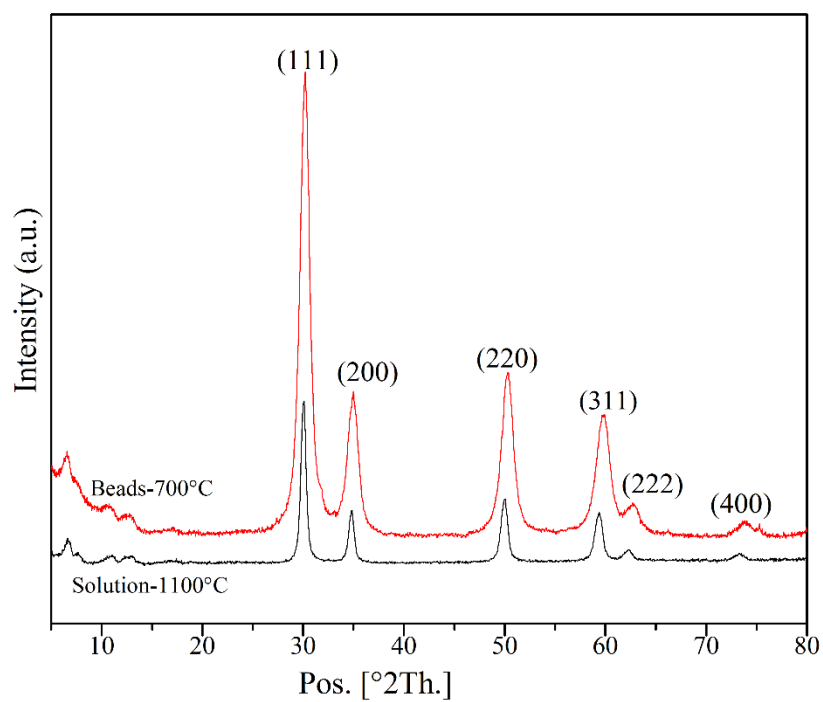
Fig. 5.3: XRD scans of holmium hafnate synthesised using both methods
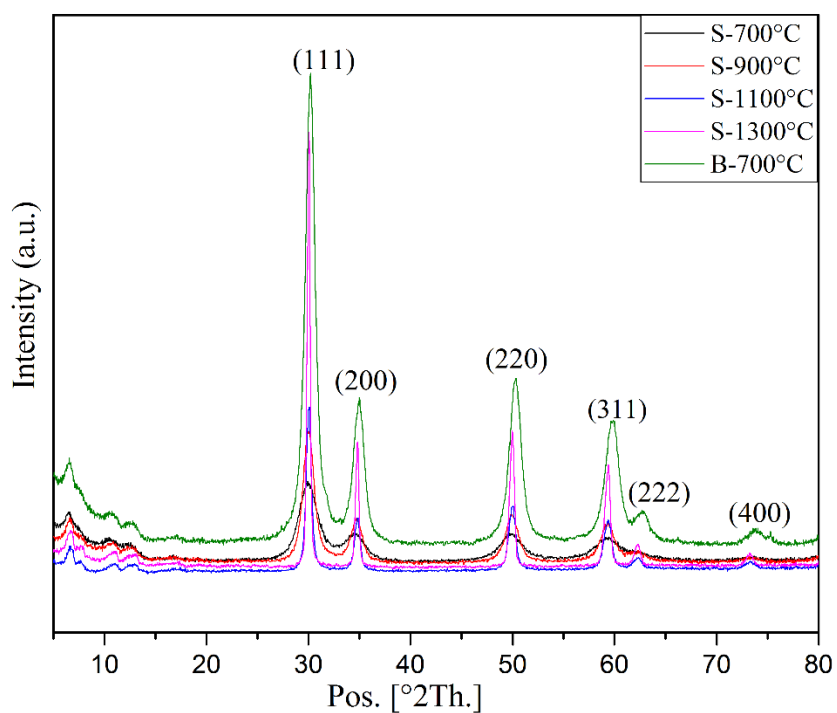
Fig. 5.4: XRD scans of holmium hafnate synthesised with solution method and calcined

from 700 to 1300°C, with bead method calcined at 700°C

Table 5.2: Structural parameters of $Ho_2Hf_2O_7$ synthesised using solution method and calcined from 700°C to 1300°C

Sample Type	Rietveld Refined Size Strain Analysis					
	Avg. Crystallite Size (nm)	Micro Strain (%)	R_{wp} (%)	R_{exp} (%)	GOF	Lattice Parameters (A°)
Solution-700°C	2.5	5.10	9.2	3.75	6.0	5.2074
Solution-900°C	5.1	2.91	8.13	3.84	4.48	5.1810
Solution-1100°C	12	1.24	9.28	4.88	3.62	5.1766
Solution-1300°C	24.7	0.60	9.47	4.25	4.97	5.1776

Morphological analysis of holmium hafnate powder obtained after solution method is using TEM is shown in Fig. 5.5. TEM image and SAED pattern are showing the amorphous of nature of the powder obtained. The rings of SAED pattern shows very less crystallinity than that of the nanopowders of holmium hafnate obtained from beads method for same conditions of heat treatment. Table 5.3 compares the interplanar spacing of holmium hafnate obtained from TEM and XRD analysis along with the XRD reference pattern for both solution and beads method. TEM and XRD results are in good agreement with each other for both methods but the results obtained from the beads method are closer to the XRD reference pattern as shown in the Table 5.3.
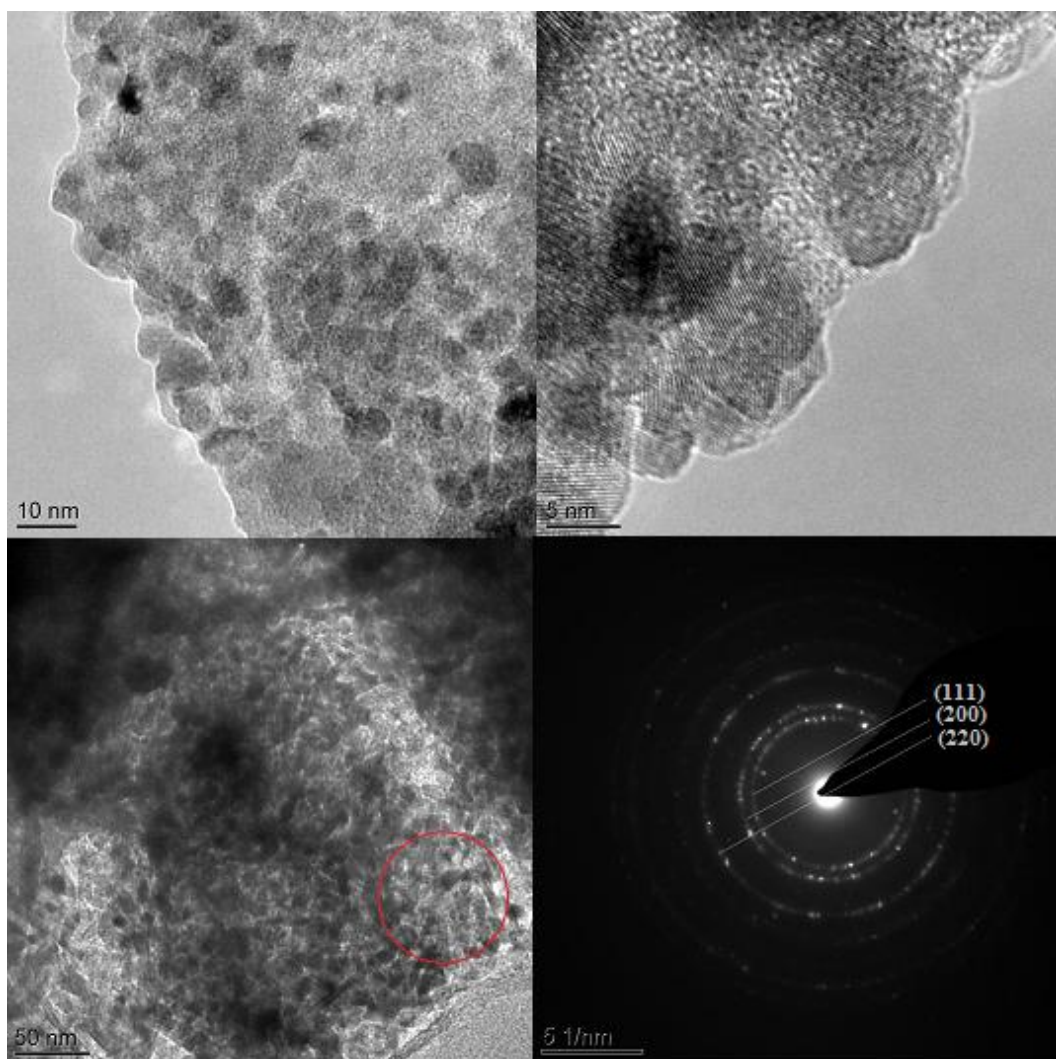
Fig. 5.5: TEM images with SAED pattern of Ho₂Hf₂O₇ calcined at 700˚C synthesised with solution method

Table 5.3: Comparison of d-spacing of Holmium Hafnate from TEM and XRD Rietveld Refinement synthesised from Solution and Alginate bead method

H	k	L	Ref. (ICDD-00-024-0473) d, A˚	Beads-700˚C		Solution-700˚C	
				XRD d, A˚	TEM d, A˚	XRD d, A˚	TEM d, A˚
1	1	1	3.00600	2.95049	2.94	2.9787	2.98
2	0	0	2.60400	2.55665	2.52	2.5830	2.37
2	2	0	1.84100	1.80979	1.78	1.8313	1.96
3	1	1	1.57000	1.54402	1.51	1.5632	1.61

The structural and morphological analysis of the holmium hafnate powders obtained from both methods revealed that the LAP (beads method) is a promising technique to obtain the nanopowders of holmium hafnate at comparatively lower temperature of 700 °C. Solution method forms the amorphous powder of holmium hafnate which after heat treatment at higher temperature of 1100 °C shows results similar to the beads method.

5.1.2. Sintering and Densification of Pellets

Holmium hafnate powder obtained from the solution method were pressed into pellets and sintered using single step sintering (SSS) and two step sintering (TSS) techniques. Relative density of pellets obtained after sintering are 33.1 % for SSS (1500°C for 2h) and 56.8 % for TSS (I- 1500°C for 5min, II- 1300°C for 96h) processed pellets and no shrinkage in the size of the pellets were observed after sintering. This behaviour can be explained that the sintering mechanism active in the powder compact is not contributing to densification and shrinkage which suggests the inactivity of grain boundary diffusion mechanism. Therefore, the grain boundary is the source of materials transport for densification and shrinkage in the crystalline powder compacts [181]. Hence, it is decided that the ceramic samples of holmium hafnate obtained through solution method are not suitable for impedance measurements therefore no further analyses were carried out.

5.2. Lanthanum Hafnate ($La_2Hf_2O_7$)

XRD pattern of lanthanum hafnate powder obtained after calcining at 900 °C for 6 h using solution method is shown in Fig. 5.6. Single phase formation of lanthanum hafnate was not observed rather some extra peaks were found which shows presence of another phase. Split peaks of lanthanum hafnate were also observed along with the second phase of lanthanum oxide (La_2O_3) as clearly seen in Fig. 5.7. XRD pattern of the powders obtained at 900 °C with

both the methods are shown in Fig. 5.7 which clearly indicates the presence of lanthanum oxide

phase along with lanthanum hafnate in case of solution method synthesis.
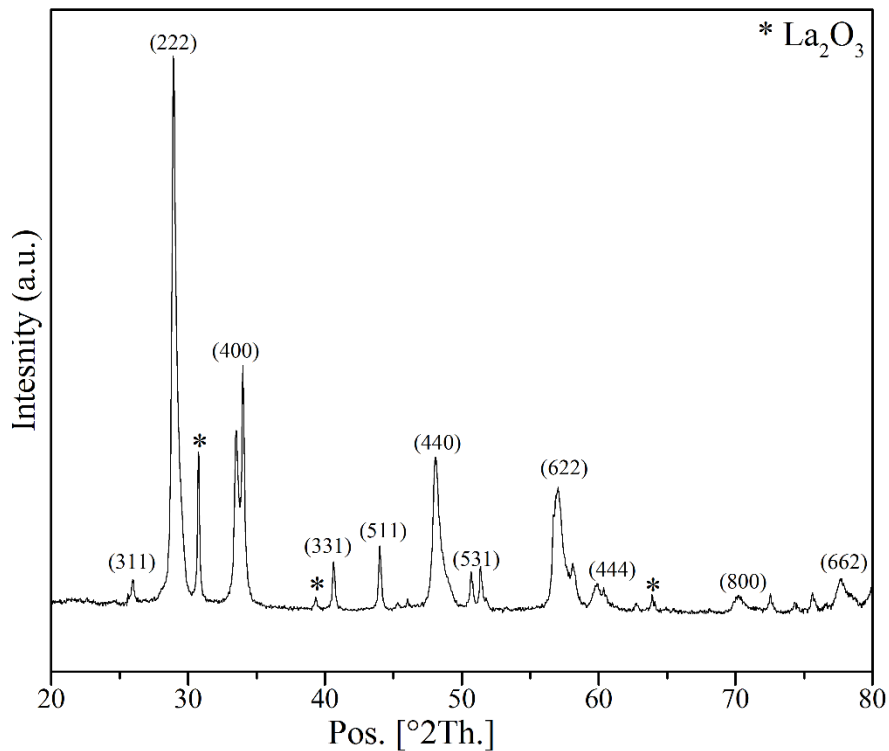
Fig. 5.6: XRD scans of Lanthanum hafnate synthesised using solution methods and calcined at 900°C for 6h

Fig. 5.8 shows the rietveld refined XRD pattern of lanthanum hafnate from solution method. The observed and the calculated pattern are not in good agreement with each other and the structural parameters obtained after rietveld refined size strain analysis are presented in Table 5.4. Lattice parameters of lanthanum hafnate obtained from the solution method are not in agreement with the one obtained from beads method and found in the literature [176, 177].
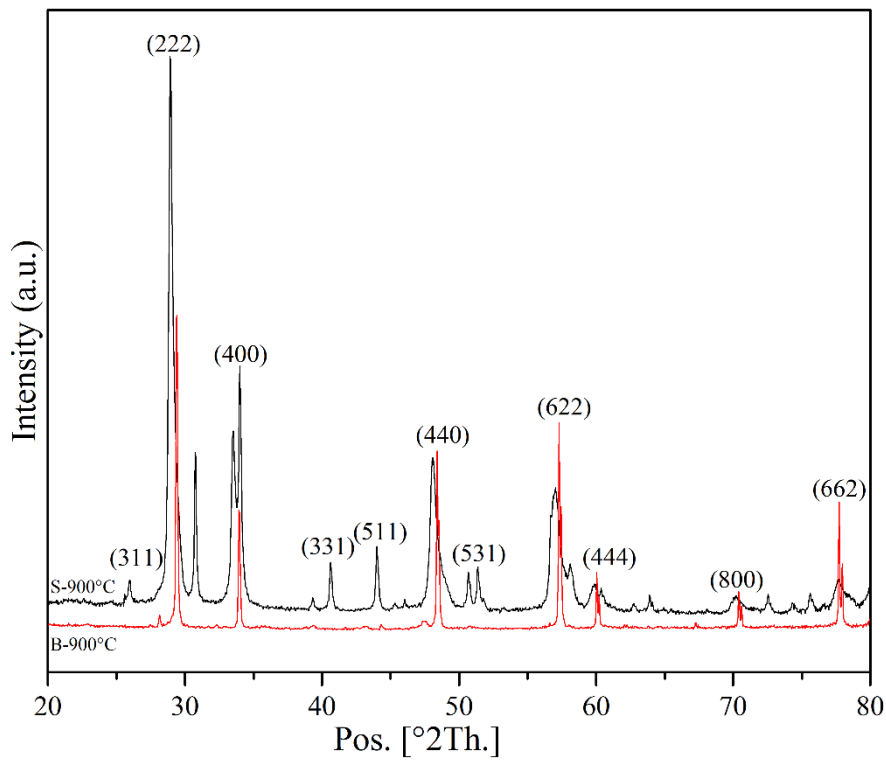
Fig. 5.7: XRD scans of lanthanum hafnate synthesised using both methods and calcined at 900°C
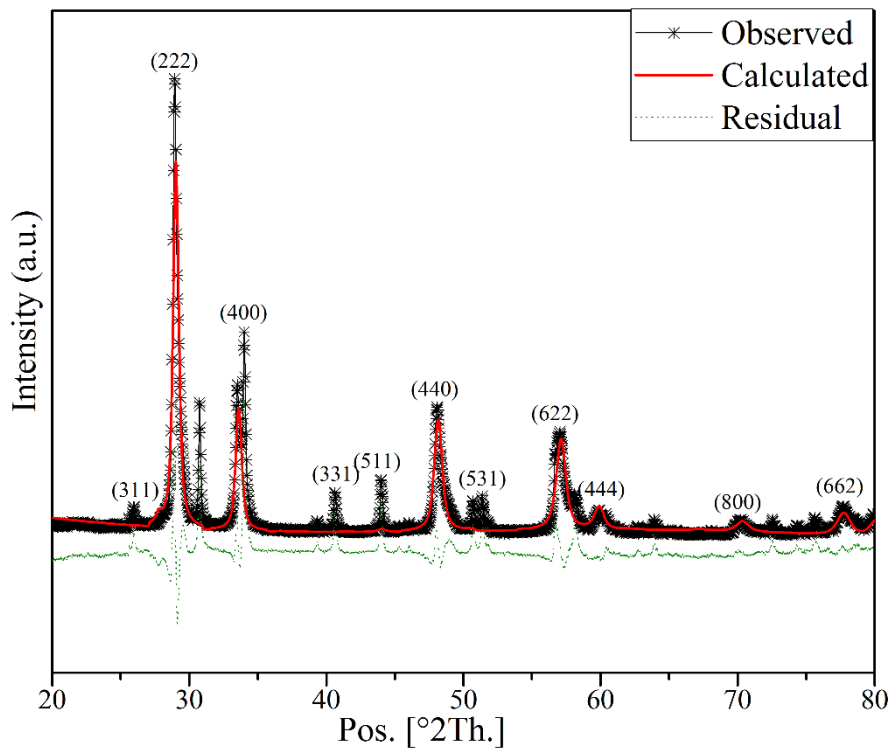
Fig. 5.8: Rietveld refined XRD data of lanthanum hafnate synthesised using solution methods and calcined at 900°C

Table 5.4: Structural parameters of La$_2$Hf$_2$O$_7$ synthesised using Solution method and Beads alginate method

Sample Type	Rietveld Refined Size Strain Analysis					
	Avg. Crystallite Size (nm)	Micro Strain (%)	R$_{wp}$ (%)	R$_{exp}$ (%)	GOF	Lattice Parameters (A°)
Solution-900˚C	14.3	1.07	25.3	3.92	41.5	10.7325
Beads-900˚C	20.8	0.78	22.9	4.28	28.6	10.7726

Morphological analysis of powder obtained through solution method is carried out using TEM and images and SAED pattern are shown in the Fig. 5.9. The bigger grain size is due to the calcination temperature (900 °C).
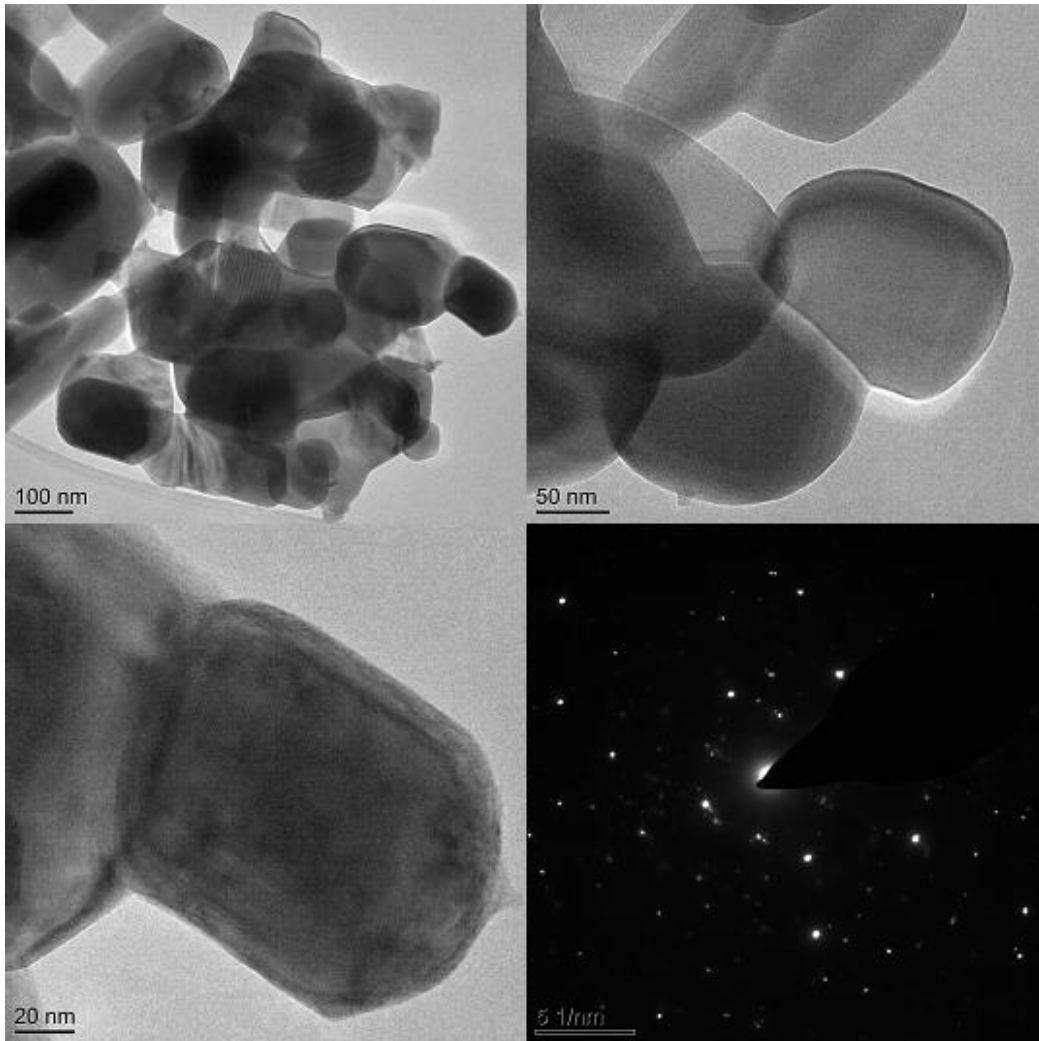
Fig. 5.9: TEM images with SAED pattern of La₂Hf₂O₇ calcined at 900˚C synthesised with solution method

TEM images are showing some amorphous grains with very less crystallinity which can also be seen from the SAED pattern. SAED pattern is not showing proper rings corresponding to the peaks of lanthanum hafnate material which indicates the presence of the impurity (La_2O_3) in it.

Table 5.5 compares the interplanar spacing corresponding to lanthanum hafnate peaks from TEM and Rietveld refined XRD analyses for both alginate beads and solution methods. The values of interplanar spacing obtained from TEM for solution method are showing much difference from the reference pattern apart from the major peak (222). The values obtained

from the XRD after rietveld refinement are in good agreement with beads method and reference pattern as well.

Table 5.5: Comparison of d-spacing of Lanthanum Hafnate from TEM and XRD Rietveld Refinement synthesised from Solution method and Alginate beads method

H	k	L	Ref. (ICDD, 01-078-5592) d, A°	Beads-900°C		Solution-900°C	
				XRD d, A°	TEM d, A°	XRD d, A°	TEM d, A°
2	2	2	3.1108	3.1015	3.16	3.0760	3.11
4	0	0	2.6940	2.6867	2.76	2.6667	2.96
4	4	0	1.9050	1.9007	1.99	1.8893	1.99
6	2	2	1.6245	1.6069	1.58	1.6124	1.41

5.2.2. Sintering and Relative density

Lanthanum hafnate powder obtained through solution method were pressed into pellet and sintered using SSS process at 1500 °C for 2 h. The relative density of the material were calculated and found 84.3 % and the diameter of the pellet was reduced to 10.88 mm from 13 mm after sintering. Hence, it is decided to carry out the impedance analysis of the pellet obtained after sintering.

5.2.3. AC Impedance Spectroscopy

Impedance measurement was carried out on the SSS sintered nanopowders over the temperature range of 400 °C to 800 °C. Complex impedance plots of the SSS processed nanopowders obtained from solution method are shown in Fig. 5.10. The results of the impedance plot at 400 °C shows a single semicircle for both heating and cooling cycles which is the indication of pure bulk contribution towards the conductivity as seen in Fig. 5.10 (a). On contrary at 550 °C two semicircles were observed which indicates the grain boundary contribution along with the bulk contribution towards the ionic conductivity as seen in Fig.

5.10 (b). The appearance of two semicircles in the impedance plots observed from 550 °C to 800 °C. The heating and cooling cycles are showing inconsistencies in the results with the increase in temperature.
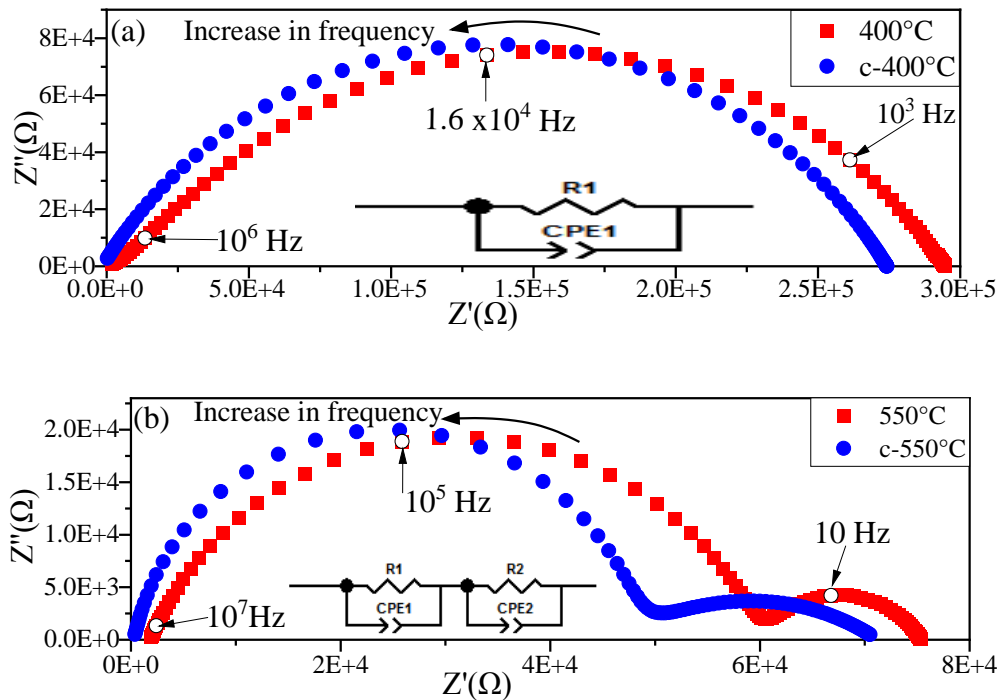
Fig. 5.10: Complex impedance plots of nanopowders obtained from solution method sintered at 1500 °C for 2h measured in heating cycle at (a) 400 °C and (b) 550 °C, (c-400 °C and c-550 °C for cooling cycle).

Temperature dependent Arrhenius plot of bulk conductivity of ceramic pellet sintered using SSS process is shown in Fig. 5.11 for both heating and cooling cycles. The value of activation energy for ionic conduction in $La_2Hf_2O_7$ (along with La_2O_3 impurity) has obtained by plotting $ln\sigma T$ against $1/T$ for ionic conductivity of single step sintered pellet measured over the range of 400 °C to 800 °C and frequency range of 100 mHz to 100 MHz for both heating and cooling cycles. The ionic conductivity increased with the increase in temperature as clearly seen from the behaviour of Arrhenius plot in Fig. 5.11 confirming that the ionic conductivity in the material is thermally activated. The bulk ionic conductivity for solution method is 2.02×10^{-5} S.cm^{-1} as compared to the one obtained from beads method 2.6×10^{-6} S.cm^{-1} at 800 °C as shown

in Table 5.6. The higher values of ionic conductivity for the biphasic material obtained from the solution method than that of beads method is due to the presence of lanthanum oxide impurity. This fact had explained in the literature [196, 197] that the presence of an insulating material in the ion conductor increases the overall ionic conductivity of the material which suggested a space charge region conductance. The presence of lanthanum oxide impurity along with lanthanum hafnate nanopowders has enhanced the ionic conductivity of ceramic sample as compared to the pure lanthanum hafnate ceramic sample, this is due to the fact that lanthanum oxide has fairly good electrical properties to act as insulators [198]. The average value of activation energy for bulk ionic conduction has been found to be 0.28 ($\pm$0.03) eV after combining data for heating and cooling cycles which is very close to the activation energy for the vacancy bulk migration (0.27-0.29) eV [196].

A comparatively steep plot of temperature dependent grain boundary conductivity was observed as shown in Fig. 5.11. The grain boundary conductivity was increasing with the increase in temperature and at 800 °C the average value of grain boundary conductivity found higher than that of bulk conductivity which is quite unexpected though. The value of grain boundary conductivity has been found to be 3.7×10^{-4} S.cm^{-1} at 800 °C The inconsistencies in the results of grain boundary conductivity for heating and cooling cycles were also observed. The average value of activation energy for grain boundary conduction has been found to be 0.84 ($\pm$0.01) eV after combining the data for heating and cooling cycles.
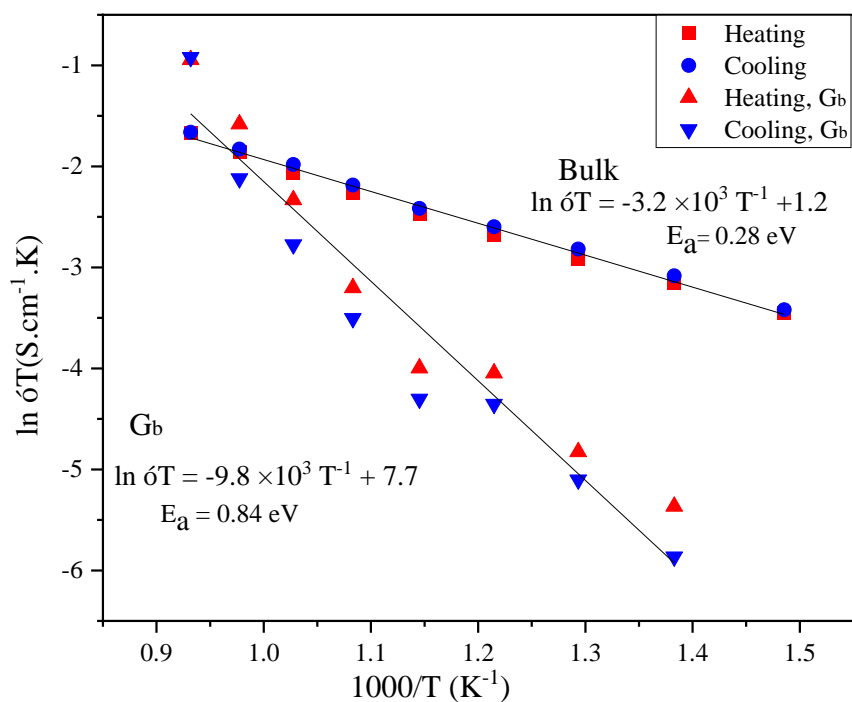
Fig. 5.11: Temperature dependence Arrhenius plot of bulk conductivity in heating and cooling cycles of nanopowders pellet sintered at 1500°C for 2h with SSS process synthesised using solution method.

Table 5.6: Corresponding activation energies and bulk conductivity values of SSS processed nanopowders obtained from beads method (BM) and solution method (SM)

Sample	Activation Energy (eV)	R^2 value	Conductivity at 600°C S.cm^{-1}	Conductivity at 800°C S.cm^{-1}
BM- Bulk	1.10	0.98822	1.5×10^{-7}	2.60×10^{-6}
SM-Bulk	0.28	0.99838	4.1×10^{-6}	2.02×10^{-5}

211

Chapter 6

Process Detail and Characterisation of LAP

This chapter consists of process details of Leeds Alginate Process (LAP) to produce nanoparticles of holmium hafnate ($Ho_2Hf_2O_7$). Details of process description and schematic diagram (Fig. 3.3) can be found in chapter 3.

6.1. Mass balance of Leeds Alginate Process (LAP)

Mass balance has been applied to all the steps of the process and a scheme of chemical reactions has been studied. The main process involves several steps including ion-exchange process, washing of beads, drying and calcination of beads. Processing of spent solution was carried out to propose the complete set of chemical reactions. TGA/DSC along with evolved gas analysis (EGA) has been performed to characterise the gaseous emissions as a result of oxidative decomposition during the calcination stage.

6.1.1. Thermoanalytical measurements for Evolved Gas Analysis (EGA)

TGA/DSC has previously been performed and mentioned in section 4.1 on the metal alginate beads to produce holmium hafnate. Here, coupled TGA/MS (Mass spectroscopy) technique is used to determine the thermal characteristics of the sample and identification of gaseous components released during heat treatment. By combining TGA with MS it is possible to gain a deep insight of oxidative decomposition process of metal alginate beads by getting more information of physical and chemical nature of the process. TGA/MS experiments were performed on the TGA coupled with MS.

6.1.2. Evolved gas analysis using TGA/MS

The composition of evolved gases with the different decomposition steps was interpreted using MS spectra through comparison of intensity of the peaks corresponding to different m/z ratios. The target signals with m/z ratios for metal alginate beads with respect to time and temperature

are presented in Fig. 6.1. Although minor signals were captured for m/z ratios of 14, 15, 16, 28, 48 and 64 as MS has the ability to detect species to 1ppm or better, and detection is done in real time as the TGA scans [199]. The target signals are focused on detecting H_2O, CO_2 and O_2 during the decomposition of metal alginate beads. There is a possibility of CO release during cracking of alginate structure and secondary reaction but the m/z ratio of carrier gas (N_2) does not allow the precise detection of CO release.
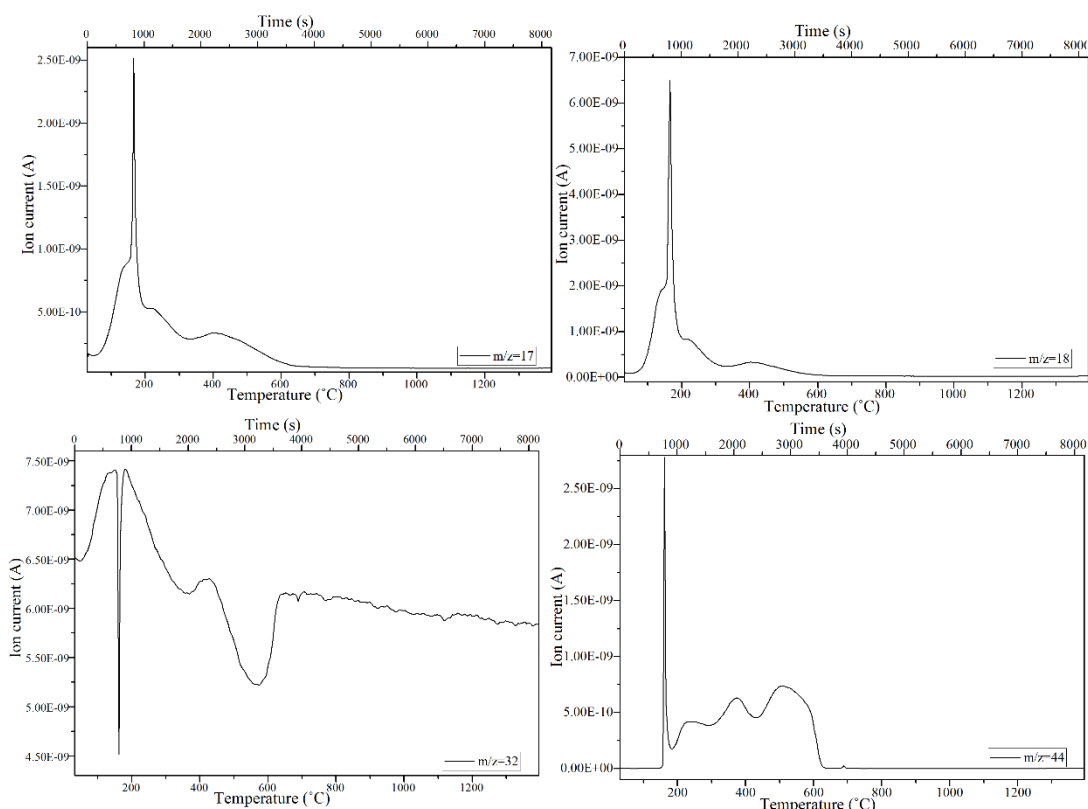
Fig. 6.1: Single ion current curves monitored using MS during decomposition of metal alginate beads for (m/z) 17, 18, 32 and 44.

During the decomposition process water release at different stage can be in the form of molecule or fragment of ion so characterized by m/z values of 17 and 18. According to ion intensities water has been released at several stages as shown in Fig. 6.1. A small bend followed by a sharp peak was observed below 200 °C which is due to the removal of moisture from the metal alginate beads [2]. Later the release of water is associated with the cleavage in alginate

213

structure and removal of hydroxyl group due to oxidative decomposition of metal alginate beads.

The signals from other m/z ratios 14, 15, 16, 48 and 64 have found negligible as compared to the intensity of carrier gas.

The release of CO_2 as a result of oxidative decomposition of metal alginate beads has been attributed to the m/z ratio 44 as shown in Fig. 6.1. MS spectra with respect to temperature and time show the major evolution of CO_2 over the temperature range of 160 °C to 565 °C and a minor kink was also observed from 685 °C to 695 °C. CO_2 evolution is found to be relevant with the decomposition of the organic structure in the metal alginate beads. Detection of CO_2 from the evolved gas analysis (EGA) confirms the decomposition of alginate structure in the TGA/DSC analysis in Section 4.1 [124]. The detection of O_2 signal corresponding to the m/z ratio 32 shows the decrease in oxygen release over the temperature range as the oxygen is being consumed by the metal alginate beads for oxidative decomposition which results in CO_2 release. The signals corresponding to all the target m/z ratios are in excellent agreement with each other over the temperature range. An increase (sharp upward peak) in signals of H_2O and CO_2 with corresponding decrease (sharp downward peak) in O_2 signals around 150 °C to 210 °C has been observed which is due to the consumption of oxygen by alginate structure for decomposition.

Oxidative decomposition of metal alginate beads has also been confirmed by doing the TGA/DSC analysis in N_2 environment as shown in Fig. 6.2. Apart from changing the media all other parameters are exactly the same as already reported [124] or found in Section 4.1.
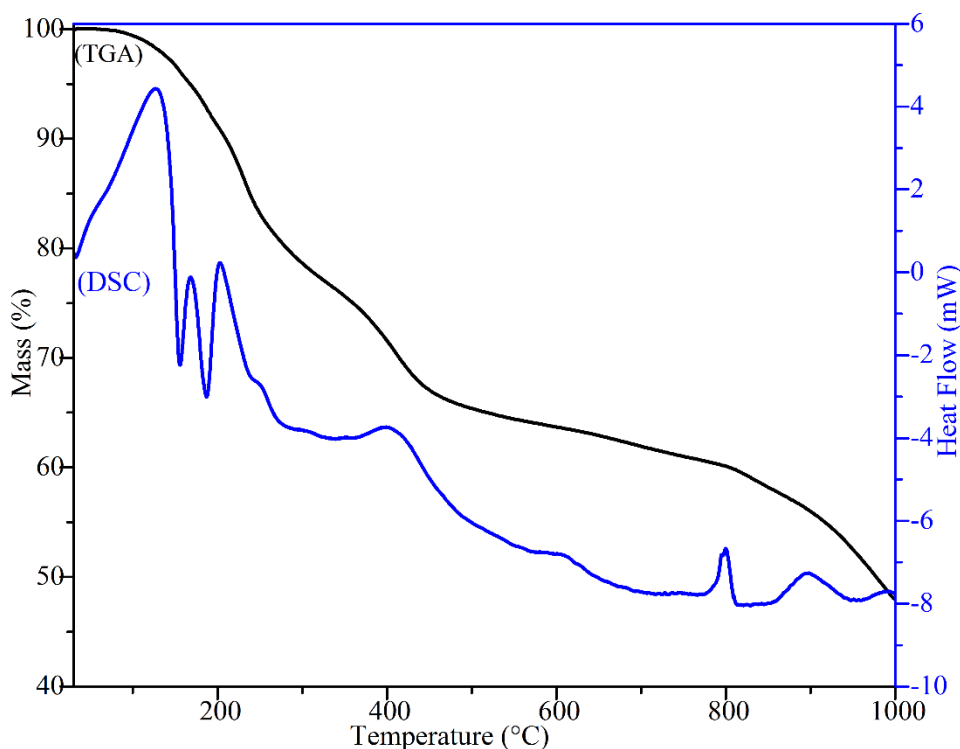
Fig. 6.2: TGA/DSC analysis of metal alginate beads in N$_2$ environment.

Exothermic peaks in the DSC curve are downwards and endothermic peaks are upwards contrary to the previous ones as the equipment used for N$_2$ media is different. TGA curve shows that the weight loss of metal alginate beads is due to the increase in temperature. Fig. 6.2 shows that the observed weight loss is half of the original weight (50%) even though the temperature has increased to 1000 °C indicating no decomposition of alginate structure. DSC curve shows the peaks and bends due to the thermal decomposition and no major exothermic peak was observed for CO$_2$ release over the temperature range of 370 °C to 485 °C, which is due to the oxidative decomposition of metal alginate beads as in Section 4.1. In case of O$_2$ environment the weight loss reached to 20% (Section 4.1).

Hence, evolved gas analysis and TGA/DSC in nitrogen environment confirmed the oxidative thermal decomposition of metal alginate beads not just pyrolysis.

6.1.3. Quantification of evolved gas analysis (EGA) data

TGA coupled with mass spectroscopy are usually used for detection and identification of evolved gases. It is beneficial to derive the quantitative information of evolved gases to propose the set of chemical reactions. It is useful to understand how the total weight loss is distributed among different components. When the mass spectrometer is attached with the TGA then it is possible to analyse the ion current data for a specific m/z ratio corresponding to the weight loss in the TGA curve. Fig. 6.3 shows the TGA and MS data for water.
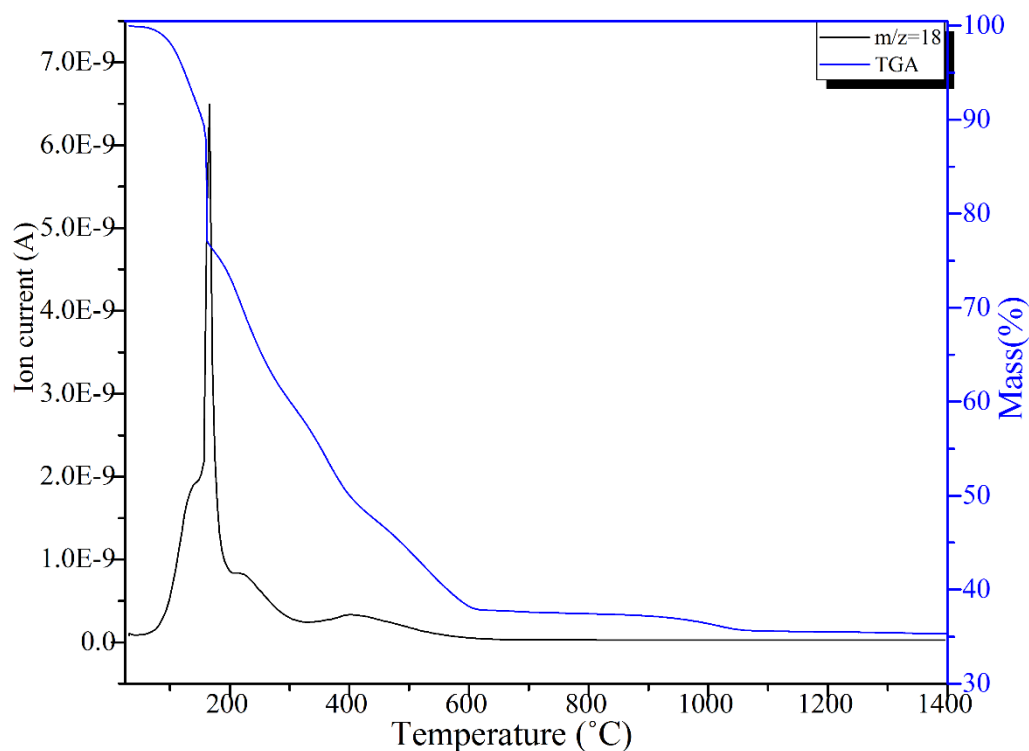
Fig. 6.3: TGA and MS data for evolved H_2O

Mass spectroscopy along with TGA confirmed the evolution of carbon dioxide during the oxidative decomposition of metal alginate beads. This evolution of CO_2 involves the major weight loss which can be clearly seen in Fig. 6.4.
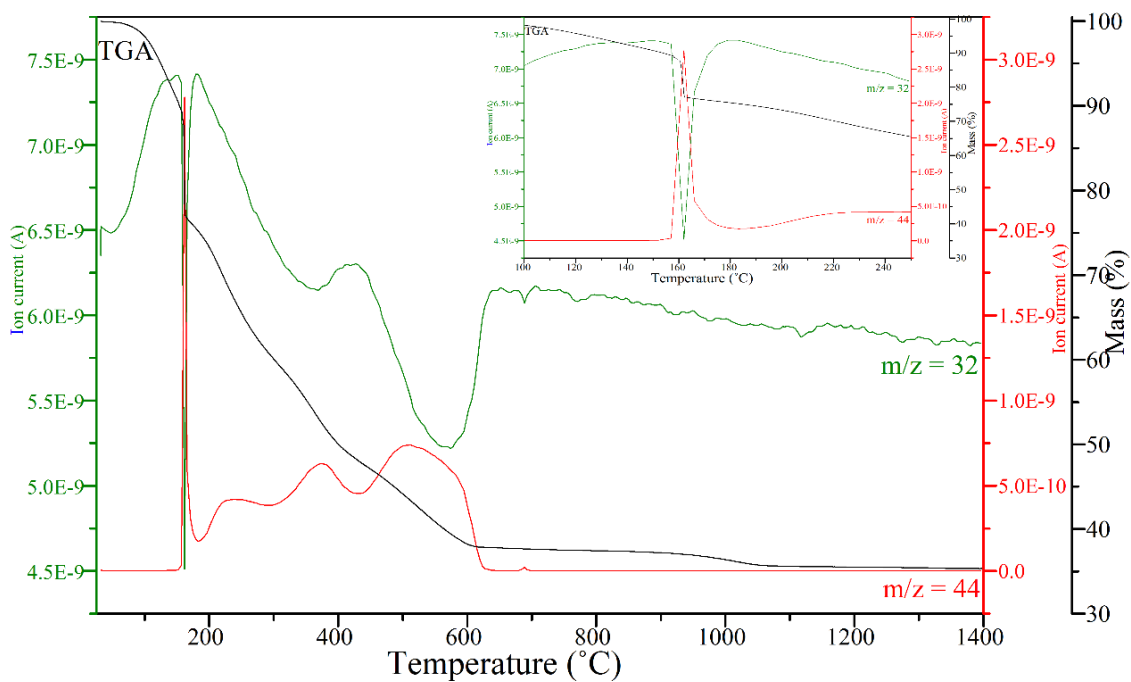
Fig. 6.4: TGA and MS data for CO$_2$ (m/z = 44) and O$_2$ (m/z =32)

TGA and MS data for m/z ratios 44 and 32 are shown in Fig. 4. Inset of Fig. 6.4 elaborates the sudden changes in CO$_2$ and O$_2$ curves corresponding to the rapid weight loss in TGA curve.

The areas under the H$_2$O and CO$_2$ curves in Figs. 6.3 & 6.4 can be related to the weight loss in the TGA curve. The area of CO$_2$ peak grows with the increase in mass of the sample [199]. Here, the mass of the sample used is 83 mg and the plot of weight loss from TGA versus integrated area under the curves.

217
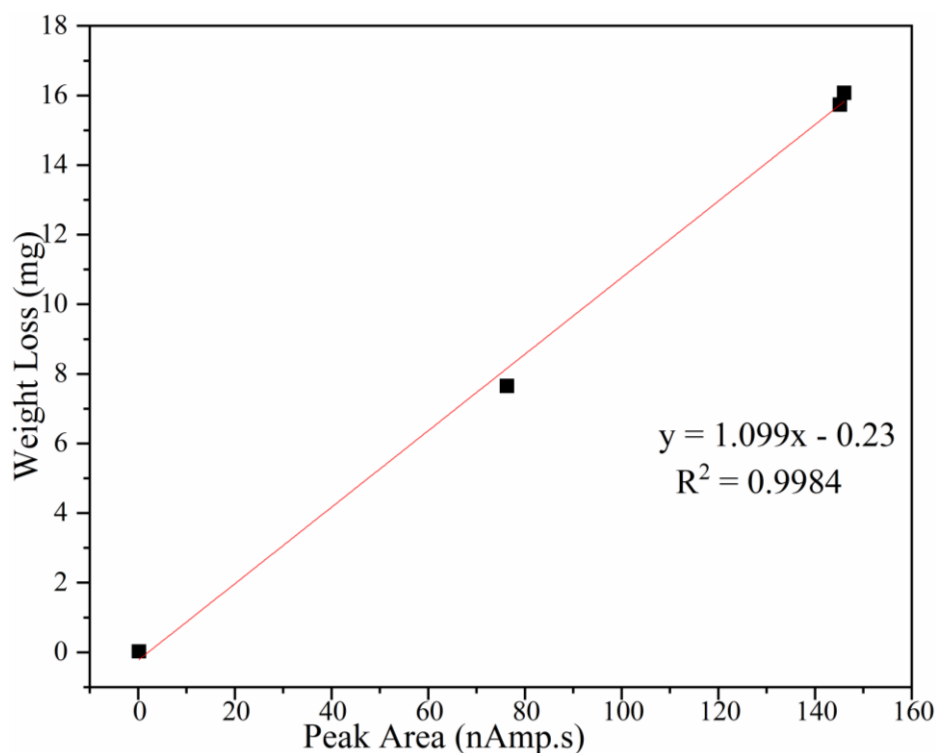
Fig. 6.5: TGA weight loss versus MS integrated area for H_2O and CO_2

It can be clearly seen in the Fig. 6.5 that a linear relationship exists between peak area and the weight loss. The straight line obtained from the linear fit of the data with the R^2 value of 0.9984. The equation obtained from the linear fit is

$$y = 1.099x - 0.23 \tag{6.1}$$

Integrating the water peak in the temperature range of 30 °C to 120 °C in Fig. 6.3 gives an area of 33.93 nAmp.s. Inputting this value in the equation (6.1) obtained from the Fig. 6.5 gave the calculated amount of 3.5026 mg of H_2O release over this temperature range. Remaining values of H_2O and CO_2 release over the different temperature ranges have been calculated after integrating the peak areas from Figs. 6.3 & 6.4, respectively and are presented in Table 6.1. It is observed that no gas release occurs above 695 °C which also confirms the determination of calcination temperature of 700 °C for complete decomposition of metal alginate beads.

Table 6.1: Quantities of H_2O and CO_2 emissions from the TGA-MS analysis of metal alginate beads

Temperature Range (°C)	H_2O (mg)	H_2O (%)	Temperature Range (°C)	CO_2 (mg)	CO_2 (%)
30-120	3.5026	4.22	30-120	0	0
120-150	4.1514	5.00	120-150	0	0
150-210	13.5185	16.29	158-210	1.9724	2.37
210-375	7.6924	9.27	210-375	7.8968	9.51
375-485	2.0493	2.47	375-485	5.8310	7.02
485-535	0.6467	0.78	485-535	3.7495	4.52
535-565	0.10964	0.13	535-565	1.9834	2.39
565-620	0	0	565-620	1.7543	2.11
685-695	0	0	685-695	0.0249	0.03

Calcination of dried metal alginate beads involved the oxidative thermal decomposition of metal alginate beads with the release of H_2O and CO_2 as confirmed by the TGA-MS analysis. An amount of 13.84 g of metal alginate beads was calcined to obtain the nanopowders of holmium hafnate. The amount of CO_2 and H_2O evolved during the calcination process is presented in Table 6.2 on the basis of the TGA-MS data in Table 6.1. Total amount of H_2O evolved during the calcination process is 5.2809 g. The total amount of 3.8702 g of CO_2 evolved after the complete oxidative decomposition of metal alginate beads during calcination process. After the calcination of metal alginate beads, pure single phase nanopowders of holmium hafnate were obtained and the quantities of CO_2 and H_2O emissions are presented in Table 6.2.

Table 6.2: Quantities of H_2O and CO_2 emissions from the calcination of metal alginate beads

Temperature Range (°C)	H_2O (g)	H_2O (%)	Temperature Range (°C)	CO_2 (g)	CO_2 (%)
30-120	0.5841	4.22	30-120	0	0
120-150	0.692	5.00	120-150	0	0
150-210	2.254	16.29	158-210	0.329	2.38
210-375	1.283	9.27	210-375	1.317	9.52
375-485	0.342	2.47	375-485	0.972	7.02
485-535	0.1078	0.78	485-535	0.625	4.52
535-565	0.018	0.13	535-565	0.331	2.39
565-620	0	0	565-620	0.292	2.11
685-695	0	0	685-695	0.0042	0.03
Total = 5.2809 g			Total = 3.8702 g		

6.2. Scheme of chemical reactions during calcination stage

Results of TGA/DSC and EGA showing complete thermal decomposition of dried metal alginate beads. Based on the results of TGA/DSC and EGA the following reaction scheme is proposed for the formation of $Ho_2Hf_2O_7$ from cation exchanged alginate beads. The coefficients of the evolved H_2O and CO_2 in below reactions can be found in Table 6.2.

$$Ho^{3+}/Hf^{4+} — ALG . xH_2O + H_2O_{(Adsorbed)} \xrightarrow{<120\ °C} Ho^{3+}/Hf^{4+} — ALG . xH_2O + H_2O_{(g)}$$

$$\Delta H = 13 \text{ J/g} \quad (6.2)$$

$$\text{Ho}^{3+}/\text{Hf}^{4+} \text{ — ALG} \cdot x\text{H}_2\text{O} \xrightarrow{120\,^\circ\text{C}-150\,^\circ\text{C}} \text{Ho}^{3+}/\text{Hf}^{4+} \text{— ALG} + x\text{H}_2\text{O}_{(g)} \qquad \Delta\text{H} = 24\ \text{J/g}$$

$$(6.3)$$

$$\text{Ho}^{3+}/\text{Hf}^{4+} \text{ — ALG} \xrightarrow{150\,^\circ\text{C}-375\,^\circ\text{C}} \text{Ho}^{3+}/\text{Hf}^{4+} \text{— (GG, MM, GM)} + \text{CO}_{2\,(g)} + y\text{H}_2\text{O}_{(g)}$$

$$\Delta\text{H} = \text{-}53\ \text{J/g} \quad (6.4)$$

$$\text{Ho}^{3+}/\text{Hf}^{4+} \text{ — (GG, MM, GM)} \xrightarrow{375\,^\circ\text{C}-485\,^\circ\text{C}} \text{Ho}^{3+}/\text{Hf}^{4+}.\ \text{O + G/M residue} + \text{CO}_{2\,(g)} + w\text{H}_2\text{O}_{(g)}$$

$$\Delta\text{H} = \text{-}6759\ \text{J/g} \quad (6.5)$$

$$2\ (\text{Ho}^{3+}/\text{Hf}^{4+}).\ \text{O + G/M residue} \xrightarrow{485\,^\circ\text{C}-620\,^\circ\text{C}} \text{Ho}_2\text{Hf}_2\text{O}_7 + \text{CO}_{2\,(g)} + z\text{H}_2\text{O}_{(g)}$$

$$\Delta\text{H} = \text{-}59\ \text{J/g} \quad (6.6)$$

Overall reaction:

$$\text{Ho}^{3+}/\text{Hf}^{4+} \text{ — ALG} \xrightarrow{O_2} \text{Ho}_2\text{Hf}_2\text{O}_7 + p\text{CO}_{2\,(g)} + q\text{H}_2\text{O}_{(g)}$$

$$\Delta\text{H} = \text{-}6834\ \text{J/g} \quad (6.7)$$
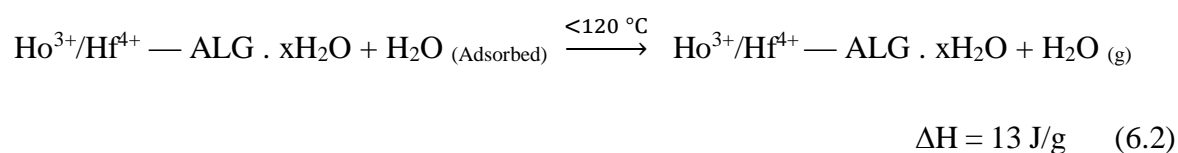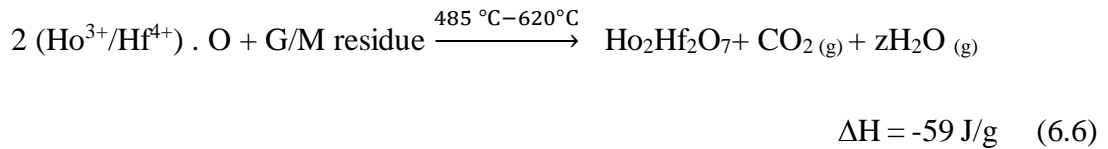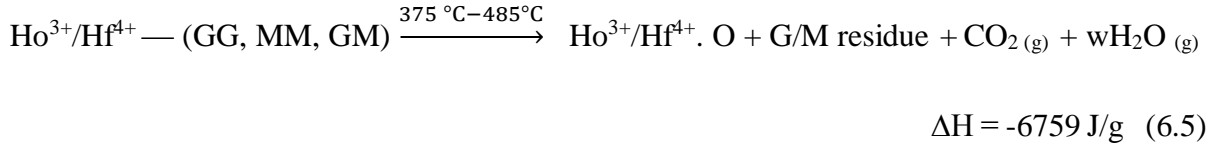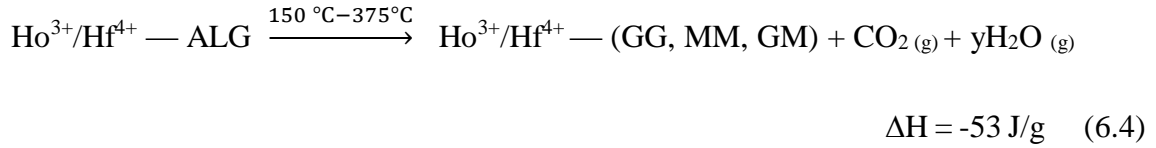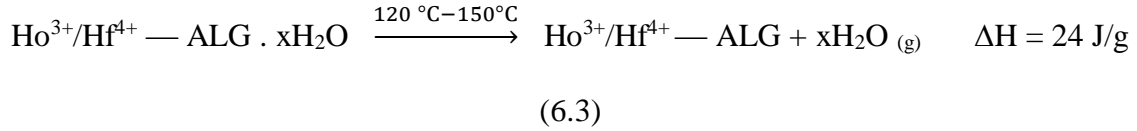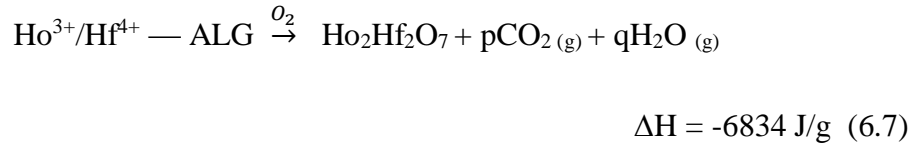
Enthalpy is calculated from DSC curve (section 4.1) on the basis of corresponding weight involved in that step. The net enthalpy change from above reactions is -6834 J/g ($\pm$10%), this shows that overall the decomposition process is exothermic in nature. This evolved heat can be utilized for the drying and calcination process of beads.

6.2.1. Block diagram with mass balance

A block diagram with complete mass balance of the LAP process has been made after carefully analysing and weighing all the contents involved in each step of the process.

Emissions during the calcination stage was quantified from the evolved gas analysis (EGA). The amount of the oxygen utilized during the calcination stage (in block diagram) was calculated from the mass balance of all the species involved in calcination. The amount of

oxygen has also been quantified from the oxygen curve (m/z = 32) in Fig. 6.4 and found 2.0 g

as shown in Table 6.3. The error in the values of oxygen quantified from EGA data and from

the mass balance has found 0.45% which is in acceptable range.

Table 6.3: Quantification of O_2 utilized during the calcination of metal alginate beads

Temperature Range (°C)	TGA – EGA (mg)	Calcination (g)	Calcination (%)
270 – 385	0.883	0.147	1.06
385 – 490	8.639	1.44	10.40
490 – 605	2.474	0.413	2.98
		Total = 2.0 g	

The spent solution was processed and from the XRD analysis of the end material it was found

to be NaCl. During the processing of spent solution H_2O and HCl evaporated at drying and

calcination stages.

On the basis of the above results the block diagram with complete mass balance of Leeds

Alginate Process (LAP) for the production of holmium hafnate ($Ho_2Hf_2O_7$) is shown in Fig.

6.6 for producing 1 g of $Ho_2Hf_2O_7$. Overall reactions of the LAP are also suggested in equations

(6.8) & (6.9).
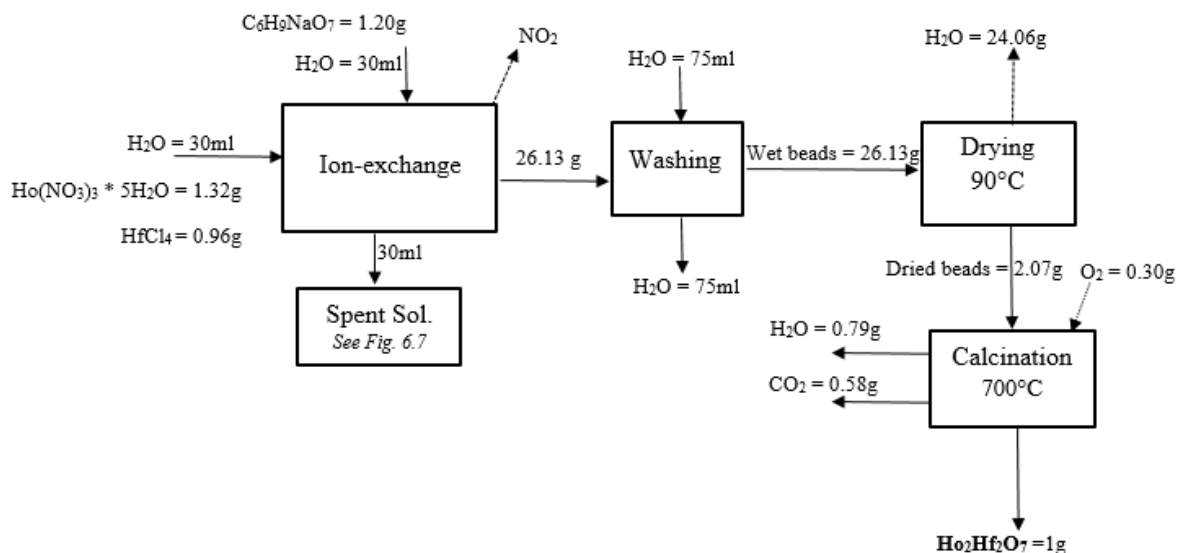
Fig. 6.6: Block diagram of Leeds Alginate Process (LAP) for the synthesis of 1g of holmium hafnate

Table 6.4: Mass balance of LAP for the synthesis of 1 g of $Ho_2Hf_2O_7$

Components	Materials In	Components	Materials Out
Ion-exchange stage			
Na-alginate sol.	30 ml	Ion-exchanged beads	26.13 g
Metal salts sol.	30 ml	Spent sol.	30 ml
		NO_2	Difference in balance (assumption)
Washing stage			
Ion-exchanged beads	26.13 g	Washed beads	26.13 g
Washing H_2O	75 ml	Washing H_2O	75 ml
Drying stage			
Wet beads	26.13 g	Evaporated H_2O	24.06 g
		Dried beads	2.07 g
Calcination			
Dried beads	2.07 g	CO_2	0.58 g
O_2	0.30 g	H_2O	0.79 g
		$Ho_2Hf_2O_7$	1 g

6.2.2. Overall reactions

$$2Ho(NO_3)_3 . 5H_2O_{(aq)} + 2HfCl_{4(aq)} \rightarrow 2HoCl_{3(aq)} + 2Hf(OH)_{4(aq)} + 2HCl_{(aq)} + 5H_2O_{(aq)}$$

$$+3/2\ O_{2(aq)} + 6NO_{2(g)}\uparrow \quad (6.8)$$

$$Ho^{3+}/Hf^{4+} — ALG \xrightarrow{O_2} Ho_2Hf_2O_7 + CO_{2\ (g)} + H_2O_{\ (g)} \qquad (6.9)$$
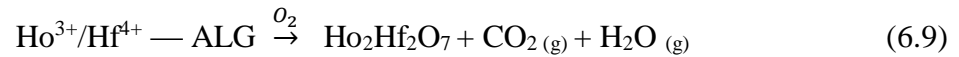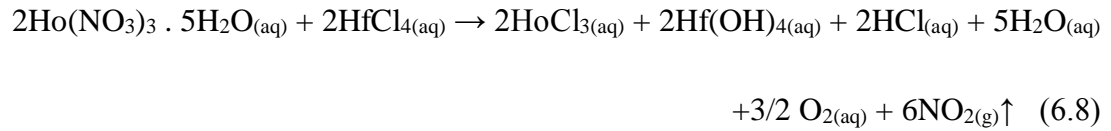
6.3. Energy Balance

Energy balance was carried out on the production of holmium hafnate employing LAP. Mass balance in block diagram (Fig. 6.6) was used to do the energy calculations of different streams.

Drying
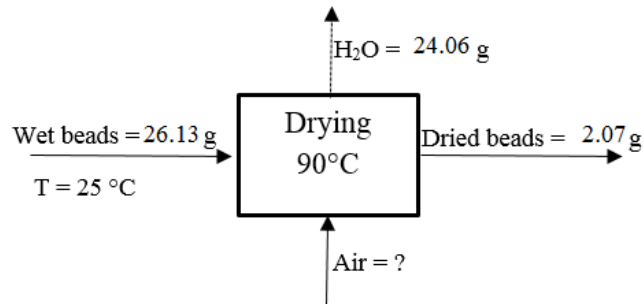
Assuming the steady state system

$$\text{Heat taken by the wet beads} = Q_{Out-I} = m\ Cp\ \Delta T$$

$$Cp\ of\ H_2O = 4.2\ Jg^{-1}{}^{\circ}C^{-1}$$

$$= (26.13)(4.2)(90 - 25)$$

$$Q_{Out-I} = 7133\ J = 7.133\ kJ$$

$$\text{Latent heat taken by } H_2O \text{ vapours} = Q_{Out-II} = m\ \Delta H$$

$$= (24.06)\ (4.2)$$

$$= 101\ J = 0.101kJ$$

$$Q_{Out} = Q_{Out-I} + Q_{Out-II}$$

$$= \textbf{7.234 kJ}$$

Energy utilized during drying stage = 7.234 kJ

Heat given by air in the oven = Q_{In} = m Cp ΔT

$$Q_{In} = Q_{Out}$$

$$7234 = m \text{ Cp } \Delta T$$

Cp of air at 90 °C = 1008 J kg^{-1} °C^{-1}

$$= 1.008 \text{ J g}^{-1} \text{ °C}^{-1}$$

Assuming oven is 100% efficient

$$m_{Air} = 7176 \text{ g} = 7.18 \text{ kg}$$

Calcination

$$Q_{In} = m \text{ Cp } \Delta T$$

$$= (2.07) (1.008)(700 - 25)$$

$$Q_{In} = 1408 \text{ J} = \textbf{1.408 kJ}$$

Heat out is calculated from the DSC curve as mentioned in equation (6.7)

$$Q_{out} = \text{-6834 J/g}$$

For 2.07 g of dried beads heat evolved is

$$Q_{out} = \text{-14146 J}$$

$$= \textbf{-14.146 kJ}$$

Total Energy balance

Heat In = Drying + Calcination

$$= 7.234 + 1.408$$

$$= \textbf{8.642 kJ}$$

$$\text{Heat Out} = \text{Exothermic reaction during calcination}$$

$$= \textbf{-14.146 kJ}$$

$$\textbf{Net Heat = -5.504 kJ}$$

The production of holmium hafante through LAP is overall an exothermic process with the heat evolution of 5.504 kJ.

Law of conservation of energy has used for the energy balance with the assumptions of no heat loss and heat capacities are independent of temperatures.

6.4. Processing of spent solution of LAP

Metal alginate beads were sieved from the ion-exchanged solution and the spent solution was collected. This solution was processed (Fig. 6.7) to know its composition.
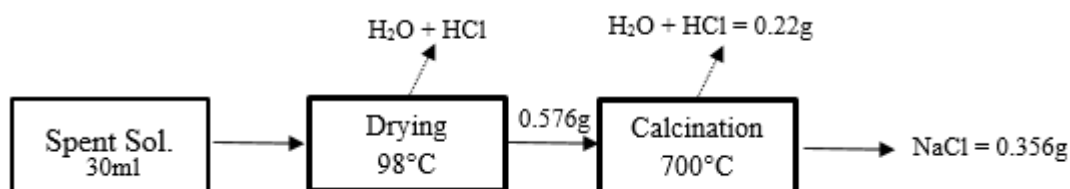
Fig. 6.7: Processing of spent solution left over from the synthesis of 1g holmium hafnate

Rietveld refinement of the XRD pattern of left over solution calcined at 700 °C for 2h is shown in Fig. 6.8. The observed XRD pattern of calcined spent solution matched with the cubic structured sodium chloride (NaCl). The observed and calculated patterns matched with each other and peaks are also indexed with the XRD reference pattern (ICDD, 01-076-3453). The residual pattern shows the difference in the sharpness of the peaks in observed and calculated patterns. Cubic defect fluorite structured powder of NaCl with unit cell lattice parameters a = b = c = 5.6530 A° and $\alpha = \beta = \gamma = 90°$ were obtained from the calcination of spent solution.
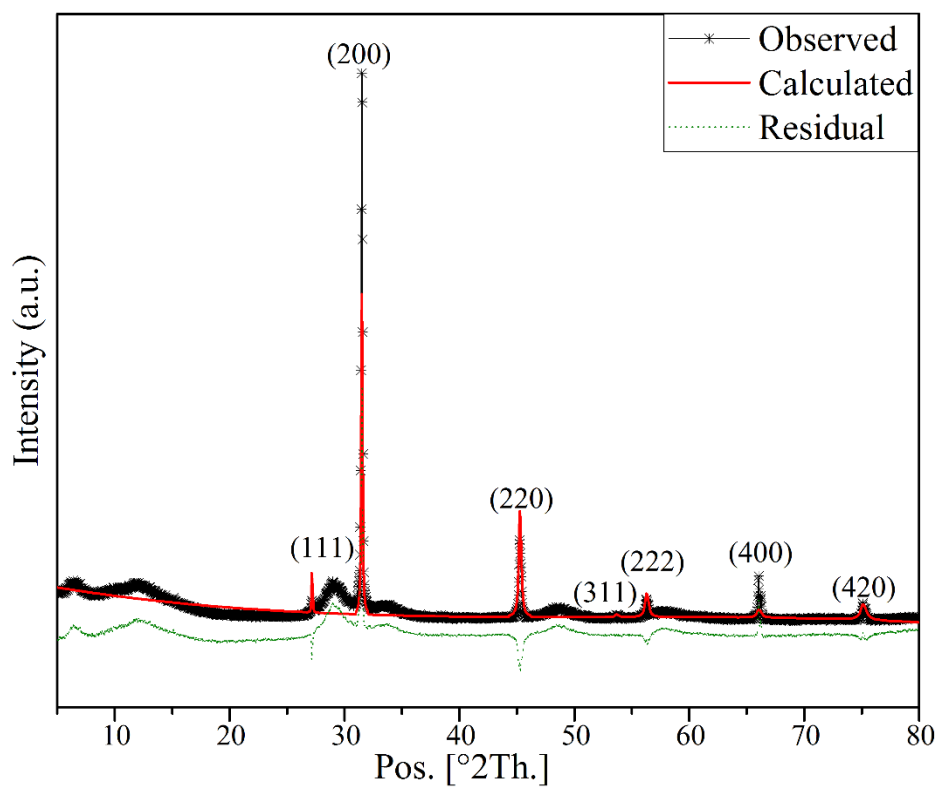
Fig. 6.8: Rietveld refined XRD analysis of spent solution powder calcined at 700°C for 2h. Patterns are indexed by ICDD, 01-076-3453 indicating the miller indices of NaCl shown at the top of the peaks

Chapter 7

Conclusions

Pyrochlore oxides with defect fluorite structure are known to be good oxide ion conductors and potential materials as solid oxide fuel cell (SOFC) electrolytes. Lanthanide based oxides with pyrochlore structure have properties for thermal barrier coating applications. It is important to synthesize the nanopowders of these materials in a sustainable manner.

Sol-gel processes has gained more attentions in the area of nanopowders based ceramic synthesis. Sols of different compounds are mixed to form multi-component compounds with measured stoichiometry. Sol-gel process also overcomes the problems of inhomogeneity and non-stoichiometry. In sol gel process ion exchange taken place at atomic scale forms small and easily sinterable particles at low temperature sintering (TSS process).

Nanoparticles of holmium hafnate ($Ho_2Hf_2O_7$) and holmium zirconate ($Ho_2Zr_2O_7$) were successfully synthesised using the sodium alginate mediated Leeds Alginate Process (LAP). Metal alginate beads were obtained after ion exchange between sodium alginate solution and metals salts solution. The gelled beads then removed from the solution and subject to drying. Thermal analysis of dried metal alginate beads using TGA/DSC is in confirmation with the HT-XRD data as onset and endset of decomposition is similar in both cases. Following these conclusions calcination temperature of 700 °C was found to be optimal. XRD analysis exhibits that single phase cubic nanoparticles of $Ho_2Hf_2O_7$ and $Ho_2Zr_2O_7$ with defect-fluorite structure and space group of $Fm\overline{3}m$ were obtained at comparatively low temperature of 700 °C using LAP. Analysis from Raman spectra confirms the defect-fluorite structure of $Ho_2Hf_2O_7$ and $Ho_2Zr_2O_7$. Raman scattering and photoluminescence under 473 nm excitation wavelength can occur simultaneously as two separate optical processes for $Ho_2Hf_2O_7$ and $Ho_2Zr_2O_7$ nanopowders. Raman spectroscopy shows the evidence of oxide-ion vacancy which is further

confirmed by the temperature dependence of the ac-impedance measurement of $Ho_2Hf_2O_7$ and $Ho_2Zr_2O_7$. Values of interplanar spacing obtained from characterization techniques of XRD and TEM agree with each other as well as XRD reference patterns. Nanoparticles are unique and suitable for SOFC applications due to their physichochemical and optical properties. Crystallite size is affected by the calcination duration. With the increase in calcination duration from 2 to 6 h crystallite size increased from 5.40 to 6.10 nm for $Ho_2Hf_2O_7$ and 8 to 10 nm for $Ho_2Zr_2O_7$. TEM analysis has carried out and peaks from XRD data and lattice planes from SAED rings are in good agreement. The d-spacing values obtained from Rietveld refinement of XRD data and TEM-SAED are comparable as well. Grain size analysis from TEM images confirms the narrow size distribution and increase in grain size with increase in calcination duration. TEM–EDX analysis confirm that $Ho_2Hf_2O_7$ and $Ho_2Zr_2O_7$ are stoichiometric.

The nanopowders of hafnate and zirconate of holmium were compacted into pellets and processed through single step sintering (SSS) and two step sintering (TSS) routes and impact of processing conditions on microstructure and ionic conductivity were studied. Nanoparticles have been helpful in compacting the materials in the form of powders for sintering purpose. High density $Ho_2Hf_2O_7$ and $Ho_2Zr_2O_7$ ceramics were successfully obtained through TSS process with lower grain growth. The TSS process is found to be a better route for processing of ceramics as the relative density of the pellets reaches to 98 % at lower temperature (1300 °C) with less grain growth for both materials as compared to the densification achieved through SSS process at higher temperature (1500 °C) is 93.5 % with grain growth of 1.59 μm for $Ho_2Hf_2O_7$ and 92 % with pronounced grain growth of 2.2 μm for $Ho_2Zr_2O_7$.

The bulk and grain boundary conductivity of $Ho_2Hf_2O_7$ and $Ho_2Zr_2O_7$ processed using SSS and TSS processes were measured using AC impedance spectroscopy. The complex impedance plots for SSS and TSS $Ho_2Zr_2O_7$ exhibit the consistent results for both heating and cooling cycles indicates that solid electrolyte respond reversibly throughout the temperature range of

measurement which is an important behaviour of solid electrolyte. The values of bulk and grain boundary conductivities of $Ho_2Zr_2O_7$ pellets prepared using TSS process are higher than that processed using SSS process. The activation energy value of SSS processed holmium zirconate has found to be 0.99 eV.

The complex impedance plots for SSS and TSS processed $Ho_2Hf_2O_7$ nanopowders exhibit consistent results for both heating and cooling cycles. The values of bulk and grain boundary conductivities of $Ho_2Hf_2O_7$ pellets prepared using the SSS and TSS process are not distinctly different and therefore the main advantage of TSS process over SSS process for processing the nanopowders of $Ho_2Hf_2O_7$ is for yielding better physical properties such as lower sintering temperature, smaller grain size and higher density.

The magnitudes of oxide ion conductivity and activation energy for ionic conduction of $Ho_2Zr_2O_7$ are better than that of $Ho_2Hf_2O_7$. Both the electrolyte materials prepared using LAP possess better ionic conductivities and activation energy values than those found in literature obtained through mehcanochemically and thermodynamically. Low sintering temperature, more densification, less grain growth and high ionic conductivity makes the TSS process more preferable route for the processing of solid electrolytes. Holmium zirconate proves to be a promising solid electrolyte by exhibiting excellent and consistent results of ionic conductivity over a wide temperature range with reversible behaviour as solid electrolytes are constantly subject to temperature variation in a practical electrochemical discs such as SOFC or high temperature sensors.

Ion-exchange based Leeds Alginate Process is therefore a highly versatile technique to produce pyrochlore oxide nanoparticles as solid electrolyte materials for solid oxide fuel cells in an environmentally friendly, cost effective and energy efficient manner.

The alginate based sol-gel technique (LAP) was also employed to prepare nanoparticles of lanthanum hafnate ($La_2Hf_2O_7$) and lanthanum zirconate ($La_2Zr_2O_7$). Beads of precursor were obtained by carrying out ion-exchange between complex metal-ion solution and sodium alginate gel. TGA/DSC and HTXRD analyses yield decomposition temperatures that are in good agreement with each other and initially a calcination temperature of 700 °C was found to be optimal. It has also observed that the split in the major peaks in the XRD pattern obtained after calcining the beads at 700 °C. This pattern is different than that found in HTXRD at 700 °C as some extra peaks were also observed which should not be present in the fluorite structure of $La_2Hf_2O_7$ and $La_2Zr_2O_7$, here it is more like transformation from fluorite to pyrochlore structure. Clean XRD patterns were obtained for the nanopowders obtained after calcining the metal alginate beads at 900 °C for 6h. The peaks observed in the patterns at 900 °C are characterised for the crystalline nanopowders of $La_2Hf_2O_7$ and $La_2Zr_2O_7$ with pyrochlore structure and space group of $Fd\bar{3}m$. The patterns confirms the completed decomposition of metal alginate beads below 700 °C and formation of pyrochlore structured $La_2Hf_2O_7$ and $La_2Zr_2O_7$ at 900 °C, which are in excellent agreement with the TGA/DSC results. Average crystallite size increased from 4.3 nm to 20.8 nm for $La_2Hf_2O_7$ and 4 nm to 31 nm for $La_2Zr_2O_7$ with the increase in calcination temperature from 700 °C to 900 °C. Raman spectra of lanthanum zirconate shows all the six Raman active modes specified for the pyrochlore structured materials. The values of interplanar spacing calculated from XRD and TEM investigations are in excellent agreement with each other as well as with the standard reference data of both materials. TEM-EDX analysis and X-ray mapping confirm the stoichiometry of $La_2Hf_2O_7$ and $La_2Zr_2O_7$.

The nanopowders of $La_2Hf_2O_7$ and $La_2Zr_2O_7$ were compacted into pellets and processed through conventional (SSS) and non-conventional (TSS) routes and found that TSS shows less grain growth (~0.9 μm) for both materials. The relative density with TSS process reaches to

98 %, nearly 7 % greater than the SSS processed sample of $La_2Hf_2O_7$ and for $La_2Zr_2O_7$ density reaches to 99 %, nearly 6 % greater than its SSS processed sample.

The values of ionic conductivities of pyrochlore structured $La_2Hf_2O_7$ and $La_2Zr_2O_7$ ceramic sample have been found significantly less than that of defect fluorite structured $Ho_2Hf_2O_7$ and $Ho_2Zr_2O_7$ ceramic sample. Although synthesis route of materials and processing of ceramic pellets are same in all cases even then the ionic conductivity for holmium hafnate ceramic sample is more than two order of magnitude higher than that of lanthanum hafnate ceramic sample and the ionic conductivity for holmium zirconate ceramic sample is more than three order of magnitude higher than that of lanthanum zirconate ceramic sample.

Hence, it is concluded that the defect fluorite structured holmium hafnate and holmium zircoante are better ionic conductors due to the presence of oxygen vacancy in the structure. In pyrochlore structures all the cations and anions are ordered with respect to the oxygen atoms, this ordering causes the pyrochlore unit cell to double with respect to that of fluorite and drastically affects ionic and thermal conductivity.

Thermoresponsive behaviour of all the ternary materials were studies by carrying out the XRD analysis of SSS processed pellets. The results showed that $Ho_2Hf_2O_7$ and $Ho_2Zr_2O_7$ maintains stable fluorite structure over the wide temperature range which is also in agreement with the cationic radius ratio (r_{Ho}/r_{Hf} = 1.43, r_{Ho}/r_{Zr} =1.41) for the fluorite structured materials (Fluorite < 1.46 < Pyrochlore). XRD results also confirm the stable pyrochlore structure of $La_2Hf_2O_7$ and $La_2Zr_2O_7$ over the entire range of heat treatment in accordance to the cationic radius ratio, (r_{La}/r_{Hf} =1.6, r_{La}/r_{Zr} = 1.61) as suitable ionic radii for the formation of the pyrochlore structure is $1.8 \geq (r_A/r_B) \geq 1.46$.

Leeds Alginate Process (LAP) has also successfully synthesised the binary oxides of the pyrochlore materials namely the holmium oxide (Ho_2O_3), hafnium oxide (HfO_2), lanthanum oxide (La_2O_3) and zirconium oxide (ZrO_2).

Solution method was used to synthesise holmium hafnate and lanthanum hafnate materials. This method involves mixing of two solutions of metal nitrate salts and then evaporating the water to attain powder. The powder then heat treated similarly as beads have been treated to obtain the nanopowders. XRD scan of the powder obtained after calcination at 700 °C through solution method is amorphous in nature.

The structural and morphological analyses showed that Solution method forms the amorphous powder of holmium hafnate which after heat treatment at higher temperature of 1100 °C shows results similar to the LAP. Holmium hafnate powder obtained from the solution method were pressed into pellets and sintered. Relative density of pellets obtained after sintering are 33.1 % for SSS and 56.8 % for TSS process and no shrinkage in the size of the pellets were observed after sintering. Hence, it is concluded that the ceramic samples of holmium hafnate obtained through solution method are not suitable for impedance measurements.

XRD pattern of lanthanum hafnate powder obtained after calcining at 900 °C using solution method does not show single phase material. Split peaks of lanthanum hafnate were also observed along with the second phase of lanthanum oxide (La_2O_3). The observed and the calculated pattern are not in good agreement with each other and the lattice parameters are not in agreement with the one obtained from beads method and found in the literature.

The relative density of the lanthanum hafnate powder obtained through solution method was found to be 84.3 % with SSS process. The higher values of ionic conductivity for the biphasic material obtained from the solution method than that of beads method is due to the presence of

lanthanum oxide impurity. The average value of activation energy for bulk ionic conduction has been found to be 0.28 eV.

Emissions during the calcination stage to form $Ho_2Hf_2O_7$ were identified and quantified from the evolved gas analysis (EGA). Oxidative thermal decomposition of metal alginate beads took place with the release of H_2O and CO_2 as confirmed by the TGA-MS analysis. The error in the values of oxygen quantified from EGA data and from the mass balance has found 0.45% which confirms the accuracy of the analysis.

A block diagram with complete mass balance of the LAP has made after carefully analysing and weighing all the contents involved in each step of the process along with energy balance. A scheme of chemical reactions was proposed for LAP demonstrating the overall exothermic nature of the process.

It is concluded that this project has fulfilled its major objectives and any proposed suggestions.

Future Work

The future work of the project includes the thermal conductivity analysis of all the synthesised materials to study their suitability for different applications. Analysing the mechanical properties of synthesised materials and testing them as an entire solid oxide fuel cell component.

Future investigations also involve the diffusion and ion exchange kinetics of metal cations with H^+ from alginic acid beads for the formation of nanoparticles as this information is essential for designing production-scale reactors. The scale up and cost analysis of the whole process are worthy of investigation.

Investigating the properties of the solid solutions of lanthanide series to find out the optimum point of ionic conductivity.

References

[1] Yang, L., Wang, S.Z., Blinn, K., Liu, M.F., Liu, Z., Cheng, Z. and Liu, M.L. 2009. Enhanced sulfur and coking tolerance of a mixed ion conductor for SOFCs: $BaZr_{0.1}Ce_{0.7}Y_{0.2-x}Yb_xO_{3-d}$. *Science*, **326** (5949), pp.126–129.

[2] Yang, L., Choi, Y., Qin, W., Chen, H., Blinn, K., Liu, M., Liu, P., Bai, J., Tyson, T.A. and Liu, M. 2011. Promotion of water-mediated carbon removal by nanostructured barium oxide/nickel interfaces in solid oxide fuel cells. *Nature Communications*, **2**, Article ID. 357.

[3] Kendall, K. and Kendall, M. 2015. High temperature solid oxide fuel cells: fundamentals, design, and applications, 2nd edition, Academic Press, ISBN 9780124104839, Oxford, UK.

[4] Zhe, C., Wang, J.H., Choi, Y.M., Yang, L., Lin, M.C. and Liu, M. 2011. From Ni-YSZ to sulfur-tolerant anodes: electrochemical behavior, modelling, in situ characterization, and perspectives. *Energy and Environmental Science*, **4**, pp.4380–4409

[5] Kim, Y., Jeon, M.K. and Im, W.B. 2013. Crystal structural study of Ho-doped ceria using X-ray powder diffraction data. *Journal of Electroceramics*, **31**, pp.254 - 259.

[6] Kilner, J.A. and Burriel, M. 2014. Materials for intermediate temperature solid-oxide fuel cells. *Annual Review of Materials Research*, **44**, pp. 365-393.

[7] Perry, N.H and Ishihara, T. 2016. Roles of bulk and surface chemistry in the oxygen exchange kinetics and related properties of mixed conducting perovskite oxide electrodes. *Materials*. **9** (858), doi:10.3390/ma9100858

[8] Sfeir, J., Hocker, T., Herle, J. V., Nakajo, A., Tanasini, P., Galinski, H. and Kuebler, J. 2007. Enhancing the lifetime of SOFC stacks for combined heat and power application. *Hexis AG, Winterthur, Switzerland*. Report no. SFOE-270182.

[9] Subramanian, M.A., Aravamudan, G. and Rao, V.S. 1983. Oxide pyrochlores-a review. *Progress in Solid State Chemistry*. **15** (2), pp.55-143.

[10] Wuensch, B.J., Eberman, K.W., Heremans, C., Ku, E.M., Onnerud, P., Yeo, E.M.E., Haile, S.M., Stalick, J.K. and Jorgensen, J.D. 2000. Connection between oxygen-ion conductivity of pyrochlore fuel-cell materials and structural change with composition and temperature. *Solid State Ionics*. **129**, pp.111-133.

[11] Badwal, S.P.S. 2001. Stability of solid oxide fuel cell components. *Solid State Ionics*. **143**, pp. 39-46.

[12] Singh, P. and Minh, N.Q. 2004. Solid oxide fuel cells: Technology status. *International Journal of Applied Ceramic Technology*, **1**(1), pp. 5-15.

[13] Edwards, P.P., Kuznetsov, V.L., David, W.I.F. and Brandon, N.P. Hydrogen and fuel cells: Towards a sustainable energy future. *Energy Policy 2008*. **36**, pp.4356–4362.

[14] Albright and Wilson, Ltd. 1938. Booklet on Manucol (Sodium Alginate).

[15] Chandran, P.R. and Arjunan, T.V. 2014. A Review of materials used for solid oxide fuel cell, *International Journal of Chemical Technology Research*. **7**(1), pp.488-497.

[16] Ivers-Tiffee, E. 2013. Why going nano with fuel cells? *Centre for Functional Nanostructures (CFN)*. http://www.cfn.kit.edu/653.php.

[17] Acres, G. 2001. Recent advances in fuel cell technology and its applications. *Journal of Power Sources*. **100**, pp.60-66.

[18] Sun, C. and Stimming, U. 2007. Recent anode advances in solid oxide fuel cells. *Journal of Power Sources*. **171**(2), pp.247-260.

[19] EG&G Technical Services, Inc. 2004. Fuel Cell Handbook (Seventh Edition). U.S. Department of Energy.

[20] Thijssen, J. 2007. The impact of scale-up and production volume on SOFC manufacturing cost. National Energy Technology Laboratory, Department of Energy, USA.

[21] Minh, N.Q., Takahashi, T. 1995. Science and technology of ceramic fuel cells. Elsevier, Amsterdam.

[22] Fergus, J., Hui, R., Li, X., Wilkinson, D.P. and Zhang, J. 2009. Solid oxide fuel cells: materials properties and performance. CRC Press, ISBN 978-1-4200-8883-0, London, NY.

[23] Singhal, S.C. and Kendall, K. 2003. High temperature solid oxide fuel cells: fundamentals, design, and applications: Elsevier Science Ltd, ISBN 1-85617-387-9, Oxford, UK.

[24] Sun, C., Hui, R. and Roller, J. 2010 Cathode materials for solid oxide fuel cells: a review. *J Solid State Electrochem*. **14** (7), pp. 1125–1144.

[25] Molenda, J. 2006. High-temperature solid-oxide fuel cells-New trends in materials research. *Materials Science-Poland*. **24**.

[26] Gonzalezcuenca, M.M. 2002. *Novel anode materials for Solid oxide fuel cells*. PhD thesis, University of Twente.

[27] Woodward, H.K. 2003. *A performance based, multi-process cost model for solid oxide fuel cells*. Masters thesis, Worcester Polytechnic Institute.

[28] Barthel, K. and Rambert, S. 1998. *Thermal Spraying and Performance of Graded Composite Cathodes as SOFC-Component*. The 5th International Symposium on functionally graded materials, Germany.

[29] Beckel, D., Muecke, U.P., Gyger, T., Florey, G., Infortuna, A. and Gauckler, L.J. 2007. Electrochemical performance of LSCF based thin film Cathodes prepared by Spray pyrolysis. *Solid State Ionics*. **178**, pp. 407-415.

[30] Pal, U.B. and Gopalan, S. 2005. Materials System for Intermediate Temperature SOFCs based on doped lanthanum-gallate electrolyte. *Journal of the Electrochemical Society*, **152** (9), pp. 1890-1895.

[31] Florio, D. Z., Fonseca, F. C., Muccillo, E. N. S. and Muccillo, R. 2004. Ceramic materials for fuel cells. *Ceramica.* **50**, (316), pp. (275-290).

[32] Martins, R. F., Brant, M. C., Domingues, R. Z., Paniago, R. M., Sapag, K. and Matencio, T. 2009. Synthesis and characterization of NiO-YSZ for SOFCs. *Materials Research Bulletin*, **44** (2), pp. 451-456.

[33] Benyoucef, A., Klein, D., Coddet, C. and Benyoucef, B. 2008. Development and characterisation of (Ni, Cu, Co)-YSZ and Cu-Co-YSZ cermets anode materials for SOFC application. *Surface and Coating Technology*. **202** (10), pp. (2202-2207).

[34] Ringuede, A., Labrincha, J.A. and Frade, J.R. 2001. A combustion synthesis method to obtain alternative cermet materials for SOFC anodes. *Solid State Ionics.* **141-142**, pp. 549-557.

[35] Hibino, T., Hashimoto, A., Yano, M., Suzuki, M. and Sano, M. 2003. Ru-catalyzed anode materials for direct hydrocarbon SOFCs. *Electrochimica Acta*. **48** (17), pp. 2531-2537.

[36] Matsuzaki, Y. and Yasuda, I. 2007. The poisoning effect of sulfur-containing impurity gas on a SOFC anode: Part I. Dependence on temperature, time, and impurity concentration. *Journal of Power Sources*, **171** (2), pp. 247-260.

[37] Faro, M. L., Rosa, D. L., Antonucci, V. and Arico, A. S. 2009. Intermediate temperature solid oxide fuel cell electrolytes. *Journal of the Indian Institute of Science*, **89** (4), pp. 363-381.

[38] EG&G Technical services. 2000. Fuel Cell Handbook (5th edition), Parsons Inc., ISBN 1603220178, Morgantown, West Virginia.

[39] Larminie, J. and Dicks, A. 2003. Fuel cell systems explained-III, John Wiley & Sons Inc., Chichester, West Sussex, UK.

[40] Hibino, T., Tsunekawa, H., Tanimoto, S. and Sano, N. 1990. Improvement of a single chamber solid-oxide fuel cell and evaluation of new cell designs. *Journal of the Electrochemical Society*, **147**, pp.1338-1343.

[41] Garay, J.E., Glade S.C., Kumar, P.A., Anselmi-Tamburini, U. and Munir, Z.A. 2006. Characterization of densified fully stabilized nanometric zirconia by positron annihilation spectroscopy. *Journal of Applied Physics*, **99**, pp.1-7.

[42] Anselmi-Tamburini, U., Garay, J.E., Munir, Z.A., Tacca, A. and Maglia, F. 2004. Spark plasma sintering and characterization of bulk nanostructured fully-stabilized zirconia (FSZ): I. Densification studies. *Journal of Materials Research*, **19**, pp.3255-3262.

[43] Sorensen, T. O. 1981. Nonstoichiometric Oxides. Academic Press, New York.

[44].http://inanoschool.au.dk/fileadmin/inano/iNANOSchool/PhD_theses_PDF/PhDAfhandling090810MichaelBrammerSillassen.pdf Dated: 13/07/2017

[45] Takahashi, T., Esaka, T. and Iwahara, H. 1977. Conduction in Bi_2O_3-based oxide ion conductors under low oxygen pressure I. Current blackening of the Bi_2O_3-Y_2O_3 electrolyte. *Journal of Applied Electrochemistry*, **7**, pp.299-302.

[46] Verkerk, M.J. and Burggraaff, A.J. 1981. High oxygen ion conduction in sintered oxides of the Bi_2O_3-Ln_2O_3 system. *Solid State Ionics*, **3** (4), pp.463-467.

[47].http://www.chimica.unipd.it/antonella.glisenti/privata/documentazione/insegnamenti/Fuel%20Cells/Bi2O3.pdf Dated: 13/07/2017

[48] Patterson, J.W., Borgen, E.C. and Rapp, R.A. 1967. Mixed conduction in Zr0.85Ca0.15O1.85 and $Th_{0.85}Y_{0.15}O_{1.925}$ solid electrolytes. *Journal of Electrochemical Society*, **114**, pp.752-758.

[49] Subbarao, E.C. 1981. Advances in ceramics-III, The American Ceramic Society, Coloumbus, OH.

[50] Sammes, N.M. and Cai, Z. 1997. Ionic conductivity of ceria/yttria stabilized zirconia electrolyte materials. *Solid State Ionics,* **100**, pp.39-44.

[51] EG&G Technical services. 2001. Fuel Cell Handbook (6th edition), Parsons Inc., ISBN 1603220178, US Department of Energy, Morgantown, West Virginia.

[52] Sammes, N.M. and Cai, Z. 1997. Ionic conductivity of ceria/yttria stabilized zirconia electrolyte materials (Correction). *Solid State Ionics*, **100**, pp.39-44.

[53] Yasuda. I. and Hishinuma, M. 1998. Ionic and Mixed Conducting Ceramics-III, The Electrochemical Society, Pennington, NJ.

[54] Atkinson, A. 1997. Chemically-induced stresses in gadolinium-doped ceria solid oxide fuel cell electrolytes. *Solid State Ionics*, **95**, pp.249-258

[55] Takahashi, T. and Iwahara, H. 1971. Ionic conduction in perovskite-type oxide solid solution and its application to the solid electrolyte fuel cell. *Energy Conversion*, **11**, pp.105-111.

[56] Ishihara, T., Matsuda, H. and Takita, Y. 1994. Doped $LaGaO_3$ perovskite type oxide as a new oxide ionic conductor. *Journal of American Chemical Society*, **116**, pp.3801-3803.

[57] Feng., M., Goodenough, J.B. 1994. A superior oxide-ion electrolyte. *European Journal of Solid State Inorganic Chemistry*, **31**, pp.663-672.

[58] Kim, J.H. and Yoo, H.I. 2001. Partial electronic conductivity and electrolytic domain of $La_{0.9}Sr_{0.1}Ga_{0.8}Mg_{0.2}O_{3-\delta}$. *Solid State Ionics*, **140**, pp.105-113.

[59] Drennan, J., Zelizko. V., Hay, D., Ciacchi, F.T. and Rajendran, S. 1997. Characterisation, conductivity and mechanical properties of the oxygen-ion conductor $La_{0.9}Sr_{0.1}Ga_{0.8}Mg_{0.2}O_{3-x}$. *Journal of Materials Chemistry*, **7**, pp.79-83.

[60] Du, Y. and Sammes, N.M. 2001. Fabrication of tubular electrolytes for solid oxide fuel cells using strontium- and magnesium-doped $LaGaO_3$ materials. *Journal of European Ceramic Society*, **21**, pp.727-735.

[61] Kendall, K.R., Navas, C., Thomas, J.K. and Loye, H.C.Z. 1995. Recent developments in perovskite-based oxide ion conductors. *Solid State Ionics*, **82**, pp.215-223.

[62] Zhang, G.B. and Smyth, D.M. 1995. Protonic conduction in $Ba_2In_2O_5$. *Solid State Ionics*, **82**, pp.153-160.

[63] Schober, T., Friedrich, J. and Krug, F. 1997. Phase transition in the oxygen and proton conductor $Ba_2In_2O_5$ in humid atmospheres below 300°C. *Solid State Ionics,* **99**, pp.9-13.

[64] Xiaogan, L. and Kale, G.M. 2007. Influence of sensing electrode and electrolyte on performance of potentiometric mixed-potential gas sensors. *Sensors and Actuators B Chemical* **123**(1), pp.254-261. DOI: 10.1016/j.snb.2006.08.017.

[65] Vanderah, T.A. 2002. Talking ceramics. *Science*, **298**, pp.1182-4

[66] Gill, K., Pandey, O.P. and Singh, K. 2011. Role of sintering temperature on thermal, electrical and structural properties of $Y_2Ti_2O_7$ pyrochlores. *International Journal of Hydrogen Energy,* **36**, pp. 14943-7.

[67] Wan, C.L., Pan, W., and Xu, O. 2006. Effect of point defects on thermal transport properties of $(La_xGd_{1-x})_2Zr_2O_7$: Experiment and theoretical model. *Phys. Rev B,* **74**, Article ID.144109.

[68] Kale, G.M. and Jacob, K.T. 1989. Gibbs energies of formation of cuprous and cupric yttrates ($CuYO_2$ and $Cu_2Y_2O_5$) and phase relations in the system copper-yttrium-oxygen. *Chem. Mater.* **1**(5), pp.515–519. https://doi.org/10.1021/cm00005a010

[69] Irshad, M. et al. 2016. A Brief Description of High Temperature Solid Oxide Fuel Cell's Operation, Materials, Design, Fabrication Technologies and Performance. *Appl. Sci.* **6** (75) doi:10.3390/app6030075.

[70] Pokhrel, M., Wahid, K. and Mao, Y. 2016. Systematic Studies on $RE_2Hf_2O_7$:5%Eu^{3+} (RE = Y, La, Pr, Gd, Er, and Lu) Nanoparticles: Effects of the A-Site RE^{3+} Cation and Calcination on Structure and Photoluminescence, *J. Phys. Chem. C*, **120**, pp.14828−14839

[71] Jitta, R., Gundeboina, R., Veldurthi, N.K., Guje, R. and Muga, V. 2015. Defect pyrochlore oxides: as photocatalyst materials for environmental and energy applications - a review. *J Chem Technol Biotechnol*, **90**, pp.1937–1948

[72] Blanchard, P.E.R., Liu, S., Kennedy, B.J. and Ling, C.D. 2013. Investigating the Local Structure of Lanthanide Hafnates $Ln_2Hf_2O_7$ via Diffraction and Spectroscopy, *J. Phys. Chem. C* 2013, **117**, pp.2266−2273.

[73] Goutenoire, F., Isnard, O., Retoux, R. and Lacorre, P. 2000. Crystal structure of $La_2Mo_2O_9$, a new fast oxide−ion conductor. *Chemistry of Materials,* **12**, pp.2575-2580.

[74] Subramania, A., Saradha, T. and Muzhumathi, S. 2007. Synthesis, sinterability and ionic conductivity of nanocrystalline Pr-doped $La_2Mo_2O_9$ fast oxide-ion conductors. *Journal of Power Sources,* **167**, pp.319-324.

[75] Bayliss, R.D., Cook, S.N., Kotsantonis, S., Chater, R.J. and Kilner J. A. 2014. Oxygen ion diffusion and surface exchange properties of the α- and δ-phases of Bi_2O_3. *Adv. Energy Mater.*, **4**(10), Article ID.1301575.

[76] Baron, B. 2004. Intermediate Temperature (500-850˚C) Solid Oxide Fuel Cell, Fuel Cell Today.

[77] Brian, C.H. and Heinzel, S.A. 2001. Materials for fuel-cell technologies. *Nature*, **414**.

[78] Adams, J. 1998. Fuel cells for transportation program, *Contrac. Annu. Prog. Rept*. 1:3. Washington, DC, US DOE.

[79] Wind, J., Spah, R., Kaiser, W. and Bohm, G. 2002. Metallic bipolar plates for PEM fuel cells. *J. Power Sources,* **105**, pp.154–58

[80] http://www.netl.doe.gov/technologies/coalpower/fuelcells/seca/primer/cell.html. Dated: 13/07/2017

[81] Jeffrey Brinker, C. and Scherer, G. W. 1990. Sol-gel science, Academic Press Inc.

[82] S. Sulubrk, C. Antic, V. Lojpur, M. M. Cincovic, and Miroslav D. DramiTanin, Sol-Gel Derived Eu3+-Doped $Gd_2Ti_2O_7$ Pyrochlore Nanopowders, Journal of Nanomaterials, Volume 2015, Article ID. 514173.

[83] Tai, W.P. 2003. Synthesis and characterization of nanocrystalline potassium tantalum oxide by sol_ gel processing, *Materials and Engineering B*, **103**, pp.83-87

[84] Hussain, C.M. 2018. Handbook of nanomaterials for industrial applications, Elsevier, ISBN: 978012813352.

[85] Smart, L.E. and Moore, E.A. 2005. An Introduction, Solid State Chemistry, (3rd edition), CRC Taylor and Francis Group.

[86] Gurikov, P. and Smirnova, I. 2018. Review, Non-conventional methods for gelation of alginate. *Gels,* **4** (14), pp.1-14.

[87] Dawson, W.J. 1988. Hydrothermal synthesis of advanced ceramic powders. *Am. Ceram. Soc. Bull*, **67**, pp.1673-78.

[88] Gombotz, W.R. and Wee, S.F. 1998. Protein release from alginate matrices. *Advanced Drug Delivery Reviews*, **31**(3), pp. 267-285.

[89] Hay, I.D., Rehman, Z.U., Ghafoor, A. and Rehm, B.H.A. 2010. Bacterial biosynthesis of alginates. J. Chem. Technol. Biotechnol., **85**, pp.752–759

[90] Teixeira, V. F., Pereira, N.R., Waldman, W.R., Avila, A., Perez, V.H. and Rodriguez, R.J.S. 2014. Ion exchange kinetics of magnetic alginate ferrogel beads produced by external gelation. *Carbohydrate Polymers,* **111**, pp.198–205.

[91] Baskoutas, S., Giabouranis, P., Yannopoulos, S.N., Dracopoulos, V., Toth, L., Chrissanthopoulos, A. and Bouropoulos, N. 2007. Preparation of ZnO nanoparticles by thermal decomposition of zinc alginate. *Thin Solid Films*, **515**, pp.8461–8464

[92] Wang, Z., Liu, J., Kale, G.M. and Ghadiri, M. 2014. Ion-exchange kinetics and thermal decomposition characteristics of Fe^{2+} exchanged alginic acid membrane for the formation of iron oxide nanoparticles. *J Mater Sci*, **49**, pp.7151–7155

[93] Glerup, M., Nielsen, O. F. and Poulsen, F. W. 2001. The structural transformation from the pyrochlore structure, $A_2B_2O_7$, to the fluorite structure, AO_2, studied by Raman spectroscopy and defect chemistry modeling. *J. Solid State Chem*, **160**, pp.25−32.

[94] Zhang, F.X., Lang, M. and Ewing, R.C. 2015. Atomic disorder in $Gd_2Zr_2O_7$ pyrochlore, *Applied Physics Letters,* **106**, Article ID. 191902.

[95] Rushton, M.J.D., Grimes, R.W., Stanek, C.R. and Owens, S. 2004. Predicted pyrochlore to fluorite disorder temperature for $A_2Zr_2O_7$ compositions. *J. Mater. Res.*, **19** (6), pp.1603–1604.

[96] Sleight, A.W. 1969. Rare earth plumbates with pyrochlore structure. *Inorg. Chem*, **8** (8), pp.1807–1808.

[97] Shamblin, J., Feygenson, M., Neuefeind, J., Tracy, C.L., Zhang, F., Finkeldei, S., Bosbach, D., Zhou, H., Ewing, R.C. and Lang, M. 2016. Probing disorder in isometric pyrochlore and related complex oxides. *Nature Materials*, **15**.

[98] Oskam, G. 2006. Metal oxide nanoparticles: synthesis, characterization and Application. *Journal of Sol-Gel Science and Technology*, **37**, pp.161–164

[99] Sevastyanov, V.G., Simonenko, E.P., Simonenko, N.P., Sakharov, K.A. and Kuznetsov, N.T. 2013. Synthesis of finely dispersed $La_2Zr_2O_7$, $La_2Hf_2O_7$, $Gd_2Zr_2O_7$ and $Gd_2Hf_2O_7$ oxides. *Mendeleev Communications*, **23**, pp.17–18

[100] Loureiro, A., Azoia, N.Z., Gomes, A.C. and Cavaco-Paulo, A. 2016. Albumin-based nanodevices as drug carriers. *Curr. Pharm. Des.*, **22**, pp. 1371-1390

[101] Martis, E., Badve, R. and Degwekar, M. 2012. Nanotechnology based devices and applications in medicine: an overview. *Chron. Young Sci.*, **3**, p. 68. 10.4103/2229-5186.94320

[102] Nikalje, A.P. 2015. Nanotechnology and its applications in medicine. *Med Chem*, **5**. 10.4172/2161-0444.1000247

[103] Laurent, S., Forge, D., Port, M., Roch, A., Robic, C., Vander Elst, L. and Muller, R.N. 2010. Magnetic iron oxide nanoparticles: synthesis, stabilization, vectorization, physicochemical characterizations, and biological applications. *Chem. Rev.*, **110**, pp. 2064–2110.

[104] Rogozea, E.A., Petcu, A.R., Olteanu, N.L., Lazar, C.A., Cadar, D. and Mihaly, M. 2017. Tandem adsorption-photodegradation activity induced by light on NiO-ZnO p–n couple modified silica nanomaterials. *Mater. Sci. Semicond. Process*, **57**, pp.1-11.

[105] Mayers, R.A. 2000. Encyclopaedia of analytical chemistry, Volume 15, J. Wiley, New York.

[106] Shojan, P., Pavunny, Y.S., Sudheendran, K., Sita, D., Rajesh, K.K., James, F.S. and Ram, S.K. 2015. Holmium hafnate: An emerging electronic device material. *Applied Physics Letters,* **106**:112902.

[107] Jones, R.L. 1997. Some aspects of the hot corrosion of thermal barrier coatings. *J. Therm. Spray. Technol.*, **6**, pp.77–84.

[108] Cahn, R.W. 1992. Concise Encyclopedia of Materials Characterization, (2nd Edition), Elsevier, Amsterdam.

[109] Cullity, B.D., Stock, S.R. and Stock, S. 2001. Elements of X-Ray Diffraction, (3rd Edition), Prentice Ha11.

[110] Klug, H.P. and Alexander, L.E. 1954. X-ray Diffraction Procedures for Polycrystalline and Amorphous Materials, Wiley, New York.

[111] Jlang, H.G., Ruhle, M. and Lavernia, E.J. 1999. On the applicability of the x-ray diffraction line profile analysis in extracting grain size and microstrain in nanocrystalline materials. *J. Mater. Res.*, **14** (2), pp.549-559.

[112] Weller, M.T. 2001. Inorganic Materials Chemistry (Oxford Chemistry Primers), Oxford University Press, UK.

[113] Williams, D.B. and Carter, C.B. 2004. Transmission electron microscopy: A textbook for materials science, Springer, USA.

[114] Harris, D.C. and Bertolucci, M.D. 1978. Symmetry and spectroscopy: an introduction to vibrational and electronic spectroscopy, Oxford University Press.

[115] Herzberg, G. 1991. Molecular Spectra and Molecular Structure II: Infrared and Raman Spectra of Polyatomic Molecules, Krieger publishing.

[116] Chen, I.-W. and Wang, X.-H. 2000. Sintering dense nanocrystalline ceramics without final-stage grain growth, *Nature*, **404**.

[117] Wang, Z.L. 2003. New Developments in Transmission Electron Microscopy for Nanotechnology. *Adv. Mater.*, **15** (18), pp.1497-1514

[118] Dumont, M.F. 2011. Nanostructures of Metallophosphates and Cyanometallates for Applications and Physical Studies. PhD thesis. University of Florida.

[119] Cahn, R.W., Haasen, P.H. and Kramer, E.J. 1992, Materials science and technology A comprehensive treatment, Volume 2A, VCH, Germany.

[120] Egerton, R.F. 2005. Physical Principles of Electron Microscopy-An Introduction to TEM, SEM, and AEM, Springer publication.

[121] Wang, Z. 2012. Novel Sol-gel Synthesis and Characterization of Oxide Nanopowders for Solid Oxide Fuel Cells. PhD thesis. University of Leeds.

[122] Jing, S.P., Love, J.G. and Badwal, S.P.S. 1997. Electrochemical techniques in studies of solid ionic conductors. *Key Eng. Mater.,* **125-126**, pp.81-132.

[123] Choi, W., Shin, H.C., Kim, J.M., Choi, J.Y. and Yoon, W.S. 2020. Modeling and applications of electrochemical impedance spectroscopy (EIS) for Lithium ion batteries. *J. Electrochem. Sci. Technol.*, **11** (1), pp.1-13.

[124] Sardar, S., Kale, G.M., Cespedes, O. and Ghadiri, M. 2020. Environmentally Sustainable Facile Synthesis of Nanocrystalline Holmium Hafnate ($Ho_2Hf_2O_7$): Promising New Oxide-ion Conducting Solid Electrolyte. *SN Appl. Sci.,* **2**:541. https://doi.org/10.1007/s42452-020-2336-9

[125] Wang, Z., Kale, G.M. and Ghadiri, M. 2012b. Novel Ion-Exchange Process for the Preparation of Metal Oxide Nanopowders from Sodium Alginate. *J. Am. Ceram. Soc.* **95**, pp. 3124–3129.

[126] Wang, Z., Kale, G.M. and Ghadiri, M. 2012a. Synthesis and characterization of CexGd 1-xO2-d nanopowders employing an alginate mediated ion-exchange process. *Chem. Eng. J.,* **198**, pp.149–153.

[127] Gladman, T. 2004. Grain Size Control, Maney Publishing.

[128] Vermaak, J.S., Mays, C.W. and Kuhlmann-Wilsdorf, D. 1968. On surface stress and surface tension: I. Theoretical considerations. *Surf. Sci.,* **12**, pp.128.

[129] Lopez-Cota, F.A., Cepeda-Sanchez, N.M., Diaz-Guillen, J.A., Dura, O.J., Lopez, O.M.A., Maczka, M., Ptak M. and Fuentes, A.F. 2017. Electrical and thermophysical properties of mechanochemically obtained lanthanide hafnates. *J. Am. Ceram. Soc.,* **100**, pp.1994-2004.

[130] Mandal, B.P., Garg, N., Sharma, S.M. and Tyagi, A.K. 2006. Preparation, XRD, and Raman spectroscopic studies on new compounds $RE_2Hf_2O_7$ (RE = Dy, Ho, Er, Tm, Lu,Y): pyrochlores or defect-fluorite?. *J. Solid State Chem.,* **179**, pp.1990–94.

[131] Liao, T.W., Chen, H.M., Shen, K.Y. and Kuan, C.H. 2015. Pure, single crystal Ge nanodots formed using a sandwich structure via pulsed UV excimer laser annealing. *Nanotechnology,* **26** (16):65301.

[132] Long, D.A. 1997. Raman spectroscopy, McGraw-Hill International Book Company. New York.

[133] Tsao, C.Y., Weber, J.W., Campbell, P., Widenborg, P.I., Song, D. and Green, M.A. 2009. Low temperature growth of polycrystalline Ge thin film on glass by in situ deposition and ex situ solid-phase crystallization for photovoltaic applications. *Appl. Surf. Sci.,* **255** (15), pp.7028-35.

[134] Katainen, E., Elomaa, M., Laakkonen, U.M., Sippola, E., Niemela, P., Suhonen, J. and Jarvinen, K. 2007. Quantification of the amphetamine content in seized street samples by Raman spectroscopy. *J. Forensic Sci.,* **52** (1), pp.88-92.

[135] Gupta, H.C., Brown, S., Rani, N. and Gohel, V.B. 2002. A lattice dynamical investigation of the Raman and the infrared frequencies of the cubic $A_2Hf_2O_7$ pyrochlores. *J. Phys. Chem. Solids,* **63**, pp.535–8.

[136] Kumar, S. and Gupta, H.C. 2012. First principles study of dielectric and vibrational properties of pyrochlore hafnates. *Solid State Sci.,* **14**, pp.1405–11.

[137] Vandenborre, M.T. and Husson, E. 1983. Comparison of the force field in various pyrochlore families. I. The $A_2B_2O_7$ Oxides. *J Solid State Chem.,* **50**, pp.362–71.

[138] Vandenborre, M.T. and Husson, E. 1984. Comparison of the force field in various pyrochlore families II. Phases presenting structural defects. *J Solid State Chem.,* **53**, pp. 253–9.

[139] Vandenborre, M.T., Husson, E. Chatry, J.P. and Michel, D. 1983. Rare-earth titanates and stannates of pyrochlore structure; vibrational spectra and force fields. *J. Raman Spectrosc.,* **14**, pp.63–71.

[140] Scheetz, B.E. and White, W.B. 1983. Temperature-dependent Raman spectra of rare-earth titanates with the pyrochlore structure: A dipolar order-disorder transition. *Opt. Eng.,* **22**: 223302.

[141] Poulsen, F.W., Glerup, M. and Holtappels, P. 2000. Structure, Raman spectra and defect chemistry modelling of conductive pyrochlore oxides. *Solid State Ion.,* **135**, pp.595–602.

[142] Saha, S. et al. 2006. High-pressure Raman and X-ray study of the spin-frustrated pyrochlore $Gd_2Ti_2O_7$. *Phys. Rev. B*, **74**:064109

[143] Lian, J., Zu, X.T., Kutty, K.V.G., Chen, J., Wang, L.M. and Ewing, R.C. 2000. Ion-irradation-induced amorphization of $La_2Zr_2O_7$ pyrochlore. *Phys. Rev. B*, **66**: 054108.

[144] Solomon, J.M., Shamblin, J., Lang, M., Navrotsky, A. and Asta, M. 2016. Chemical ordering in substituted fluorite oxides: A computational investigation of $Ho_2Zr_2O_7$ and $Re_2Th_2O_7$ (RE = Ho, Y, Gd, Nd, La). *Sci Rep,* **6**, pp.1–9.

[145] Stanek, C.R. and Grimes, R.W. 2002. Prediction of rare earth $A_2Hf_2O_7$ pyrochlore phases. *J. Am. Ceram. Soc.,* **86**, pp.2139–41.

[146] Maczka, M., Sanjuan, M.L., Fuentes, A.F., Hermanowicz, K. and Hanuza, J. 2008. Temperature-dependent Raman study of the spin-liquid pyrochlore $Tb_2Ti_2O_7$. *Phys Rev B,* **78** (8):134420.

[147] Hess, N.J., Begg. B.D., Conradson, S.D., Mccready, D.E., Gassman, P.L. and Weber, W.J. 2002. Radiation-induced disorder in compressed lanthanide zirconates. *J. Phys. Chem. B*, **106**: 4663.

[148] Maczka, M., Sanjuan, M.L. and Fuentes, A.F. et al. 2009. Temperature-dependent studies of the geometrically-frustrated pyrochlores $Ho_2Ti_2O_7$ and $Dy_2Ti_2O_7$. *Phys. Rev. B,* **79** (13).

[149] Lu, D.Y. and Guan, D.X. 2017. Photoluminescence associated with the site occupations of Ho^{3+} ions in $BaTiO_3$. *Scientific Reports*, **7**:6125.

[150] Heremans, C., Wuensch, B.J., Stalick, J.K. and Prince, E. 1995. Fast-ion conducting Y_2 $(Zr_yTi_{1-y})_2$ O_7 pyrochlores: neutron Rietveld analysis of disorder induced by Zr substitution. *J Solid State Chem.*, **117**, pp.108–121.

[151] Popov, V.V. et al. 2017. Features of formation and evolution of crystal and local structures in nanocrystalline $Ln_2Zr_2O_7$ (Ln = La - Tb). *J. Phys.: Conf. Ser.,* **941**, Article ID. 012079.

[152] Rietveld, H.M. 1969. A Profile Refinement Method for Nuclear and Magnetic Structures, *J. Appl. Crystallogr.,* **2,** pp.65–71.

[153] Young, R.A. 1993. The Rietveld Method, Oxford University Press Inc., New York.

[154] Artini, C., Pani, M., Lausi, A., Masini, R. and Costa, G. A. 2014. High Temperature Structural Study of Gd-Doped Ceria by Synchrotron X-ray Diffraction (673 K ≤ T ≤ 1073 K) *Inorg. Chem.,* **53**, pp. 10140–10149.

[155] Turner, K.M. et al. 2017. Pressure induced structural modifications of rare-earth hafnate pyrochlore. *J. Phys. Condens. Matter*, **29**, pp. 255401

[156] Shevchenko, A.V., Lopato, L.M. and Kiryakova, I.E. 1984. Interaction of HfO_2 with Y_2O_3, Ho_2O_3, Er_2O_3, Tm_2O_3, Yb_2O_3, and Lu_2O_3 at high temperatures. *Inorg. Mater.,* **20**, pp.1731.

[157] Dijk, M.P., Burggraaf, A.J., Cormack, A.N. and Catlow, C.R.A. 1985. Defect structures and migration mechanisms in oxide pyrochlores. *Solid State Ionics*, **17**, pp.159–167.

[158] Wilde, P.J. and Catlow, C.R.A. 1998. Defects and diffusion in pyrochlore structured oxides. *Solid State Ionics*, **112**, pp.173–183.

[159] Adamu, M. and Kale, G.M. 2016. Novel sol-gel synthesis of $MgZr_4P_6O_{24}$ composite solid electrolyte and newer insight into the Mg^{2+}-ion conducting properties using impedance spectroscopy. *J. Phys. Chem. C*, **120** (32), pp.17909-17915.

[160] Sardar, S., Kale, G.M. and Ghadiri, M. 2020. Influence of processing conditions on the ionic conductivity of holmium zirconate ($Ho_2Zr_2O_7$). *Ceramics International*, **46**, pp.11508-11514. https://doi.org/10.1016/j.ceramint.2020.01.177

[161] Sardar, S., Kale, G., Ghadiri, M. and Cespedes, O. 2019. Structural study of holmium zirconate nanoparticles obtained through carbon neutral sol gel method. *Thermochimica Acta,* **676**, pp.120-129

[162] Stopyra, M., Niemiec, D. and Moskal, G. 2016. Synthesis, characterization and thermal diffusivity of holmium and praseodymium zirconates. *Arch. Metall. Mater.*, **61**(2B), pp.1249–1254

[163] Sayed, F.N., Jain, D., Mandal, B.P., Pillai, C.G.S. and Tyagi, A.K. 2012. Tunability of structure from ordered to disordered and its impact on ionic conductivity behavior in the $Nd_{2-y}Ho_yZr_2O_7$ (0.0≤y≤2.0) system. *RSC Advances*., **2**, pp.8341–8351

[164] Shannon, R.D. 1976. Revised effective ionic radii and systematic studies of interatomic distances in halides and chalcogenides. *Acta Cryst. A,* **32**, pp.751–767.

[165] Rousseau, D.L., Bauman, R.P. and Porto, S.P.S. 1981. Normal mode determination in crystals. *J. Raman Spectrosc.,* **10** (1), pp.253–290.

[166] Zhou, W. and Heather, F.G. 2016. What can electron microscopy tell us beyond crystal structures? *Eur. J. Inorg. Chem.,* pp.941-950.

[167] Uvarov, V. and Popov, I. 2013. Metrological characterization of X-ray diffraction methods at different acquisition geometries for determination of crystallite size in nano-scale materials, *Mater. Charact.,* **85**, pp.111–123.

[168] Chiaramonti, A.N. and Marks. L.D. 2005. Thickness Series: Weak signal extraction of ELNES in EELS spectra from surfaces. *J. Mater. Res.,* **20,** pp.1619–1627.

[169] Gao, et al., 2012. Hierarchical assembly of multifunctional oxide-based composite nanostructures for energy and environmental applications. *Int. J. Mol. Sci.*. **13**, pp.7393–7423.

[170] Malek, M.F., Mamat, M.H., Musa, M.Z., Khusaimi, Z., Sahdan, M.Z., Suriani, A.B. et al. 2014. Thermal annealing-induced formation of ZnO nanoparticles: Minimum strain and stress ameliorate preferred *c*-axis orientation and crystal-growth properties. *Journal of Alloys and Compounds*, **610**. pp.575-588.

[171] Bellon, O., Sammes, N.M. and Staniforth, J. 1998. Mechanical properties and electrochemical characterisation of extruded doped cerium oxide for use as an electrolyte for solid oxide fuel cells. *J. Power Sources,* **75**.

[172] Wang, Z.Kale, G.M. and Tang, X. 2014. Sintering behavior and ac-conductivity of dense $Ce_{0.8}Gd_{0.2}O_{1.9}$ solid electrolyte prepared employing single step and two-step sintering process. *Journal of Materials Science*, **49** (8), pp.3010-3015.

[173] Guidara, S., Feki, H. and Abid, Y. 2016. Impedance, AC conductivity and electric modulus analysis of L-Leucine L-Leucinium picrate. *J. Alloys Compd.,* **663**, pp.424−429.

[174] Mehranjani, A.S., Cumming, D.J., Sinclair, D.C. and Rothman, R.H. 2017. Low-temperature co-sintering for fabrication of zirconia/ceria bi-layer electrolyte via tape casting using a Fe_2O_3 sintering aid. *Journal of the European Ceramic Society,* **37,** pp.3981–3993.

[175] Interpreting unexpected events and transition in DSC results. TA instrument. http://tainstruments.com

[176] Gu, S., Zhang, S., Xu, D., Li, W. and Yan, J. 2018. Evolution of microstructure and hot corrosion performance of $La_2Hf_2O_7$ ceramic in contact with molten sulfate-vanadate salt. *Ceramics International,* **44**, pp.2048–2057.

[177] Lumpkin, G.R., Whittle, K.R., Rios, S., Smith, K.L. and Zaluzec, N.J. 2004. Temperature dependence of ion irradiation damage in the pyrochlores $La_2Zr_2O_7$ and $La_2Hf_2O_7$. J. *Phys. Condens. Matter,* **16,** pp.8557-8570.

[178] Yang, J., Shahid, M., Zhao, M., Feng, J., Wan, C. and Pan, W. 2016. Physical properties of $La_2B_2O_7$(B=Zr, Sn, Hf and Ge) pyrochlore: First-principles calculations, *Journal of Alloys and Compounds,* **663**, pp.834-841.

[179] Vorozhtcov, V.A., Stolyarova, V.L., Lopatin, S.I., Simonenko, E.P., Simonenko, N.P., Sakharov, K.A., Sevastyanov, V.G. and Kuznetsov, N.T. 2018. Vaporization and thermodynamic properties of lanthanum hafnate. *Journal of Alloys and Compounds,* **735**, pp.2348-2355.

[180] Hynes, A. P., Doremus, R. H. and Siegel, R.W. 2002. Sintering and characterization of nanophase zinc oxide. *J. Am. Ceram. Soc.,* **85** (8), pp.1979–87.

[181] Li, J. and Ye, Y. 2006. Densification and grain growth of Al_2O_3 nanoceramics during pressureless sintering. *J. Am. Ceram. Soc.*, **89** (1) pp.139–43.

[182] Kang, S-J. L. 2005. Sintering Densification, Grain Growth and Microstructure. Elsevier, Oxford.

[183] Senda T. and Bradt, R.C. 1990. Grain Growth in Sintered ZnO and ZnO–Bi2O3 Ceramics. *J. Am. Ceram. Soc.*, **73** (1), pp.106–14.

[184] X.-H. Wang, P.-L. Chen, and I.-W. Chen, ''Two-Step Sintering of Ceramics with Constant Grain-Size, I: Y2O3,'' *J. Am. Ceram. Soc.*, **89** [2] 431–7 (2006).

[185] Ghosh, A., Suri, A.K., Rao, B.T. and Ramamohan, T.R. 2007. Low-temperature sintering and mechanical property evaluation of nanocrystalline 8mol% yttria fully stabilized zirconia. J. *Am. Ceram. Soc.*, **90** (7), pp.2015–23.

[186] MacDonald, D. and McKubre, M. 1987. Impedance Spectroscopy. Emphasizing Solid Materials and Systems, (MacDonald, J. R. Edition), Chapter 4, Section 4.3, John Wiley & Sons, New York.

[187] Kharton, V.V., Yaremchenko, A.A., Naumovich, E.N. and Marques, F.M.B. 2000. Research on the Electrochemistry of Oxygen Ion Conductors in the Former Soviet Union. III. $HfO^{2-,}$ CeO^{2-} and ThO^{2-} Based Oxides. *J. Solid State Electrochem.*, **4** (5), pp.243–66.

[188] Bovina, E.A., Tarasova, J.V. and Chibirova, F. 2011. Syntesis of lanthanum zirconate hydrosols by the ion exchange method. *Journal of Physics: Conference Series,* **291**, Article ID. 012037. doi:10.1088/1742-6596/291/1/012037

[189] Pecharsky, V.K. and Zavalij, P.Y. 1992. Fundamentals of Powder Diffraction and Structural Characterization of Materials, (2nd Edition), Springer.

[190] Fuertes, M.C. and Porto Lopez, J.M. 2004. Mechanochemical synthesis and thermal evolution of La^{3+}–ZrO_2 cubic solid solutions. *Ceramics International*, **30** (8), pp.2137-2142.

[191] JCPDS-International Centre for Diffraction Data, File No.17-0450, 1995.

[192] Kido, H., Komarneni, S. and Roy, R. 1991. Preparation of $La_2Zr_2O_7$ by sol–gel route, *J. Am. Ceram. Soc*, **74** (2), pp. 422-424

[193] Mitterdorfer, A. and Gauckler, L.J. 1998. $La_2Zr_2O_7$ formation and oxygen reduction kinetics of the $La_{0.85}Sr_{0.15}Mn_yO_3O_2$ (g)/YSZ system. *Solid State Ionics*, **111**, pp.185-218.

[194] Radha, A.V., Ushakov, S.V. and Navrotsky, A. 2009. Thermochemistry of lanthanum zirconate pyrochlore. *J. Mater. Res.*, **24** (11), pp.3350-3357.

[195] Paul, B., Singh, K., Jaron, T., Roy, A. and Chowdhury, A. 2016. Structural properties and the fluorite-pyrochlore phase transition in $La_2Zr_2O_7$: The role of oxygen to induce local disordered states. *Journal of Alloys and Compounds,* **686**, pp.130-136.

[196] Maier, J. 1985. Space charge regions in solid two-phase systems and their conduction contribution-I. Conductance enhancement in the system ionic conductor-'inert' phase and application on $AgC1:A1_2O_3$, and $AgCl:SiO_2$. *J. Phys. Chem. Solids*, **46** (3), pp.309-320.

[197] Vaidehi, N., Akila, R., Shukla, A.K. and Jacob, K.T. 1986. Enhanced ionic conduction in dispersed solid electrolyte systems $CaF_2-Al_2O_3$ and CaF_2-CeO_2. *Mat. Res. Bull.*, **21**, pp.909-916.

[198] Kakushima, K., Tsutsui, K., Hattori, T. and Iwai, H. 2005. Lanthanum Oxide for Gate Dielectric Insulator, *Proceedings of IEEE Conference on Electron Devices and Solid-State Circuits*. Howloon, Hong Kong, pp.161-166. doi:10.1109/EDSSC.1635231.

[199] Slough, C.G. 2005. Quantitative mass measurements from the mass spectrometer trend data in a TG/MS system, *Journal of ASTM international*, **2** (9).

Appendix

A.1. Holmium Oxide (Ho_2O_3)
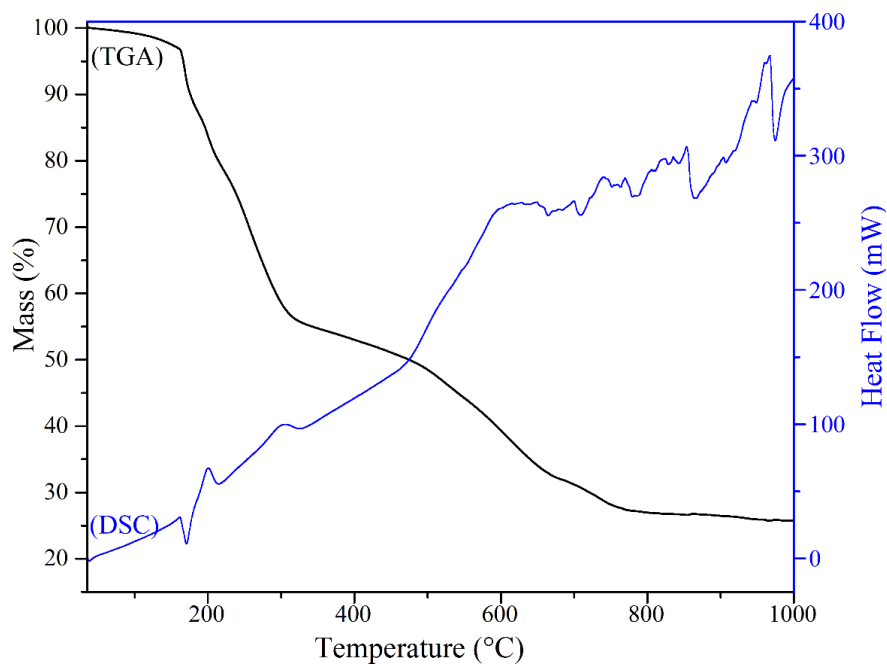
Fig. A.1: TGA/DSC analysis of metal (holmium) alginate beads
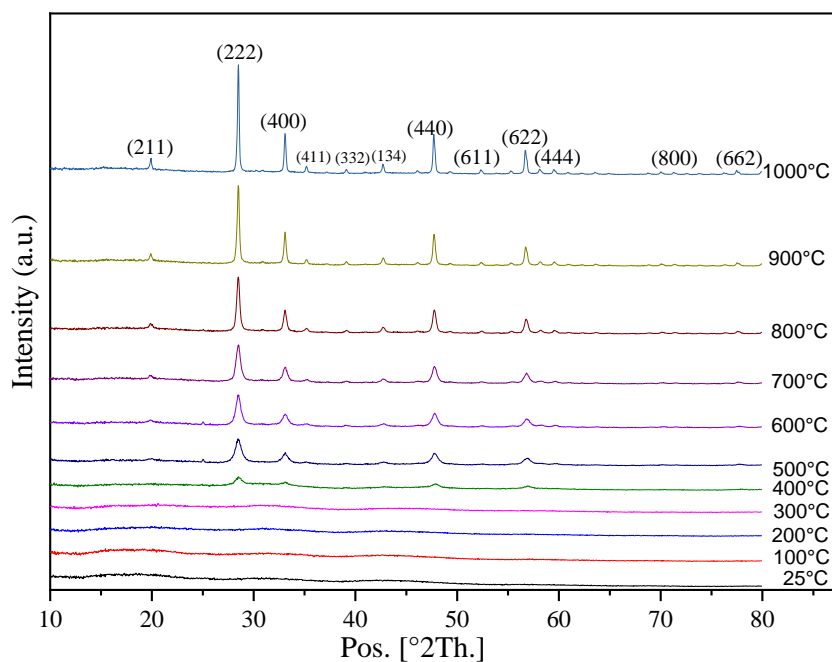
Fig. A.2: HTXRD scans of metal (holmium) alginate beads

Table A.1: Structural parameters of metal oxides

Sample	Rietveld Refined Size Strain Analysis					
	Avg. Crystallite Size (nm)	Micro Strain (%)	R_{wp} (%)	R_{exp} (%)	GOF	Lattice Parameters (A°)

252

Ho$_2$O$_3$	15.6	0.978	4.76	1.89	6.34	10.6139
HfO$_2$	7.7	2.034	7.52	2.20	11.6	a = 5.1279, b = 5.1794, c = 5.2945
La$_2$O$_3$	269.5	0.055	16.21	5.10	10.1	a = b = 3.9384, c = 6.1310
ZrO$_2$	10	1.478	12.84	3.66	12.3	a = b = 3.5943, c = 5.1798
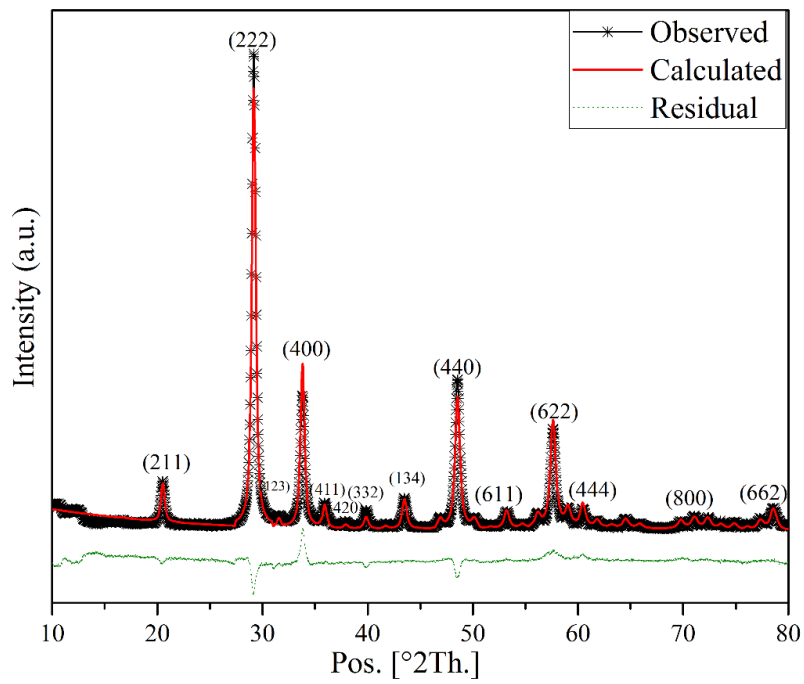
Fig. A.3: Rietveld refined XRD results of holmium oxide
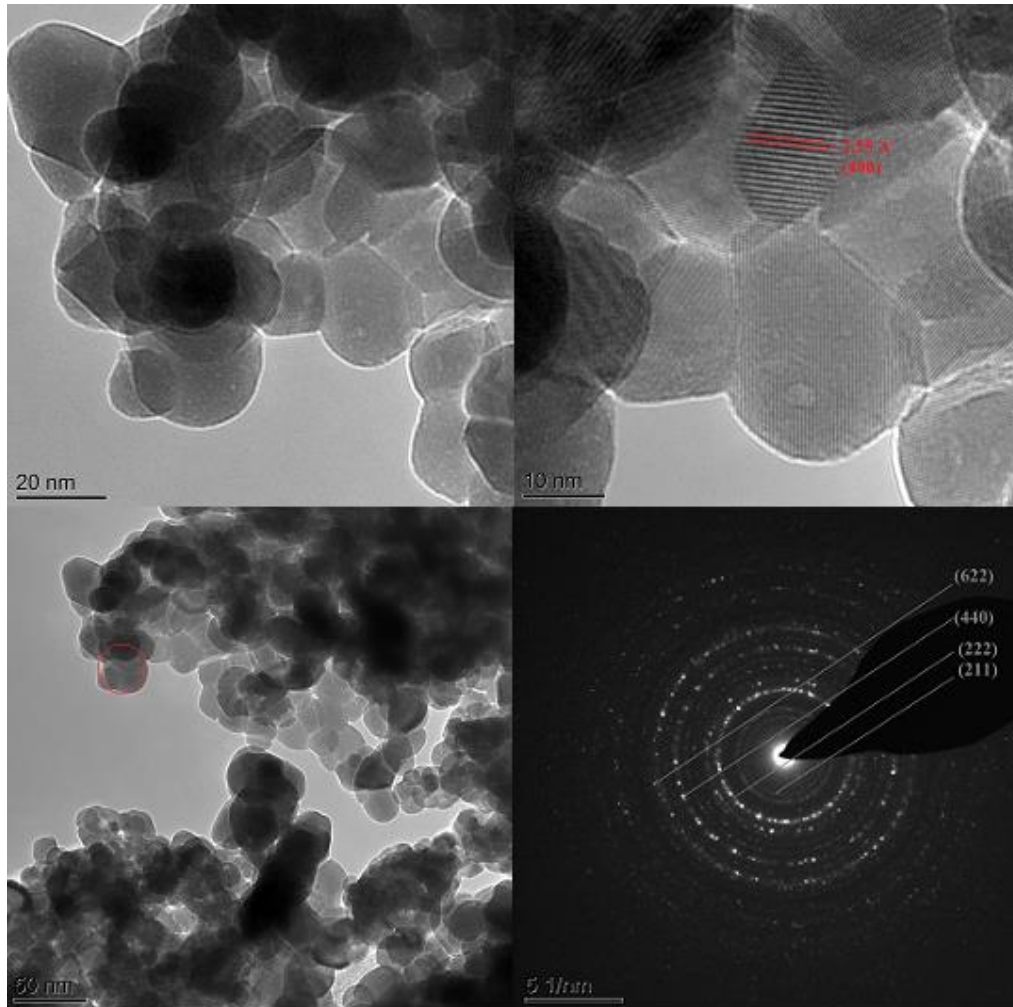
Fig. A.4: TEM and SAED scans of holmium oxide nanopowders

Table A.2: Comparison of d-spacing of Holmium Oxide from TEM and XRD Rietveld Refinement

h	k	L	Ref. (ICDD-01-074-1829) d, A˚	XRD d, A˚	TEM d, A˚
				700˚C-2h	700˚C-2h
2	1	1	4.32990	4.3268	4.4
2	2	2	3.06170	3.0638	3.01
4	0	0	2.65150	2.6516	2.55
4	4	0	1.87490	1.8757	1.87

A.2. Hafnium Oxide (HfO₂)

254
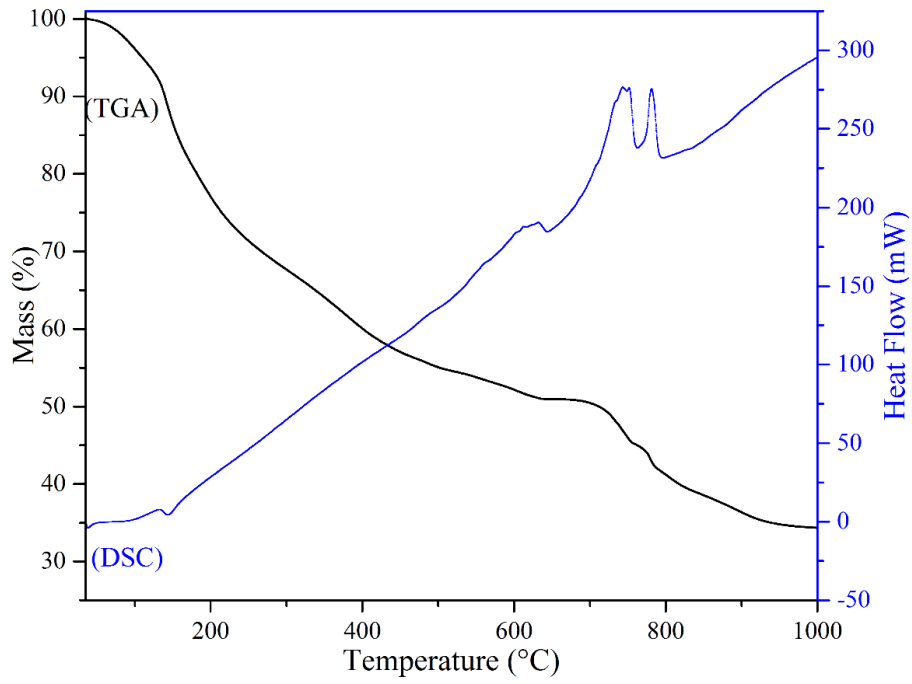
Fig. A.5: TGA/DSC analysis of metal (hafnium) alginate beads
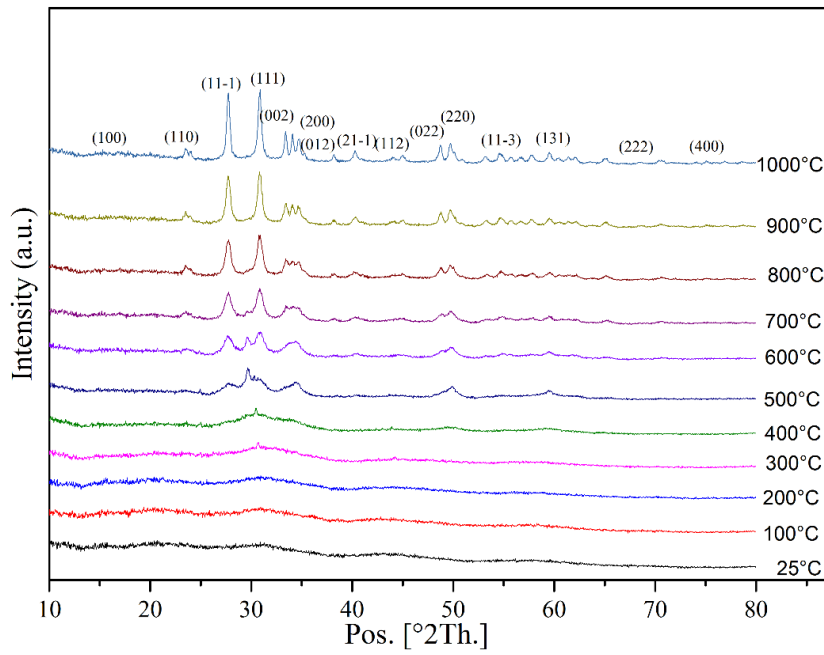
Fig. A.6: HTXRD scans of metal (hafnium) alginate beads

255
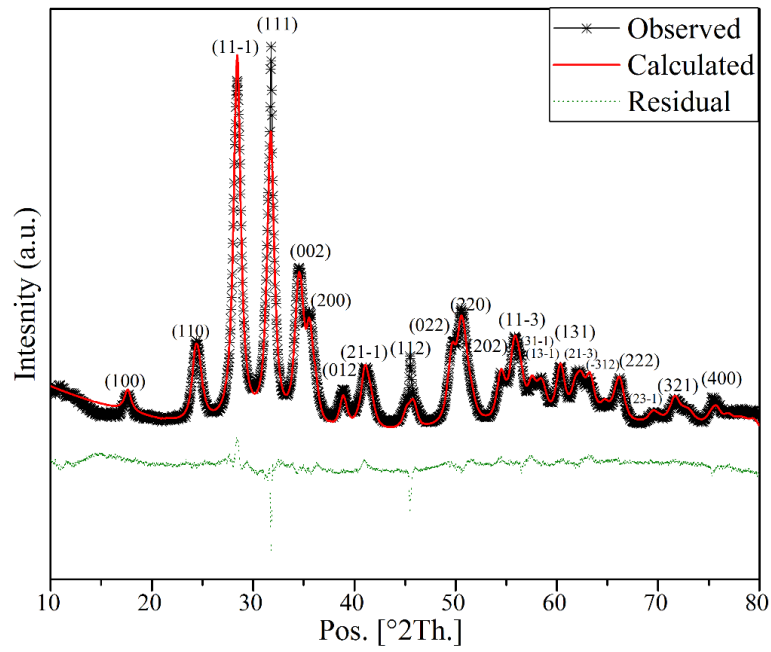
Fig. A.7: XRD analysis of hafnium oxide nanopowders with rietveld refinement
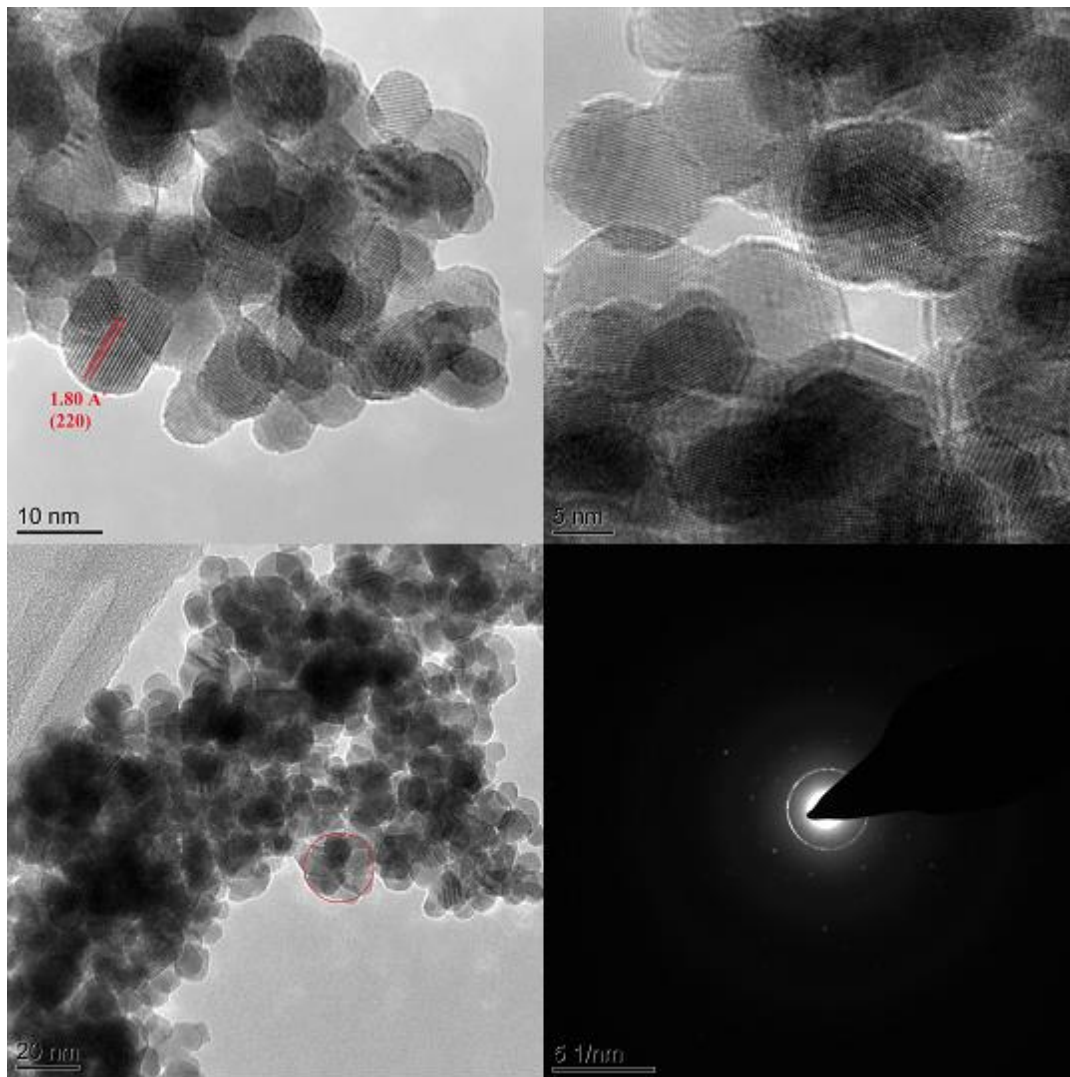
Fig. A.8: TEM images and SAED pattern of hafnium oxide nanopowders

Table A.3: Comparison of d-spacing of Hafnium Oxide from TEM and XRD Rietveld Refinement

h	k	L	Ref. (ICDD-04-004-3850) d, A˚	XRD d, A˚	TEM d, A˚
				700˚C-2h	700˚C-2h
1	1	0	3.61350	3.6156	3.60
1	1	1	2.82580	2.8264	2.74
2	0	0	2.52660	2.5272	2.52
2	2	0	1.80670	1.8067	1.80

A.3. Lanthanum Oxide (La$_2$O$_3$)
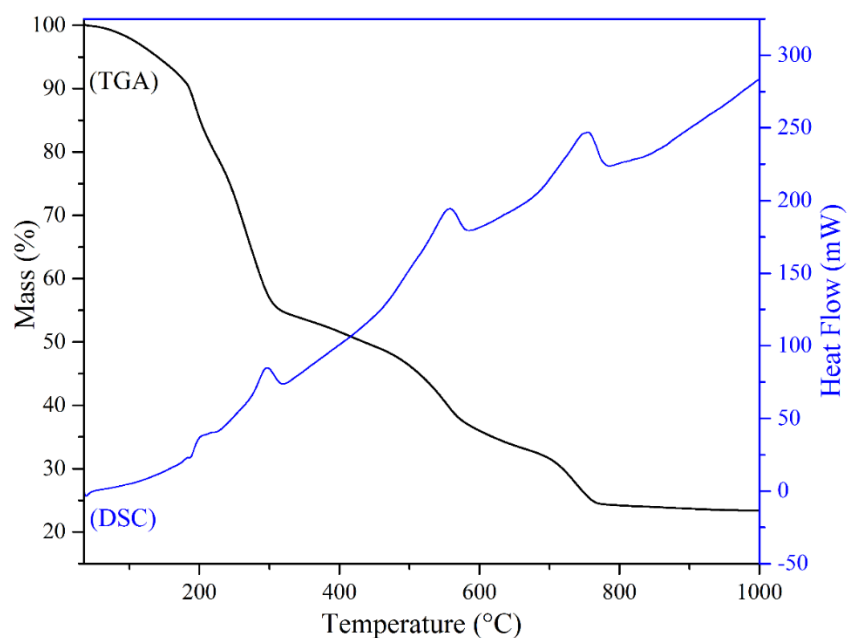
Fig. A.9: TGA/DSC analysis of metal (lanthanum) alginate beads
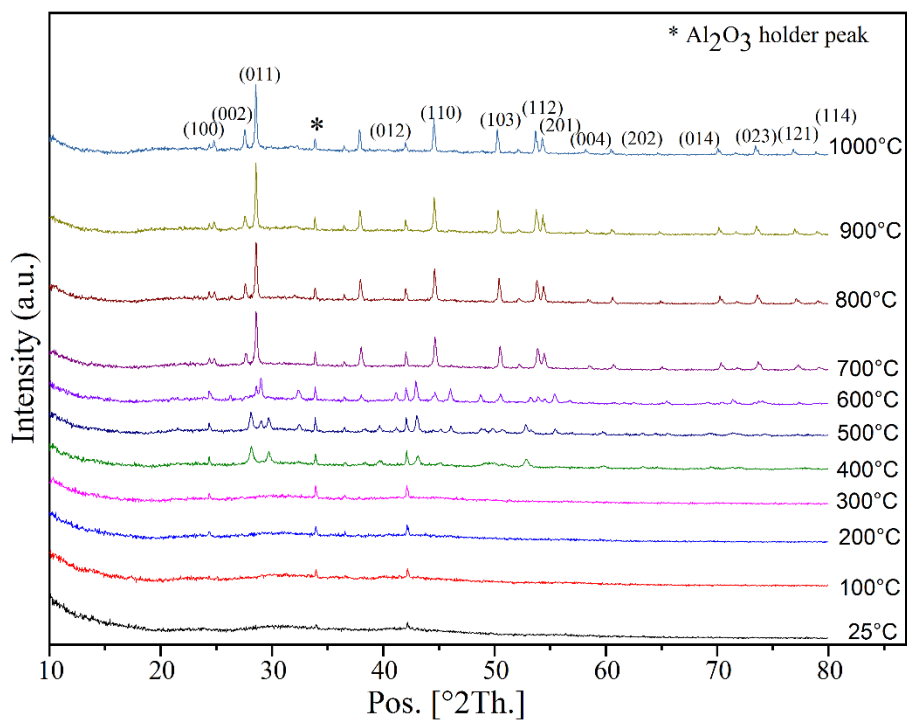
Fig. A.10: HTXRD scans of metal (lanthanum) alginate beads
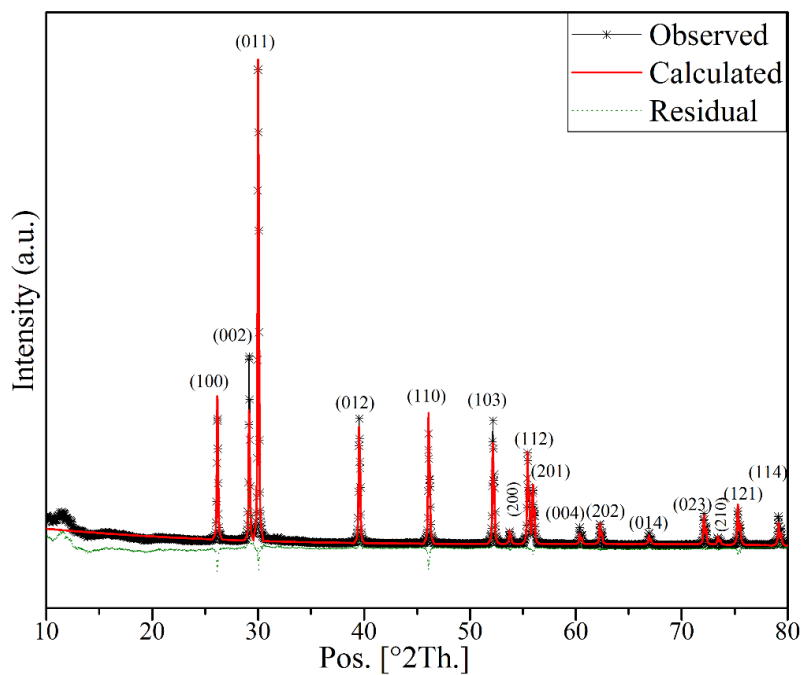
Fig. A.11: Rietveld refined XRD analysis of lanthanum oxide nanopowders
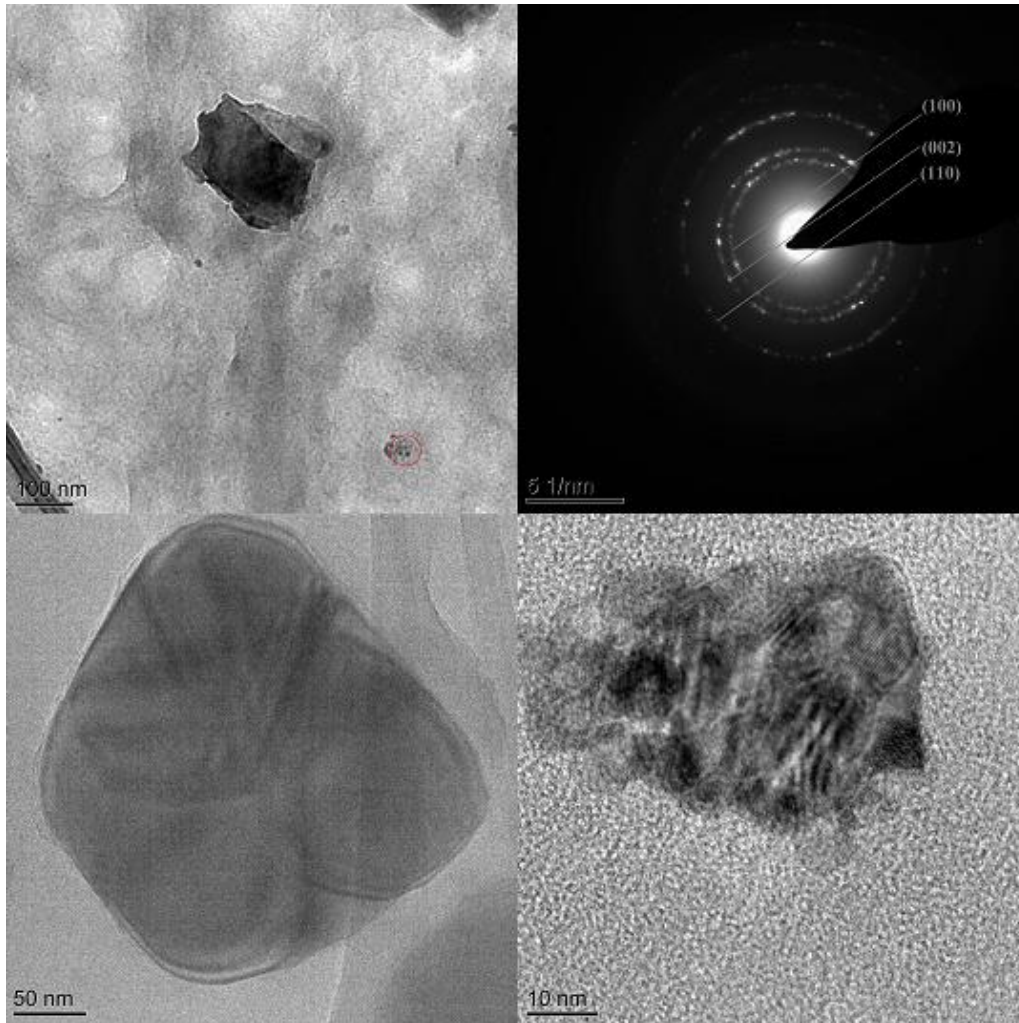
Fig. A.12: TEM and SAED analyses of lanthanum oxide

Table A.4: Comparison of d-spacing of Lanthanum Oxide from TEM and XRD Rietveld Refinement

h	k	L	Ref. (ICDD-01-071-5408) d, A°	XRD d, A°	TEM d, A°
				1000°C-6h	1000°C-6h
1	0	0	3.40690	3.4067	3.42
0	1	1	2.97860	2.9796	3.07
0	1	2	2.27980	2.2794	2.36
1	0	3	1.75360	1.7038	1.65

A.4. Zirconium Oxide (ZrO$_2$)
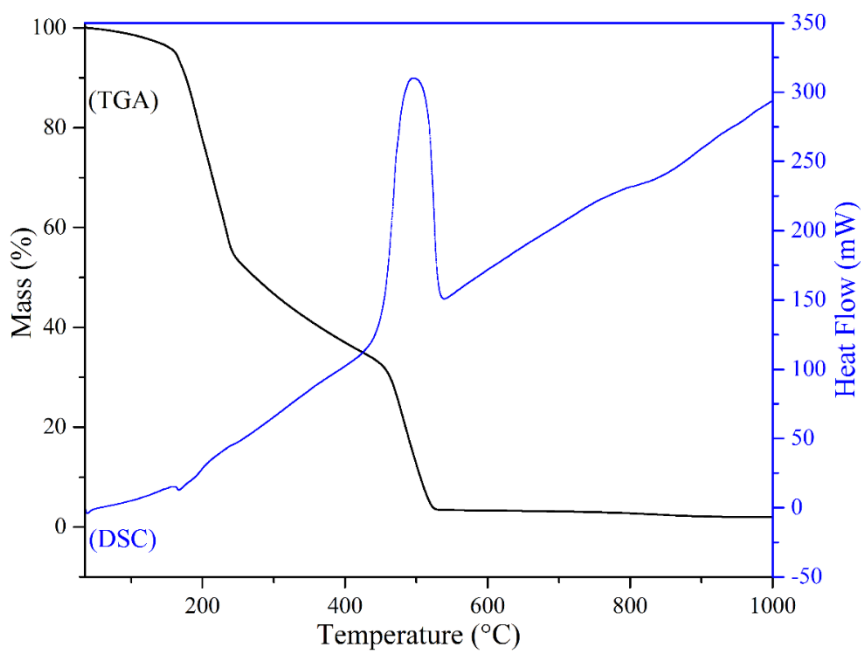
Fig. A.13: TGA/DSC analysis of metal (zirconium) alginate beads
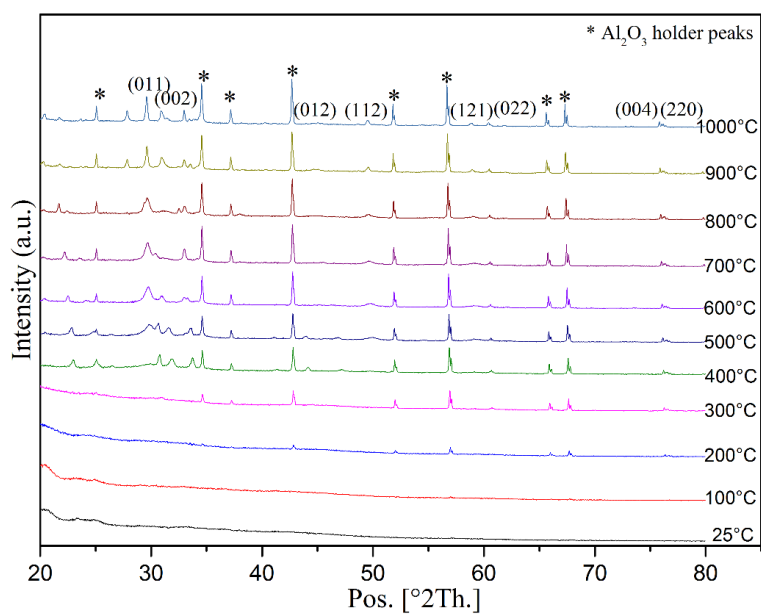
Fig. A.14: HTXRD scans of metal (zirconium) alginate beads
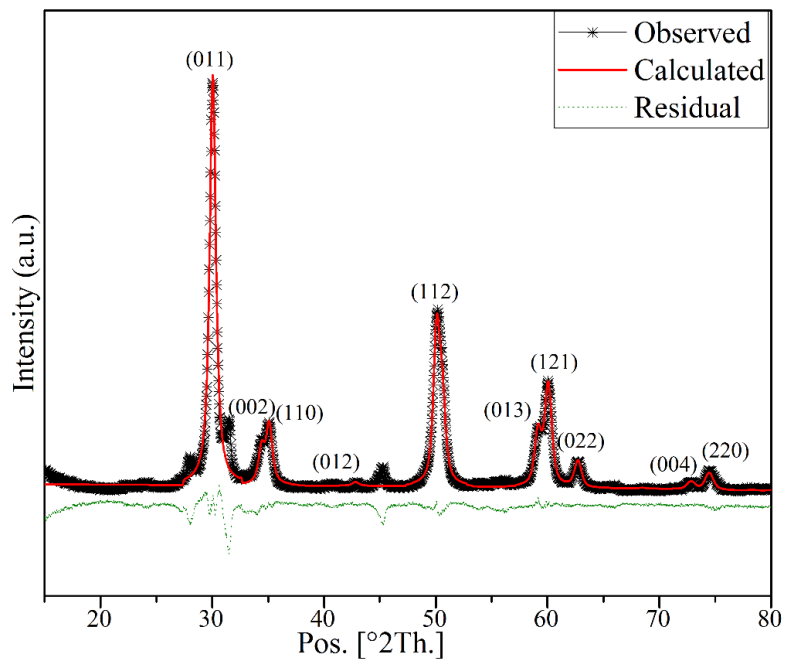
Fig. A.15: XRD data of zirconium oxide nanopowders with rietveld refinement
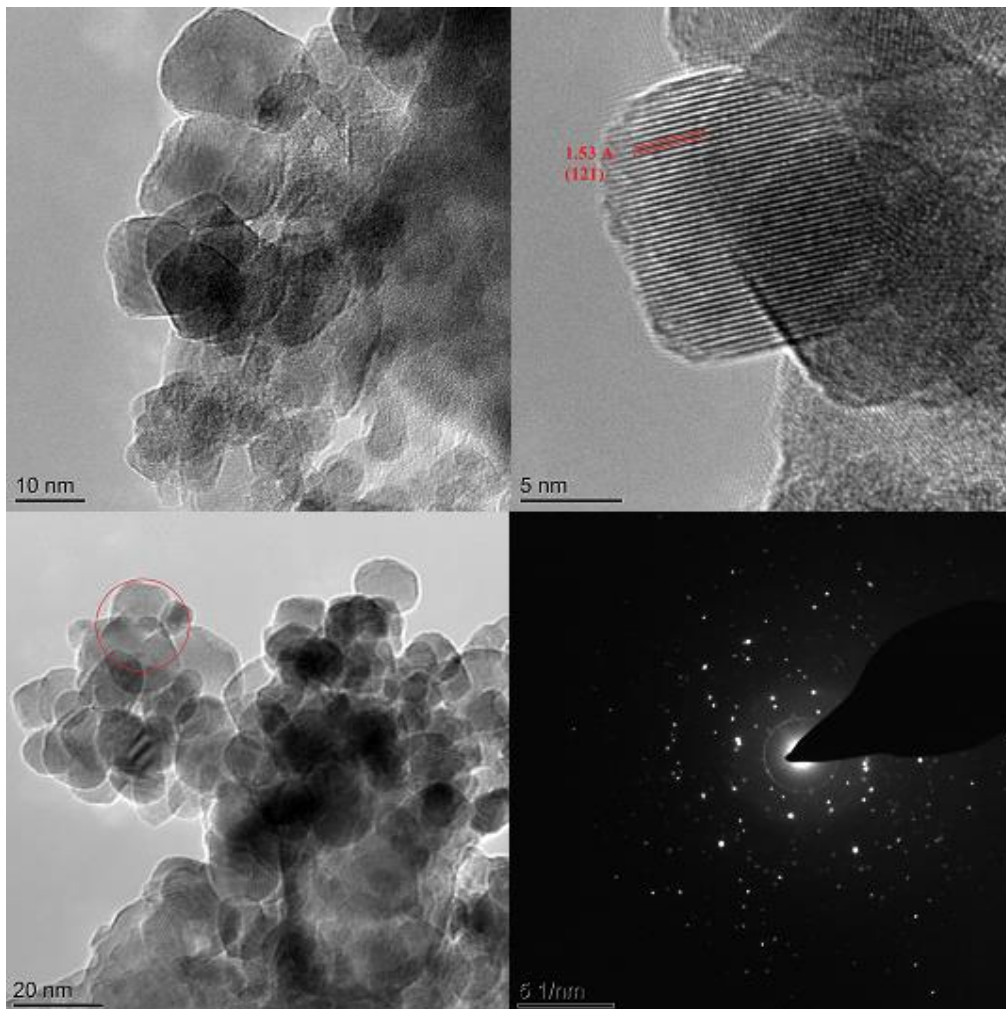
Fig. A.16: TEM and SAED analysis of zirconium oxide nanopowders

Table A.5: Comparison of d-spacing of Zirconium Oxide from TEM and XRD Rietveld Refinement

h	K	L	Ref. (ICDD-01-070-7358) d, A°	XRD d, A°	TEM d, A°
				700°C-2h	700°C-2h
0	1	1	2.96880	2.9684	2.87
0	0	2	2.60600	2.6071	2.63
1	1	2	1.82410	1.8245	1.88
1	2	1	1.54290	1.5126	1.53

A.5. Bode Plots of Holmium Zirconate for SSS and TSS process pellets
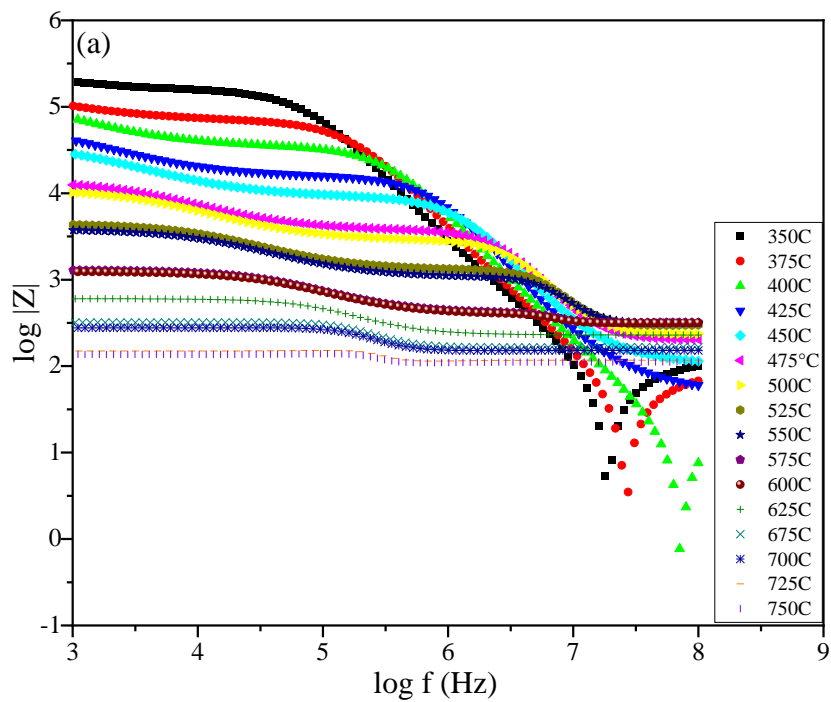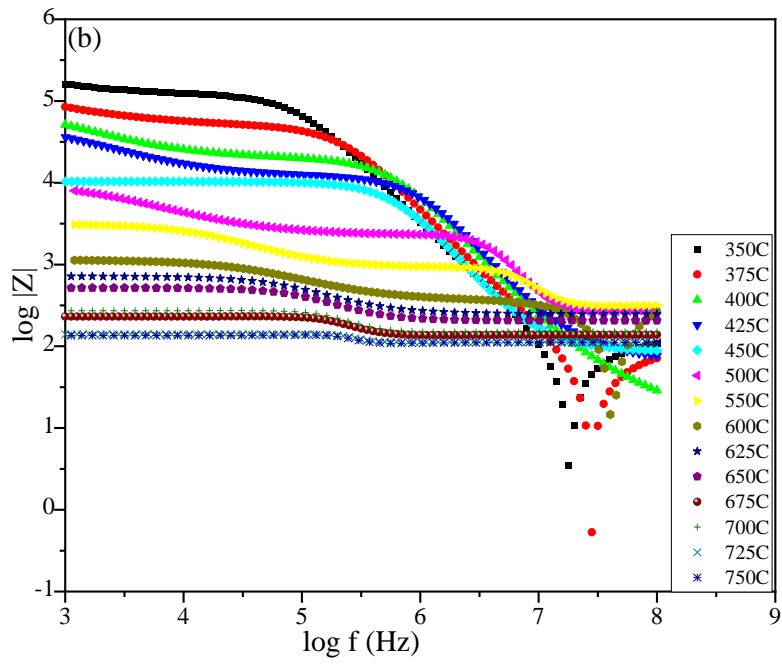
Fig. A.17: Bode plots of Ho$_2$Zr$_2$O$_7$ pellet sintered at 1500°C for 2h (a) heating (b) cooling
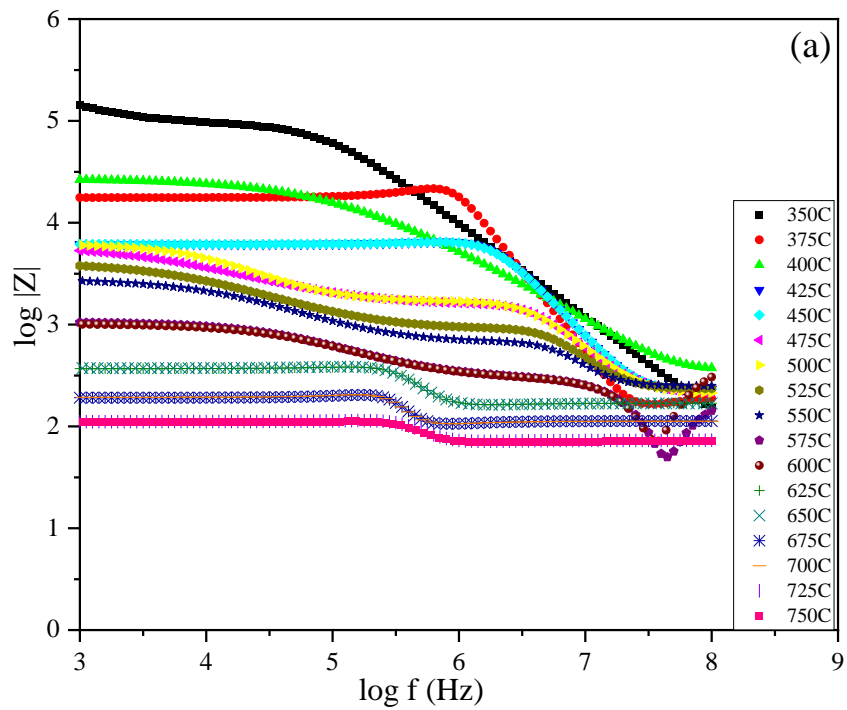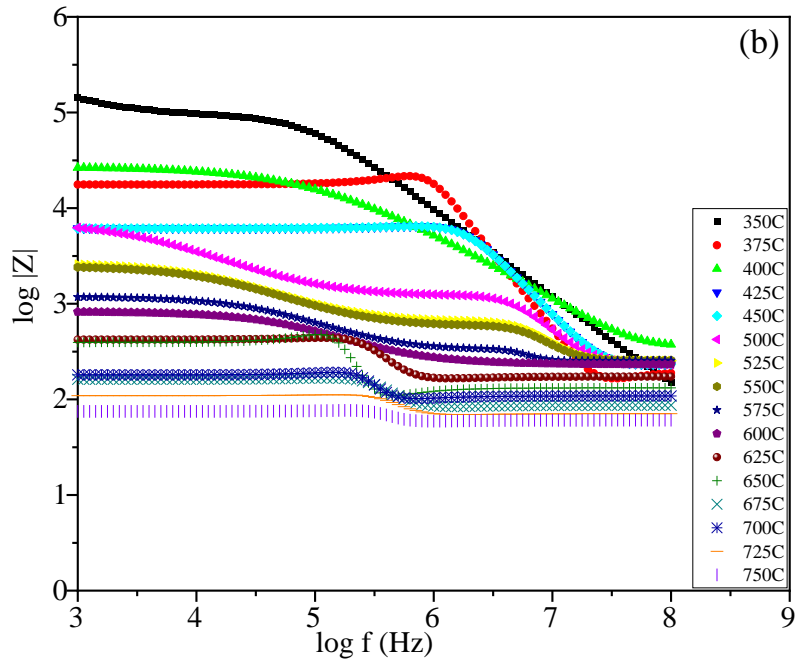
Fig. A.18: Bode plots of Ho₂Zr₂O₇ pellet with two step sintering; I-1500°C-5min, II-1300°C -96h (a) heating (b) cooling

A.6. AC impedance data of holmium hafnate prepared through granules and sintered using SSS process
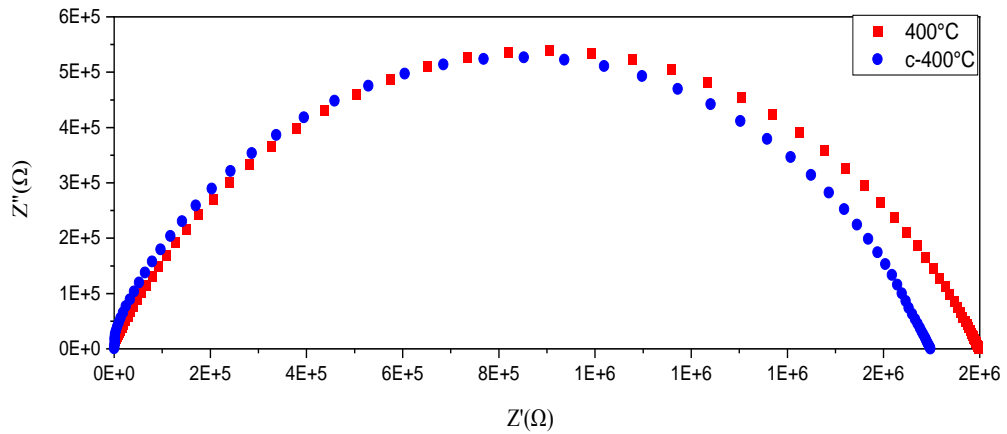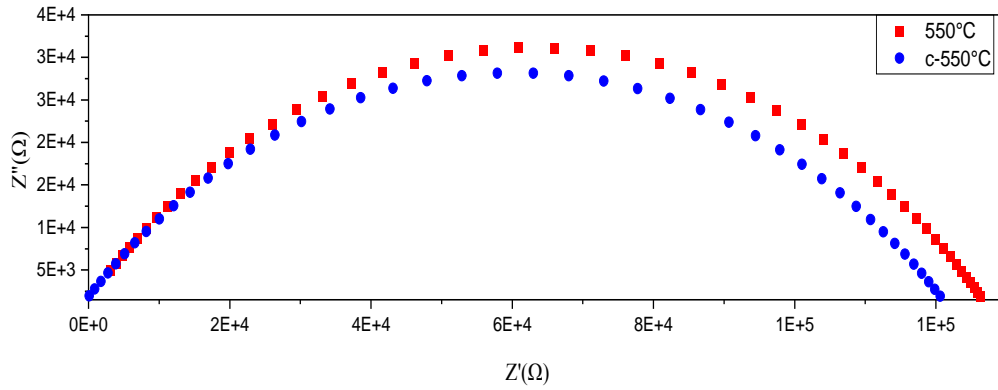
Fig. A.19: Complex impedance plots of holmium hafnate nanopowders obtained from granules method sintered at 1500 °C for 2h measured in heating cycle at (a) 400 °C and (b) 550 °C, (c-400 °C and c-550 °C for cooling cycle).
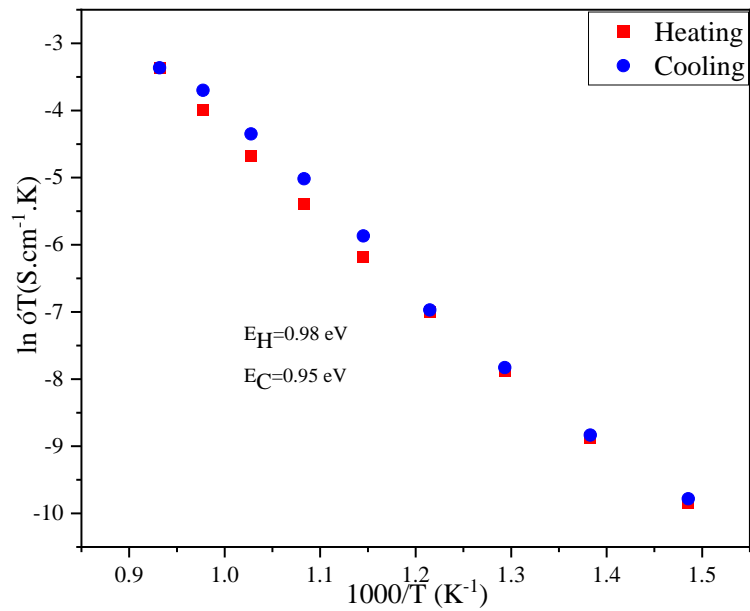
Fig. A.20: Temperature dependence Arrhenius plot of bulk conductivity in heating and cooling cycles
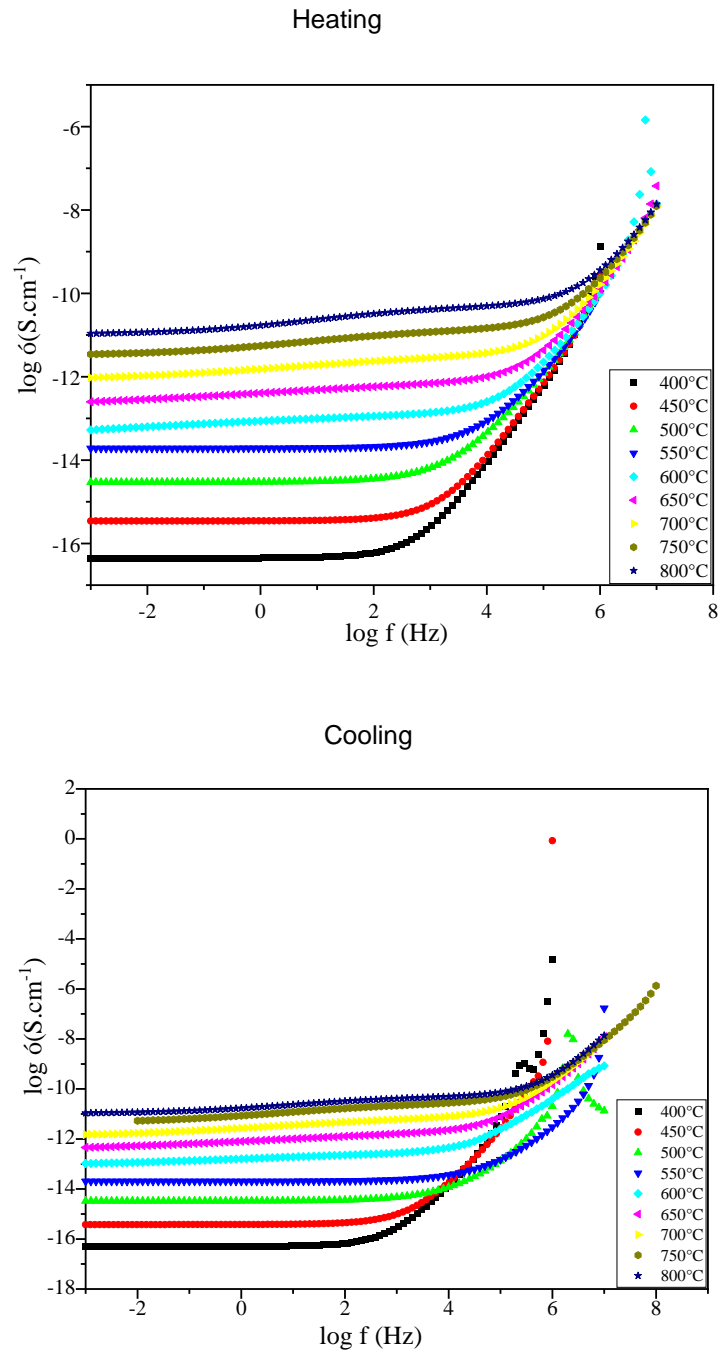
Fig. A.21: Frequency and temperature dependence of the real parts of Ho₂Hf₂O₇ conductivity (a) heating (b) cooling sintered using SSS process.

A.7. TGA/DSC and XRD scans of unwashed metal alginate beads
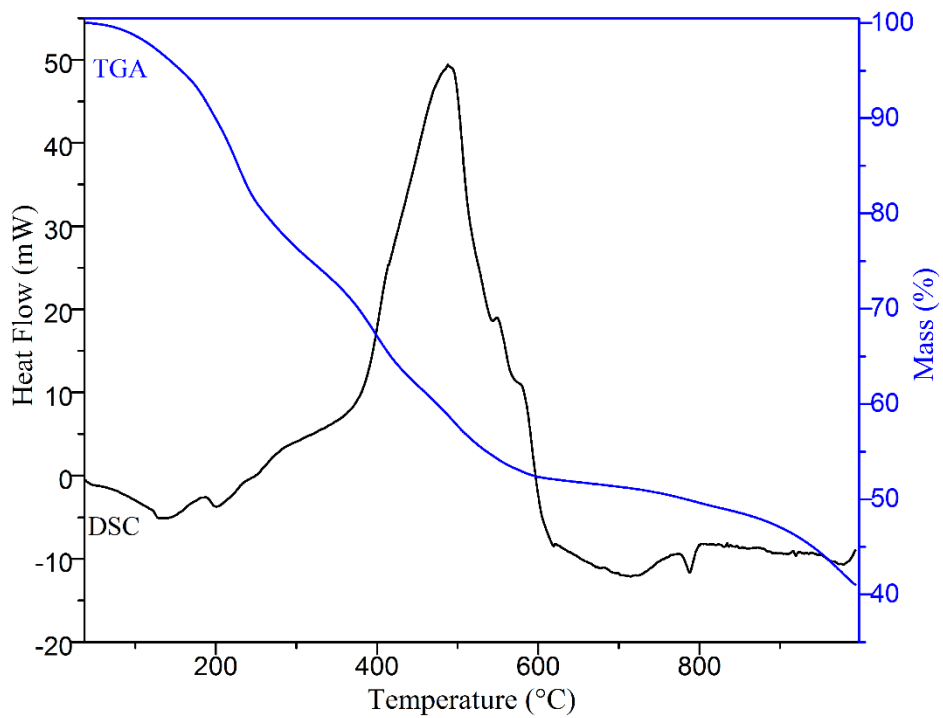
Fig. A.22: TGA/DSS analysis of unwashed metal alginate beads
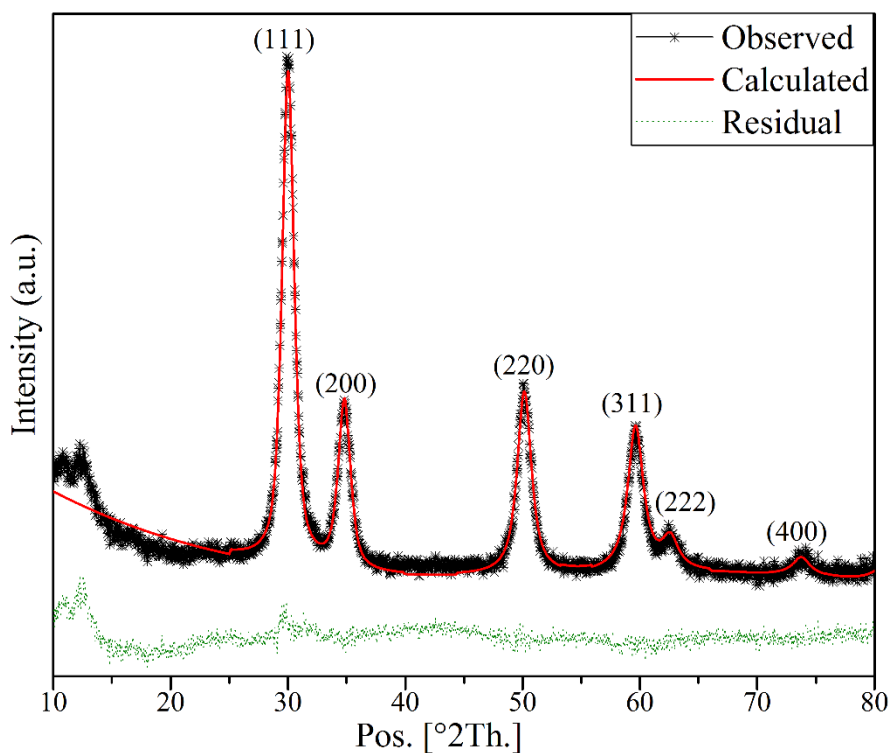
Fig. A.23: Rietveld refined XRD of holmium hafnate nanoparticles obtained from the unwashed

metal alginate beads